Committed Individuals Solving Challenging Problems

REACTION
ENGINEERING
INTERNATIONAL

OPTIMIZED FUEL INJECTOR DESIGN for MAXIMUM IN-FURNACE NO_X REDUCTION and MINIMUM UNBURNED CARBON

FINAL REPORT

October 1, 1995 - September 30, 1997

M. P. Heap, J. Brouwer, K. A. Davis, A. F. Sarofim, M. J. Bockelie, E. G. Eddings
Reaction Engineering International

D. W. Pershing, J. P. Klewicki
University of Utah

R. H. Hurt
Brown University

R. A. Lisauskas
D. B. Riley, Inc.

January 1998

DE-AC22-95PC95103

Reaction Engineering International
77 West 200 South Suite 210
Salt Lake City, UT 84101

University of Utah
College of Engineering
Merrill Engineering Building
Salt Lake City, UT 84112

Brown University
Division of Engineering
Box D
Providence, RI 02912

D. B. Riley, Inc.
Riley Research Center
45 McKeon Road
Worcester, MA 01610

ABSTRACT

Reaction Engineering International (REI) has established a project team of experts to develop a technology for combustion systems which will minimize NO_x emissions and minimize carbon in the fly ash. This much need technology will allow users to meet environmental compliance and produce a saleable by-product. The team consists of REI, experts in NO_x formation and control and combustion modeling; Dr. Robert Hurt (Brown University), an expert in char reactivity; Dr. Joseph Klewicki (University of Utah), an expert in two-phase mixing; Riley Stoker Corporation, experts in firing systems; and the Electric Power Research Institute (EPRI), an industrial partner to maintain focus on the end-user.

This study is concerned with the NO_x control technology of choice for pulverized coal fired boilers, "in-furnace NO_x control," which includes: staged low-NO_x burners, reburning, selective non-catalytic reduction (SNCR) and hybrid approaches (e.g., reburning with SNCR). The program has two primary objectives:

1) To improve the performance of "in-furnace" NO_x control processes.

2) To devise new, or improve existing, approaches for maximum 'in-furnace' NO_x control and minimum unburned carbon.

The program involves: 1) fundamental studies at laboratory- and bench-scale to define NO reduction mechanisms in flames and reburning jets; 2) laboratory experiments and computer modeling to improve our two-phase mixing predictive capability; 3) evaluation of commercial low-NO_x burner fuel injectors to develop improved designs, and 4) demonstration of coal injectors for reburning and low-NO_x burners at commercial scale.

The specific objectives of the two-phase program are to:

1 Conduct research to better understand the interaction of heterogeneous chemistry and two phase mixing on NO reduction processes in pulverized coal combustion.

2 Improve our ability to predict combusting coal jets by verifying two phase mixing models under conditions that simulate the near field of low-NO_x burners.

3 Determine the limits on NO control by in-furnace NO_x control technologies as a function of furnace design and coal type.

5 Develop and demonstrate improved coal injector designs for commercial low-NO_x burners and coal reburning systems.

6 Modify the char burnout model in REI's coal combustion code to take account of recently obtained fundamental data on char reactivity during the late stages of burnout. This will improve our ability to predict carbon burnout with low-NO_x firing systems.

The commercial products resulting from this effort will not only include improved fuel injector hardware for low-NO_x firing systems, but also improved computational tools to help the utility boiler operator determine the optimum low-NO_x firing configuration taking account of both corrosion potential and increases in unburned carbon.

In addition to REI, the program participants include the University of Utah, Brown University, DB Riley and EPRI. Computer simulation is central to the whole program, providing both data evaluation and generalization. The two-phase mixing studies carried out at the University of Utah were planned to develop data to validate the two-phase mixing models in *GLACIER*. In Phase II, the two phase experimental system will be used to help develop fuel injection hardware by screening designs to determine how to optimize particle mass distribution at the injector exit as a function of location and particle size.

Studies at Brown University are concentrating on two aspects of char reactivity with respect to char oxidation and the reduction of NO. In Phase I, the emphasis has been placed on the development of an advanced burnout model that can be integrated with *GLACIER* and the construction of an apparatus that will allow the hypothesis that young chars have a higher potential to reduce NO than old chars. In Phase II, the emphasis will shift from carbon burnout to NO reduction.

The combustion testing in Phase I was carried out at the University of Utah in bench- and pilot-scale facilities. The work will continue in Phase II and will be augmented by full-scale testing at DB Riley on the U-Furnace Test Facility with the LEBS Firing System.

In Phase I, the simulation task concentrated on fuel injection systems and on the evaluation of advanced burnout models for predicting LOI from low-NO_x firing systems. In Phase II there will be more emphasis on evaluating pilot-scale data; but full system simulations will be important since computer modeling is the only way to evaluate multiple burner effects at scale.

1.0 EXECUTIVE SUMMARY

1.1 PROGRAM GOALS AND ORGANIZATION

The study described in this report is concerned with the NO_x control technology of choice for pulverized coal fired boilers; i.e., "in-furnace NO_x control" which includes staged low-NO_x burners, reburning, selective non-catalytic reduction (SNCR) and hybrid approaches, e.g. reburning with SNCR. The program has two primary objectives:

1) To improve the performance of "in-furnace" NO_x control processes.

2) To devise new, or improve existing, approaches for maximum "in-furnace" NO_x control and minimum unburned carbon.

The program involves: 1) fundamental studies at laboratory- and bench-scale to define NO reduction mechanisms in flames and reburning jets; 2) laboratory experiments and computer modeling to improve our two phase mixing predictive capability; 3) evaluation of commercial low-NO_x burner fuel injectors to develop improved designs; and 4) demonstration of coal injectors for reburning and low-NO_x burners at commercial scale.

The specific objectives of the two phase program are to:

1 Conduct research to better understand the interaction of heterogeneous chemistry and two phase mixing on NO reduction processes in pulverized coal combustion.

2 Improve our ability to predict combusting coal jets by verifying two phase mixing models under conditions that simulate the near field of low-NO_x burners.

3 Determine the limits on NO control by in-furnace NO_x control technologies as a function of furnace design and coal type.

4 Develop and demonstrate improved coal injector designs for commercial low-NO_x burners and coal reburning systems.

5 Modify the char burnout model in REI's coal combustion code to take account of recently obtained fundamental data on char reactivity during the late stages of burnout. This will improve our ability to predict carbon burnout with low-NO_x firing systems.

The commercial products resulting from this effort will not only include improved fuel injector hardware for low-NO_x firing systems but also improved computational tools to help the utility boiler operator determine the optimum low-NO_x firing configuration taking into account both corrosion potential and increases in unburned carbon.

In addition to REI, the program participants include the University of Utah, Brown University, DB Riley and EPRI. Computer simulation is central to the whole program, providing both data evaluation and generalization. The two phase mixing studies carried out at the University of Utah were designed to develop data to validate the two phase mixing models in ***GLACIER.*** In Phase II, the two phase experimental system will be used to help develop fuel injection hardware by screening

designs to optimize particle mass distribution at the injector exit as a function of location and particle size.

Studies at Brown University are concentrating on two aspects of char reactivity with respect to char oxidation and the reduction of NO. In Phase I the emphasis has been placed on the development of an advanced burnout model that can be integrated with ***GLACIER*** and the construction of an apparatus that will allow the hypothesis that young chars have a higher potential to reduce NO than old chars. In Phase II the emphasis will shift from carbon burnout to NO reduction.

The combustion testing in Phase I was carried out at the University of Utah in bench- and pilot-scale facilities. The work will continue in Phase II and will be augmented by full-scale testing at DB Riley with the LEBS Firing System.

In Phase I the simulation task concentrated on fuel injection systems and on the evaluation of advanced burnout models for predicting LOI from low-NO_x firing systems. In Phase II there will be more emphasis on evaluating pilot-scale data; however, full system simulation will be important since computer simulation is the only way to evaluate multiple burner effects at scale.

1.2 CARBON IN ASH AND LOW-NO_x FIRING CONDITIONS

1.2.1 EXPERIENCE WITH LOW-NO_x FIRING SYSTEMS

When the program was conceived it was thought that the major impact on boiler performance associated with in-furnace NO_x reduction technologies was the increase in unburned carbon in the fly ash. Recently, the utility industry has been made aware of another problem, increased rates of waterwall wastage in units fitted with low-NO_x firing systems, particularly supercritical units firing eastern bituminous coals.

For those boilers required to implement some form of NO_x control to meet Clean Air Act Amendment Phase I limits, low-NO_x burners and/or combustion modification was the preferred option. Although many regarded low-NO_x burners the equivalent of “plug and play”, field experience has been completely to the contrary (Jones, 1997). Most plants that have installed low-NO_x burners report an increase in LOI (Loss on Ignition). An increase in 10% unburned carbon means a 1% loss in combustion efficiency. But the increased costs associated with ash disposal could dwarf the fuel replacement costs associated with this loss in efficiency. Some increase in LOI was expected. However, recently another problem has surfaced. Approximately ten percent of Phase I units are experiencing accelerated waterwall tube wastage associated with low-NO_x firing. The extent varies from “noticeable but manageable” to a “significant increase” in subsequent forced outages. Availability has a major impact upon the cost of power produced by a particular plant. Thus the cost of low-NO_x firing systems may be significantly greater than the equipment/installation cost.

1.2.2 INTEGRATION OF CBK WITH *GLACIER*

GLACIER, REI’s reacting CFD code, includes a char oxidation model with a mean oxidation rate and a new Carbon Burnout Kinetic (CBK) model has been added. CBK is a coal general formulation designed to evaluate the total extent of carbon burnout and flyash carbon content for pulverized coal particles with known temperature/oxygen histories.

The comprehensive CBK model was used in a series of one-dimensional reacting flow simulations to better understand the roles of the various individual phenomena described in the code on the overall prediction of carbon burnout. The thermal annealing submodel was found to have a large effect on reactivities and burnout levels at combustion temperatures and times typical of pulverized-coal fired boilers. The submodel of statistical kinetics and densities has a small effect throughout most of burnout, but contributes significantly to the long tails observed in laboratory burnout curves. Finally, the submodel of carbon/mineral interactions contributes substantially to the long burnout tails. None of these individual component submodels can be deleted from CBK without some loss of general predictive capability. For boiler applications however, coarse binning can be used in the submodel of statistical kinetics and densities without introducing significant error. The CBK model describes all of the significant features of the Sandia char combustion database.

In order to prepare this model for integration into a comprehensive ***GLACIER*** code, careful sensitivity analyses were carried out in an effort to reduce the computational demands of the thermal annealing submodel. Numerous test cases were examined to find the optimal limits of integration and step size, considering both accuracy and speed.

GLACIER has been modified to accept/provide appropriate data for transferal between the two codes. Fuel specific quantities (***GLACIER*** inputs) are shared and ensemble-averaged values for oxygen concentration, gas temperature, and radiative environment temperature for statistical particle "clouds" (***GLACIER*** calculation results) are input to CBK. CBK has been modified to compile results for each particle cloud and to determine and output total unburned carbon in flyash.

Table 1 compares unburned carbon calculated by the original ***GLACIER*** char burnout model and the ***GLACIER***/CBK model with the actual field measurements.

Table 1: Predicted and Measured Unburned Carbon (%)

	GLACIER	CBK	Measured
Keystone Pre-retrofit	5	6.7	4 to 5
Keystone Post-retrofit	16.2	14	8 to 12
Hammond Pre-retrofit	3	4	4
Hammond Post-retrofit	7		8

1.3 BOILER SIMULATIONS

The lower furnace of two boilers, Keystone Unit 2 and Hammond Unit 4, have been modeled using ***GLACIER***. Keystone Unit 2 is a Combustion Engineering, Inc. Combined Circulation Balanced Draft Divided Furnace Steam Generator rated at 850 MW_e consisting of two identical tangential-fired furnaces. Each of four burner stacks consists of eight levels of coal burners alternating with air inlets. In 1994, the unit was retrofitted with an ABB C-E Services, Inc. Low-NO_x Concentric Firing System (LNCFS) Level III. The LNCFS Level III system utilizes both Close Coupled Over Fire Air (CCOFA) and Separated Overfire Air (SOFA). The low-NO_x retrofit has put Keystone Unit 2 in compliance with Federal Government NO_x emission regulations, but at the expense of increases in both waterwall tube corrosion and LOI. Corrosion rates of up to 50-70 mil/

year have been observed in certain regions of the front and back waterwalls at CCOFA and SOFA inlet port elevations. One furnace (Furnace "B") was modeled up to the nose with a 660,000 node Computational Fluid Dynamics (CFD) grid. ABB-measured coal flow rates are used in the model with sufficient combustion air for an excess oxygen level of 3.5% at the superheater entrance.

Georgia Power's Hammond Unit 4 is a 500 MW_e opposed-wall-fired facility with 24 burners. Prior to low-NO_x retrofit, the unit included Foster-Wheeler's Intervane burners. After retrofitting, the unit included Foster Wheeler's Controlled-Flow/Split-Flame burner, advanced overfire air (an independent windbox stream for improved penetration/control) through 8 directly opposed ports, and 4 underfire air ports. This furnace was simulated with a symmetry plane along the vertical center from front to rear with more than 480,000 computational nodes.

As mentioned, Keystone is a twin furnace, tangentially-fired unit with eight burner levels firing from four burner stacks on the front and rear walls. Figure 1.1 shows the predicted carbon burnout as a function of burner level and burner location for pre- and post-retrofit designs. Similar predictions, carbon burnout as a function of burner, are available for Hammond and allow the following same general conclusions to be drawn:

1 The predicted burnout shows that all burners do not contribute equally to the final burnout level.

2 Particle burnout varies with burner height and location.

3 Unburned carbon is highest, as expected, for the post-retrofit cases.

These predictions of unburned carbon point to one major conclusion:

- Any evaluation of an in-furnace NO_x control technology must consider the total system and may be very boiler specific.

One must now consider possible methods for improving burnout without creating any undue impact on NO_x emissions. Increasing the fineness of the coal delivered to each burner is not necessarily required. It may not be necessary to modify every burner; it might be possible to operate the bottom rows more fuel rich and add air to the upper burners. An initial analysis of the OFA systems suggests that burnout could be improved by an improved OFA design. But, any option requires an accurate fireside simulator for a proper evaluation.

Although not part of the original scope, ***GLACIER*** has been used to determine the conditions that might lead to waterwall corrosion at Keystone. ***GLACIER*** does not predict corrosion rates but does provide an accurate picture of conditions close to the wall that might contribute to corrosion, including:

- Local gas concentrations including carbon monoxide, hydrogen sulfide and sulfur dioxide.

- Heat flux to the wall, because this can affect deposit formation and slagging.

- Particle deposition rates at the wall.

- Carbon and sulfur content of the particles being deposited at the wall.
- Deposition rates of FeS particles present in the coal stream.

The measured corrosion rates in the Keystone boiler are highest on the front and rear walls above the close coupled over fire air near the separated over fire air, and lower on the side and center walls. Figure 1.2 compares the fraction of unburned carbon in the wall deposit on the rear wall for the pre- and post-retrofit simulations. Shown also are measured wastage rates. The simulations suggest that high corrosion rates in excess of 50 mils/year occur in regions of the waterwall where there are high gradients in gas concentrations.

Figure 1.3 compares the burnout history for one particle cloud starting from the same location in the fuel injector for both the pre- and post-retrofit cases. Figures 1.3a and 1.3b show two particle sizes entering from the burners on the front wall at level six near the center wall. The smaller particle does not burnout in the post-retrofit case. Figure 1.3c presents the same information but for a particle cloud entering from the front side coal nozzle at the same level. This particle cloud does not burn out rapidly in either the pre- or post-retrofit cases. In fact the post-retrofit case shows significant unburned carbon. This emphasizes the point made earlier that in order to solve the problems attributed to low-NO_x firing it is necessary to consider the total system if the most cost effective solution is to be identified.

1.4 HOMOGENEOUS AND HETEROGENEOUS CHEMISTRY ASSOCIATED WITH NO REDUCTION IN FLAMES AND REBURNING JETS

1.4.1 COUPLING BETWEEN NO_x REDUCTION AND CARBON BURNOUT

As discussed in Subsection 1.2, the available field data suggests that use of low-NO_x firing systems invariably results in an increase in unburned carbon. To quantify the relationship between NO_x and unburned carbon under well defined conditions, a series of experiments was conducted in the 100,000 Btu/hr U furnace under both premixed and diffusion conditions utilizing a Utah bituminous coal. Duplicate impactor samples were obtained for particle size and composition analysis at four distinct conditions, each with an overall stoichiometric ratio of 1.15; the measured NO level for these conditions was as follows:

- Premixed, base case: NO_x = 912 ppm
- Diffusion burner, axial flame: NO_x = 484 ppm
- Premixed, staged, short rich zone residence time case: NO_x = 500 ppm
- Premixed, staged, long rich residence time case: NO_x = 166 ppm

Figure 1.4 summarizes the NO_x and unburned carbon results for the four different cases. These small scale results are in good agreement with full-scale data; as the NO_x emissions are decreased, the unburned carbon losses increase. The following observations are significant:

1. The gas-stabilized, axial flame provides significant NO_x reduction with only a modest increase in carbon loss relative to the idealized premixed case.

2. The carbon loss seems to be dominated by the largest particles (greater than 10 microns) and, in the very low NO_x case, it appears that the carbon problem is simply large particles which were not completely burned within the combustion zone prior to the thermal quench.

3. While a long, fuel rich residence time is highly desirable for NO_x control purposes, it will likely lead to LOI problems.

4. There is some evidence of soot formation based on the very fine particulate data.

These results clearly suggest that if one wishes to simultaneously achieve good carbon burnout and low NO_x emissions, it will be necessary to provide sufficient oxygen early in the combustion process to ensure that the largest particles are completely burned. This will inevitably result in the production of significant NO_x which must subsequently be destroyed. Therefore, one major focus of this project was on the chemical mechanisms for destruction of NO_x after it has been produced. The next two subsections focus specifically on the optimization of the homogeneous and heterogeneous mechanisms for this destruction. The final portion of this section examines practical concepts designed to embody the optimized reduction processes without negative impact on carbon burnout.

1.4.2 HOMOGENEOUS NO REDUCTION PROCESSES

It is now well established that reburning or secondary fuel injection can be used to reduce previously formed NO; however, conventional reburning has the drawbacks that it requires a separate fuel addition system and, dispersion of the reburning fuel can be difficult in a large boiler. In addition, if pulverized coal is used as the reburning fuel, the ultimate effectiveness is limited (1) by the fact that the reburning coal contains fuel nitrogen itself, and (2) by the problem of ensuring that the largest particles in the reburning coal burn completely prior to the convective passages. The reburning coal can be micronized but this increases control costs.

In this project detailed measurements were made with a large reburning coal jet fired into combustion products. The reburning coal jet was fired axially down the center of the furnace into typical combustion products containing 500 ppm NO (created externally). Figure 1.5 illustrates the detailed results for the NO concentrations as a function of radial and axial location. At the first sampling point (9 inches), the emissions have actually increased on the center line due to the oxidation of the nitrogen in the reburning coal. By 33 inches the emissions have dropped across the flow field and the jet itself has spread to the walls (as indicated by CO profiles, not shown). The ultimate NO_x concentration in the exhaust was 190 ppm for the case as shown in Figure 1.4. At the 33 inch sampling point the mean concentrations of the other major species were relatively uniform at the levels indicated below:

Species	Concentration	Species	Concentration
CO	6500 ppm	CH4	900 ppm
Acetylene	5000 ppm	HCN	35 ppm
NH3	<2 ppm		

Conventional reburning chemistry would suggest that the drop from the NO levels shown at 33 inches in Figure 1.5 to the final 190 ppm exhaust value was due to the oxidation of the remaining hydrocarbon species. However, as the following subsections will indicate, it is also likely that the decrease was, in part, associated with the oxidation of CO and the burnout of residual char. It is also interesting to note that the reduction occurs relatively uniformly across the furnace radius once the reburning fuel has spread in search of the available oxygen.

Previous work by some of the authors had suggested that CO could be participating in the reburning process in a manner not anticipated by the currently accepted hydrocarbon mechanism. To evaluate this hypothesis, several different types of experiments were conducted as part of this program. Figure 1.6 compares the results from simple CO reburning in which CO was added downstream of the primary flame with that of natural gas. In each case the initial (primary zone) NO was 500 ppm. At stoichiometries near 1.0 (lower amounts of reburning fuel), CO is not as effective as natural gas at incinerating the primary zone NO. However, by a reburning stoichiometry of 0.8, the results are indistinguishable. These results clearly demonstrate that CH radical attack is not the only mechanism for reducing NO.

To investigate the temperature sensitivity of the NO/CO reactions, a series of experiments was conducted in which the reburning fuel was added at different distances from the primary burner. Figure 1.7 summarizes these results for the primary zone stoichiometry of 1.05, a reburning zone stoichiometry of 0.9, and an overall stoichiometric ratio of 1.15. With natural gas as the reburning fuel it is desirable to add the gas as far from the addition of the final burnout air as possible to maximize the reaction time available in the fuel rich reburning zone. The gas results even suggest that the highest temperature is the most desirable. The CO reburning results again suggest that a mechanism other than hydrocarbon radical attack must be significant. This mechanism appears to have an interesting temperature sensitivity; the greatest reduction occurs at an injection point approximately 7.5 feet from the burner where the flue gas temperature is about 2400 °F. This is in marked contrast to the natural gas results, although the reductions are almost equally significant even at this reburning stoichiometry.

To confirm the importance of CO reactions, a series of experiments was conducted where NO was injected into combustion products at different distances along the furnace. Figure 1.8 summarizes these results for initial stoichiometries of both 0.85 and 0.95. Interestingly the lowest exhaust NO_x emissions occurred when the NO was injected at 4.5 feet from the burner which corresponds to the same gas temperature noted as the optimum in the CO reburning experiments (Figure 1.7). Further, at the optimum position, there was no dependence on the bulk stoichiometry.

In summary, these three different kinds of experiments prove rather conclusively that there exists an important reaction mechanism between CO and NO which, if properly utilized, can help decrease NO from large particles in the early part of the flame.

1.4.3 HETEROGENEOUS NO REDUCTION PROCESSES

Unfortunately it is not simple to isolate the importance of heterogeneous NO reduction reactions under realistic combustion conditions; however, two different approaches were used to evaluate this issue. First, the University of Utah U-furnace was used to provide overall guidance. Figure 1.9 shows the results of reburning experiments where the reburning fuel was a wood char containing essentially no (less than 0.2% by weight) fuel nitrogen. These experiments were

conducted with and without oxygen present to evaluate the importance of O_2 on the process. The primary zone stoichiometry was operated slightly fuel rich to eliminate oxygen from the primary flow. The char was transported with nitrogen containing a controlled amount of oxygen. The initial NO (with no char injection) was approximately 500 ppm. As the data in Figure 1.9 indicate, a 60% NO reduction was achieved when the char transport stream was normal air (21% O_2). Reductions greater than 80% were achieved when the entire system was operated oxygen deficient. It must be recognized that, particularly in the case where oxygen is present, the reburning reduction is likely due to a combination of homogeneous and heterogeneous effects. In the presence of oxygen, heterogeneous oxidation of the char to form CO and subsequent homogeneous reaction of the CO with NO occurs. In addition, particularly because of the no oxygen results, it appears likely that some heterogeneous reduction of NO on char is occurring. It should also be noted that the char used in these studies has a relatively high surface area because it was prepared from a wood pyrolysis process.

Figure 1.10 summarizes fundamental results which were obtained as part of the study by Professor Hurt at Brown University. The different symbols indicate data from the combustion of lignite chars, Illinois #6 chars, and petroleum cokes. These data were collected in a laboratory flame reactor where the different solid materials were injected downstream of a primary flame producing 1,000 ppm NO with 1% oxygen. The temperature at the point of fuel injection was approximately 2450 °F and the downstream residence time was nominally 100 msec. The data are reported as NO reduction reactivity expressed as an apparent heterogeneous rate constant. The char and coke samples did produce reactivities on the same order as the highest reactivity kinetics measured by Aarna and Suuberg. Again, however, the reduction cannot be solely attributed to heterogeneous NO reactions because of the presence of CO.

In conclusion, the result of the laboratory and bench scale experiments suggests that the heterogeneous NO reduction process should not be neglected. Because of the discovery of the CO/ NO destruction reaction mechanism, the results are not unambiguous but they do suggest the possibility of direct heterogeneous reduction.

1.4.4 INTEGRATED CONTROL CONCEPTS

The results of the experimental studies described previously have shown that to ensure adequate carbon burnout is achieved with the largest particles (and indeed all coal particles), sufficient oxygen must be provided early in the flame zone. This will unfortunately also ensure that a portion of the coal nitrogen is likewise oxidized and necessitates subsequent reduction of some NO. Our results have demonstrated that NO can be effectively reduced by hydrocarbons, by CO, and likely by hot char surfaces. It is also well known that NO can be selectively reduced by ammonia and other NH- and CN- compounds. Thus, there appears to be four possible paths to achieve low NO_x emissions (less than 0.2 lbs NO_2/MBtu) while simultaneously not increasing carbon loss and LOI:

1. Reduction in coal particle size in conjunction with optimized low-NO_x burners.

2. Conventional natural gas reburning downstream of the primary combustion zone.

3. Coal reburning plus downstream chemical addition for selective reduction.

4. Improved low-NO_x firing systems optimized for both minimum NO_x and acceptable LOI.

In prior studies the authors have worked extensively on the first three control concepts and shown that, in fact, from a scientific perspective they are all capable of producing very low NO_x emissions. Unfortunately these techniques are not attractive to many commercial clients because of economic considerations; they are all relatively expensive when the additional capital and operating expenses are fully considered. If possible, most utilities would like to avoid the use of selective reducing chemicals and/or large amounts of natural gas. Therefore, we believe the fourth option to be the most economically attractive and have focused the last portion of our Phase I efforts toward two alternatives which appear promising:

- Particle size and stoichiometry segmentation
- Gas stabilized axial flames

Each of these is discussed in the following subsections and they are also the focus of the pilot scale experimental work proposed for Phase II.

1.4.4.1 Segmented Firing

Figure 1.11 illustrates the segregated premixed pulverized coal (SPPC) burner that was created for this program to evaluate the desirability of coal and stoichiometry segmentation. The burner consists of inner and outer premixing chambers, each with separate primary coal and secondary air injection. A wide range of experiments were conducted varying overall excess air, inner stoichiometry, outer stoichiometry, inner/outer velocity ratio and inner/outer coal split. Figure 1.12 summarizes typical results for an overall stoichiometry of 1.05 with a 50/50 coal split. Here the NO_x emissions are reported as a function of the inner and outer stoichiometric ratios. Note that the minimum NO_x emissions do not occur when the stoichiometries are balanced at 1.05; rather, the optimum conditions are with a slightly fuel rich inner annulus (SR_i = 0.8) and an excess air outer annulus (SR_o = 1.3). These results were all obtained under overall excess air conditions; no attempt was made to stage the burner and further reduce the NO_x.

Table 2 summarizes results from all the SPCC burner studies, again at an overall stoichiometry of 1.05. Note that in every case the lowest NO_x emissions occur when the largest fuel stream is staged, but the degree of staging required changes depending on the distribution of the coal. Overall these results suggest that if the largest coal particles were concentrated in an outer stream which was operated under excess air conditions, it should be possible to achieve high burnout and low emissions. Under uniform conditions at an overall stoichiometric ratio of 1.05 the NO emissions was 650ppm.

Table 2: Segmented Premixed Pulverized Coal Burner (overall SR = 1.05)

Inner/Outer Split (%)	SR_i	SR_o	NO (ppm)
75/25	0.5	2.6	480
50/50	0.8	1.3	460
25/75	1.6	0.9	425

1.4.4.2 Gas Assisted Axial Flames

In a previous DOE funded program the authors discovered that if a small amount of natural gas was added around the periphery of an axial coal jet (to ensure firm flame anchoring on the fuel injector) significant emission reductions could be achieved. In the current program we discovered this process could be even further enhanced by adding the natural gas on the axis of the pulverized fuel jet. Figure 1.13 summarizes these results which are of particular interest because, when properly designed, this scheme would allow the pulverized coal to be burned under near stoichiometric conditions which favor the carbon oxidation. NO emissions of only 132 ppm were achieved with 4% natural gas and a coal jet stoichiometry of 0.9. Similar low emissions were also achieved for even higher coal jet stoichiometries, but more gas was required. Emission levels below 150 ppm without the use of any selective reduction chemicals would be very economically attractive. A portion of the Phase II studies would focus on the optimization of this concept in the University of Utah L1500 pilot-scale facility at 5 MBtu/hr.

1.5 PILOT-SCALE TESTS

Pilot-scale testing was not included in the original Phase I tests plan. However, because of the success of the bench-scale studies and the pressures imposed by the utilities with problems associated with low-NO_x firing systems, we have accelerated the schedule and preliminary tests have been carried out in the L1500.

The double concentric swirl burner had a coal injector with a central core and an outer annulus which could be fed with different grinds or the same grind. Two grinds were used a standard grind of 70% less than 200 mesh and a fine grind of 90% less than 325 mesh. Figure 1.14 compares three cases:

- the standard grind in both the core and the annulus;
- 75% of the coal as the standard grind in the annulus and 25%t of the fine grind in the core; and
- the reverse - 25% of the fine grind in the annulus and 75% of the standard grind in the core.

The preliminary data were taken under excess air conditions and show variations in NO emission with particle size stratification. There is an indication that at low excess air or when the burner is staged that the trends with particle size distribution may change. These data suggest that the radially stratification could be an effective way of controlling both NO_x and unburned carbon.

Figure 1.15 shows our concept for a low-NO_x burner modified with an improved coal injector to allow radial stratification by size through two annular coal pipes and in-situ reburning with an axial fuel jet that could be gas, oil or coal.

1.6 MODELING LOW-NO_X BURNERS

1.6.1 FUEL INJECTORS

Two commercial coal nozzles have been modeled. One had an annular coal injector and one a vane coal spreader. Simulations were performed on geometries with and without the tangential inlet section. Figure 1.16 illustrates the effects of the coal nozzle on various size particles. The gray surface in the center is the movable sleeve in the center of the coal pipe. The cross sectional planes are colored to illustrate variations in particle mass density and the black lines/circles display a few typical particle cloud trajectories. (The line is the statistical mean position, while the circles represent the variance about that mean.) The larger particles from every starting location quickly reach the wall and pass axially through the coal pipe in the valleys between anti-roping bars. The smaller particles tend to follow the flow and rarely hit the anti-roping bars. The intermediate size particles, which include the majority of the total mass, impact the roping bars, but do not remain in the valleys. This tends to more evenly distribute these particles. Another effect of this design is to segregate the intermediate and large particles into the ellipses, as opposed to the annulus. Since the exit area of the annulus and the ellipses are similar, the proportion of smaller particles exiting the ellipses/annulus are also similar. Another feature of this coal pipe, despite the presence of the anti-roping bars, is the maldistribution in the angular direction. The colors in the image represent the log of mass density and show significant variability in the exit plane.

1.6.2 COMMERCIAL LOW-NO_X BURNERS

Two commercial low-NO_x burners have been modeled as single burners, the DB Riley CCV II burner and the Foster Wheeler Split Flame Burner.

The controlled flow split flame simulation is particularly interesting because of its complex structure. Data from the coal nozzle simulation were used to establish the inputs for the single flame model. Immediately upon injection, the fine coal particles in the inner annulus mix into the hot core air and begin to devolatilize leading to ignition within the divergent. The four ellipses containing the bulk of the particle mass however, do not ignite until the end of the divergent. The simulations show why this is a low-NO_x burner, predicted exhaust NO levels were less than 200 ppm for this single flame. Once ignited, the elliptical streams of larger particles become fuel rich and destroy the NO formed from the smaller particles ain the early regions of the flame.

1.6.3 PROTOTYPE LOW-NO_X BURNERS

In support of the preliminary pilot scale tests the double concentric swirl burner has been modeled. The results, illustrated in Figure 1.17, show percent char integrated across the flame as a function of axial distance from the burner. The burner simulated two stratified coal distributions, big inside refers to all particles bigger than 80 microns passing down the central core and all particles less than 80 microns passing down the outer annulus. The percent char first increases as the volatiles are released and then decreases as char oxidation begins. These are preliminary calculations but they show that the radial variation of particles by size affects carbon burnout; however the process is complicated because the ignition distance varied in these calculations.

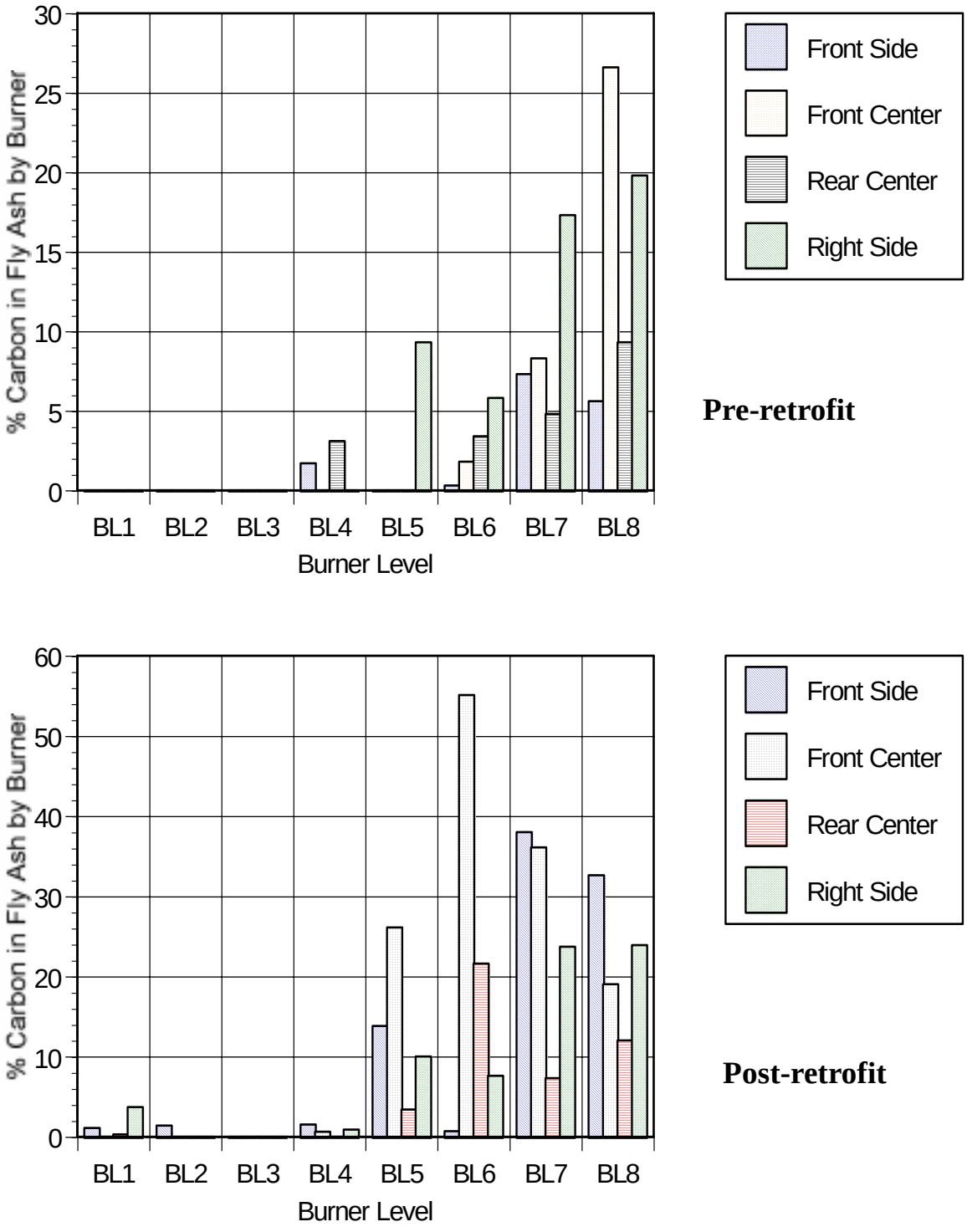

Figure 1.1 Pre-retrofit and post-retrofit carbon in flyash by burner level - Keystone Unit 2.

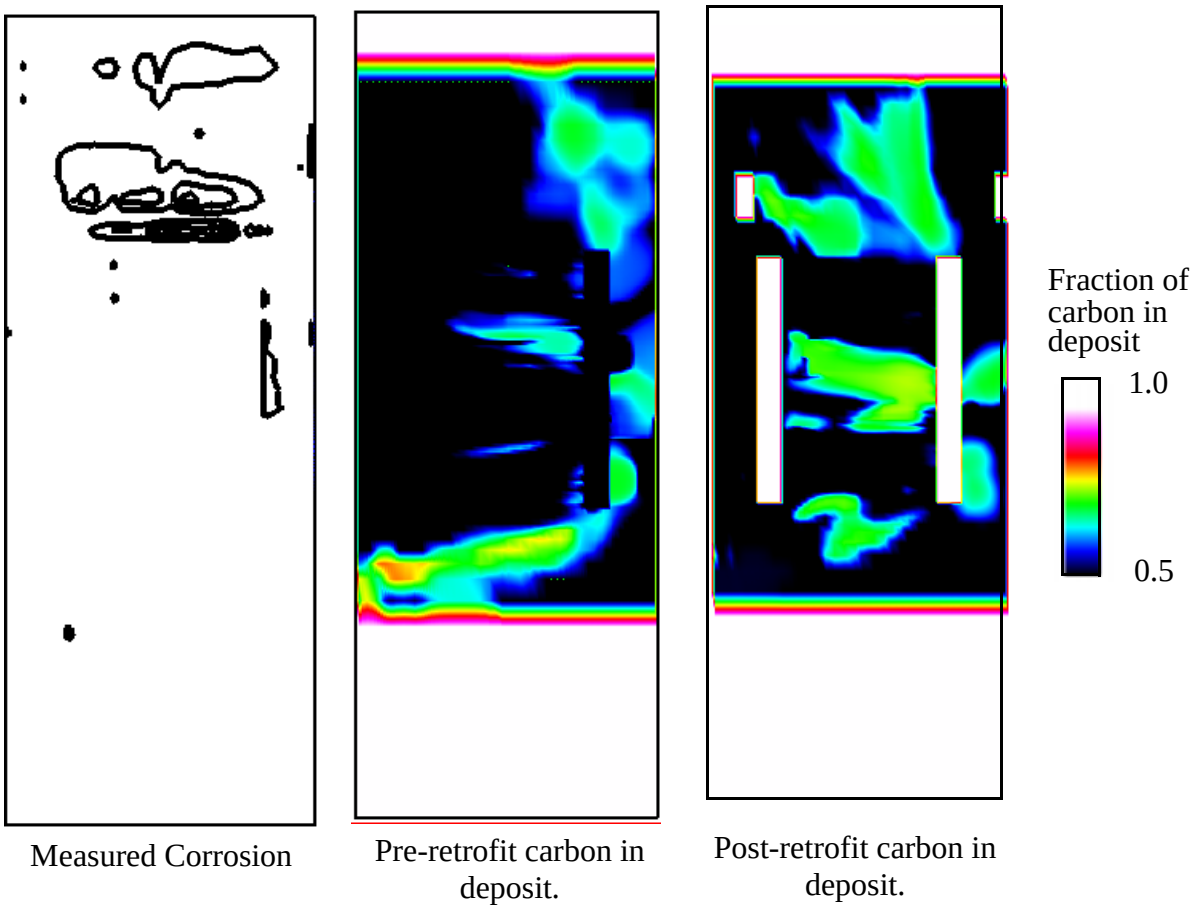

Figure 1.2 Measured corrosion on Keystone rear wall and fraction of carbon in deposit.

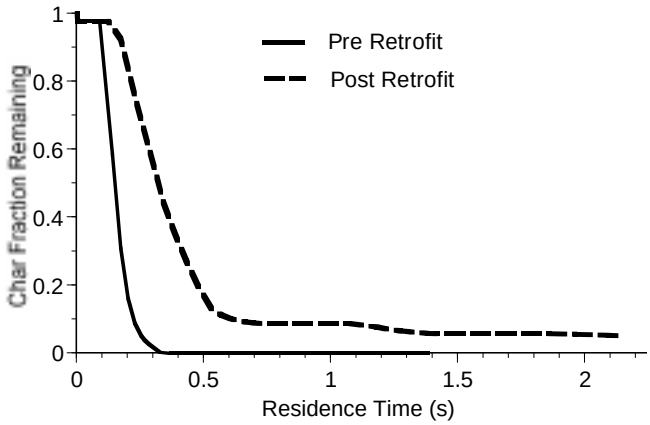

a) 43 micron coal particle entering from the front center nozzle on level 6

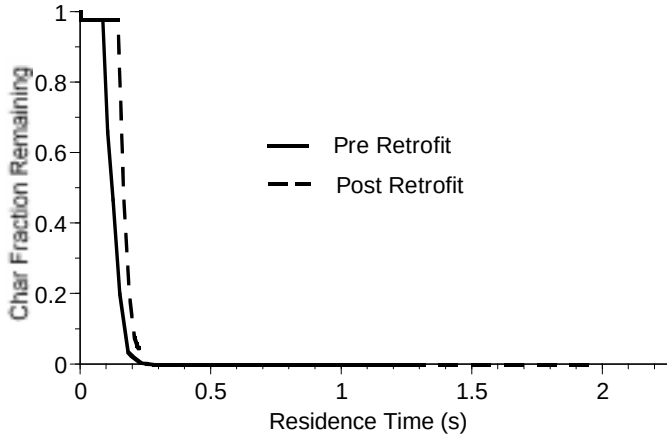

b) 85micron coal particle entering from the front center nozzle on level 6

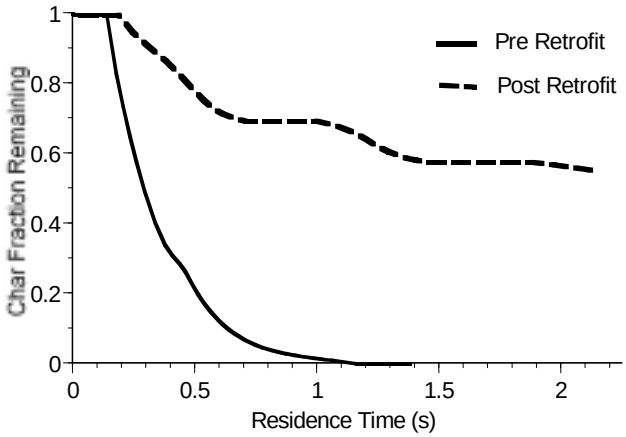

c) 43 micron coal particle entering from the front side nozzle on level 6

Figure 1.3 Fractional char remaining as a function of residence time.

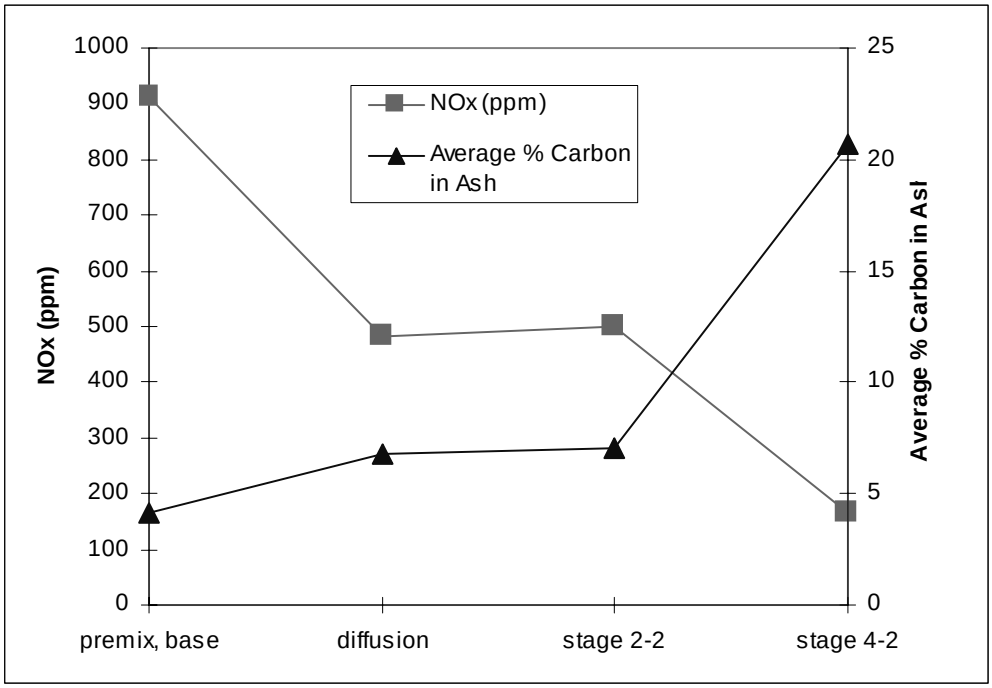

Figure 1.4 NOx and LOI for four different combustion conditions.

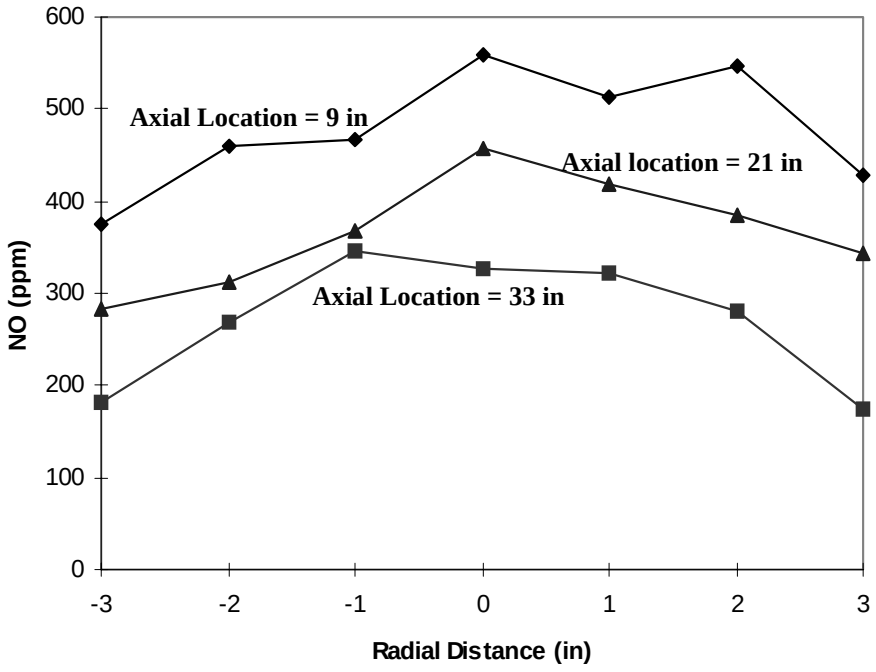

Figure 1.5 NO concentration at 3 axial locations in the large coal reburning jet as measured by the Fourier Transform Infrared (FTIR) instrument.

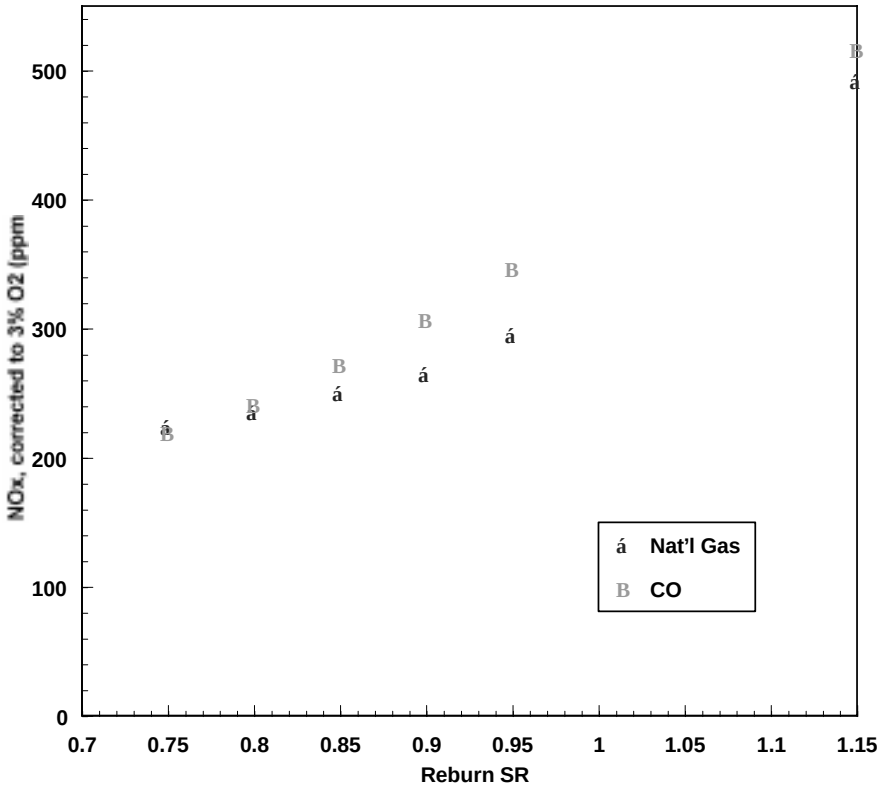

Figure 1.6 NO as a function of reburn stoichiometric ratio for CO and natural gas injection.

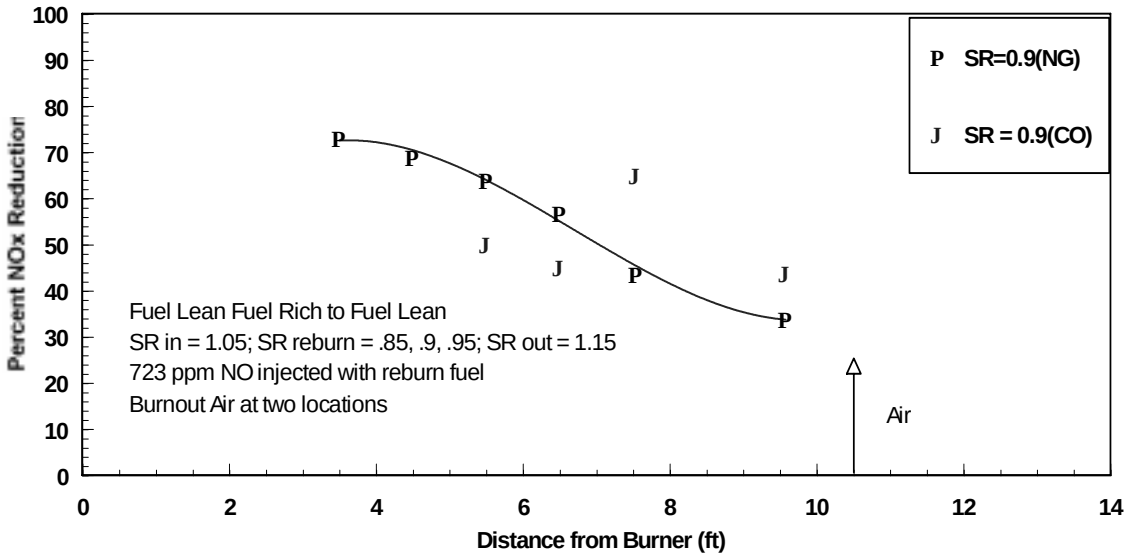

Figure 1.7 NO reduction with CO and natural gas injection at SR = 0.9.

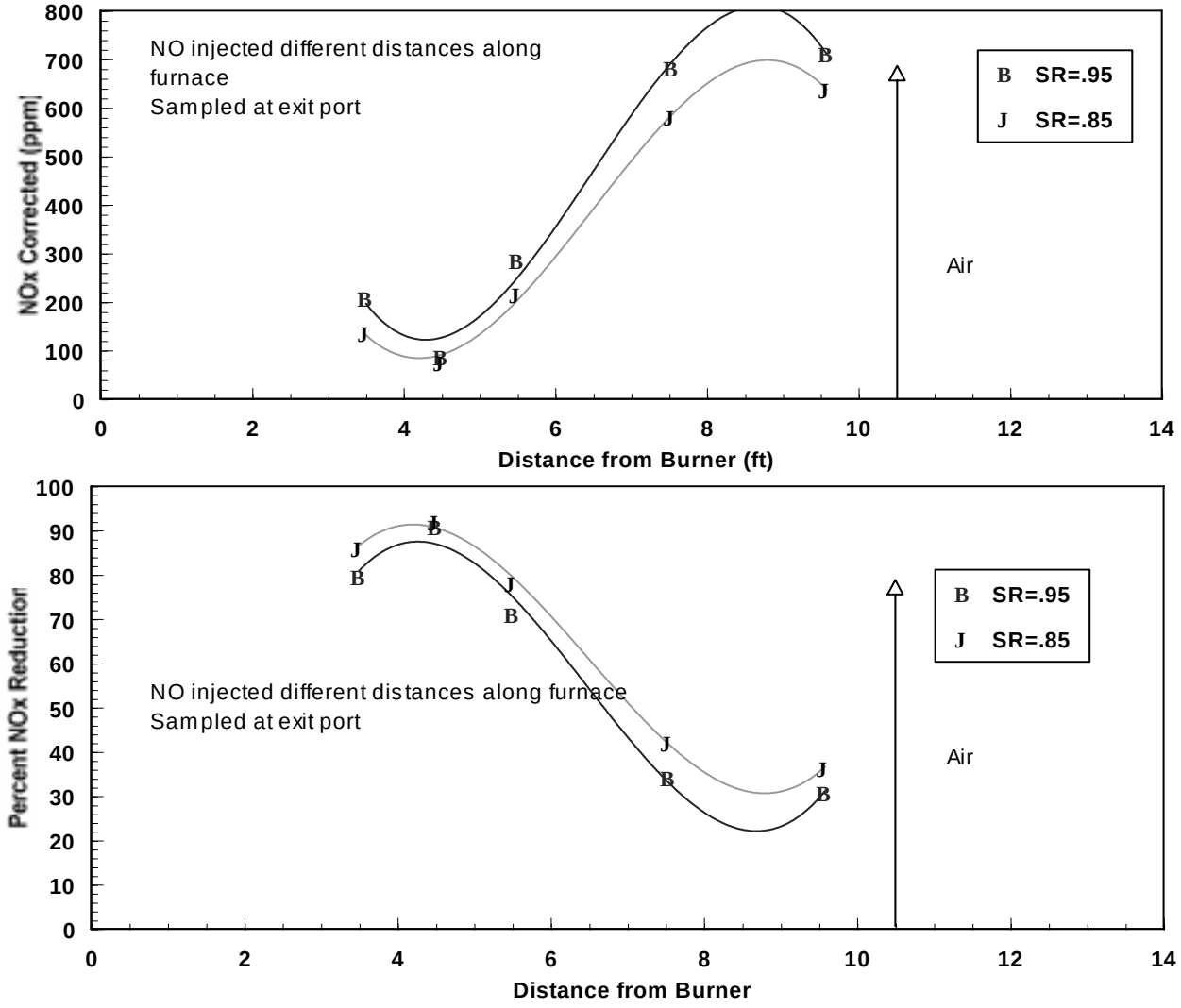

Figure 1.8 NO reduction for SR = 0.85 and SR = 0.95.

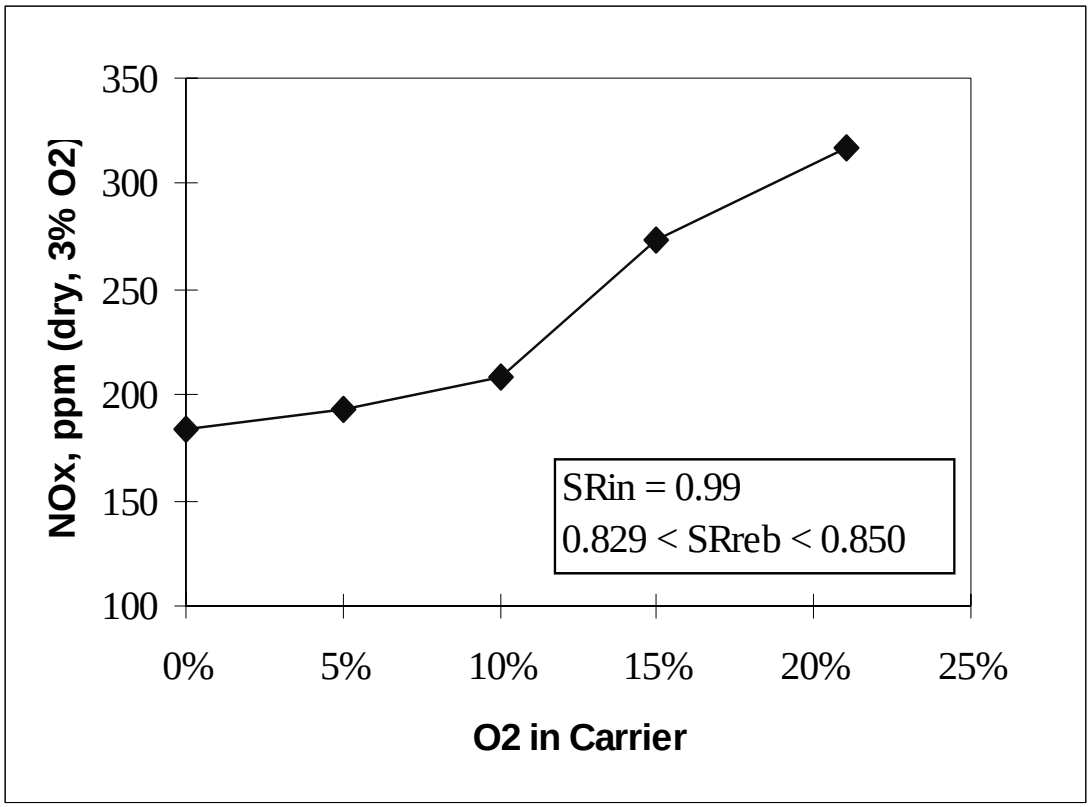

Figure 1.9 Char reburning of NO - dependence upon O_2 in carrier gas.

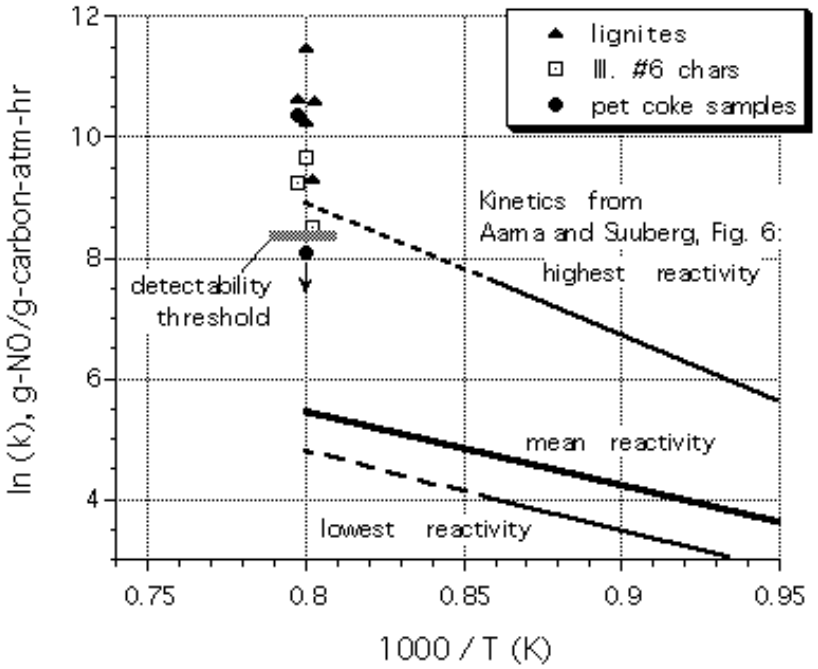

Figure 1.10 NO reduction reactivities for a variety of solid fuels expressed as apparent heterogeneous rate constants at 1250 K. Measured points are compared to literature values reviewed by Aarna and Suuberg, 1996.

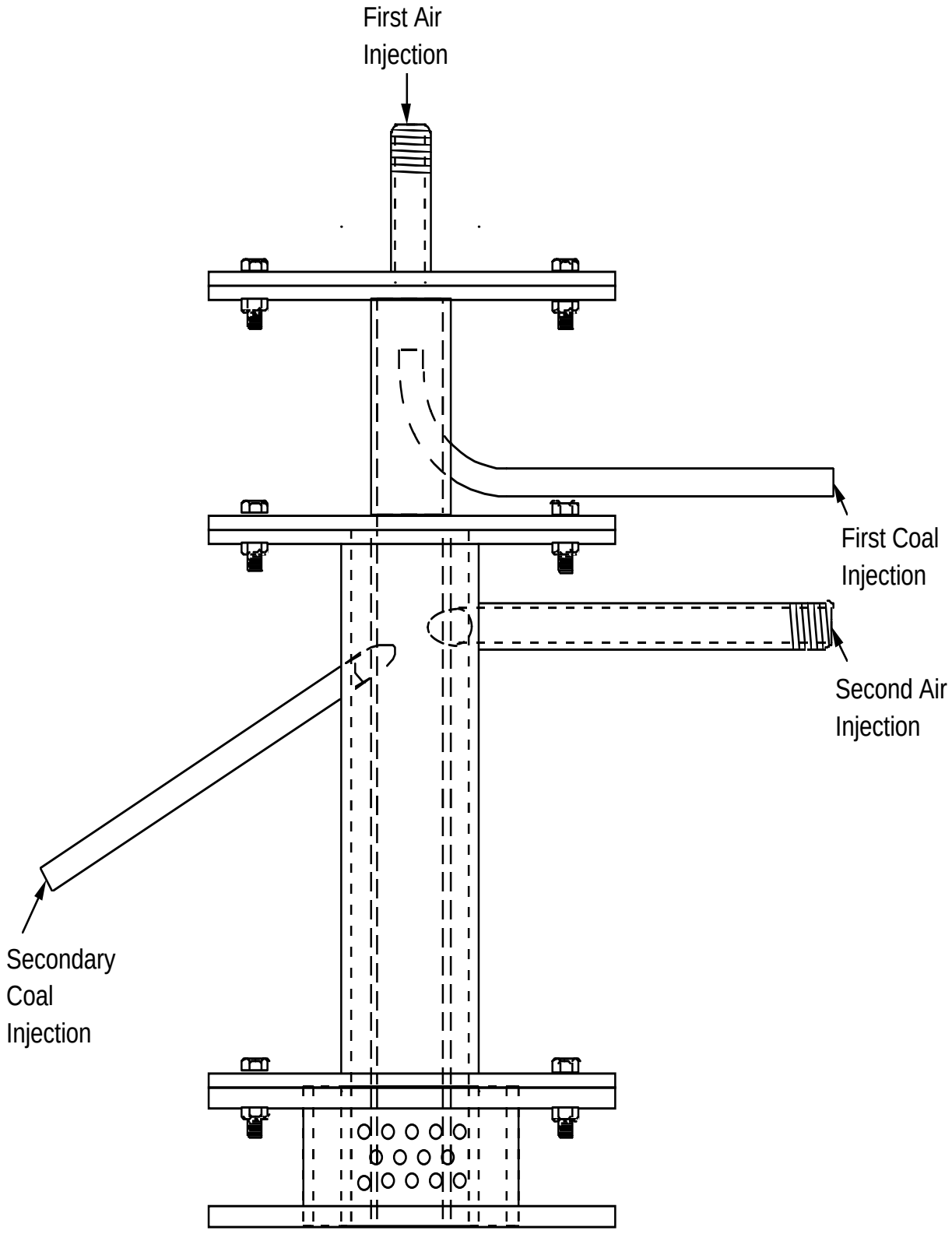

Figure 1.11 Segregated premixed pulverized coal (SPPC) burner.

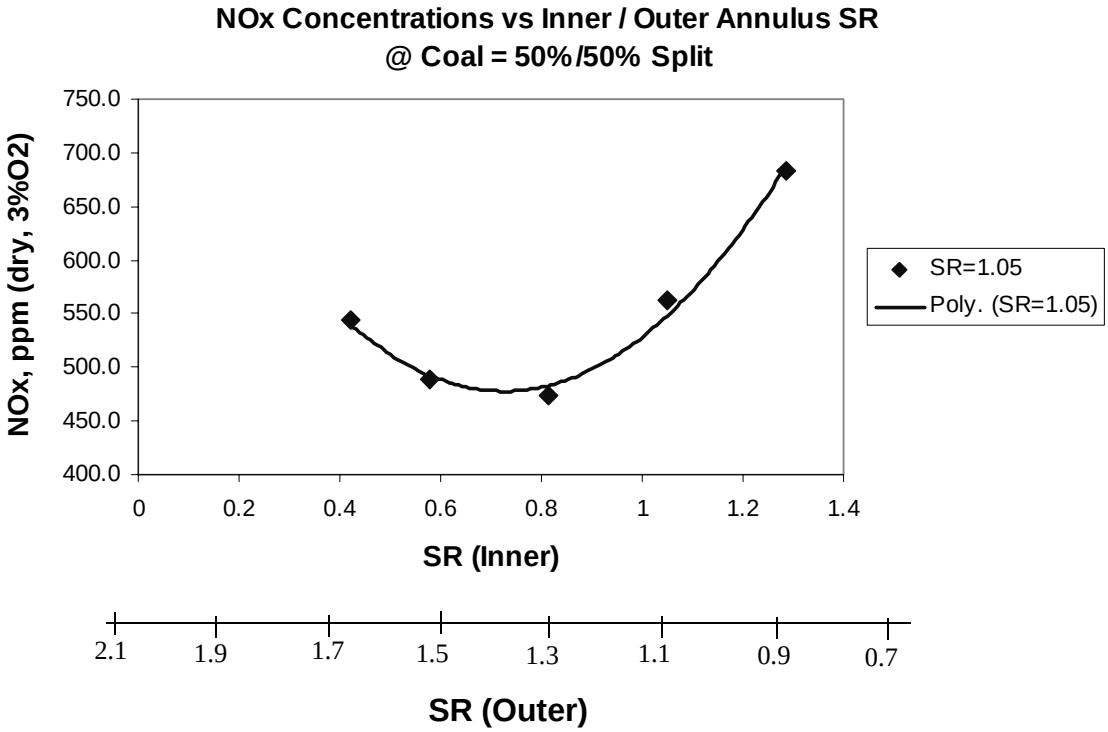

Figure 1.12 NO_x concentration vs inner/outer annulus stoichiometreic ratio and coal = 50%/50% split.

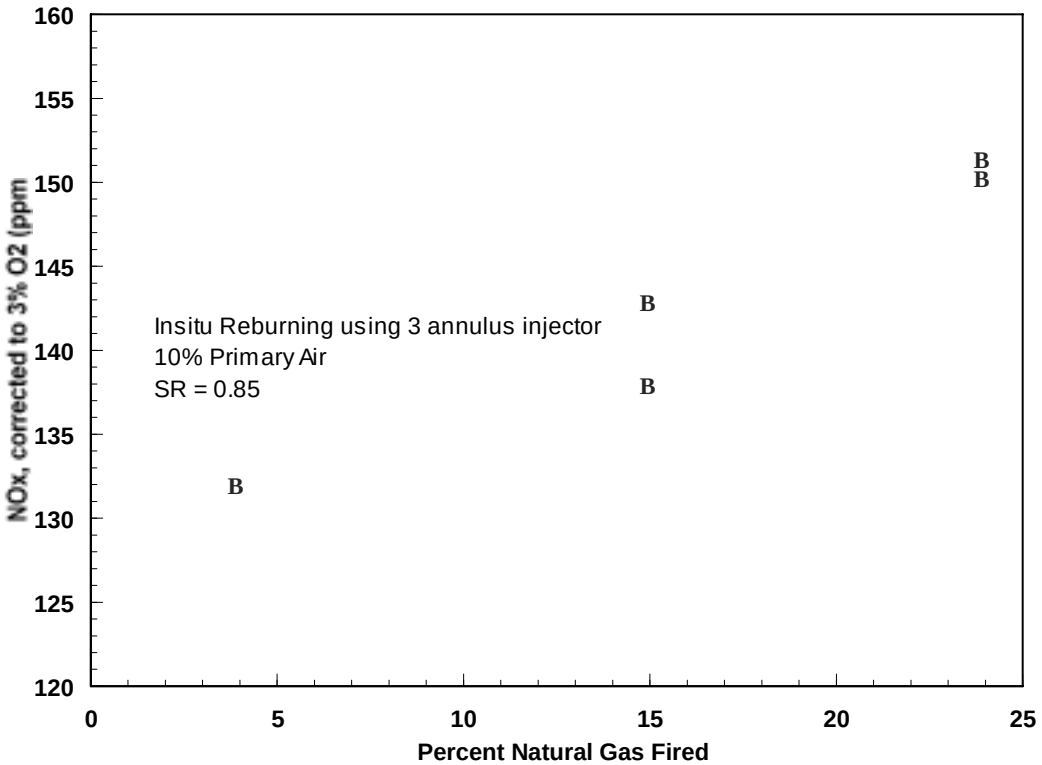

Figure 1.13 NO emissions as a function of natural gas firing..

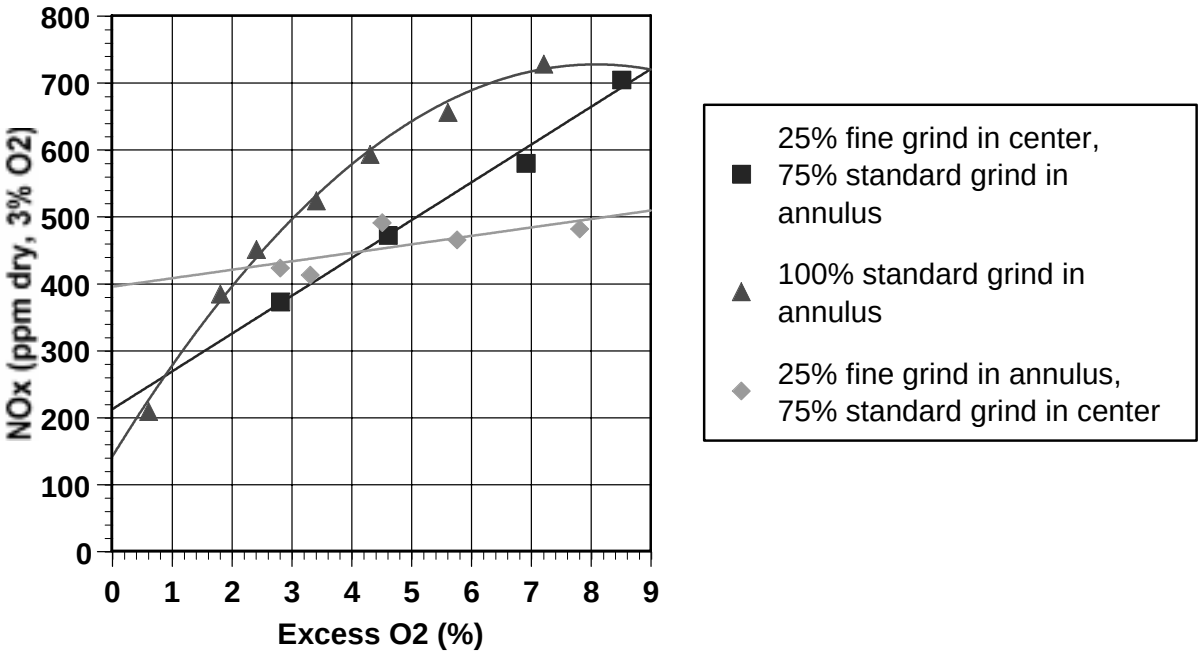

Figure 1.14 NO_x results as a function of coal grinds with double concentric swirl burner.

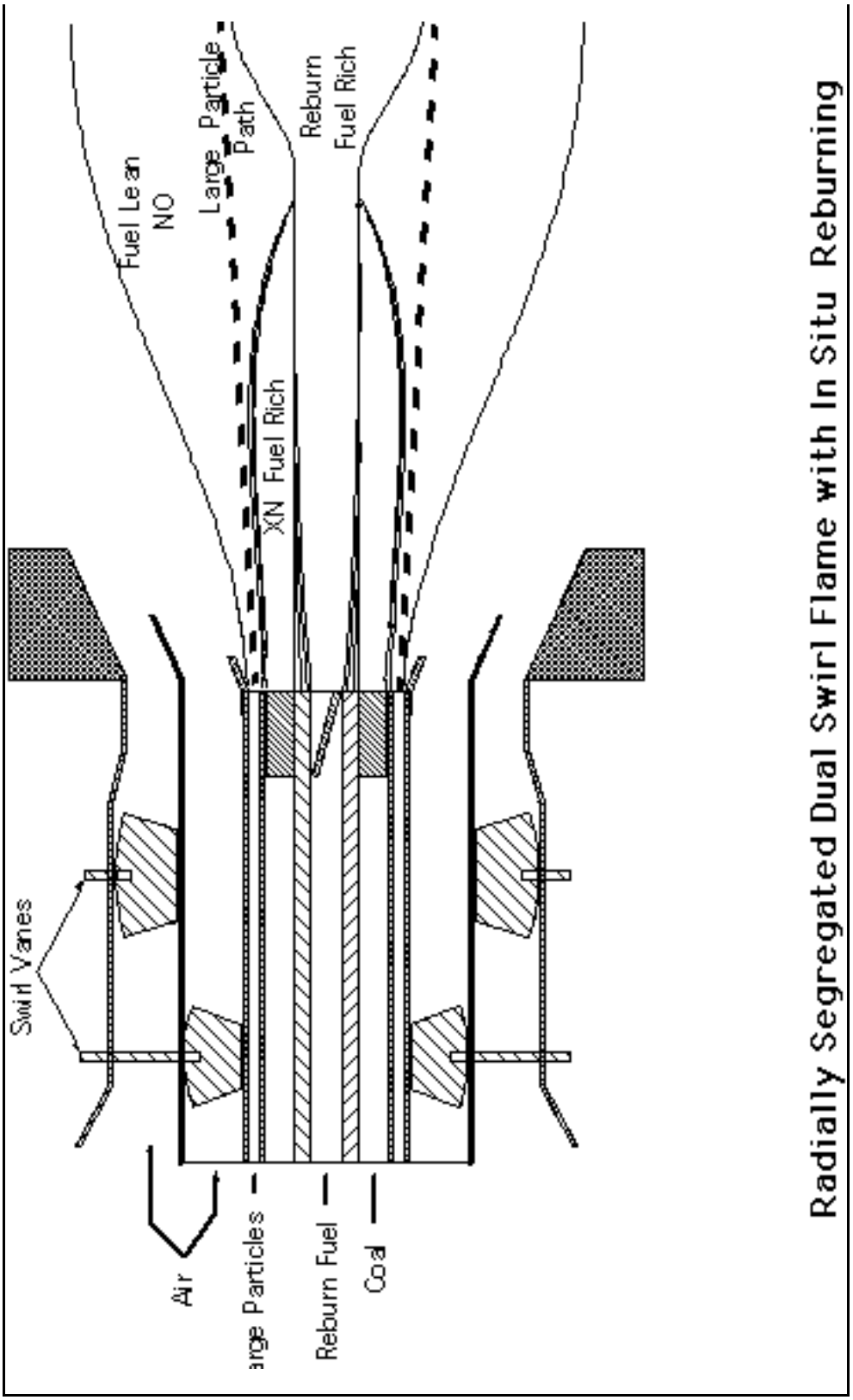

Figure 1.15 Modified low-NO_x burne.r

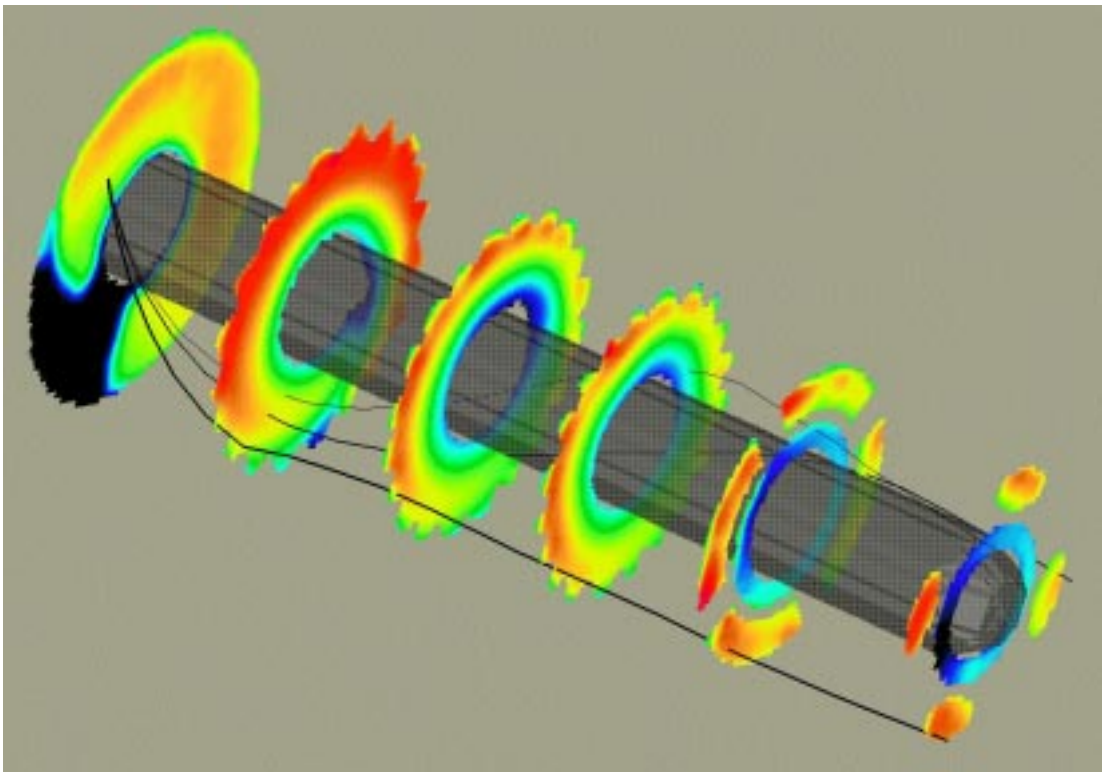

Figure 1.16 Effects of the coal nozzle on various particle sizes.

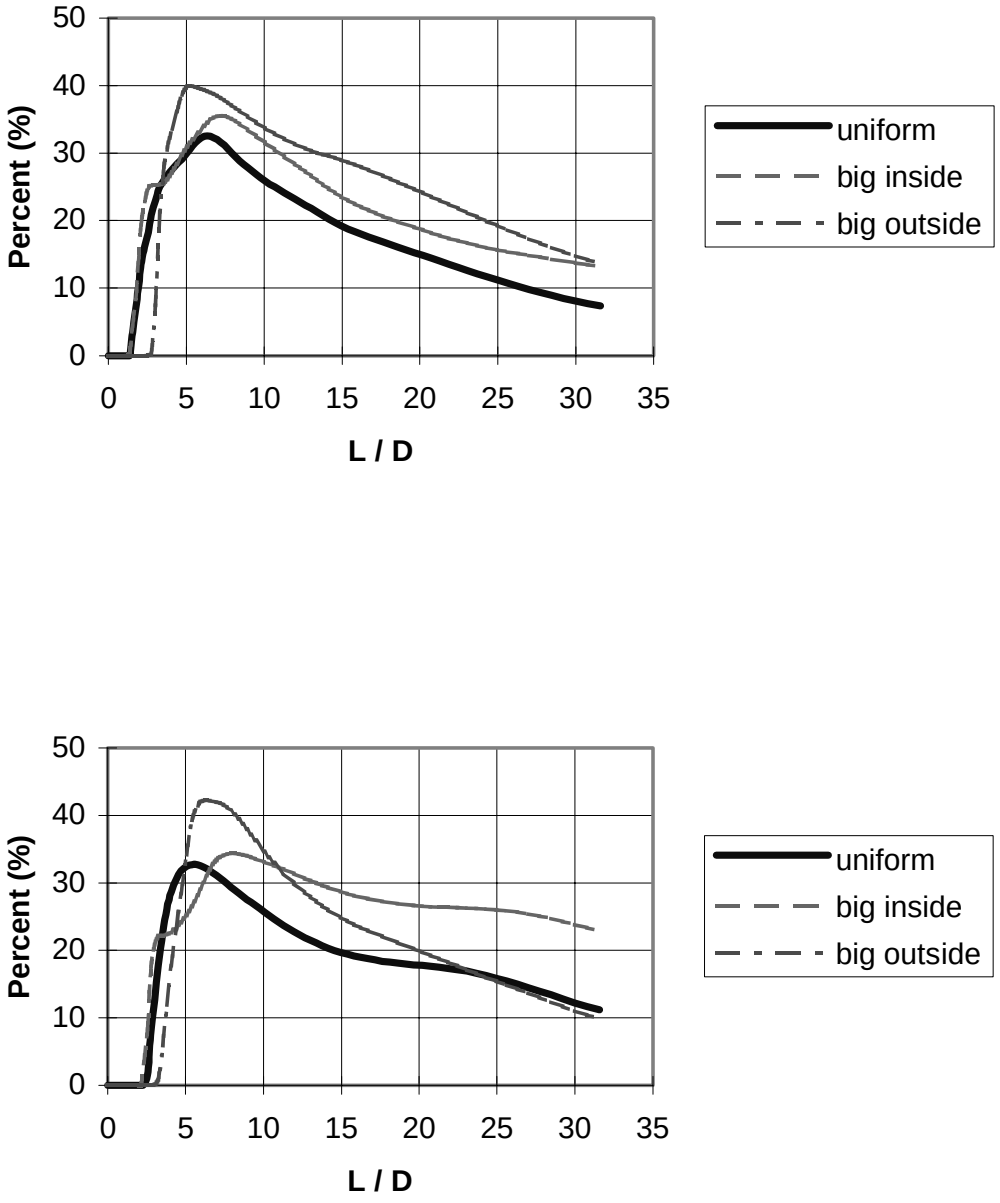

Figure 1.17 .Average char content (normalized by incoming coal flow) as a function of axial distance into the furnace for the cases of fuel lean (top) and fuel rich (bottom) conditions.

2.0 INTRODUCTION

Coal is this country's most abundant energy source and one of the US Department of Energy's goals is to encourage and ensure the continual use of coal in an environmentally acceptable manner. Although coal is abundant, both mining and utilization can have serious environmental consequences if appropriate controls are not enforced. The presence of heteroatoms makes utilization through combustion a potential source of atmospheric pollutants. Species such as sulfur and nitrogen form gaseous pollutants, SO_2 and NO, and trace metals can form toxic aerosols. Coal is not a renewable energy source, thus CO_2 emissions contribute to global warming. However, coal is and will continue to be a major source of electrical energy well into the twenty-first century and probably beyond, until there is widespread public acceptance of nuclear energy. Also, consider the demand for energy in China and India, two counties with large populations and abundant supplies of coal. Coal will be the fuel of choice for new power plants, and considering economic realities, it will be used primarily in conventional pulverized coal fired steam generators. Thus, the problem of coal utilization is a global one and it is essential that reliable, cost effective environmental control technologies be developed not only for application in the US but also world-wide.

2.1 PROGRAM GOALS

The study described in this report is concerned with the primary NO_x control technology for pulverized coal fired boilers "in-furnace NO_x control" which includes staged low-NO_x burners, reburning, selective non-catalytic reduction (SNCR) and hybrid approaches; e.g., reburning with SNCR. The program has two primary objectives:

1) To improve the performance of "in-furnace" NO_x control processes.

2) To devise new, or improve existing, approaches for maximum "in-furnace" NO_x control and minimum unburned carbon.

When the program was conceived it was thought that the major impact on boiler performance associated with in-furnace NO_x reduction technologies was the increase in unburned carbon in the fly ash. Recently, the utility industry has been made aware of another problem, increased rates of waterwall wastage in units fitted with low-NO_x firing systems particularly supercritical units firing eastern bituminous coals.

For those units required to implement some form of NO_x control to meet Clean Air Act Amendment Phase I limits, low-NO_x burners and/or combustion modification was the preferred option. Although many regarded low-NO_x burners the equivalent of "plug and play," field experience has been completely to the contrary (Jones, 1997). Most plants that have installed low-NO_x burners report an increase in LOI (Loss on Ignition). An increase in 10% unburned carbon means a 1% loss in combustion efficiency. But the increased costs associated with ash disposal could dwarf the fuel replacement costs associated with this loss in efficiency. Some increase in LOI was expected; however, recently another problem has surfaced with units fitted with low-NO_x burners - waterwall tube wastage. Approximately ten percent of Phase I units are experiencing accelerated waterwall tube wastage associated with low-NO_x firing. The extent varies from noticeable but manageable to a significant increase and subsequent forced outages. Availability has

a major impact on the cost of power produced by a particular plant. Thus the cost of low-NO_x firing systems may be significantly greater than the equipment/installation cost.

Waterwall corrosion is usually associated with reducing conditions on the wall. However, deposition of carbon-rich ash and sulfur on the walls can also accelerate corrosion rates. Thus, although the original program plan concentrated on the problem of increased LOI under low-NO_x firing conditions, much of the study is applicable to the corrosion problem.

Two in-furnace NO_x reduction techniques, reburning and staged low-NO_x burners involve similar processes that affect NO_x reduction and carbon conversion; thus the program plan was based on the following hypotheses:

1 NO destruction processes are key in both low-NO_x burners and coal reburning and there are indications that heterogeneous chemistry may play a role.

2 The current level of understanding of gas phase chemistry and coal pyrolysis far surpasses our ability to predict heterogeneous effects and two-phase mixing in the near field of pulverized coal flames.

3 The two phase mixing taking place in the near field of the fuel injector/burner controls both NO emission level and unburned carbon in the fly ash. New insights on heterogeneous processes and two-phase mixing will enable us to design an improved firing system for simultaneously minimizing NO_x and unburned carbon.

4 NO reduction on char was always thought to be slow, but rates were measured with old char and, with the exception of De Soete (1979), concentrated on direct reduction. Little information is available on NO char reactions under rich conditions in the presence of NH_3 and HCN. These reactions might account for reburning performance with coal.

4) Char reactivity with respect to burnout depends on the age of the char. Old chars loose their reactivity and the late stages of burnout may require more time to complete carbon conversion than might be expected based on the extrapolation of rates measured on high carbon char. Perhaps the reactivity of char with respect to NO also varies with time.

The program involves:

- Fundamental studies at laboratory- and bench-scales to define NO reduction mechanisms in flames and reburning jets;
- Laboratory experiments and computer modeling to improve our two phase mixing predictive capability;
- Evaluation of commercial low-NO_x burner fuel injectors to develop improved designs; and
- Demonstration of coal injectors for reburning and low-NO_x burners at commercial scale.

The specific objectives of the two phase program are to:

1 Conduct research to better understand the interaction of heterogeneous chemistry and two phase mixing on NO reduction processes in pulverized coal combustion.

2 Improve our ability to predict combusting coal jets by verifying two phase mixing models under conditions that simulate the near field of low-NO_x burners.

3 Determine the limits on NO control by in-furnace NO_x control technologies as a function of furnace design and coal type.

5 Develop and demonstrate improved coal injector designs for commercial low-NO_x burners and coal reburning systems.

6 Modify the char burnout model in REI's coal combustion code to take account of recently obtained fundamental data on char reactivity during the late stages of burnout. This will improve our ability to predict carbon burnout with low-NO_x firing systems.

The commercial products resulting from this effort will not only include improved fuel injector hardware for low-NO_x firing systems but also improved computational tools to help the utility boiler operator determine the optimum low-NO_x firing configuration, taking into account both corrosion potential and increases in unburned carbon.

2.2 PROGRAM ORGANIZATION

Thirty-three months after the proposal was written the commercial products resulting from this R&D program - improved fuel injection systems for low-NO_x firing systems and improved computer simulation tools to establish limits of NO_x control achievable with in-furnace NO_x control technologies under equipment and operational constraints are still valid and needed. Similarly, the original task structure for Phases I and II ensure maturity of the technology and maximize the opportunity for commercial deployment. In the intervening time outside influence suggested changes in emphasis, but the basic organizational structure remains applicable.

The program consists of:

- Two fundamental studies, one concerned with char reactivity and the other with the development and application of a technique to study two phase mixing close to the particle injector.
- Combustion system testing at three scales: bench-, pilot- and full-scale.
- Computer simulation at three levels: burner components, single burners and field operating boilers.

The task structure and participating organizations are shown in Figure 2.1; not shown is the Program Management task.

Computer simulation is central to the whole program; it provides both data evaluation and generalization. The two phase mixing studies carried out at the University of Utah were planned to develop data to validate the two phase mixing models in *GLACIER.* Since it is impossible to get meaningful data in the near field of a pulverized coal flame, these studies are being carried out under isothermal conditions. In Phase II, the two phase experimental system will be used to help develop fuel injection hardware by screening designs to optimize particle mass distribution at the injector exit as a function of location and particle size.

Studies at Brown University are concentrating on two aspects of char reactivity with respect to char oxidation and the reduction of NO. In Phase I the emphasis has been placed on the development of an advanced burnout model that can be integrated with *GLACIER*, and the construction of an apparatus that will allow the hypothesis to be tested that young chars have a higher potential to reduce NO than old chars. In Phase II the emphasis will shift from carbon burnout to NO reduction.

The combustion testing in Phase I was carried out at the University of Utah in bench- and pilot-scale facilities. This work will continue in Phase II and will be augmented by full-scale testing at the DB Riley U-Furnace Test Facility with the LEBS Firing System.

In Phase I the simulation task concentrated on fuel injection systems and on the evaluation of advanced burnout models for predicting LOI from low-NO_x firing systems. In Phase II there will be more emphasis on evaluating pilot-scale data, but full system simulation will be important since computer simulation is the only way to evaluate multiple burner effects at scale.

2.3 PHASE I REPORT ORGANIZATION

The major sections of this Phase I Final Report correspond to the major program tasks:

- Section 3 describes the results of the char reactivity studies.
- Section 4 describes the design, construction and operation of an experiment to study two phase mixing phenomena in the near field of particle laden jets.
- The results of bench-scale combustion studies and preliminary pilot-scale tests are presented in Section 5.
- Computer simulations of fuel injectors, burners and boilers are presented in Section 6.
- The Phase II Program Plan is presented in Section 7.

2.4 REFERENCES

De Soete, G.G., “Mechanism of Nitric Oxide Reduction on Solid Particles: Kinetic Study of NO Reduction on A1203 graphite and soot,” Report on EERC Subcontract No. 8318-6, IFP Report No. 27622, 1979.

Jones, C. “Maladies of Low-NO_x Firing Come Home to Roost” p.54, Power, February 1997.

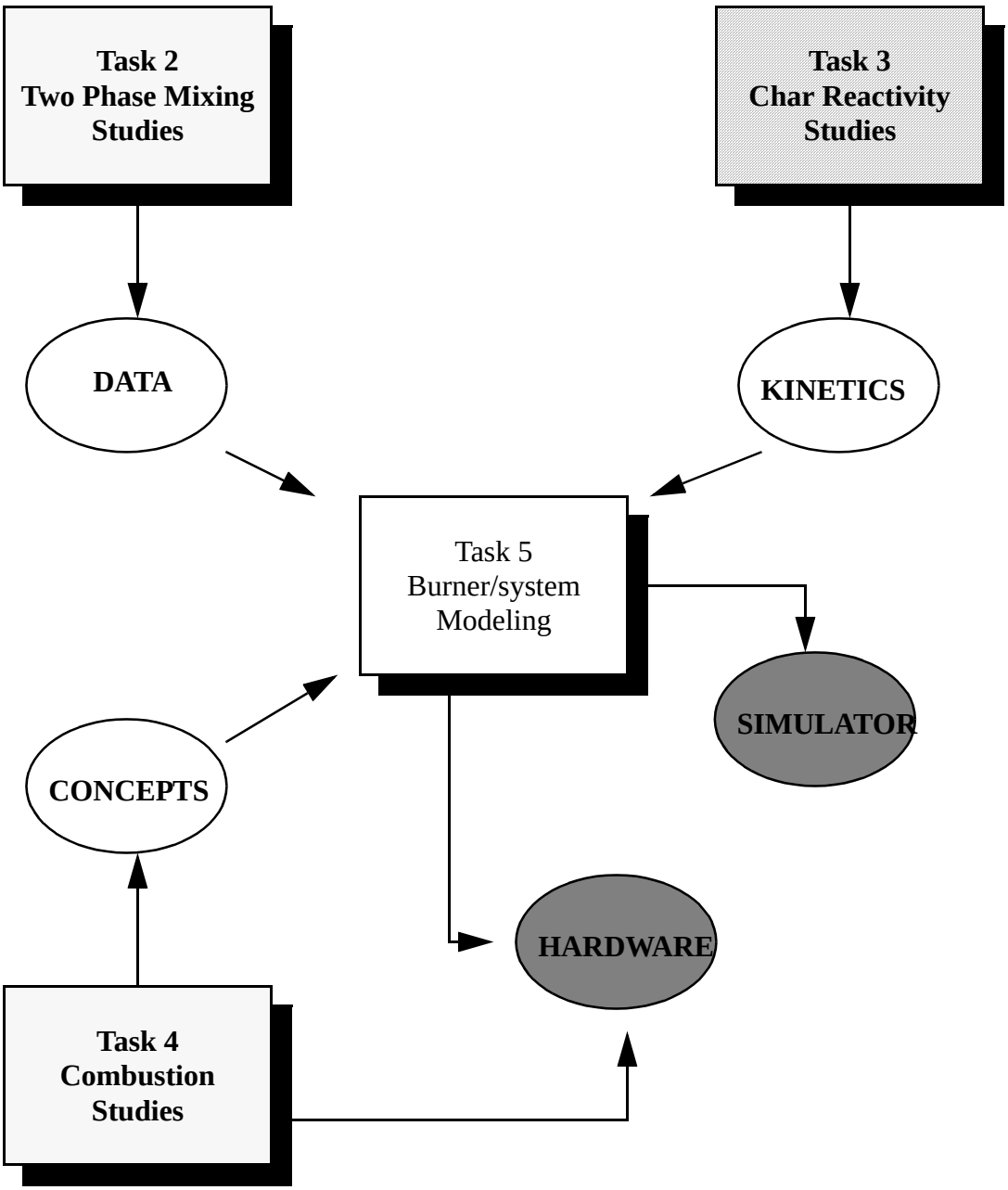

Figure 2.1 General program organization.

3.0 RESULTS AND DISCUSSION-CHAR REACTIVITY

3.1 OBJECTIVE

This section describes modeling and laboratory-scale experiments related to char reactivity as it effects carbon burnout, heterogeneous NO reduction, and the NO_x/LOI trade-off in pulverized coal fired furnaces. Major activities in this task are:

1. Developing an ash inhibition model to describe the very latest stages of combustion and its integration into the carbon burnout kinetic model (CBK);

2. Testing the CBK code in order to determine the key parameters influencing carbon burnout and to guide the implementation into REI furnace simulators;

3. Using CBK in the simulation of idealized furnace environments to explore the effects of flame structure (temperatures and degree of staging) on LOI, and to search for optimal conditions achieving simultaneous minimization of NO_x and LOI; and

4. Measuring the NO reduction activity of very young chars to assess the potential role of heterogeneous processes in reburning zones and in regions of primary burner flames.

Results of these four activities are presented, in turn, in the sections below followed by a list of the overall conclusions.

3.2 DEVELOPMENT OF ASH INHIBITION MODEL

Most sets of published char combustion kinetics are not specifically designed to model the complete carbon burnout process in pulverized coal fired boilers. A major goal of this task is to complete, enhance, and apply a new char combustion model recently developed under DOE-FETC funding at Sandia National Laboratories and Brown University. The Carbon Burnout Kinetic Model (CBK) integrates the unified, rank-dependent, high-temperature char combustion kinetics developed at Sandia National Laboratories, with submodels of char deactivation due to (1) thermal annealing, (2) mineral inhibition, and (3) time-dependent effects of statistical kinetics. The CBK model is a coal-general formulation that is specifically designed to predict the total extent of carbon burnout and ultimate fly ash carbon content for prescribed temperature/oxygen histories typical of pulverized coal combustion systems.

The first released version of the code was CBK Version 5 (CBK5), whose predictions had been compared to long residence time data from a flame-supported, hot-wall reactor at Sandia with the reactivities of unburned carbon samples from commercial coal combustors. The results were promising and integration of CBK5 into REI's multidimensional codes was initiated. During the project, CBK5 was tested against single particle temperature trajectories and against drop tube furnace data acquired at the U.K. utility PowerGen for a suite of international coals. (The latter effort was part of a parallel EPRI-funded effort to develop a stand-alone LOI predictor with validity for a wide range of international coals.) The testing revealed weaknesses in CBK5 which can be traced to the ash inhibition submodel. The ash model failed in two respects: it predicted a reactivity loss that began too early in the burnout process (at conversions less than 50%) leading to particle

temperatures that decrease too rapidly in the early-to-intermediate stages of conversion. This is contrary to observations in the early-to-intermediate stages [Hurt, 1993] and also results in a continuously decreasing temperature profile that does not include a rather abrupt decrease in particle temperature at 60 - 90% burnout (a near extinction event) as is observed for many coal chars [Hurt and Davis, 1994]. In addition, the results of calculations simulating PowerGen drop tube experiments suggested that CBK was overestimating the importance of ash; burnout was often underpredicted for high ash coals and overpredicted for low ash coals. Based on the above results the early phase of the project was devoted to improving the submodel of ash inhibition and integrating the submodel into a new version of CBK (Version 6). The new submodel formulation is summarized below.

There is very good experimental evidence for mineral effects in the late stages of char combustion. This evidence includes results from drop tube furnace studies by Vleeskens and Nandi [1986], where the degree of carbon burnout showed a negative correlation with coal ash content, and the recent experiments of Lunden [1996], in which demineralization was observed to increase the high-temperature combustion rate measured in a laboratory entrained-flow reactor. Single-particle imaging studies provide a very clear picture of mineral effects during combustion of 100 - 200 mm particles at a gas temperature of 1250 K [Hurt and Davis, 1994]. Under these conditions the late stages of combustion for many particles consist of the removal of carbon islands from a coherent ash framework by a very slow process that has been referred to as “ash decarburization” [Hurt and Davis, 1994].

Ash can slow combustion in the later stages by several physical mechanisms: (a) by acting as an additional resistance to oxygen transport to the reacting surface and (b) by occupying volume within the particle and thus reducing the carbon mass and carbon surface per unit particle volume. This latter “dilution” effect reduces the global rate expressed on an external area basis and, for a homogeneous ash distribution, can be predicted by the classical Thiele theory of gas-solid reactions [Hurt and Davis, 1994]. The new model of ash inhibition, describes both the dilution and mass transport effects and is outlined below.

If oxidation proceeds uniformly throughout the particle, a uniformly spatial distribution of ash could be assumed; if oxidation occurs exclusively near the external surface, a better assumption would be the presence of an inorganic film covering a carbon-rich core. Since the observed mode of burning parameters are much closer to zero than to one (with typical values of 0.2 [Mitchell, et al., 1992]), the shrinking core behavior with an exterior ash film is the better approximation. The ash inhibition model therefore assumes the presence of a porous ash film surrounding a carbon-rich core that is otherwise unaffected by oxidation, as shown in Figure 3.1. The core region has a constant local mass fraction of mineral matter equivalent to the overall mineral mass fraction in the unreacted char, $(M_a/V_p)_o$. A mass balance on the inorganic fraction yields:

$$M_a = (\pi/6)\, d_c^{\,3}\, (M_a/V_p)_o + (\pi/6)(d_p^{\,3} - d_c^{\,3})\, \rho_{af} \qquad (3.1)$$

where the first term accounts for ash in the carbon-rich core, and the second term accounts for ash in the outer film. This expression ignores the effects of vaporization and inorganic reactions involving mass changes. Examining the terms in Equation 3.1, $(M_a/V_p)_o$ can be expressed as:

$$(M_a/V_p)_o = M_a / (M_{t,o} / \rho_o) = X_{a,o}\, \rho_o \qquad (3.2)$$

and the ash mass as:

$$M_a = X_a M_p = X_a \rho (\pi/6) d_p^3 \quad (3.3)$$

and the ash density as:

$$\rho_{af} = \rho_{a,n} (1 - \theta_{af}) \quad (3.4)$$

where θ_{af} is the porosity of the ash film, $\rho_{a,n}$ is the density of nonporous ash, and the subscript "o" denotes properties of the unreacted char. The ash film thus has a volume determined by its mass, the nonporous ash density, $\rho_{a,n}$, and the porosity of the ash film, θ_{af}. Inserting equations 3.2, 3.3, and 3. 4 into 3. 1 and rearranging yields:

$$d_c = d_p \left[\frac{\left(X_a \rho - \rho_{a,n} (1 - \theta_{af})\right)}{\left(X_{ao} \rho_o - \rho_{a,n} (1 - \theta_{af})\right)} \right]^{1/3} \quad (3.5)$$

This result allows the calculation of the core diameter, d_c, from geometric considerations alone, knowing the constants $\rho_{a,n}$, θ_{af} , $X_{a,o}$, ρ_o , and the instantaneous overall particle diameter, d_p, and density, ρ. The latter two parameters can be calculated from the mode of burning equations described elsewhere [Mitchell, et al., 1992]. The ash film thickness is easily evaluated as:

$$\delta_{af} = (d_p - d_c) / 2 \quad (3.6)$$

and, following Hampartsoumian et al. [1989], the effective diffusivity through the ash film can be estimated by the empirical correlation:

$$D_{eff} = D \theta_{af}^{2.5} \quad (3.7)$$

where D is the molecular diffusivity. Solving the one-dimensional mass transfer equation in spherical coordinates at pseudo-steady state yields the molar flow of oxygen, N, across the porous ash film:

$$N = 2\pi D_{eff} \left[\frac{d_p d_c}{d_p - d_c} \right] (C_{ps} - C_{cs}) \quad (3.8)$$

where C_{ps} is the oxygen concentration at the outermost particle surface and C_{cs} is the oxygen concentration at the outer surface of the reacting carbon-rich core. We can also equate N to the molar flow arriving at the outer particle surface:

$$N = Sh \, \pi D d_p (C - C_{ps}) \quad (3.9)$$

Eliminating C_{ps} from Equations 3.8 and 3.9 and converting oxygen concentration to partial pressure by the ideal gas law, the following expression is obtained for the overall mass transfer coefficient, representing the combined diffusional resistances in the boundary layer and ash film:

$$k_p = \frac{Sh\ D\ d_p \theta_{af}}{\left(Sh\ \delta\ \tau d_c R T_m + \theta_{af} d_c^2\ R\ T_m\right)} \tag{3.10}$$

where D_{eff} is given by equation 3.7 and k_p is defined implicitly by:

$$N = (\pi / 6)\ d_c^{\ 2}\ k_p\ (P_{ox} - P_{ox,s}) \tag{3.11}$$

Again N is the molar flow of oxygen (mol/sec) and $P_{ox,s}$ is now interpreted as the oxygen concentration at the surface of the carbon-rich core. CBK accounts for Stefan flow and therefore uses an alternate expression for the molar flow, N (see Mitchell, et al., [1992]). *Sh* is the Sherwood number (CBK uses 2.0) and T_m is the mean film temperature, $(T_g + T_p) / 2$. The dilution effect is accounted for by computing the reacting external surface using d_c rather than d_p .

Use of Equations 3.5 and 3.10 require specification of the nonporous ash density, $\rho_{a,n}$, and the ash film porosity, θ_{af}. The nonporous ash density depends on the ash chemistry, particularly the iron content; which for the purposes of this model is taken to be 2.6 g/cm^3, a reported density of nonporous slag [Reid, 1981]. CBK5 treats the ash film porosity as a model parameter that is constant throughout conversion. The new model in CBK6 allows θ_{af} to vary as depicted in Fig. 3.1. The model treats the ash-forming minerals as distinct grains which are gradually liberated as the reaction front proceeds inward into the char particle. At low conversion, the population of grains residing on the surface is small and the ash film is sparse. The thickness of the "film" may be approximated by the characteristic diameter of the grains and the corresponding porosity is very high. As grains are added to the film, porosity decreases, and at some point grains begin to stack, increasing the film thickness.

The simplest mathematical model of this process assumes monodisperse grains whose continual addition fills a monolayer film until a critical porosity is reached, at which time the film begins to grow in thickness at constant porosity. This model has two parameters: the characteristic grain size, which is also the minimum ash film thickness, δ_m, and the critical porosity, which is also the porosity of a thick (multilayer) film, θ_{taf}. The model is implemented in CBK6 as follows: The overall particle density, ρ, and diameter, d_p, are first computed from the mode of burning relations [Mitchell et al., 1992] and are then used to compute trial values for d_c and δ from Equations 3. 5 and 3. 6 assuming θ_{af} is equal to the thick film limit, θ_{taf}. If $\delta > \delta_m$, then the ash film is indeed thick and Equation 3.10 is used to compute a mass transfer coefficient. If $\delta < \delta_m$, which occurs at low conversion, δ is set equal to δ_m and θ_{af} is computed from:

$$\theta_{af} = 1 - \left[\frac{X_a \rho - X_{ao}\rho_o \left(1 - \frac{2\delta_m}{d_p}\right)^3}{\rho_{a,n} - \rho_{a,n}\left(1 - \frac{2\delta_m}{d_p}\right)^3}\right] \tag{3.12}$$

which is simply Equation 3. 5 rearranged to a form explicit in θ_{af}.

The set of equations above define the new ash inhibition model in CBK6. Calculations with CBK6 show that the location of the near-extinction event is quite sensitive to the value of δ_m, while the reaction rate in the high conversion tail following near-extinction is quite sensitive to θ_{taf}. A

value for δ_m was therefore chosen to match the range of conversions in which near-extinction is observed for 100 μm particles of several bituminous coals [Hurt, 1993], and values of θ_{taf} were optimized for each coal to match the conversion profiles in Figure 3.2. The results are shown as dashed curves in Figure 3.2. A near optimal value for minimum film thickness, δ_m, is 1 μm, while values of θ_{taf} fall in the range from 0.16 - 0.25 for various coals with a mean value of 0.21 which is recommended for unknown coals. Specific values of θ_{taf} are: 0.18 for Illinois #6, hot wall data; 0.20 for Illinois #6, reinjection data; 0.25 for Pocahontas #3, 0.16 for Pittsburgh #8; 0.22 for Beulah lignite; and 0.26 for Lower Wilcox lignite. These porosities are lower than values expected for close packing of spheres (0.3 - 0.5), suggesting that the ash film is partially fused under conditions in the laboratory entrained flow reactor. Indeed, char particles extracted from the reactor in the late stages of combustion show evidence of partial fusion under an optical microscope where many ash-rich particles appear to have glassy rather than granular surfaces. But, they are irregular rather than spherical in shape indicating that ash viscosity remained high.

3.2.1 THE INTEGRATED CBK6 CODE

This section describes the CBK6, a FORTRAN kinetics code that integrates the global char oxidation model of Mitchell et al. [1992] with four distinct deactivation submodels, including the ash inhibition model described in the previous section. The main CBK program defines particle classes representing discreet joint distributions in particle size, reactivity, and density, as specified by the user with a 7x7x7 matrix representing a typical full calculation. For each particle class, the main program calls a subroutine that computes the burnout profile by passing a representative particle through a temperature and oxygen history prescribed by the user. These single-particle burnout calculations incorporate the thermal annealing and ash inhibition submodels, which are applied separately to each particle class as they effect different particle classes in different ways. The main program records the resulting burnout profiles for each particle class and continuously computes mean fuel properties as appropriate weighted averages. Written in this way, the code is particularly suited for post-processing applications, in which a CFD-based simulator supplies predicted vectors of the particle temperature/oxygen histories.

A few words should be said about the behavior of the integrated model, the relative importance of the various deactivation mechanisms, and the extent to which the CBK model as a whole has been validated. Target data sets for CBK include Figure 3.2, the low reactivities of unburned carbon in commercial ash measured in a previous study, and the observations of abrupt extinction events in single-particle optical data and lower-temperature imaging studies. The basis for model validation is summarized below:

1. The original one-film kinetics [Hurt and Mitchell, 1992] were derived from a large set of optical and extractive data taken in the Sandia Coal Combustion Laboratory (CCL) laminar flow reactor.

2. The thermal annealing submodel predictions have been independently compared to high-temperature annealing experiments conducted in inert environments [Hurt et al., 1996] (see below).

3. The statistical kinetic model has been fit to measured particle temperature distributions in the CCL [Hurt et al., 1996b].

4. The integrated CBK model has been fit to long-residence time data for five parent coals taken in a heated-wall reactor at Sandia [Hurt et al., 1996] (see below).

5. Calculations have been done to make a semiquantitative comparison of the CBK model predictions with measured reactivities in residual carbon from commercial boiler fly ash samples. Using typical temperature histories in boilers, CBK successfully predicts the general trend of low reactivities in these materials and the correct magnitudes.

The CBK model is observed to provide an adequate description of the data in Figure 3.2, though some improvement is still needed for the low rank coals. The model also predicts the correct qualitative behavior in each of the other cases and ascribes the various char deactivation phenomena to the combined effects of thermal annealing, ash inhibition, and the preferential removal of more reactivity of the less reactive material (dealt with through statistical kinetics). The relative importance of these deactivation mechanisms varies, however, and no one mechanism is the dominant cause of char deactivation in all experiments.

Some generalizations can be made about the roles of the various deactivation models, based on numerical studies with the complete CBK model. First, the prolonged burnout "tails" in Figure 3.2 are due primarily to statistical kinetics and ash inhibition. Thermal annealing has only a small effect on the shape of these curves, because the highest particle temperatures are achieved early, partially stabilizing the chars to further annealing.

Second, based on one-dimensional boiler simulation studies, the low reactivity of unburned carbon in commercial ash samples is due primarily to statistical kinetics and thermal annealing. Ash inhibition is only a minor contributor to the low reactivity of unburned carbon, at least as measured in the aforementioned study. The thermal annealing submodel predicts boiler chars to be less reactive than the entrained-flow reactor chars by about a factor of 4 in zone I (N/N_o), by virtue of differing temperature histories alone. The zone II reactivity ratio would then be $(4)^{1/2}$ or a factor of 2. The integrated CBK model predicts this annealing effect plus an additional effect of statistical kinetics (~ factor of 2) and a smaller effect of ash inhibition (for reasons discussed above). The net effect is the prediction fly ash carbon reactivities in zone II that are typically a factor of 4 less than those of the Sandia entrained-flow reactor chars . This can be compared with factors of 2 - 7 reported experimentally in zone II. The inevitable uncertainty in the temperature histories of the field samples prevents a conclusive validation of the model based on these data alone, but prediction of the correct trend and order of magnitude is encouraging.

Thirdly, the extinction events observed in entrained-flow reactor studies can be reproduced by CBK as inflection points in the temperature profiles of single particles in the late stages of combustion (70 - 90% conversion). CBK predicts this behavior to be due primarily to the ash inhibition effect. In imaging studies, extinction events have also been observed for particles with very little ash [Hurt and Davis, 1994], an effect that cannot be reproduced by CBK in its current version. More work is needed on the mechanisms of near-extinction in pulverized coal-char combustion.

More complete documentation on the CBK model can be found in a topical report prepared for the DOE. A paper on the CBK model has also been accepted in *Combustion and Flame* and is in press (July 1997).

Note: While the inorganic content of boiler fly ash is very high (typically > 90%), the particular residual carbon extracts used in the kinetic experiments [Hurt and Gibbins, 1995] were density-separated fractions with low ash contents (~ 20 wt-%), comparable to those of fresh chars. Ash inhibition is therefore not a likely explanation for their observed low reactivity. Many unburned carbon particles in boiler fly ash samples appear to have carbon-rich surfaces and do not resemble the mixed organic/inorganic particles found in samples extracted from laboratory reactors in the late stages of combustion. This is consistent with the results of simulations which show that while the overall fuel conversion is >99%, much of the unburned carbon material originates from coal particles whose particle-specific conversions can be as low as 30 - 50%. When these carbon-rich particles are density separated from the bulk ash, the inorganic content of the carbon-rich sample is low and its combustion behavior is not greatly affected by ash inhibition, a phenomenon of the late stages of single-particle combustion.

3.3 MODEL TESTING AND SENSITIVITY STUDIES

After completion of CBK6, work focused on code documentation and testing, as well as on sensitivity studies to determine the relative importance of the various submodels under boiler relevant conditions (described below). Improvements were also made to the CBK Version 6 code, primarily in the area of numerics. Convergence problems in the lowest level kinetic subroutine have been observed in a small number of cases, and these have led to occasional problems in larger simulations which typically call this particular routine over 1000 times. Error checking was introduced in numerous locations to avoid run time errors in these large simulations. Typical CBK run times have been observed to be less than 5 seconds on a 166 MHz Pentium PC using a 7x3x7 matrix of reactivities, densities, and sizes, along with 100 time steps.

3.3.1 SENSITIVITY STUDIES TO IDENTIFY KEY FACTORS AFFECTING LOI

A series of one-dimensional simulations were carried out to understand the intrinsic sensitivities of the carbon burnout process to various fuel parameters and model features. Simulations were carried out to test the effect of coal rank, ash content, and flame temperature. Additional simulations were carried out with and without the advanced features in CBK (annealing, ash inhibition, etc.) to measure the sensitivity of LOI to each effect. These simulations are designed to provide insight into the basic process sensitivities without exhaustive detailed, multidimensional simulations. The results are shown in Figures 3.3 - 3.6. Most of the simulations were carried out under the conditions listed in Table 3.1. Exceptions to this are noted in the captions of Figures 3.3 - 3.6.

Figure 3.3 demonstrates the effect of coal rank on LOI at constant particle size distribution. Conditions are as in Table 3.1 except for the variable coal carbon content. Increase in coal rank, as indicated by carbon content, leads to large increases in LOI. The magnitude of the differences can be appreciated by comparing the predicted LOI values (2 - 15%) to a typical maximum threshold for fly ash use in concrete of 3 wt-%. The observed effects are due primarily to decreases in char reactivity and volatile loss with increasing rank. A similar sensitivity to rank is believed to be typical of industrial practice, but there it is mitigated by increases in grindability for many higher rank bituminous coals.

Figure 3.4 demonstrates the effects of ash content on LOI and the effects of the ash inhibition model in CBK6. Increasing ash is seen to decrease LOI, a trend that is also reported in the field. At the same time, however, the ash inhibition submodel in CBK6 is seen to have a large effect on the LOI prediction. Including the effect of ash inhibition is seen to increase the LOI prediction by up to 5 percentage points (at 10% ash), or by a factor of 10 (0.2 to 2.3 at 40% ash). These combined results can be understood by considering two separate effects of ash on LOI. The addition of

inorganic material to the ash stream "dilutes" the unburned carbon and reduces LOI, defined as the weight of carbon divided by the combined weight of carbon and inorganic material. As coal ash content increases, this effect becomes larger and LOI tends to decrease. At the same time, physical inhibition of the oxidation reaction by ash in the late stages of combustion, as described by CBK, reduces reaction rates, lowers carbon conversion, and thus increases LOI. As ash content increases this effect becomes larger and LOI tends to increase. Under conditions relevant to industrial practice, the first effect dominates and LOI decreases with increasing coal ash content, in agreement with industrial experience. Since the ash inhibition submodel has such a large impact on the absolute LOI prediction, however, it should be regarded as an essential submodel within CBK.

Figure 3.5 shows the effect of increasing gas temperature on carbon burnout in an isothermal environment with and without annealing effects. In the absence of annealing, LOI decreases sharply with increasing gas temperature between 1200 and 1300 K. At 1400 K, LOI is already 1.2% in this simulation, decreasing to 0.25% at 2000 K. Above 1300 K, when the annealing submodel is activated, LOI increases dramatically, by as much as 11 percentage points. Above 2000 K, the LOI values predicted with the annealing submodel are approximately ten times higher than those predicted without annealing.

Interestingly, at a temperature of about 1175 K the two curves cross, and at lower temperatures use of the annealing submodel *improves* burnout. This can be easily explained as follows. The simple kinetics used in the absence of annealing effects yield char reactivities comparable to those observed in the original Sandia experiments. In this sense, the no-annealing curve in Figure 3.5 represents the behavior predicted by the original Sandia kinetics. The annealing submodel was designed to start with a very reactive young char, but to reproduce the Sandia char reactivities after exposure to temperature histories similar to those in the Sandia flow reactor. At higher temperatures and/or longer times, the extent of annealing is greater than in the Sandia reactor and the submodel predicts less reactive chars. At lower temperatures and/or shorter times, the young chars should be less severely annealed than the Sandia chars and should, indeed, exhibit higher reactivities and better burnout, as seen in Figure 3.5.

More information on the effects of annealing is contained in Figures 3.8 and 3.9, which consider the effects of flame zone structure on LOI and NO_x/LOI, respectively.

Finally, simulations were carried out to assess the importance of statistical kinetics to LOI prediction, with the results shown in Figure 3.6. These simulations use the conditions in Table 3. 1, except for coal carbon and hydrogen contents, which were varied to represent a set of eight coals under study in a parallel project sponsored by EPRI. Activation of the statistical kinetic submodel led to increases in LOI from 1 to 4 percentage points. This increase is due to the low reactivity tail of the distribution and its disproportionate effect on the late stages of combustion. The ratio of LOI predicted by statistical kinetics to LOI predicted by simple kinetics was between 1.3 and 1.5 in all cases. Statistical kinetics is seen to have a significant effect on absolute LOI levels, but not as large an effect as exhibited by the annealing or ash inhibition submodels. Overall the statistical kinetic submodel is recommended for use in boiler simulations, but may also be omitted in cases where approximate solutions are desired and run times are critical.

These one-dimensional calculations, while ignoring many features of furnace operation, give a simple and useful picture of the relative importance of various fuel-related effects in carbon burnout.

3.4 EFFECTS OF FLAME STRUCTURE ON NO_x / LOI

Many utilities have reported significant increases in LOI following the installation of low-NO_x combustion systems, but the detailed mechanisms leading to these increases are not fully understood. A previous study [Hurt et al., 1995] speculated that thermal annealing played a role in the burnout characteristics of low-NO_x combustion systems, but this hypothesis has never been tested. The CBK model, now complete, includes a working model of thermal annealing, and can be used to examine the role of annealing on low-NO_x combustion. Note that the other deactivation mechanisms described by CBK (statistical kinetics and ash inhibition) are late stage effects that influence carbon burnout in all systems but do not depend on the flame zone structure or staging characteristics in any significant way.

The goal in Phase I of this task was to carry out simple simulations that illustrated the basic sensitivities without incorporation of manufacturer-specific design details of low-NO_x burners. One-dimensional simulations were therefore carried out to explore the effect of flame structure on unburned carbon. These simple sensitivity studies revealed some important aspects of low-NO_x burner operation.

Figure 3.7 shows the effect of fuel staging on LOI in a one-dimensional system. The idealized furnace is divided into a fuel-rich zone followed by an oxygen-containing burnout zone approximating the near burner region and the upper furnace, respectively. A set of typical conditions are considered and calculations performed to assess the effects on LOI when residence time and temperature in the fuel rich zone are varied.

The detailed conditions are as follows: the total residence time, t_{tot}, of the combustor is fixed at 2 seconds; the fuel-rich zone is depleted in oxygen and is given a variable residence time, t_1, and temperature, T_1; the burnout zone is given a constant oxygen concentration of 5% and a gas temperature of 1600 K (representing typical mean values); and a variable residence time of $t_{tot} - t_1$, to keep the total residence time fixed even though the fuel-rich zone residence time varies. The simulations were carried out with a typical high-volatile coal (80% carbon, daf) possessing a Rosin-Rammler particle size distribution with 75% through 200 mesh, and a high-temperature volatile loss of 50%.

Results are shown in the plot in Figure 3.8. In the absence of a fuel-rich zone ($t_1 = 0$) LOI is 1.7%, producing what would be a concrete-quality ash based on most state specifications in the U.S. As the size (residence time) of the fuel-rich zone increases, representing deeper degrees of staging, LOI increases for all cases, as expected. In general, this increase is due to two effects: (1) decreased residence time in the oxygen-containing zone, and (2) thermal annealing in the fuel-rich zone, which reduces char reactivity prior to the onset of oxidation. The relative importance of these two effects can be seen be examining the individual curves in Figure 3.8. The lowermost curve, generated without the annealing model, shows the effect of residence time alone. LOI is observed to increase from 1.4% to 2.6% as the residence time in the fuel-rich zone increases from 0 to 500 msec. The remaining three curves all account for thermal annealing, whose effects increase with increasing temperature in the fuel-rich zone. At 1800 K annealing effects are of about equal importance with the residence time effects, while at 2000 K annealing plays a larger role than does residence time, increasing LOI from 1.7% to 5.0% as residence time in the fuel-rich zone increases from 0 to 500 msec. It is interesting that the model predicts a very large increase in LOI if the mean flame zone temperature reaches 2200 K, outside the range of normal operation.

There are additional factors, however, that contribute to the increase in LOI with low-NO_x burners, which cannot be accounted for in one-dimensional simulations. Chief among these is the imperfect mixing of the secondary, tertiary, and/or overfire air with the fuel-rich flame core. If this mixing process is incomplete, or slow, distinct fuel-rich packets may persist for long times, perhaps even to the furnace exit, contributing additional unburned carbon. This is particularly relevant for overfire air systems, in which this mixing must occur across a length scale comparable to the furnace width involving jet penetration into a crossflow.

3.4.1 NO_x / LOI OPTIMIZATION

In many types of combustion systems there is an inherent tradeoff between NO_x emissions and unburned fuel or PIC emissions, as they show the opposite trends with respect to stoichiometry. Rich operation favors low-NO_x emission, while lean operation ensures complete burnout and low emissions of products of incomplete combustion (PIC). The tradeoff occurs in coal combustion primarily through the opposite effects of mixing intensity on NO_x and unburned carbon. There is very strong motivation to develop a low-NO_x burner system for coal that does not increase unburned carbon emissions. In general, the problem can be regarded as a search for flame structures that minimize NO_x and LOI simultaneously.

To help identify optimal conditions for NO_x and LOI, another set of 1-D calculations were carried out with CBK as shown in Figure 3.9. These calculations consider, in a very simple way, the effect of changing flame zone conditions on NO_x formation by incorporating the nitrogen release kinetics of Pohl and Sarofim [1976]. This idealized calculation assumes that there is a probability of conversion of fixed nitrogen species to NO that is different in fuel-rich and fuel-lean regions. An effective low-NO_x flame will force the release of a large fraction of the total fuel nitrogen within the fuel-rich zone. This simplified picture assumes that the homogeneous kinetics of fixed nitrogen oxidation (to NO) and reduction (to N_2) are fast compared to the heterogeneous release rates. In the absence of mixing limitations this is reasonable, as decay times for fixed nitrogen species are on the order of several milliseconds [De Soete, 1974].

Figure 3.9 shows the result of the calculation, in which residence time and temperature in the fuel-rich zone were varied, not independently as in Fig. 3.8, but in a manner that ensures a constant LOI of 2.3%. For example, as temperature is increased, annealing tends to increase LOI, and the residence time must be reduced to compensate. Thus we explore a variety of flame zone conditions producing constant LOI, and calculate for each the fraction of fuel-nitrogen carried into the fuel-lean zone (1 - fraction released in the rich zone), a parameter related to ultimate NO_x emissions. Figure 3.9 shows that there is an optimum set of conditions in the fuel-rich zone (temperature and time) that minimize the NO_x parameter. At low temperatures, the kinetics of nitrogen release are slow and the fraction of nitrogen carried into the fuel-lean zone is high. As temperature increases, so does the rate of nitrogen release and the NO_x parameter falls to a more favorable value. As temperature is increased further, however, annealing becomes progressively more important, the residence time in the fuel-rich zone must be significantly reduced to maintain constant LOI, and the time is insufficient for nitrogen release in the fuel-rich zone. This behavior reflects the fact that annealing has a higher effective activation energy than nitrogen release, and is more sensitive to temperature increases beyond a certain temperature threshold.

It is noteworthy here that the conditions in the optimum window (T = 1750 to 1950 K, rich residence time 70 to 130 msec) are close to those of industrial practice. To the project team's

knowledge, this is the first calculation that suggests the presence of optimal flame temperatures for combined NO_x/unburned carbon emissions. This calculation highlights the important role of the annealing submodel when considering detailed questions of optimal burner/furnace design. Although these calculations provide useful insight, the optimal conditions are similar to those used in modern low-NO_x burner systems and do not show large potential for improvement. The next paragraph on future plans discusses a different feature of low-NO_x burners that may possibly be exploited for LOI optimization: size segregation effects.

3.5 HETEROGENEOUS NO_x REDUCTION

The goal of this task is to understand the contributions of heterogeneous reactions to solid fuel reburning, and to identify the effect of char age on reburning activity. The kinetic expressions in use at REI indicate the heterogeneous reaction is too slow to contribute to the reburning process, but most prior kinetic studies employed chars that were pre-stabilized by long-time heat treatment, and may be relatively unreactive as a consequence. This study focuses, therefore, on the measurement of NO reduction activity for very young chars, and the quantification of the effect of char age (heat treatment history) and parent coal rank. A set of laboratory experiments and kinetic analyses were completed within this task, as described below.

Experiments were carried out using a flame-supported entrained flow reactor equipped with an extractive sampling system and NO_x analysis instrumentation (see sketch in Figure 3.10). Methane, oxygen, and an argon/NO mixture were fed to a Henken honeycomb flat-flame burner, yielding approximately 30 slpm of hot gas downstream of the primary flame containing about 1000 ppm of NO and 1 volume-% oxygen. A variety of solid reburning fuels were entrained in a small secondary flow (1 slpm) and metered to the reactor at a uniform mass flow over the course of each 2 minute experiment. The gases downstream of the secondary flame are sampled by a small diameter, stainless steel, water-cooled probe, are then passed through an ice bath, a silica gel dryer, and then to a chemiluminescent NO_x analyzer (Model 10AR from Thermoelectron). The volume of the entire sampling system was minimized in order to reduce the time lag and produce well-defined step-changes in NO concentration on the strip chart recorder. The total extent of NO reduction was obtained by integrating the concentration profiles over the course of the experiment. Additional information on the experimental conditions is given in Figure 3.10.

Due to heat losses, the centerline temperature in the reactor decreases with height, and most of the NO reduction occurs in an active region in the lower zone of the quartz chimney close to the injection point. The system operates as a differential reactor, achieving small but reproducible reductions in NO, depending on the nature of the solid fuel employed. The stoichiometric ratio for the primary flame is 1.1 and for the secondary, reburn flame varies from 0.48 to 0.69 depending on the solid fuel and feed rate.

The experimental procedure is as follows. The primary flame is established and the post-flame oxygen concentration measured with a separate insertable probe directly calibrated for 1 vol-% O_2. The NO concentration is continuously monitored on a strip chart recorder, and a steady baseline value established prior to the introduction of secondary solid fuel. The secondary (reburn) fuel is added quickly at a constant, preset, volumetric flow, using a modified syringe pump feeder. The solid fuel is added over the course of 1 - 2 minutes, and the extent of NO reduction determined by integrating the area under the strip chart recorder between the actual and extrapolated baseline NO concentrations. After approximately one minute, the NO concentration is observed to return to the

baseline value in all cases except with the raw bituminous coal, where a small offset is observed (the final NO concentration is lower than the initial). This latter effect is believed to be do to deposition of tar and soot in the sampling lines and reactor walls under the fuel-rich conditions in the secondary flame. This hysteresis has a relatively small effect on the reported NO reduction for the raw bituminous coal.

The experiments focused on young chars from two coals of widely varying rank, and a petroleum coke, which has previously been reported by REI to show significant reburning activity in larger-scale tests. The young chars were prepared in the same flow reactor, but in a separate experiment. Experiments with catalytically doped chars were also planned originally, but recent work in other laboratories has greatly lessened the need for these particular experiments. The emphasis in Phase I was therefore shifted toward the effects of char age, and the completion of experiments on a larger number of solid fuel samples (11).

3.6 RESULTS

Tables 3.2 - 3.4 and Figure 3.11 summarize the results of the NO reduction experiments for 11 different solid fuels. This study addresses possible heterogeneous effects, and thus chars and low-volatile fuels were the main focus of study with two raw coals included for reference. Table 3.2 shows the large variations in the percentage NO reduced, from 0 for a heat treated petroleum coke to 40% for the raw bituminous coal. The two highest amounts both derive from experiments with high-volatile fuels (Illinois #6 coal and Beulah lignite). The chars from these materials had activities that were lower, and were a pronounced function of preparation conditions, most notably heat treatment temperature and time. The next section discusses the results in detail by fuel type.

3.6.1 LIGNITE AND LIGNITE CHARS

The raw lignite shows the highest activity (13%), but only by 4% over the young lignite char (case 5) prepared by extractive sampling in the flame reactor. The char in case 5 is typical of the char present after devolatilization in case 1, thus the comparison between 1 and 5 indicates the relative roles of homogeneous and heterogeneous mechanisms. The apparent heterogeneous mechanism accounts for 9/13 or about 70% of the activity.

Entries for samples 2 - 4 show a pronounced effect of heat treatment on NO reduction activity. Following heat treatment at 950 ^{o}C for two hours, the activity has been reduced to about 10% of that for the raw lignite. There are two possible explanations for the effect of heat treatment: it reduces char activity (through reduction in surface area, surface reactivity, and catalytic effects), and/or it reduces the residual volatile material in the char which is active through a homogeneous mechanism. To assess the second possibility, measurements were made of residual volatile matter contained in selected samples from Table 3.2. These measurements are shown in Table 3.3 along with high-temperature volatile yields for the two coals employed.

For the lignite chars, residual volatile matter is not a satisfactory explanation for their activity for several reasons. Based on the raw lignite results, which yield an estimate of the role of volatile matter, the amount of residual volatile matter in the chars is far too small to account for their activity. Also, the lignite chars have a much higher reactivity than the bituminous chars, and this trend is inconsistent with the rank trends in volatile activity, which show bituminous volatile matter to be

more active. For some of the other materials (bituminous chars and petroleum cokes) residual volatile matter is indeed a plausible explanation for their activity, as will be discussed shortly.

3.6.2 ILLINOIS #6 COAL AND CHARS

The Illinois coal has a very high NO reduction activity, and the low value of the corresponding flame char (sample 3) suggests it is almost all due to volatile matter. Further, the activity for bituminous char samples 8 and 9 could reasonably be explained by residual volatile matter. For each sample 8 and 9, the ratio of its activity to that of the raw coal is quite similar to the ratio of volatile contents. No firm conclusion can be drawn about the origin of the low but measurable activities for the bituminous chars; it may reflect a homogeneous or a heterogeneous effect.

3.6.3 PETROLEUM COKE

Experiments were performed on a raw and heat treated petroleum coke sample supplied by REI, which in earlier reburning studies in the University of Utah U-Furnace had shown a significant activity. The raw coke in the Brown experiments also showed a significant activity, higher than all the other char samples except the two youngest lignite chars. Heat treatment of the coke at 950 ^{o}C for two hours liberated 7% volatile matter and resulted in a fully carbonized product with no measurable activity. It is likely that the observed activity of raw petroleum coke is related to its residual volatile content.

3.7 APPARENT HETEROGENEOUS KINETICS

For all but the two raw coals, the NO reduction activities in Table 3.2 were converted to apparent heterogeneous rates and compared to a large set of literature values compiled in the recent review by Aarna and Suuberg [1996]. The kinetic analysis is based on the first-order rate expression for NO reduction:

$$d\,M_{NO}/dt = -k_s\,P_{NO}\,M_C \qquad (3.13)$$

with k_s in g-NO/g-carbon-atm-sec. A pre-exponential factor was calculated for each material assuming a typical activation energy of 133 kJ/mol [Aarna and Suuberg, 1996]. For purposes of comparison with the literature kinetics, an apparent heterogeneous rate constant is also reported at a standard reference temperature, 1250 K.

Pre-exponential factors were obtained by integrating Equation 3.13 along the nonisothermal profile to obtain the total fraction of NO reduced. A temperature was assigned for the kinetic analysis by averaging the temperatures in the active high-temperature zone (near the injection port) where most of the reduction occurs. Temperatures were assigned based on radiation-corrected thermocouple measurements in post flame region without the presence of reburning fuel. An accurate assignment of temperature required corrections for the effect of reburning fuel and carrier gas, acting both as a heat sink and as a source of heat through exothermic reaction with the 1% oxygen at the start of the reburn zone. For the char materials, the extent of exothermic reaction with oxygen in the active zone is unclear; for this reason temperatures were calculated with and without the exothermic correction and a mean value reported. This causes a +/-50 K uncertainty in effective reaction temperature.

The results of the kinetic analysis are shown in Table 3.4 and the Arrhenius plot of Figure 3.11. Figure 3.11 also shows three lines from the Aarna and Suuberg review [1996] representing the mean kinetic law for a wide variety of materials, and lines representing the highest and lowest reported values (considering only those data sets with measurements at temperatures above 1100 K). The rates measured in this study are much higher than the mean line, and most samples are more reactive than the most reactive material in the high-temperature literature data. The wide range of lignite activities caused by different heat treatment conditions is easily seen. As discussed earlier, the apparent high reactivities of the coke and Illinois #6 may in fact be due to homogeneous effects related to the residual volatile matter. The high activity of the lignite char, however, is primarily a true heterogeneous effect.

This study clearly demonstrates the effect of heat treatment on NO reduction activity under reburning conditions, either through changes in char reactivity, and/or through reduction in residual volatile matter in some cases. Because of the high reactivity of the very young chars, heterogeneous effects should indeed be important in reburning environments, at least for some coal types. With this conclusion, the goals set for Phase I have been achieved and the need for robust, fully quantitative kinetics for heterogeneous reburning chemistry have been demonstrated. As discussed in the original proposal, a different reactor configuration will be necessary to properly measure these kinetics in Phase II. High-temperature, rank-dependent kinetics for the NO/char reaction will find use in the design and optimization of reburning systems, and perhaps also in design and optimization of the primary combustion zone.

3.8 REFERENCES

Aarna, I., Suuberg, E. "A Review of the Kinetics of the Nitric Oxide Carbon Reaction, Fuel in press, 1996.

De Soete, G.G., *Proceedings of the Fifteenth Symp. (Int.) on Combustion,* The Combustion Institute, Pittsburgh, PA pp. 1093 - 1102 (1974).

Hampartsoumian, JE. Pourkashanian, M., and Williams, A. *Journal of the Institute of Energy*, March, pp. 48-56 (1989).

Hurt, R. H. "Reactivity Distributions and Extinction Phenomena in Coal Char Combustion" *Energy and Fuels* 7 721-733 (1993).

Hurt, R. H. and Davis, K. A., "Near-Extinction and Final Burnout in Coal Combustion," *Proceedings of theTwenty-Fifth (International) Symposium on Combustion*, 1994, pp. 561-568.

Hurt, R. H., Davis, K. A., Yang, N. Y. C., and Headley, T. R. "Residual Carbon from Pulverized Coal Fired Boilers 2: Morphology and Physicochemical Properties, accepted for publication in Fuel, May 1994

Hurt, R.H., Gibbins, R.J., *Fuel* 74 (4) 471-480 (1995).

Lunden, M., private communication, 1996

Mitchell, R. E., R. H. Hurt, L. L. Baxter, and D. R. Hardesty "Compilation of Sandia Coal Char Combustion Data and Kinetic Analyses: Milestone Report" SAND92-8208 June 1992.

Pohl, J. and Sarofim, A. *Proceedings of the Sixteenth Symp. (Int.) on Combustion,* The Combustion Institute, Pittsburgh, PA pp. 491 - 501 (1976).

Reid, W. T., Chapter 21 in *Chemistry of Coal Utilization, 2nd Supplementary Volume,* M.A. Elliott, ed., John Wiley and Sons, 1981.

Vleeskens, J. M. and Nandi, B. N. "Burnout of coals: Comparative bench-scale experiments on pulverized fuel and fluidized bed combustion" *Fuel* 65 797-802 (1986)

Table 3.1: Typical Combustor Conditions and Fuel Properties Used in Simulations

Residence time	1.5 seconds
Gas temperatures	2000 - 1500 K, linear decrease in time
Excess air	20%
Particle size distribution	Rosin-Rammler,70% < 200 mesh 0.1% > 50 mesh
Coal ash content	10%
wt-%C in coal (daf)	83%
wt-%H in coal (daf)	5.5%
Other fuel properties:	determined from correlations based on %C, %H

Table 3.2: Results of NO Reduction Experiments

Sample #	Description	Solids feed rate, g / min	% NO Reduction
1.	raw lignite	1.54	13
2.	lignite char 600 ^{o}C in Ar, 2hr	1.55	6
3.	lignite char 950 ^{o}C in Ar, 2 hr	1.55	4
4.	lignite char 1200 ^{o}C in N_2, 2 hr	1.55	1.5
5.	lignite char 1400 ^{o}C, 50 msec, 1% O_2 (in flame reactor)	0.92	9
6.	lignite char #3 after exposure to ozone / air mixture	1.55	5.5
7.	Illinois #6 raw coal	1.09	40.
8.	Illinois #6 char 950 ^{o}C in Ar, 10 min	2.0	2.5
9.	Illinois #6 char 1400 ^{o}C, 50 msec, 1% O_2 (in flame reactor)	0.75	0.8
10.	raw petroleum coke	2.01	5.6
11.	pet. coke, heat treated 950 ^{o}C in Ar, 10 min	2.1	<0.5

Table 3.3: Relative Volatile Content of Selected Samples from Table 3.2

Starting Sample	*Final Sample*	*weight loss on preparation*
2. lignite char, 600 ^{o}C in Ar, 2hr	3. lignite char 950 ^{o}C in Ar, 2 hr	2%
3. lignite char 950 ^{o}C in Ar, 2 hr	4. lignite char, 1200 ^{o}C in N_2, 2 hr	2%
3. Illinois #6 char 400 ^{o}C, 50 msec	4. Illinois #6 char 1200 ^{o}C in N_2, 2 hr	3%
10. raw pet. coke 200 ^{o}C in N_2, 2 hr	11. pet. coke, heat treated 950 ^{o}C in Ar, 10 min	7%

Table 3.4: NO Reduction Results as Apparent Heterogeneous Kinetics

Sample #	*Description*	*Mean Temperature in active zone (K)*	*preexpo. factor, A* ---- *g-NO/g-carbon-atm-hr* ----	*ln($k_{1250\ K}$)*
2.	lignite char 600 ^{o}C in Ar, 2hr	1320	$1.8 \cdot 10^{10}$	10.6
3.	lignite char 950 ^{o}C in Ar, 2 hr	1320	$1.2 \cdot 10^{10}$	10.2
4.	lignite char 1200 ^{o}C in N_2, 2 hr	1320	$0.45 \cdot 10^{10}$	9.3
5.	lignite char 1400 ^{o}C, 50 msec, 1% O_2 (in flame reactor)	1320	$3.8 \cdot 10^{10}$	11.5
6.	lignite char #3 after exposure to ozone / air mixture	1320	$1.7 \cdot 10^{10}$	10.6
8.	Illinois #6 char 950 ^{o}C in Ar, 10 min	1310	$0.68 \cdot 10^{10}$	9.7
9.	Illinois #6 char 1400 ^{o}C, 50 msec, 1% O_2 (in flame reactor)	1310	$0.41 \cdot 10^{10}$	9.3
10.	raw petroleum coke	1305	$1.4 \cdot 10^{10}$	10.3
11.	pet. coke, heat treated 950 ^{o}C in Ar, 10 min	1305	-- below detection limit --	

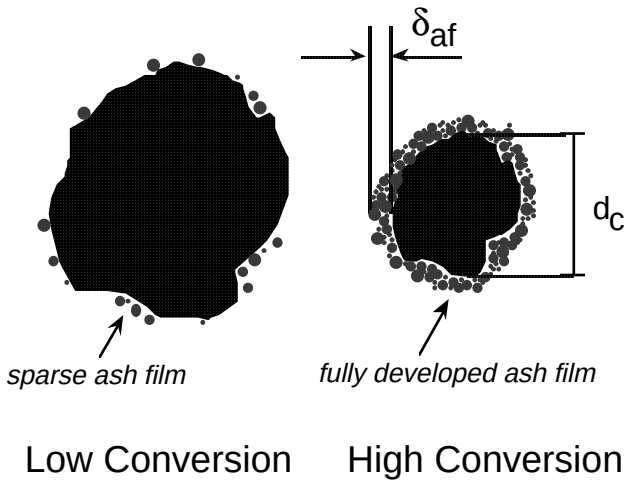

Figure 3.1 Physical basis for the ash inhibition model in CBK6.

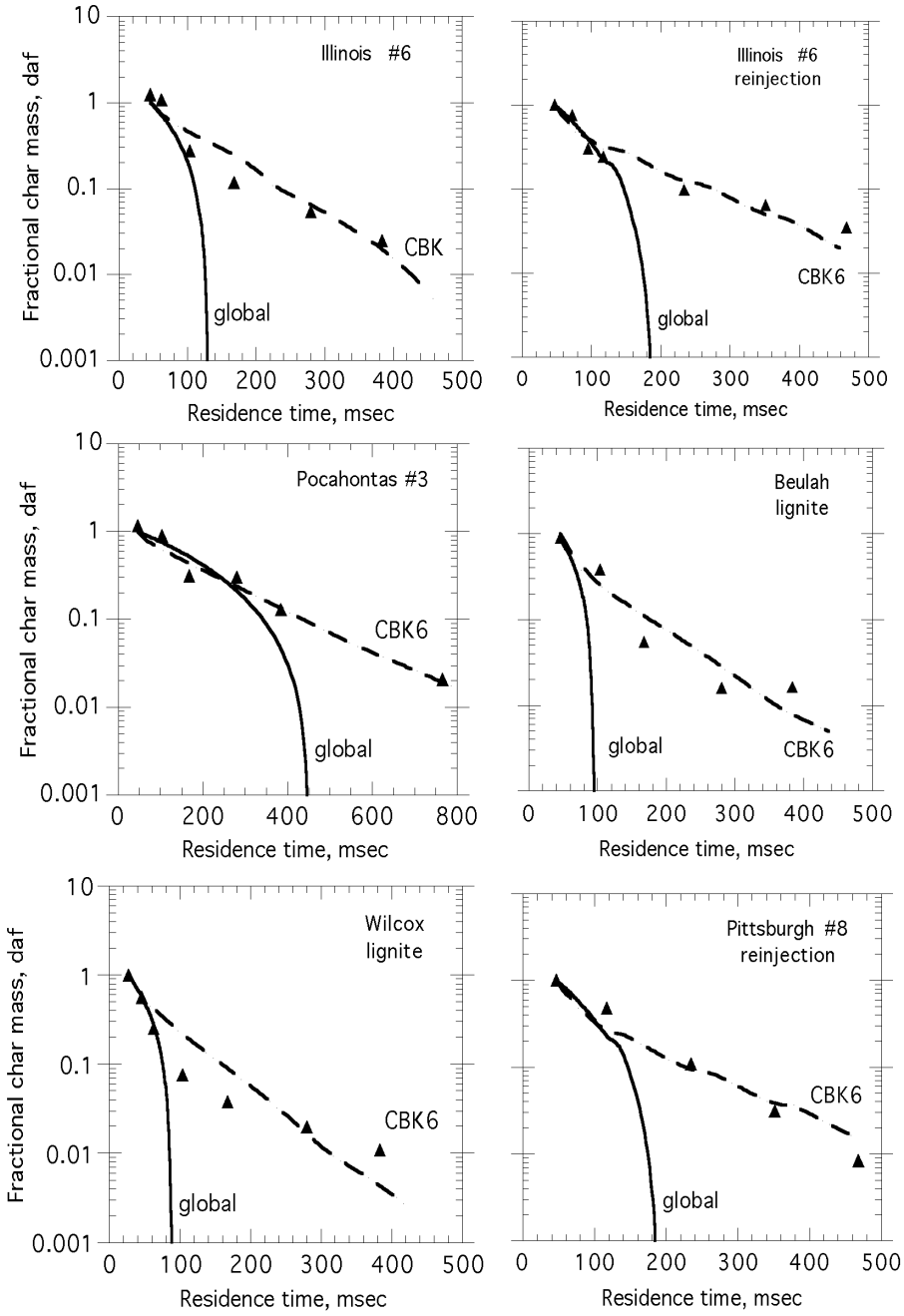

Figure 3.2 Comparison of measured conversion profiles from one-dimensional laboratory reactors (points) with predictions of the simple, global model of Hurt and Mitchell, [1992] (solid curves) and the CBK model (dashed curves).

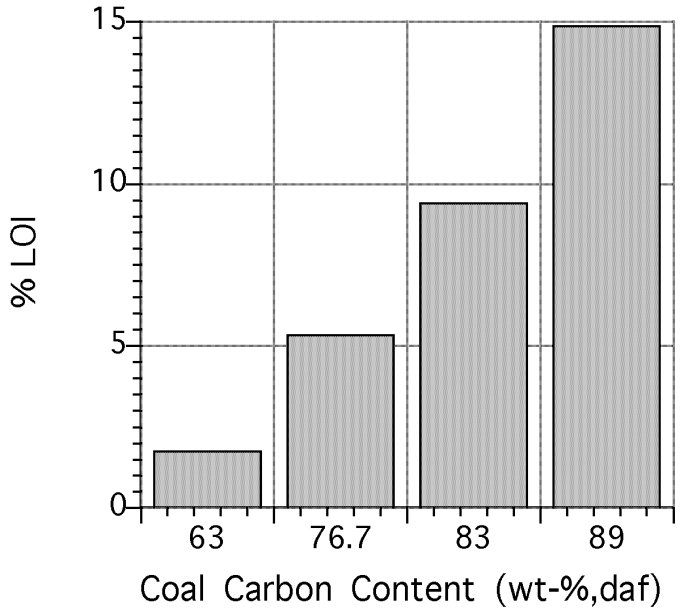

Figure 3.3 Effect of coal rank on LOI at constant fineness and furnace conditions.

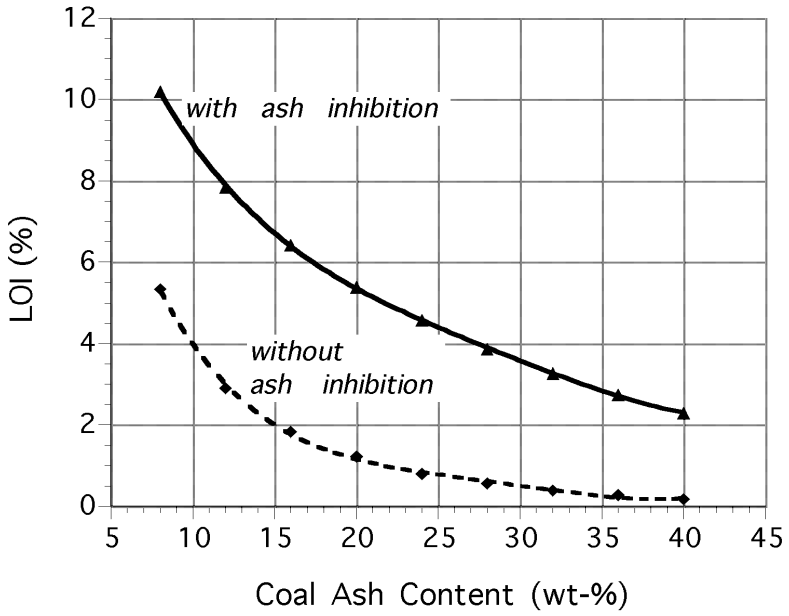

Figure 3.4 Effect of coal ash content on LOI and the effect of the ash inhibition sub-model.

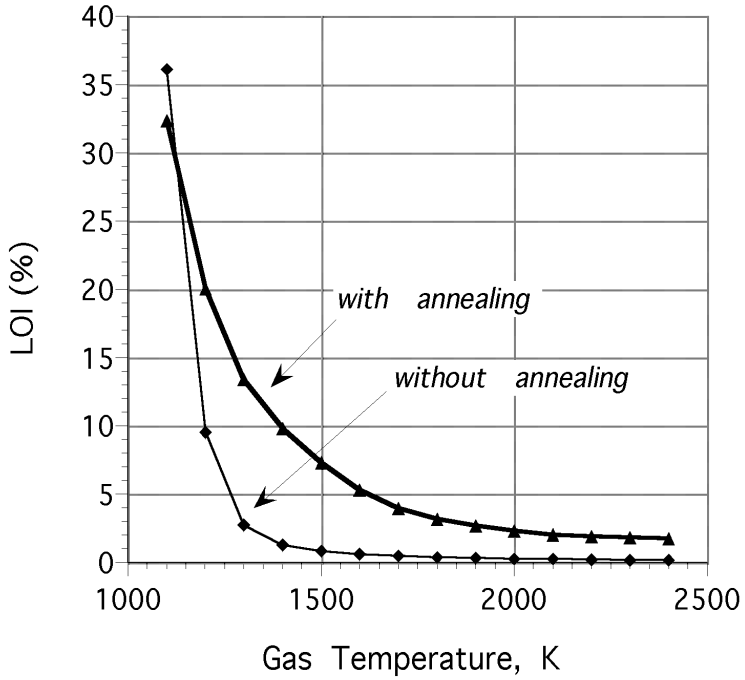

Figure 3.5 Role of annealing in LOI prediction; effect of gas temperature in isothermal environments.

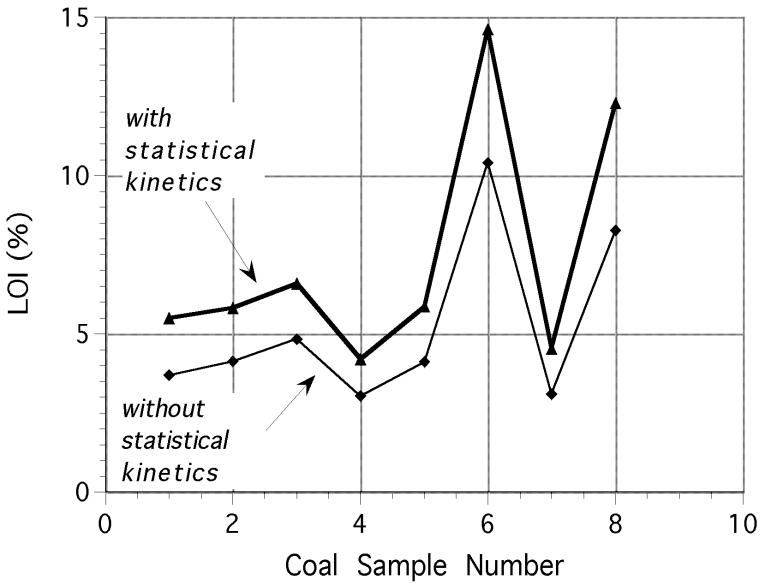

Figure 3.6 The effect of statistical kinetics on LOI prediction.

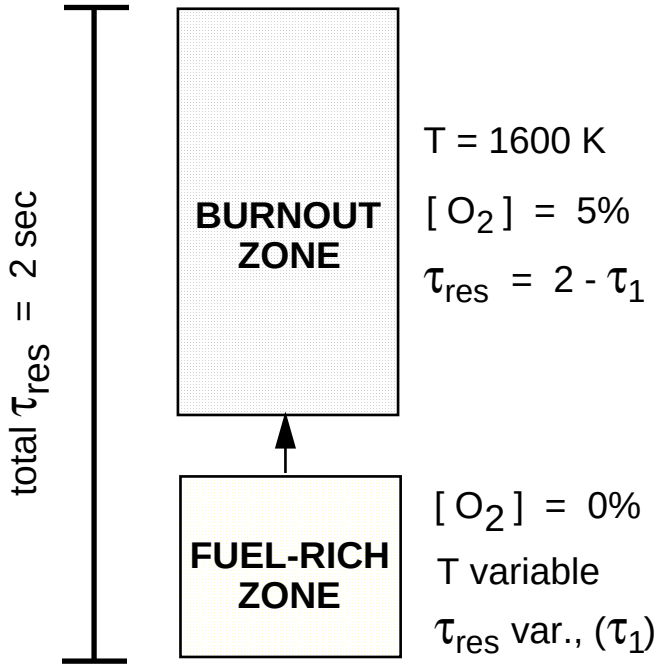

Figure 3.7 Sketch of the two-zone furnace descriptioin used in scoping studies of the carbon burnout processes in staged combustors.

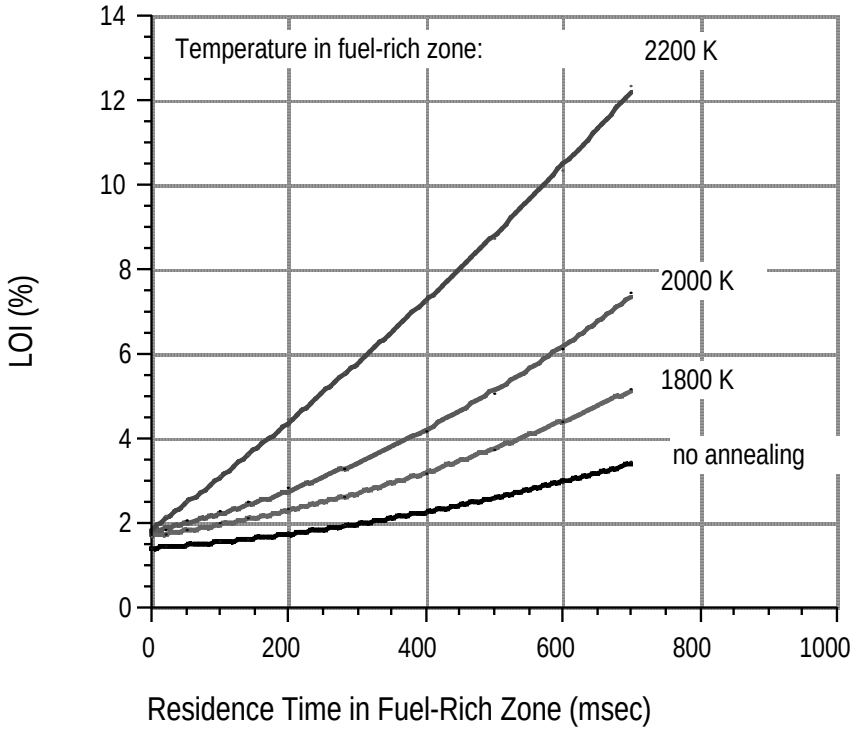

Figure 3.8 Simulated effect of staging and flame zone conditions on LOI.

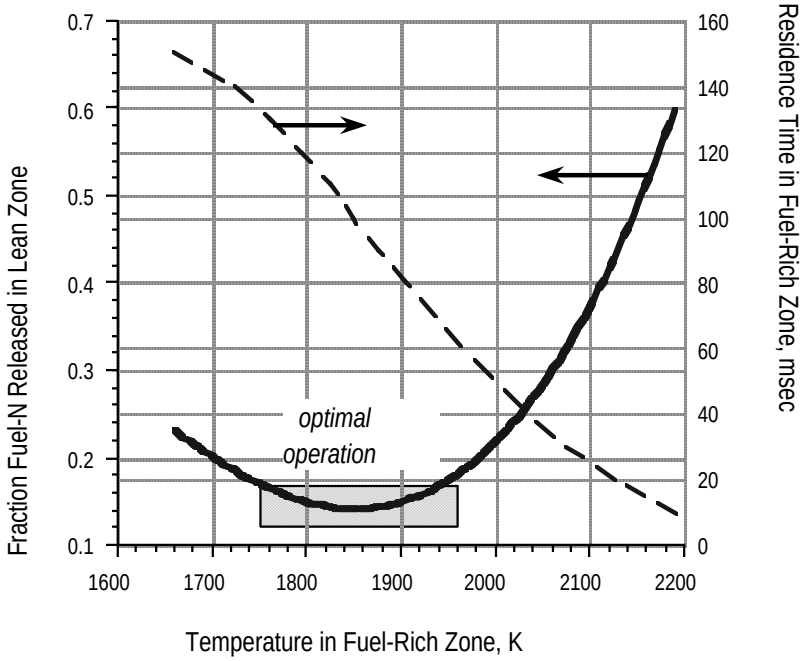

Figure 3.9 Simultaneous NO_x/LOI Optimization Through CBK Calculations in an Idealized, 1-dimensional staged combustor. Calculations use fuel nitrogen release kinetics of Pohl and Sarofim [1976] of the form: $(1/N_N)\, dN_N / dt = -9.3 \cdot 10^3 \exp(-22700/RT)$ with N_N defined as the moles of nitrogen remaining in the solid fuel, and for RT in cal/mol.

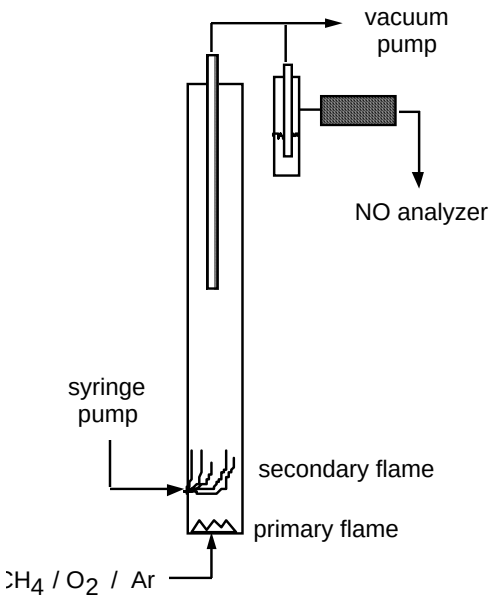

Table 1. Experimental conditions

- gas temperature at injection point: 1626 K
- nominal residence time: 100 msec
- O_2 concentration after primary flame: 1.0 %.
- NO concentration after primary flame: 1000 ppm
- total flow: 30 standard liters per minute

Figure 3.10 Sketch of the flame reactor.

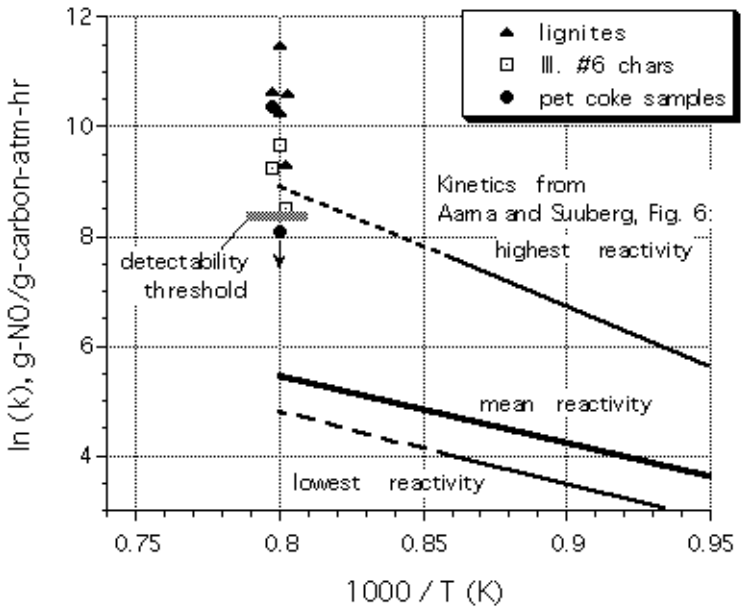

Figure 3.11 NO reduction reactivities for a variety of solid fuels expressed as apparent heterogeneous rate constants at 1250 K. Measured points are compared to literature values reviewed by Aarna and Suuberg, 1996.

4.0 RESULTS AND DISCUSSION-TWO PHASE MIXING

4.1 INTRODUCTION

This chapter describes and discusses the outcomes from the two phase mixing studies performed at the Physical Fluid Dynamics (PFD) lab, University of Utah. The goal of these studies is to gain a better understanding of the mechanisms underlying the dispersion of particles in the near-field of the injector. In particular, this research focused on 1) obtaining accurate descriptions (both instantaneous and statistical) of the fluid velocity field, and 2) correlating these descriptions with the injector characteristics and with the dispersion of the suspended phase. The motivations for these studies, in the context of the broader project goals, are to aid in the validation and further development of the computational models being employed, as well as to provide data bases quantifying the influences of injector geometry and operating parameters (e.g., influence of primary jet coal spreader and secondary-to-primary jet velocity ratio). The remainder of this subsection includes a brief discussion regarding the most significant fundamental issues relevant to particle dispersion, followed by a discussion of the present strategy for exploring these issues. The remainder of this chapter contains a description of the experimental facility and experimental techniques, followed by a presentation and discussion of results. This chapter closes by drawing some conclusions from the results to date, as well as a discussion of the important issues that should be explored in the follow-on (Phase II) portion of this research project.

It is widely held that a critical (if not most important) parameter describing particle dispersion is the Stokes number, $St = t_p/t_f$, where t_p is the aerodynamic response time and t_f is a characteristic time of the fluid turbulence. For $St << 1$, particles are nearly in dynamic equilibrium, and thus will essentially follow the fluid motion. Conversely, for $St >> 1$ the trajectory of the particle is nearly unaffected by the fluid motion. Owing to the fact that at any instant a turbulent flow field is comprised of a range of motions have differing time scales (and that these motions rapidly evolve in time as well), St is a stochastic parameter. From ***GLACIER***-based computations of the near field of a typical coal-fired furnace injector (P.J. Smith, private communication), a typical average Stokes number is 0.3. For $St \sim 1$, particles are primarily effected by a subset of the turbulent eddies. Consistent with this, there is a growing body of evidence (Kamalu et al. 1989, Longmire and Eaton 1990, Wicker and Eaton 1994) that the large scale coherent motions within a turbulent flow can have dramatically disproportionate influence on the time-averaged characteristics of particle dispersion.

Particularly relevant to this issue, and to the present research, is the study by Wicker and Eaton (1994), in which they explored the dynamics and control of particle laden coaxial jets with and without swirl. Their observations indicated that the coherent motions characteristic of the shear layers between the primary and secondary jets as well as between the secondary jet and ambient fluid play a predominant role on the particle dispersion. Furthermore, changing the flow via plane wave excitation, and/or exit plane vortex generators, and/or swirl caused significant modifications to the resulting net dispersion. The unifying notion underlying these observed modifications is that the trends in the net dispersion can be predictably altered by changing the Stokes number. Given that in coal fired furnace applications changing the particle response time (i.e., changing the particle size) is generally not a practical alternative, the rational choice is to modify the coherent motions most responsible for dispersion. This, of course, is what adding vortex generators or primary jet coal spreaders achieves. Modifications such as these are statistically reflected in changes in the length and time scales of the turbulence.

An important notion underlying the strategy undertaken in the present work is the fact that any net (i.e., time averaged) modification of the dispersion of particles results from the cumulative effect of instantaneous eddies acting within the flow. For the case of near unity Stokes number this issue is complicated by the fact that only a subset of the entirety of the motions is responsible for the bulk of particle transport. Given this, the method for achieving the above goals is to draw connections between the net changes in particle dispersion (for a specific flow configuration), and the coherent structure of the turbulence. This is done by measuring the statistical spatial distributions of the flow and particles, and the instantaneous spatial distributions of the flow and particles. In this way, exploration of the instantaneous (and/or conditional) flow properties allows one to reliably determine the instantaneous flow features that, when averaged, lead to the observed average behavior. Of course, obtaining instantaneous spatial distributions of the velocity field in a particle laden flow is not easy, and thus a considerable portion of this effort has been devoted to the development of measurement techniques that allow this to be accomplished. For this reason prior to a discussion of results we first describe the experimental facility and its capabilities, and then discuss the Molecular Tagging Velocimetry (MTV) flow measurement technique and its use in particle laden flows.

4.2 EXPERIMENTAL FACILITY AND PARAMETERS

4.2.1 GENERAL DESCRIPTION

The purpose of the experimental facility developed is to provide a precisely controllable environment to explore the influences of flow modifications on particle dispersion in the baseline configuration of a coaxial jet. Primary considerations in the facility design included the ability to accurately set a wide variety of primary-to-secondary jet velocity ratios, accurately control the rate of primary jet particle injection, accurately maintain constant flow rates for both the primary and secondary jets under continuous operation, allow optical access for the velocity and particle measurement techniques (described below), and easily allow different nozzle configurations and/or jet modifications to be installed.

The baseline experimental facility was manufactured by Engineering Laboratory Design and in its original configuration was used for turbulent boundary layer research. Extensive modifications and additions have been made to the baseline design to accommodate the needs of the present research. The addition of a much larger test section, a particle filtration tank, two pumps, and associated piping has increased the fluid volume capacity from 190 l to nearly 950 l. The primary (central) jet and the secondary (annular) jet are each driven by a 1120 W centrifugal pump. In its generic configuration, the primary flow line and the secondary flow line are 30.0 mm and 75.0 mm in diameter, respectively. The wall thickness of the primary jet nozzle is 1.5 mm. One of two independent systems can be used to inject particles into the primary flow line approximately 30 diameters upstream of the jet orifice. A 375 W progressing cavity pump system is used to inject particles if high back pressures are present. If the system pressures are low, a gravity feed system (“hour glass” configuration with various orifice sizes to control the particle mass flow rate) is used. Since each pump motor is separately controlled, various secondary to primary jet velocity ratios and particle mass loading ratios can be generated and precisely adjusted.

The test section measures 0.5 meters in height and width and 0.6 meters in length. The coaxial jet orifice located in the center of the upstream test section wall issues fluid horizontally into the test

section. The test section is configured such that the flow experiences a sudden expansion immediately downstream of the jet orifice. The top and one side wall of the test section is made of 9.5 mm thick quartz plate to allow passage of an ultraviolet laser beam (used in the MTV measurements) with minimal loss of power. The test section was made as large as possible to minimize wall effects. Preliminary flow visualization studies clearly indicated, however, that the jet was in fact confined. This was evidenced by large recirculation zones existing in the regions between the jet axis and the surrounding test section walls.

Since the experiment facility recirculates, particle filtration is necessary to prevent the contamination of the secondary stream with particles, as well as the re-admission of particles to the primary flow during the course of an experiment. The initial particle filtration system employed a relatively small scale in-line flow expansion incorporating a stainless steel mesh filter arrangement. The capacity of this system was not sufficient, however, to prevent mass flow variations due to particle build-up. The current (final) particle filtration component is now located in the return flow line downstream of the test section. It consists of a large 570 l stainless steel tank containing several baffle elements and four 75 micron stainless steel mesh filters. (Note that all components exposed to the flow must be non-reactive to the MTV chemical, e.g., stainless steel, glass or PVC.) The removal of particles retained in the holding tank is facilitated by two large union ball valves, one placed upstream and one placed downstream of the filtration tank. When the tank needs to be cleaned these valves are closed, the unions are disconnected, and the tank is drained. The major benefit of this design is that the tank can be isolated for cleaning without having the cumbersome task of draining and refilling the entire 950 liters of the facility. A schematic of the experimental facility displaying the major system components is given in Figure 4.1. Figures 4.2 and 4.3 are images of the experimental facility in which the major system components are shown.

4.2.2 FACILITY CAPABILITIES

The maximum average flow speed, for the primary and secondary jet are 2.5 m/s and 1.6 m/s, respectively. This equates to a maximum Reynolds number of 1.2×10^5 based on the secondary jet diameter. A typical actual low-NO_x emission pulverized coal electric utility boiler operates at a Reynolds number of approximately 1.33×10^5 (cold air flowing at 20 m/s with a 0.1 m diameter orifice). Thus the experiment and actual boiler Reynolds numbers are reasonably well matched.

Maximum flow speeds are limited not only by the primary and secondary pump size, but also by pump cavitation and vibration constraints. Both pumps cavitate at high rates of revolution. The ensuing water vapor bubbles interfere with MTV laser lines generating unacceptably high velocity errors. High pump speeds also generate undesirable structural vibration which further hinders successful application of the MTV technique. For these reasons, pump speeds must be kept at moderate levels.

4.2.3 PARTICLE MASS LOADING RATIOS

The maximum particle mass loading ratio that can be investigated in this study is limited by the MTV technique. Excessively dense particle clouds interfere with MTV laser lines to the point that a significant fraction of useful data cannot be obtained. Particle mass loading ratios in the neighborhood of 5% to 10% have been found to create negligible MTV errors. These mass loadings also closely match those used in actual low-NO_x emission pulverized coal electric utility boilers,

except in the coal pipe and in the immediate vicinity of its exit where mass loadings can reach values near 50%. A mass loading of 10% is generally considered the upper limit for a case where particle-particle interactions can be neglected for coal in air. Owing, however, to the fact that in the present study a water analogue is employed, the ratio of the density of the particle to the density of the carrier fluid is much less than in an actual furnace application. Thus, volumetrically, the present experiments have a much higher solid content than a coal-in-air system at the same mass loading. The compromise situation is to use primary jet (coal pipe) mass loadings in the range of 5% to 10%. For these loadings the particles interact in the pipe and near the exit, but farther downstream do not -- just as in the coal-in-air systems being modeled. More discussion on the impact of particles on the MTV technique is given in the Fluid Velocity Measurements section below.

4.2.4 PARTICLE SELECTION

Particle selection was made on the basis of required physical properties (corrosion resistance, size, density, optical properties), availability, and cost. Calculations combined with experimentation indicate that a 0.1 mm diameter approximately spherical glass shot with a specific gravity of 2.5 is suitable in that it is readily available in large quantities at a reasonable cost, does not corrode in the MTV photoluminescent chemical/water environment, does not cause MTV chemical degradation, reflects light well for concentration measurements, and matches the Stokes number of pulverized coal in air (0.3) reasonably well. Stainless steel ball bearings and yttrium stabilized zirconia particles were considered for use, however, they were rejected due to lack of availability (the hundreds of thousands of stainless steel ball bearings needed were not readily available), and high cost (zirconia particles would have exceeded a cost $4,000 for the quantity needed).

The glass particles used are manufactured from high grade, optical crown glass annealed in an 85 percent true spherical shape. They are typically used in surface cleaning, peening, and finishing operations so they are designed to resist corrosion, wear, and fracture. In addition, the glass particles are crystal clear, free from surface films, and no more than two percent exhibit milkiness, scores, or scratches. This leads to highly constant light reflective properties that are independent of particle orientation. These features offer distinct advantages in the particle concentration data reduction analysis.

4.2.5 STOKES NUMBER

The Stokes number (St) is defined as the ratio of the particle time scale, t_p, to an appropriate fluid time scale, t_f. Thus, in a turbulent flow its average value is a local, nondimensional, statistically based parameter. Stokes' formula for a spherical particle in creeping flow is $t_p = (2\rho_p+\rho_f)d_p2/36\mu$, where ρ_p and d_p are the particle density and diameter, respectively and ρ_f and μ are the fluid mass density and dynamic viscosity, respectively. Since the drag on a particle depends on the relative velocity between the particle and the carrier fluid, a creeping flow approximation, on the average, is applicable. Substituting appropriate values into Stokes' equation yields a particle time scale estimate of 0.0017 seconds.

Kolmogoroff (1941) argued that the lower limit for the fluid time scale is given by $t_f = (\nu L/U^3)^{1/2}$ where ν is the kinematic viscosity of the fluid and U and L are a characteristic flow velocity and length scale, respectively. Substituting appropriate values into this equation yields an estimate for the Kolmogoroff time scale of 0.00014 seconds for the flow field in the present experiments. Only

in the extreme case, however, would one expect that particles would respond to the frequency associated with the smallest eddies in the flow. On the other hand, an estimate for the upper limit, and arguably a more accurate estimate of the fluid time scale, is the width of the annular jet, R_2-R_1, divided by the maximum secondary flow velocity, V_s. Underlying this estimate is the classical notion that the integral scale eddies contain most of the energy. Thus, for a typical experiment t_f = (R_2-R_1)/ V_s = 0.0225 (m)/1.6 (m/s) = 0.014 s, which yields a Stokes number estimate of 0.12 for the present experiments.

4.3 EXPERIMENTAL TECHNIQUES

4.3.1 FLUID VELOCITY MEASUREMENTS VIA MTV

Fluid velocity measurements were made using an adaptation of the nonintrusive Molecular Tagging Velocimetry (MTV) technique. (Note that this technique was previously called Laser Induced Photochemical Anemometry or LIPA. Owing, however, to the fact that the technique can be used in either gas or liquid flows, the more appropriate acronym MTV is now employed, see Gendrich and Koochesfahani 1996.) For the past six years, MTV has been used extensively in the PFD lab for both applied (e.g., Maynes 1997) and fundamental (e.g., Lee 1995, Hill 1997) studies of unsteady, turbulent and spatially complex flows.

4.3.2 MTV METHOD

The MTV technique relies on the relatively long emission lifetime of certain ultra-violet activated phosphors. The present experiments used the photoluminescent chemical, 1-Br-Np*Gβ-CD*ROH Ternary Complex (hereafter, Gβ-CD) developed by Ponce et al. (1993). Excitation by a 308nm light (produced by a Lumonics EX-700 excimer laser) yields visible spectrum emission (green) that can be imaged by our gated intensified CCD camera (Xybion model ISG-250) up to about 12 ms after the laser pulse. The time delay between when the laser fires and when the camera shutters is controlled by a pulse/delay generator. During this time delay the line of excited Gβ-CD is displaced as a result of the fluid motion. Duration of the camera exposure is set at less than 20% of the delay. For the line (or multiple line) method, determination of the velocity relies on the pointwise subtraction of the undisplaced (non-time delayed) line position from the displaced (time-delayed) line positions. For short time delays (relative to the flow physics), Δt, the instantaneous component of velocity perpendicular to the line, u, is accurately determined using the Lagrangian formula, $u = \Delta x / \Delta t$. An image of a typical displaced line is shown in Figure 4.4. Note that the actual displacements used are quite small. An image of a typical instantaneous u(r) velocity profile is shown in Figure 4.5. Typically 64 images are averaged to compute the undisplaced Gβ-CD marker position. The number of displaced Gβ-CD images used to compute velocity statistics depends on the type of information sought (300 images or more is common to obtain reliable mean and root mean square [RMS] statistics in free shear flows). According to the analysis of Hill and Klewicki (1996), for the pure fluid case and except near the extreme edges of the jet (where the mean velocity is small and flow angles are large), the maximum error in the instantaneous velocity is less than about 8% for the time delay and camera lens magnification used in the present experiments.

4.3.3 MTV WITH PARTICLES

The addition of solid particles to a flow field negatively impacts the MTV technique. In fact, for sufficiently high particle densities these difficulties become insurmountable. Fortunately, the particle mass loading ratios used in the present study renders MTV data analyzable. Considerable effort has been devoted to developing a novel data reduction algorithm that overcomes the negative effects created by particle injection. A summary of this new algorithm is now given.

The MTV data reduction algorithm for a pure fluid is relatively straightforward requiring few, or in most cases, no velocity error detection and adjustment schemes. After analyzing several preliminary particle-laden MTV data sets however, it became apparent that the addition of particles to the flow field intermittently created highly undesirable spurious effects. These negative effects include light reflections, particle interference, and shadowing effects. The fluid velocity errors stemming from occasional particle interference must be detected and appropriately dealt with since only a relatively few spurious points can result in significant errors in the fluid velocity statistics.

The problems were identified by conducting experiments with and without particle injection under identical primary and secondary pump speed conditions. At a Stokes number in the range of 0.1 to 1.0 and a mass loading ratio of approximately five percent some turbulence modification is expected (as reported in the literature). The turbulence intensity (root mean square velocity fluctuation) at some locations, however, was calculated to be two and in some cases three times greater than the particle free case. At this point, the MTV data reduction algorithm was considered suspect.

Detailed visual inspection of digitized images highlighted the problem. A subtle, and perhaps the most serious problem, occurs when a particle interferes with the laser line in such a way that a transverse cut through the MTV line yields a nearly linear light intensity profile with a sharp discontinuity, as opposed to the smoothly varying intensity profile observed for the pure fluid case. A common MTV data reduction algorithm step involves applying a second order curve fit to the highest intensity portion of the light intensity versus position profile. Applying a second order curve fit to a discontinuous intensity profile, however, yields grossly erroneous results. Although analysis has indicated that there is less than a one percent occurrence rate for this type of problem, when it does occur it greatly skews average velocity and turbulence statistics. A new MTV data reduction algorithm which includes several error detection and correction steps has been developed to resolve the problems created by the addition of particles to the flow field. A summary of the major steps in this new algorithm follows.

First, the raw light intensity data in each frame is read into a dummy array. A threshold and two-dimensional Gaussian smoothing routine is then evoked which serves to suppress spurious light reflections yet preserve the basic position and intensity profile of the MTV line. Although this step tends to distort the MTV line a small amount (no more than a pixel or two), the goal is only to find the approximate location of the MTV line. Now that the approximate position of the MTV line in each image is known, the code reverts back to analyzing the raw data, thus preserving data fidelity. With this information the code searches only in the immediate neighborhood of the MTV line for the location of maximum light intensity (i.e., the MTV line center). This serves to greatly reduce the chance of mistaking particle light reflections for the MTV line.

Before a second order curve fit is applied to the light intensity versus position profile, it is analyzed to ensure that the intensity varies continuously. If this is not the case the code assigns the

velocity at this pixel location to be identical to the velocity just previously analyzed. That is, in effect it assigns the same velocity at two neighboring pixels. This is justified for two reasons. First, one does not expect the velocity to be much different between two adjacent pixels (the physical distance separating pixels is on the order of tenths of a millimeter). Secondly, these intensity profile abnormalities created by particle interference are random and occur in less than one percent of the data. Thus, errors introduced by this scheme are minimal, especially when hundreds of images are analyzed to compute turbulence statistics. Note also that while this correction strategy is currently being employed, other strategies, such as choosing the mean of the velocities on either side of the spurious point, may just as easily be employed. Given the rate of occurrence of these errors, however, the difference between the two is felt to be statistically negligible.

The last major feature of the new algorithm is that deformed MTV line locations and intensities are compared between images to ensure that an entire erroneous frame is not used in data analysis. Although turbulence will change deformed laser line locations from image to image, the present flow field is steady in the mean so it is possible to successfully apply a reasonable displacement threshold to screen out entire frames of erroneous data. This step is incorporated into the algorithm since occasionally a particle interferes with the laser line during the laser pulse in a such a way that it deflects the line and/or significantly reduces its intensity.

4.3.4 PARTICLE DISTRIBUTION MEASUREMENTS

Planar particle number density data are acquired by directing a sheet of laser light into the test section, capturing light reflections off particles on videotape, and digitizing these images for subsequent analysis. Figure 4.6 shows a typical instantaneous image of particles illuminated in a plane perpendicular to the jet 7.5 diameters downstream of the jet exit. The analysis is conceptually straight-forward in that our goal is simply to count the number of particles contained in a laser sheet of known length, width and thickness. From this a net particle density may be computed, and by knowing the mass densities of the particles and fluid allows an instantaneous mass loading to be computed. Of course, for comparative purposes if one keeps the laser sheet dimension fixed, then just the resulting distribution of particles imaged gives an accurate relative measure of mass loading. For the sake of simplicity, the data below are presented in this manner.

If particle reflections occupied only one pixel then a simple threshold scheme could be applied to locate particles in each image. Complications stem from the fact that particle reflections almost always occupy more than one pixel. Further complications arise from the fact that particle variations (variations from a truly spherical shape, impurities, etc.) result in particles appearing throughout a range of pixel diameters and light intensities. Resolving particles that are in close vicinity to each other adds further difficulty. The problem thus becomes locating particle centers and defining an adequate light intensity threshold.

A computer code has been developed to locate particle centers accurately. The algorithm involves first applying a smoothing routine to clearly define points of maximum light intensity (particle centers) followed by defining an intensity threshold dependent on the maximum light intensity (brightest particle) in any given image. This computer code has been tested on a number of data sets and appears to work well. In this chapter, particle concentration data are presented in a probabilistic fashion (probability of a particle being present at a given location downstream of the jet exit).

4.3.5 FLOW VISUALIZATION

Although not an extensive component of the present study, a suitable Laser Induced Fluorescence (LIF) flow visualization/passive scalar mixing technique has been developed to aid in interpreting both the MTV and especially the particle concentration results. The visualization is accomplished by injecting a prescribed amount of fluorescein (Schmidt number in water of 1800, specific gravity of 1.000) into the flow at one of two locations: the injection of fluorescein at the particle injection location yields primary jet development information, while secondary jet development information can be obtained by injecting fluorescein just upstream of the secondary flow pump. Fluorescein has the property that it emits light in the visible spectrum when excited by the light from our Argon laser (488 nm and 512 nm are the dominant wavelengths). Jet development and scalar mixing information can therefore be obtained at various planar locations by directing the laser sheet into the test section and recording light intensity images on videotape for subsequent analysis. A typical instantaneous LIF image is shown in Figure 4.7.

Only a few LIF experiments can be conducted before the background fluorescein concentration level becomes too great. Once the fluorescein concentration in the system is too high, the facility must be drained and refilled. The effect fluorescein has on the MTV photoluminescent chemical used in the present study is unknown at this time. If it is found, however, that fluorescein has no deleterious effects on these chemicals it may be possible to acquire flow visualization, particle concentration, and MTV data simultaneously with proper argon ion laser, UV laser, and camera synchronization.

4.4 RESULTS AND DISCUSSION

This section first presents results for the coaxial jet configuration for two values of the secondary-to-primary jet velocity ratio, as well as for cases of particles or no particles for a primary jet particle mass loading of 5%. Particle dispersion measurements are then presented for the case in which a configuration mimicking a coal spreader is added to the primary jet. For the coaxial jet studies, mean and RMS axial velocity profiles at a number of axial locations downstream of the jet exit are first presented. LIF and particle dispersion results are then discussed in the context of these measurements. Owing to the unusual capabilities provided by the MTV technique, we are able to obtain detailed information relating the spatial scale of the turbulence structure, which, as discussed in Section 4.1 of this chapter, is felt essential to understanding the mechanisms underlying the characteristics of the net particle dispersion. In this regard, spatial correlations of the axial velocity are presented for a single axial location downstream of the jet exit. Finally, the mock coal spreader results are presented and compared to ***GLACIER*** code based computations.

4.4.1 VELOCITY FIELD STATISTICAL PROFILES

4.4.1.1 Mean and RMS Statistics without Particles

Mean radial velocity profiles for secondary-to-primary jet velocity ratios of V_s/V_p = 0.5 and 1.0 and at axial locations of x/d = 2.5, 5.0 and 7.5 are shown in Figures 4.8-4.10. For these velocity ratios the Reynolds numbers based on the secondary jet diameter and secondary mean velocity are 5.55×10^4 and 1.1×10^5 respectively. These profiles, which are based upon ensemble of 320 independent instantaneous profiles, show the evolution of the jet in the near field. In particular, it is

apparent that strong shear layers exist for small x/d, and, as expected, these shear layers spread with increasing axial distance. As shown in Figure 4.8 (x/d = 2.5), the primary jet initially undergoes acceleration owing to the confining nature of the annular jet. Similar phenomena have been observed previously (e.g., Ribero and Whitelaw 1980). As the jet develops, momentum exchange takes place between the inner and outer cores. By x/d = 7.5 for V_s/V_p = 0.5, this leads to a non-identifiable secondary core and a significantly decreased peak in the primary jet. Similarly, by x/d = 7.5 for V_s/V_p = 1.0, a broad central region encompassing a radial distance about equal to the outer jet radius exists.

Figures 4.11-4.13 show the axial velocity RMS profiles corresponding to the mean profiles of Figures 4.8-4.10. For the purpose of assessing the intensity of the turbulence relative to the mean momentum, these profiles are normalized by the local mean value. Note that because the mean velocity becomes very small near the edge of the jet this normalization leads to very high values at the jet periphery. Examination of the RMS profiles indicates that at x/d = 2.5 low relative turbulence primary and secondary core regions exist for both the V_s/V_p = 0.5 and 1.0 cases. At x/d = 5.0, however, the secondary core is non-existent for V_s/V_p = 0.5, but persists beyond x/d = 7.5 for V_s/V_p = 1.0. The primary core remains beyond x/d = 7.5 for both velocity ratios.

Comparison of the mean and RMS profiles indicates that the peaks in the RMS profiles align with regions having a high radial gradient in the mean profiles. This, of course, results from the fact that the production term in the axial turbulent stress transport equation contains the mean gradient, dU/dr. Owing to the fact that the jet exit condition for the V_s/V_p = 0.5 case necessarily produces a higher mean shear between the primary and secondary cores than in the V_s/V_p = 1.0 case, the larger relative RMS values in the vicinity of this internal shear layer is expected. Similarly, based upon an identical argument, a higher relative RMS is observed for the V_s/V_p = 1.0 case in the outer shear layer for x/d = 2.5 and 5.0. (At x/d = 7.5, apparently turbulence intensity from the inner shear layer for V_s/V_p = 0.5 has diffused all to the outer edge, and thus nearly equal magnitude relative intensities are observed.) As expected, the peaks in the RMS profiles diminish with decreasing mean gradient. This is associated with the downstream spread of momentum. A central issue relating to these pure fluid measurements is the correlation between the spread of momentum and the dispersion of particles, which is addressed in the later sections below.

4.4.1.2 Mean and RMS Statistics with Particles

Measurements of the mean and RMS axial velocity at the same velocity ratios and x/d positions used in the pure fluid experiments were also conducted for a primary jet mass loading of 5%. As is exemplified below, the results with particles exhibit only very subtle differences (in these statistics) from the pure fluid case. For this reason only the results at x/d = 2.5 and 7.5 are displayed and discussed. These results do, however, provide a sufficient context for discussing the effects of particle coupling with the turbulence, as well as discussing the detailed correlation data presented below.

In addition, it should be noted that an important outcome of the MTV particle measurements was the detection of a small, but significant, variation in the facility mass flow rate that occurred after particles were injected for a long time. This variation was due to an increasing pressure drop associated with the accumulation of particles in the filter element. As discussed in the facility description above, this problem has been solved by adding a much larger (570 l) filtration tank. In this regard, it is worth noting that since MTV provides profile data directly, this mass flow rate

variation was readily discovered. On the other hand, it is doubtful that this problem (which only appeared after a significant operating time) would have been detected using a pointwise technique such as LDV.

Figure 4.14 presents the particle laden flow mean profiles at x/d = 2.5 for V_s/V_p = 0.5 and 1.0. Comparison with Figure 4.8 indicates that these profiles display a high degree of similarity with the pure fluid case. Close examination suggests, however, that for the particle laden case both the primary and secondary jet cores may be slightly larger than in the pure fluid case. A similar feature is also suggested by mean profiles at x/d = 7.5 in Figure 4.15. In particular, the results for V_s/V_p = 1.0 indicate that a slightly fuller profile for r/R < 0.8 (R = d/2) is preserved in the particle laden case. Interestingly, the particle laden x/d = 7.5, V_s/V_p = 0.5 case shows identifiably less radial spread than the pure fluid case. Examination of the dimensional profiles (not shown) indicates, however, that the maximum centerline velocity is slightly larger in the particle laden case -- which is also consistent with a more highly preserved primary core.

The RMS axial velocity results for x/d = 2.5 and 7.5 are shown in Figures 4.16 and 4.17, respectively. As with the mean velocity results, these data are highly similar to the pure fluid cases at the same axial locations, except for the x/d = 7.5, V_s/V_p = 0.5 case which shows a different shape than its corresponding pure fluid case. At present, the reasons underlying this difference remain unclear. Perhaps somewhat expected, however, the RMS data also tend to show slightly higher peak values, as well as slightly more scatter.

4.4.2 FLUORESCEIN AND PARTICLE CONCENTRATION DISTRIBUTIONS

The mean and RMS profiles above give indications relating to how momentum is spread downstream of the jet exit. In this section results are presented relating to the distribution of a passive scalar (Sc = 1,800) and solid particles, both introduced through the primary jet at the same velocity ratios as for the cases discussed above.

4.4.2.1 Scalar Concentration Distributions

Scalar concentration contour plots for x/d = 5.0 and V_s/V_p = 1.0 and 0.5 are shown in Figures 4.18 and 4.19 respectively. Similarly, the concentration contour plots for x/d = 10.0 and V_s/V_p = 1.0 and 0.5 are shown in Figures 4.20 and 4.21. In these figures, the contour values are average grayscale light intensities (normalized by the brightest intensity value of 255). Thus, a contour value of 1.0 is the maximum, and a value of 0.01 corresponds to nearly pure water. The stepwise appearance of the light intensity is due to the 10 x 10 pixel cell (equivalent to an area of 2 mm^2) averaging technique employed. In interpreting these results it is important to note that the primary jet velocity was kept constant, as was the flow rate of fluorescein fed into the primary jet. Thus, the fluorescein concentration in the primary jet was identical in each experiment. In addition, close control was maintained regarding the constancy of the laser power, as well as the optical configuration. The entire facility was drained and refilled with fresh water from experiment to experiment to prevent background fluorescein levels from interfering with the concentration measurements.

Comparison of Figure 4.18 with Figure 4.19 clearly indicates that at x/d = 5.0 more of the core fluid is spread throughout the jet for the V_s/V_p = 1.0 case. Examination of Figures 4.20 and 4.21 indicates that this trend persists at x/d = 10.0 Based on these results it is strongly suspected that,

since scalar concentration is conserved, at a velocity ratio of 1.0 the turbulent transport in the shear layer between the secondary jet and the ambient flow is a dominate feature of the mixing process. Since the respective contour sizes are significantly smaller for the 1.0 velocity ratio case, vigorous mixing occurring in the outer shear layer region must be what is responsible for spreading the fluorescein dye to negligible concentration levels (e.g., below .01, see Figure 4.20). A similar process was observed relating to the spread of momentum in that the $V_s/V_p = 1.0$ case consistently exhibited a wider jet, especially for $x/d > 5.0$. Of course, this increased spreading for $V_s/V_p = 1.0$ must also be related to the more rapid erosion of the high concentration core. Apparently, the more wake-like shear layer structure of the region between the primary and secondary jets for $V_s/V_p = 1.0$ is more efficient at transporting passive scalar to the outer shear layer. In terms of the vorticity field, the primary difference here is that the $V_s/V_p = 1.0$ case is much more likely to produce counter-rotating motions in the inner shear layer than is the $V_s/V_p = 0.5$ case.

4.4.2.2 Particle Concentration Distributions

Figures 4.22-4.25 are contour plots showing particle dispersion in planes normal to the jet axis at a particle mass loading ratio of 5% at the same downstream locations and velocity ratios as Figures 4.18-4.21. The values of the contours in these figures are average particle number densities (ratio of the total number of particles found to occupy a given pixel location to the total number of particles in all the frames analyzed). These figures show self consistent trends in two respects. First, the $V_s/V_p = 1.0$ experiments kept the particles more confined near the jet axis when compared to the $V_s/V_p = 0.5$ case. In fact, based on these results, there is evidence (albeit limited) that some particles are actually reintroduced back into the jet axis as indicated by the elevated contour value of .006 in the central region of the plot shown in Figure 4.24. (This may be related to the aforementioned effect of the more wake-like inner shear layer for the $V_s/V_p = 1.0$ case.) Secondly, experiments at the lower velocity ratio resulted in an approximate 15 percent increase in particle spreading in the radial direction when compared to experiments with the velocity ratio set at 1.0.

It is significant to note that the particle results in Figures 4.22-4.25 exhibit trends that are opposite those for the passive scalar shown in Figures 4.18-4.21. The “brief explanation” for why this occurs is that part of the mechanism determining the particle trajectories is associated with the inertia of the particle itself. This is in contrast to the scalar which, except for molecular diffusion effects, follows the fluid motion exactly (at each instant). This phenomenon of more rapid radial particle transport than radial scalar or momentum transport has been previously noted and attributed to particle inertia effects (e.g., Lilly 1973, Hinze 1975). Thus, apparently the $V_s/V_p = 0.5$ case is more effective at producing an outward trajectory for particles (of the specified size) originating in the primary core, than is the $V_s/V_p = 1.0$ case. In this case, a primary consideration is the erosion of the secondary core, which leads to a single signed velocity gradient from the primary core to the ambient fluid. On the other hand, the wake-like shear layer that exists for the $V_s/V_p = 1.0$ case (which was more effective in transporting the scalar) does not provide an effective mechanism for producing a large radial component to the particle trajectories. As is discussed below, these rather dramatic differences are most likely linked with changes in scale of the dominant eddies within the flow. It is interesting to note, however, that the mean profile data provided above does gives some indication that this effect may be somewhat modulated by the particles themselves in that the flow with particles appeared to be slightly better at preserving the jet core momentum to locations farther downstream.

4.4.3 SPATIAL CORRELATIONS

An important attribute of the MTV technique employed is that it provides the instantaneous profile data that permits the spatial structure of the turbulence to be studied directly (i.e., without having to infer spatial structure from temporal autocorrelations). In this section we examine the normalized two point spatial autocorrelations of the axial velocity for "probe" separations in the radial directions, e.g.,

$$R_{uu}(\Delta r,0,0,0) = u(\overline{r,0,0,0)u(r+\Delta r,0,0,0)}/u'(r,0,0,0)u'(r+\Delta r,0,0,0) \quad (4.1)$$

where, an overbar denotes time averaging and a prime denotes the RMS. The data presented in this section is, to the author's knowledge, the first of its kind in particle laden flow.

4.4.3.1 Correlations without Particles

Spatial correlations for the pure fluid case at x/d = 7.5 for reference positions near the center of the internal shear layer (i.e., at r/R = 0.72, where R = d/2 and d is the diameter of the secondary jet pipe) and near the center of the outer shear layer (i.e., at r/R = 1.44) are shown in Figures 4.26-4.29. The results in Figures 4.26 and 4.27 are for $V_s/V_p = 0.5$, while the results in Figures 4.28 and 4.29 are for $V_s/V_p = 1.0$. (To re-familiarize the reader, recall that the normalized correlation peaks at a value of 1.0 at zero spatial separation.) The correlation in Figure 4.26 indicates a single sharp peak that drops below 0.2 for $\Delta r/R$ values greater than about 0.5. The shape of this correlation is nearly symmetric for values of $\Delta r/R < 0.5$ on either side of the reference point. In contrast, for the reference position r/R = 1.44 (Figure 4.27), the correlation is slightly asymmetric and exhibits a slower decrease for increasing $\Delta r/R$. The results in this figure for positive $\Delta r/R > 0.5$ indicate a slightly increasing correlation. This apparently anomalous result may, however, be attributed to the fact that the outer region of the jet is only intermittently turbulent. Given that these intermittent regions are characterized by large scale, single-signed vorticity mixing layer-like eddies (recall that the mean gradient profile is strongly single-signed for these conditions), this increased correlation simply reflects that the motions responsible for the correlation are also the primary source of the RMS as well. Overall, the results in Figures 4.26 and 4.27 are felt to reflect the existence of large scale motions that nearly span the entire half width of the flow.

In contrast, however, the results for $V_s/V_p = 1.0$ in Figures 4.28 and 4.29 indicate an intriguing double peaked structure. In both cases the separation between these peaks is about 1.5, or equivalently our estimate for the separation distance between the inner (wake-like) and outer shear layers. These results are therefore interpreted to indicate that even at x/d = 7.5 the internal structure of the turbulence is still dominated by the large scale flow features that have their origin at the jet exit, and that these internal structures are in quite strong communication. These results are felt to be especially striking since the mean and RMS profiles showed little indication of this underlying structure. Overall, the results for $V_s/V_p = 1.0$ exhibit a more rapid decrease from the peak than do the $V_s/V_p = 0.5$ results. This is taken to generally reflect more localized eddy structures.

4.4.3.2 Correlations with Particles

Figures 4.30-4.33 show the R_{uu} correlations in the particle laden flow (at a mass loading of 5%) for the same flow conditions as presented in Figures 2.26-4.29 respectively. The $V_s/V_p = 0.5$ results for reference position r/R = 0.72 are quite similar to the pure fluid case shown in Figure 4.26,

although some significant differences are noted. In particular, while the decrease in correlation for negative $\Delta r/R$ is nearly identical in both cases, for positive $\Delta r/R > 0.5$ a nearly constant correlation value of 0.25 is preserved in the particle laden flow. This is contrasted with the significantly smaller values near 0.1 in the pure fluid case. Similar results are observed for reference probe at $r/R = 1.44$. That is, while the drop-off from the peak in the particle laden for negative $\Delta r/R$ may be slightly more rapid, a low level correlation of about 0.25 persists all the way to the jet centerline. Furthermore, for positive $\Delta r/R$ a correlation plateau near 0.5 persists well into the intermittent region. Overall these results are felt to reflect that for the $V_s/V_p = 0.5$ case, in which the jet is generically characterized by large scale shear layer like eddies, the presence of particles slightly enhances the scale of the turbulence.

For the $V_s/V_p = 1.0$ case with particles the situation is substantially different from the pure fluid case. These differences are reflected in both Figures 4.32 and 4.33, which show the correlations for reference positions $r/R = 0.72$ and 1.44 respectively. In both of these cases, while the primary peak exhibits a slight broadening, the strong secondary peaks observed in the pure fluid case are completely nonexistent. Furthermore, the particle laden flow correlations decrease in magnitude all the way to zero, and if placed side-by-side, their non-zero extent would be barely overlapping. Thus, in this case the interpretation consists of two essentially non-communicating internal structures.

4.4.3.3 Implications Relating to Particle Dispersion Observations

In contrast to just the mean and RMS data, the correlation data go far in explaining the observed trends in the passive scalar and particle dispersion results. For example, recall that for the passive scalar the $V_s/V_p = 1.0$ case exhibited greater mixing, while in the particle laden flow the $V_s/V_p = 0.5$ case produced greater dispersion. Regarding the passive scalar, we now see that the enhanced transport is most likely resultant from the strong communication between the inner and outer structures (shear layers) that occurs in the pure fluid case. Conversely, owing to the effect of the particles on the turbulence itself, in the particle laden case the inner and outer structures for the $V_s/V_p = 1.0$ case are essentially non-interacting. Furthermore, the $V_s/V_p = 0.5$ data gave strong indications that by $x/d = 7.5$ the jet is dominated by large scale structures that nearly span the entire jet half width. These structures are the likely culprits for generating the larger radial trajectories responsible for the enhanced dispersion. Compounding this is the fact the above data also indicate that for the $V_s/V_p = 0.5$ case (as well as in the $V_s/V_p = 1.0$ case for each correlation structure individually) the presence of particles actually enhanced the average scale of the turbulence slightly. At the level of the instantaneous motions within the turbulence, the major distinction between the $V_s/V_p = 0.5$ and 1.0 is speculated to be the instantaneous presence of inner and outer eddy structures that do not strongly interact. Regarding the reduced particle dispersion, this is likely to be linked with opposing sign gradient motions in the wake-like region dividing the primary and secondary jets. Evidence for the existence of these features is given in the instantaneous velocity profile of Figure 4.34.

4.4.4 MOCK COAL SPREADER RESULTS

In addition to revealing information relating to the underlying turbulence mechanisms in the particle laden annular jet, an important component of the measurement program is the characterization of flow configurations and flow management devices that are employed in actual

coal-fired furnace applications. As stated in Section 4.1, such characterizations not only provide useful information relating to the effect of any given device, but also provide important contributions to code validation and development. To these ends, experiments were conducted using a device that generically mimics a coal spreader. This device, which is pictured in an end view in Figure 4.35, consists of a solid core that is centrally supported in the primary jet. At the exit of the jet, four vanes at a fixed angle of 15^o with the pipe axis, segregate and add swirl to the flow. Owing to the fact that a primary purpose of the experiments was to validate the ***GLACIER*** code results of Section 6.0, this device was intended to physically simulate the generic features of the numerically simulated flow configuration.

The experiments consisted of measuring particle concentration at x/d = 0.2 downstream of the primary jet exit for a condition of no secondary jet flow, a mass particle loading of 5%, and primary jet average velocity of 2.0 m/s. For the purposes of enhancing spatial resolution, the field of view of the measurement camera was reduced to cover only the upper left quadrant of the jet (see Figure 4.35). The results from this experiment are shown in Figure 4.36. As is readily apparent, within the quadrant itself, a significant variation of particle concentration develops. This variation yields the highest concentration near the outer edge of the pipe in the vicinity of the junction between the coal spreader blade and the pipe wall. Comparison of these results with the ***GLACIER*** code results in Figure 6.11 are qualitatively in agreement, and thus provide an increased level of confidence regarding the computational results. Generally, it is known that the effect of the coal spreader blades is to add a swirl component to the flow. Given the partitioned nature of the flow, this swirl is likely to take the form of concentrated streamwise vortices. A radial momentum balance outward from the core of these vortices indicates the presence of a concentrated low pressure region at the vortex centers. (The magnitude of the low pressure region depending on the streamline curvature produced by the vortex.) Therefore, it is speculated that the region of high particle concentration coincides with this region of low pressure. Of course, further MTV measurements for this configuration (as well as other coaxial jet modifications) can be used to clarify such issues.

4.5 REFERENCES

F. H. Champagne and I. J. Wygnanski, “An Experimental Investigation of Coaxial Turbulent Jets,” *International Journal of Heat and Mass Transfer,* **14**, 1445, (1971).

C. T. Crowe, J. N. Chung, and T. R. Troutt, “Particle Mixing in Free Shear Flows,” *Prog. Energy Combust. Sci*., **14**, 171, (1988).

J. Fan, H. Zhao, and K. Chen, “An Experimental Study of Two-Phase Turbulent Coaxial Jets,” *Experiments in Fluids*, **13**, 279, (1992).

C. P. Gendrich and M. M. Koochesfahani, “A Spatial Correlation Technique for Estimating Velocity Fields Using Molecular Tagging Velocimetry,” *Experiments in Fluids*, **22**, 67, (1996).

R. B. Hill, *Boundary Layer Vortex Generation*, Ph.D. dissertation, Department of Mechanical Engineering, University of Utah, (1996).

R. B. Hill and J. C. Klewicki, “Data Reduction Methods for Flow Tagging Velocity Measurements,” *Experiments in Fluids*, **20**, 142, (1996).

J. O. Hinze, *Turbulence*, McGraw-Hill, 1959.

N. Kamalu, L. Tang, T. R. Troutt, J. N. Chung and C. T. Crowe, "Particle Dispersion in Developing Shear Layers," in *Mechanics of Two-Phase Flow* (edited by S. L. Lee and R. Durst), Institute of Applied Mechanics, National Taiwan University, Taipei, Taiwan, ROC, 199, (1989).

N. W. M. Ko and K. M. Lam, "Flow Structures of Coaxial Jet of Mean Velocity Ratio 0.5," *AIAA Journal*, **27**, 513, (1989).

A. N. Kolmogoroff, "The Local Structure of Turbulence in Imcompressible Viscous Flow for Very Large Reynolds Numbers," *Dokl. Akad. Nauk. SSSR* **30**, 299, (1941).

K.-Y. Lee, *Shear Wake Interactions with a Circular Cylinder*, Ph.D. dissertation, Department of Mechanical Engineering, University of Utah, (1994).

G. P. Lilly, "Effect of Particle Size on Particle Eddy Diffusivity," *Industrial and Engineering Chemistry Fundamentals*, **12**, 268 (1973)

E. K. Longmire and J. K. Eaton, *Structure and Control of a Particle-Laden Jet*, Report No. MD-58, Thermosciences Division, Department of Mechanical Engineering, Stanford University, (1990).

R. D. Maynes, *On Rotating Bluff Body Flows*, Ph.D. dissertation, Department of Mechanical Engineering, University of Utah, (1997).

A. Ponce, P. A. Wong, J. J. Way, and D. G. Nocera, "Intense Phosphorescence Triggered by Alcohols upon Formation of a Cyclodextrin Ternary Complex," *J. Phys. Chem*. **97**, 1137, (1993).

M. M. Ribero, and J. H. Whitelaw, "Coaxial Jets With and Without Swirl," *J. Fluid Mechanics*, **96**, 769, (1980).

R. B. Wicker, and J. K. Eaton, *Structure and Control of a Particle-Laden Coaxial Jet With and Without Annular Swirl*, Report No. MD-68, Stanford University, (1994).

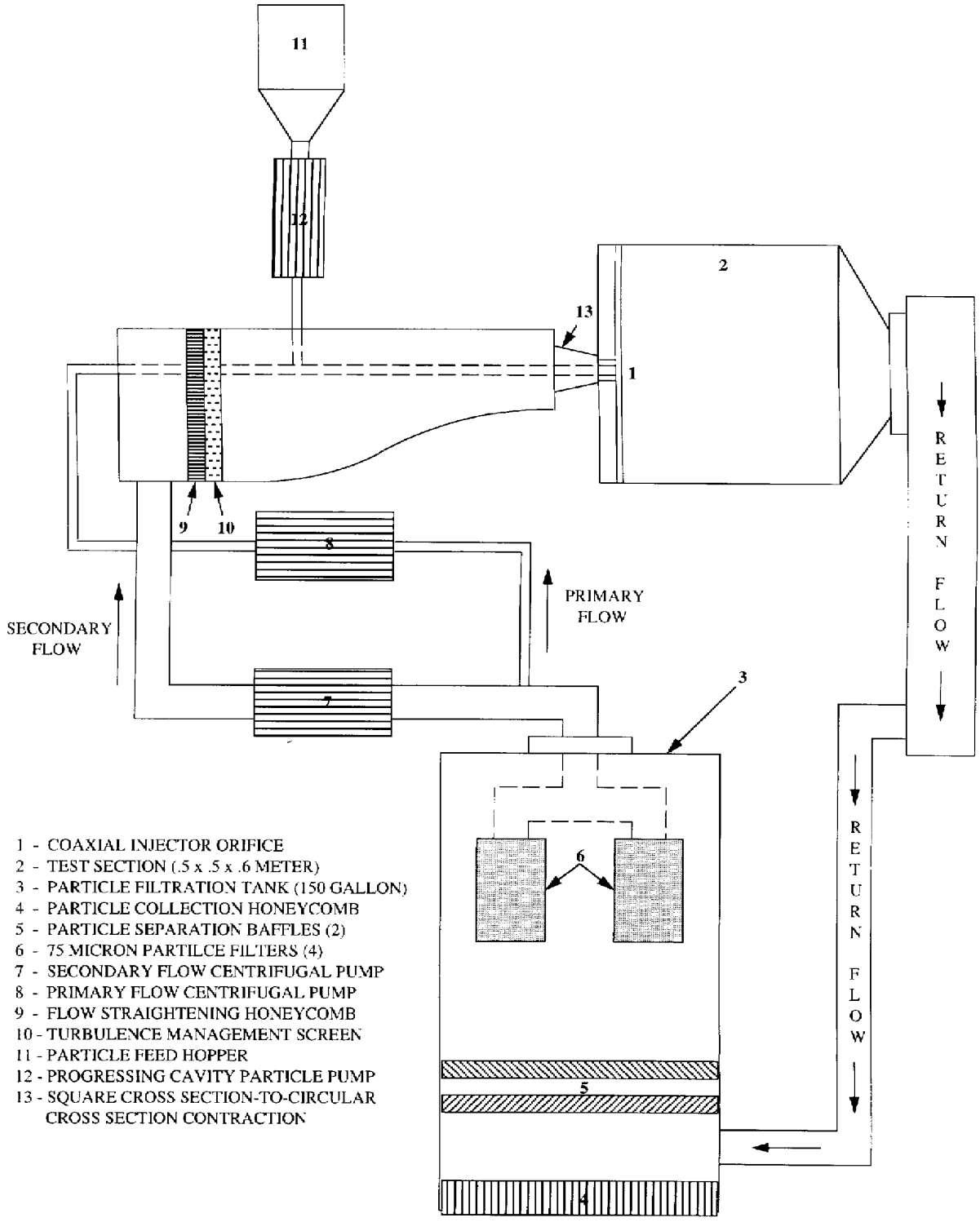

Figure 4.1 Schematic of the annular jet flow facility.

Figure 4.2 Photograph of the annular jet facility.

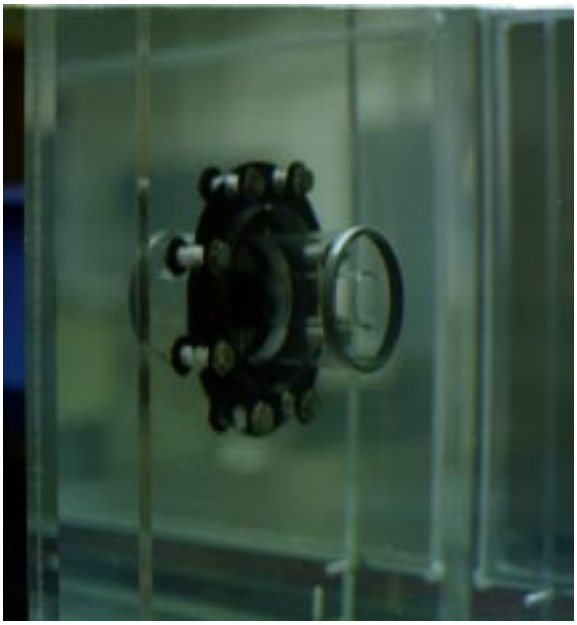

Figure 4.3 Close-up photograph of the annular jet.

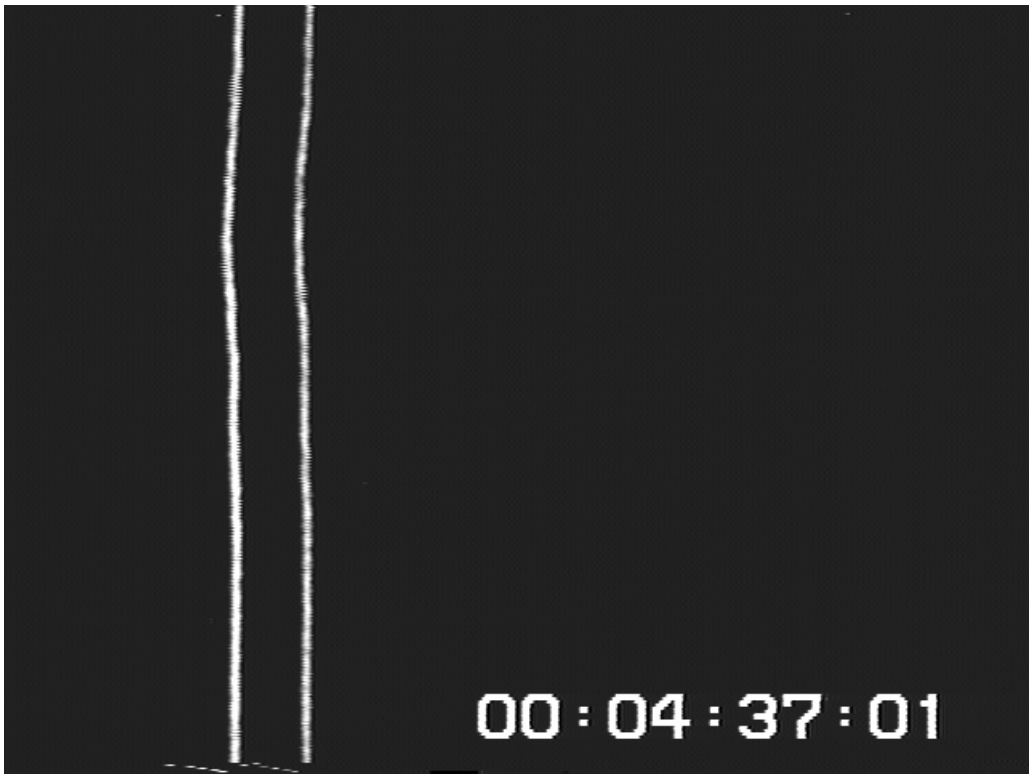

Figure 4.4 Video image of displaced MTV lines (x/d = 2.5, V_s/V_p = 0.5, no particles).

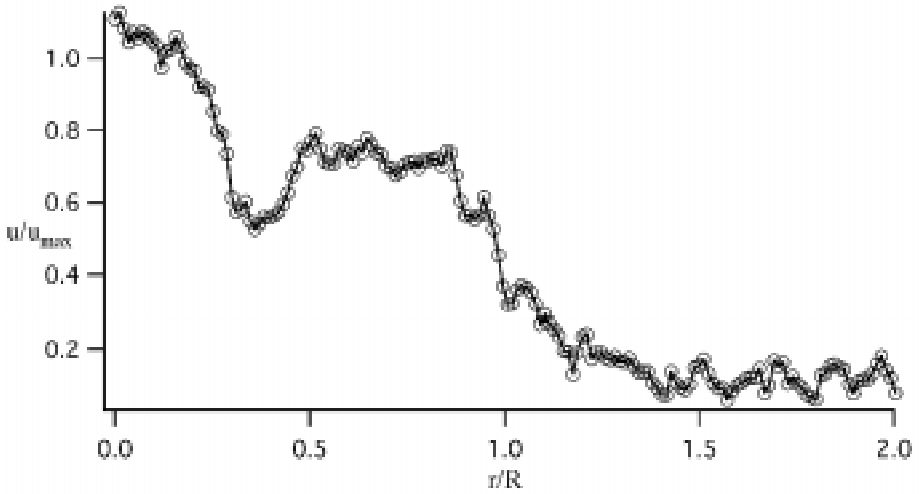

Figure 4.5 Typical instantaneous velocity profile (x/d = 2.5, V_s/V_p = 0.5, 5% particle mass loading).

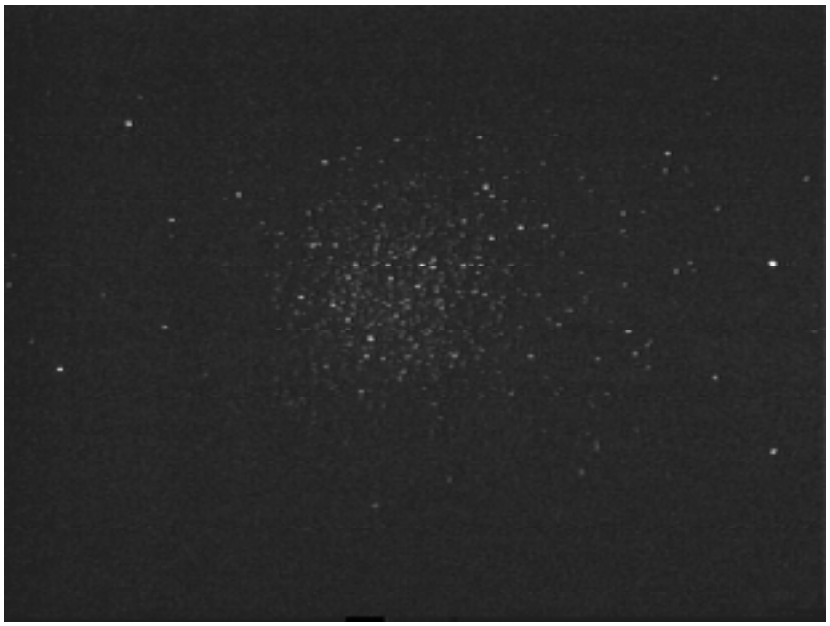

Figure 4.6 Typical instantaneous particle image (x/d = 7.5, V_s/V_p = 1.0, 5% particle mass loading).

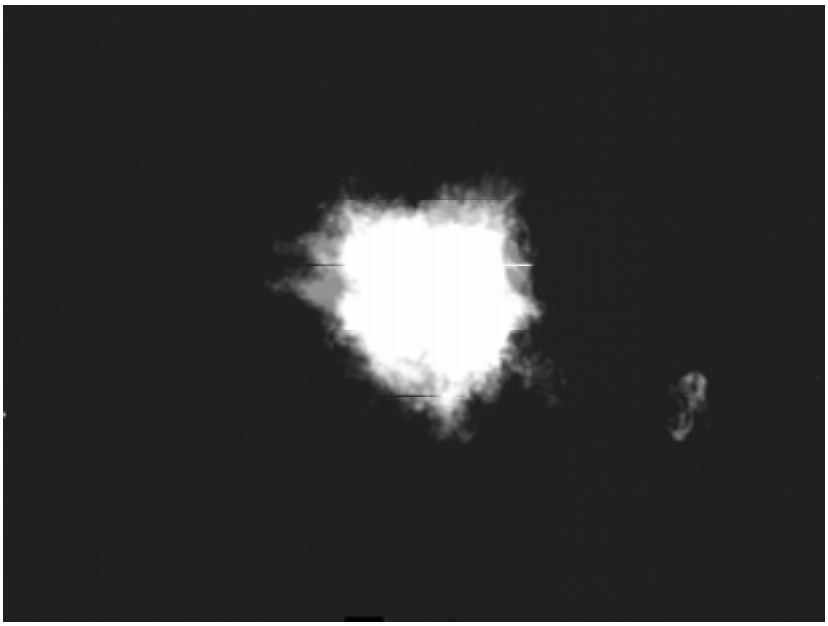

Figure 4.7 Typical instantaneous LIF image (x/d = 7.5, V_s/V_p = 1.0).

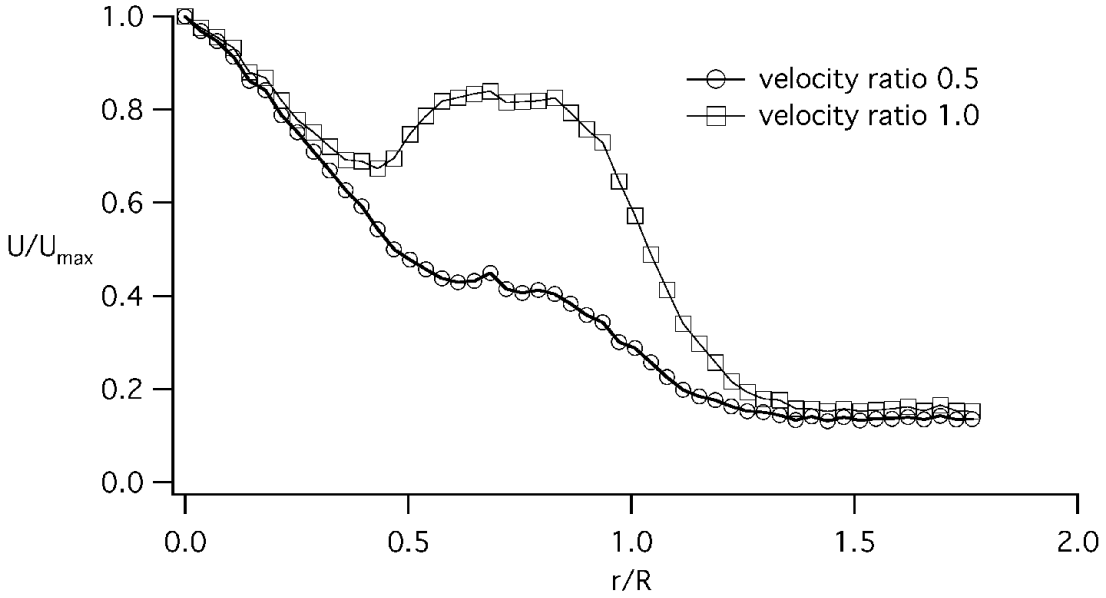

Figure 4.8. Mean axial velocity profiles at x/d = 2.5, pure fluid case.

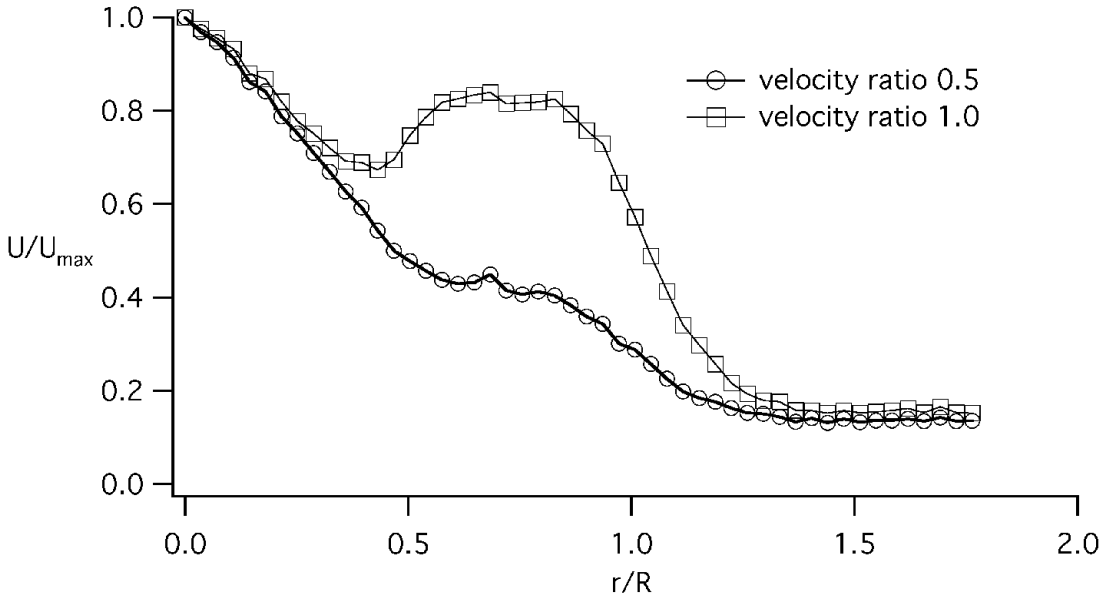

Figure 4.9 Mean axial velocity profiles at x/d = 5.0, pure fluid case.

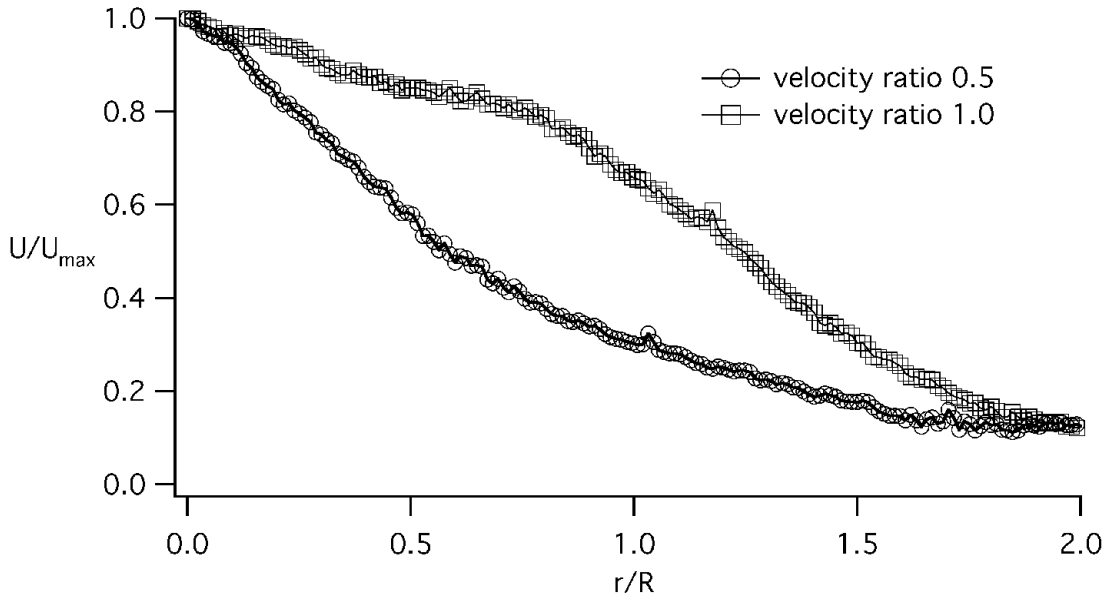

Figure 4.10 Mean axial velocity profiles at x/d = 7.5, pure fluid case.

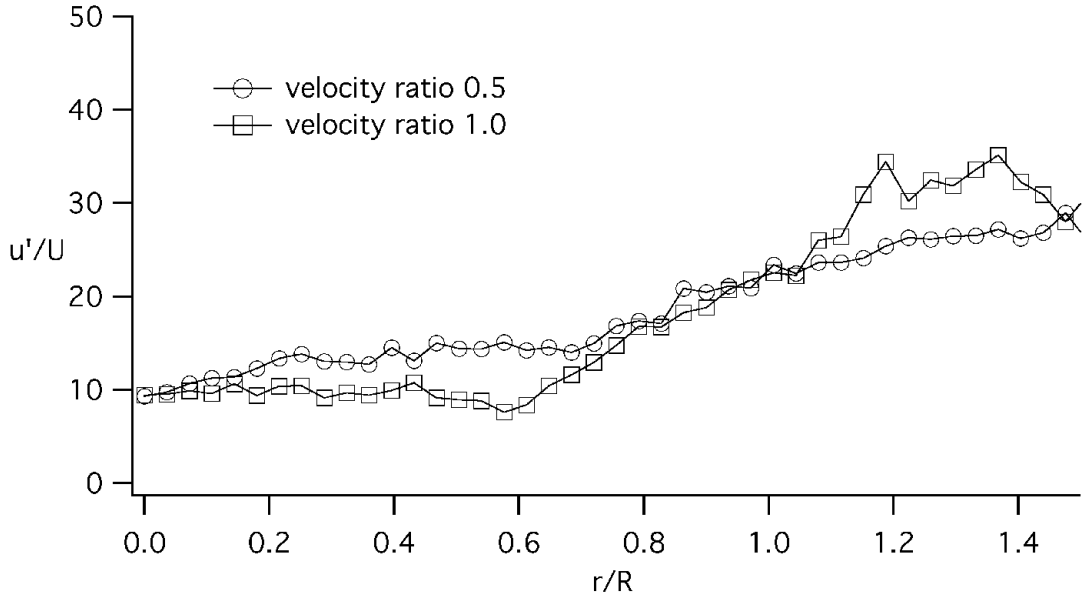

Figure 4.11 RMS axial velocity profiles at x/d = 2.5, pure fluid case.

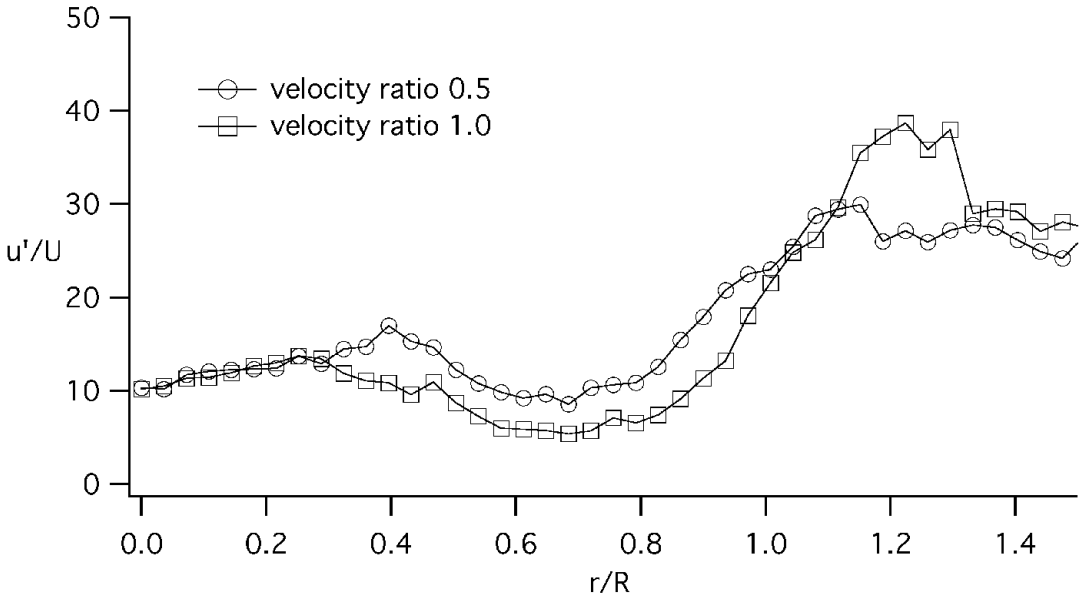

Figure 4.12 RMS axial velocity profiles at x/d = 5.0, pure fluid case.

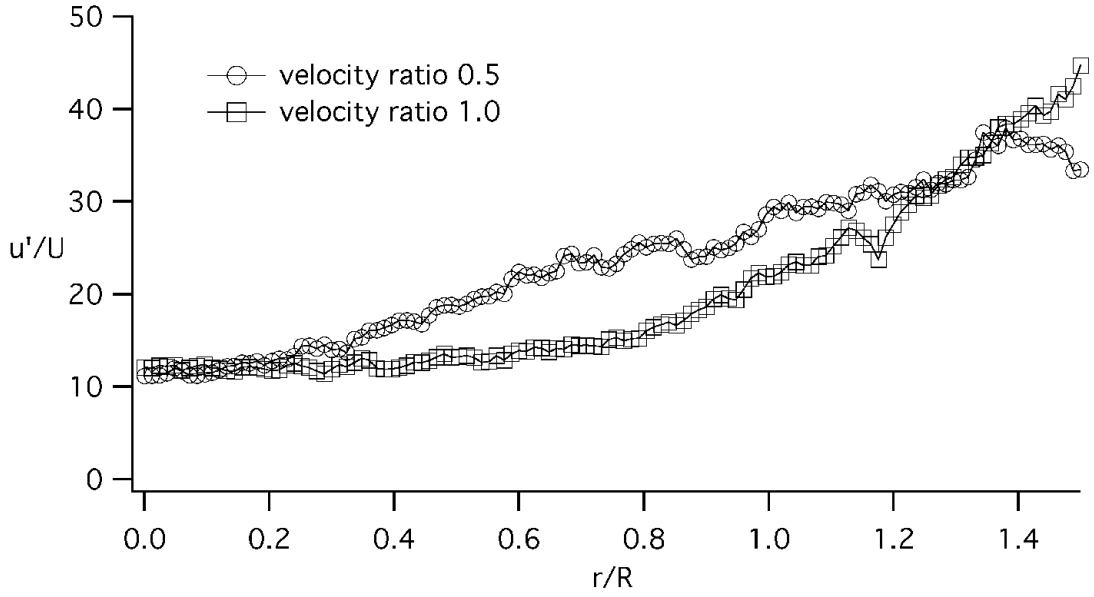

Figure 4.13 RMS axial velocity profiles at x/d = 7.5, pure fluid case.

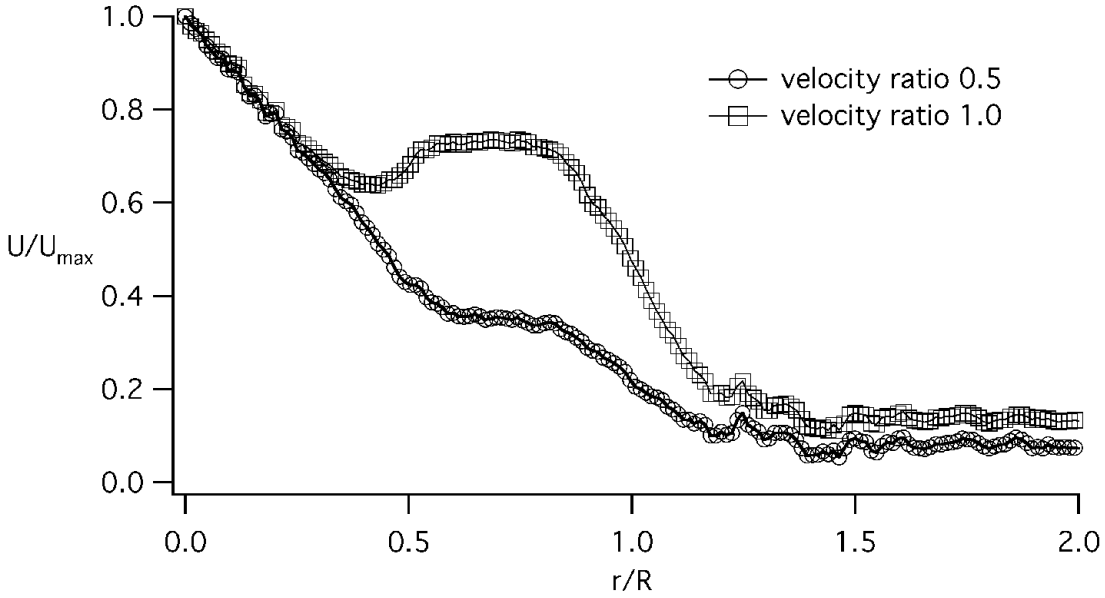

Figure 4.14 Mean axial velocity profiles at x/d = 2.5, 5% mass particle loading.

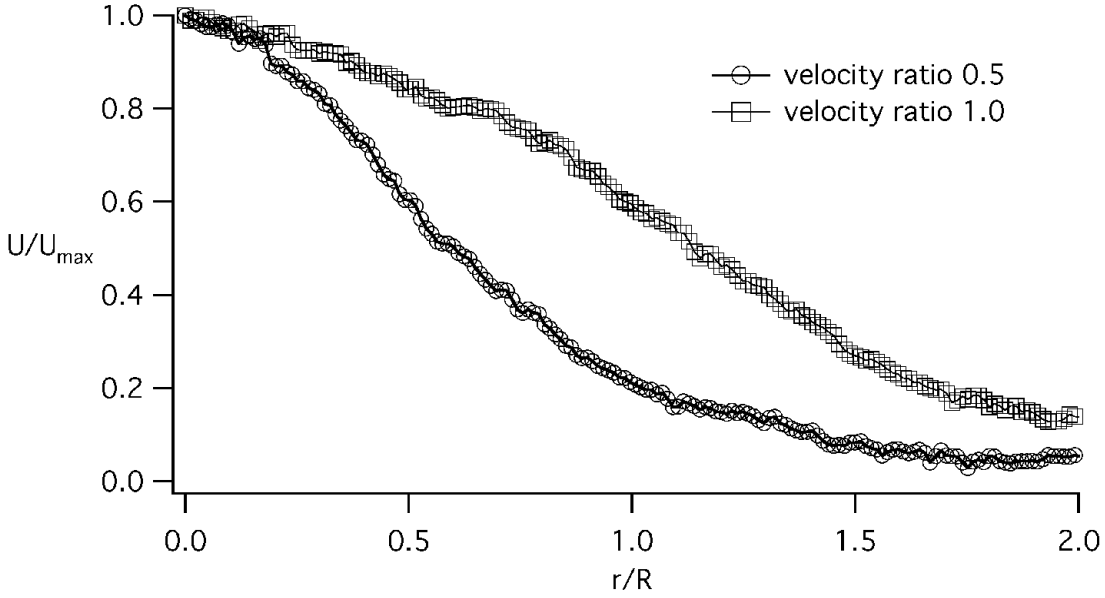

Figure 4.15 Mean axial velocity profiles at x/d = 7.5, 5% mass particle loading.

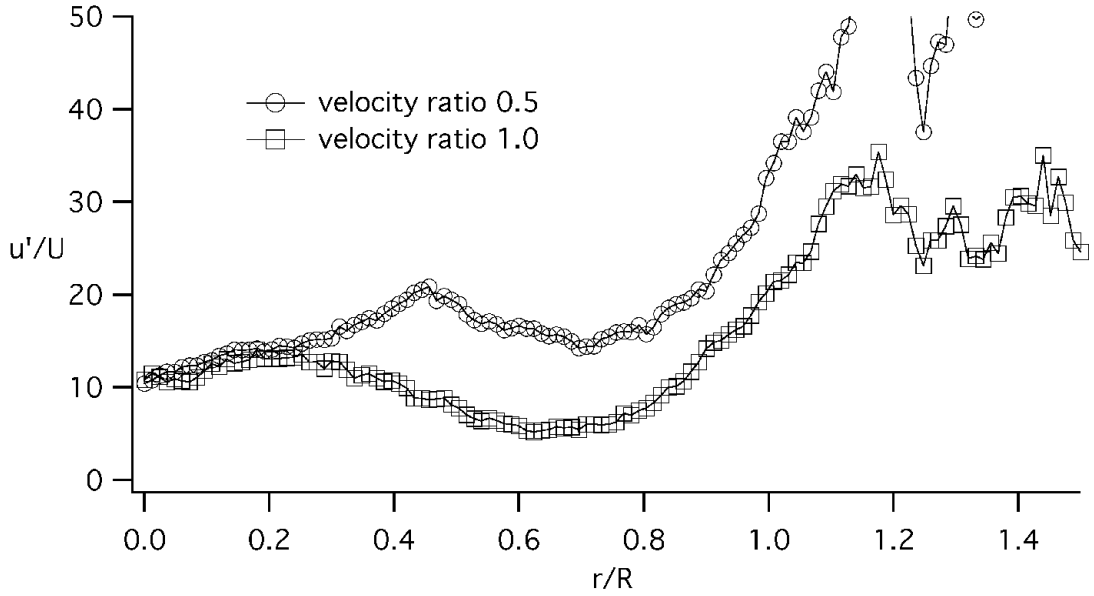

Figure 4.16 RMS axial velocity profiles at x/d = 2.5, 5% mass particle loading.

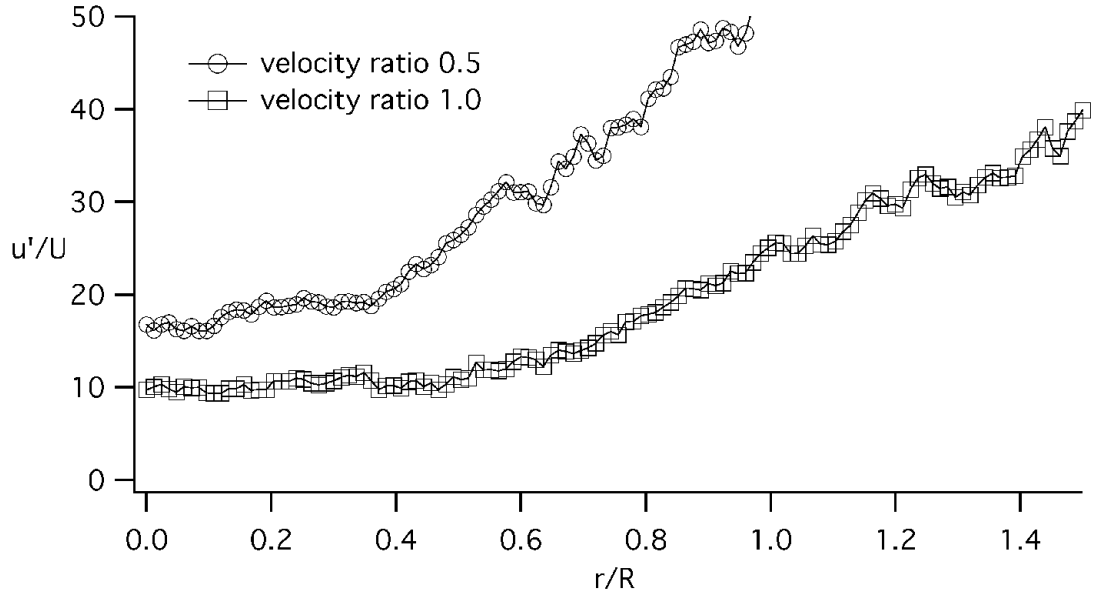

Figure 4.17 RMS axial velocity profiles at x/d = 7.5, 5% mass particle loading.

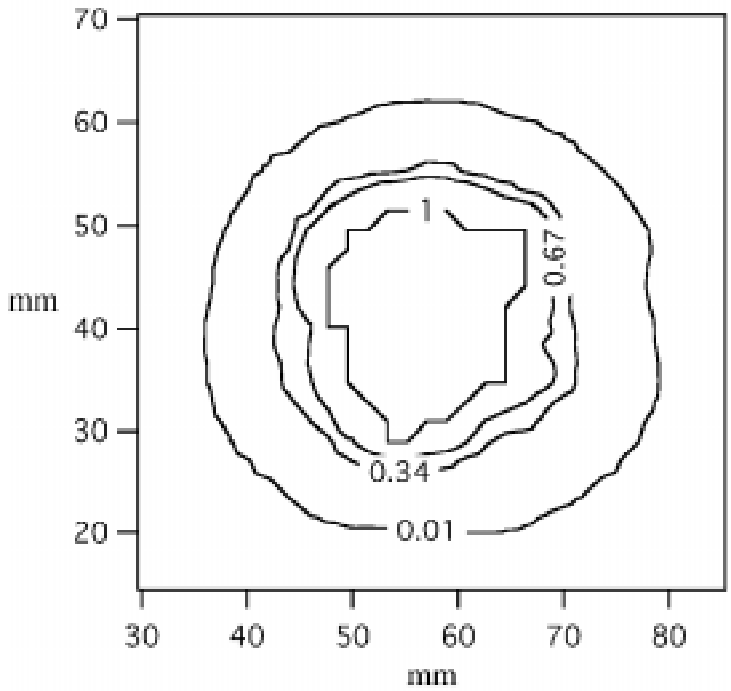

Figure 4.18 Fluorescein concentration contours at x/d = 5.0, Vs/Vp = 1.0.

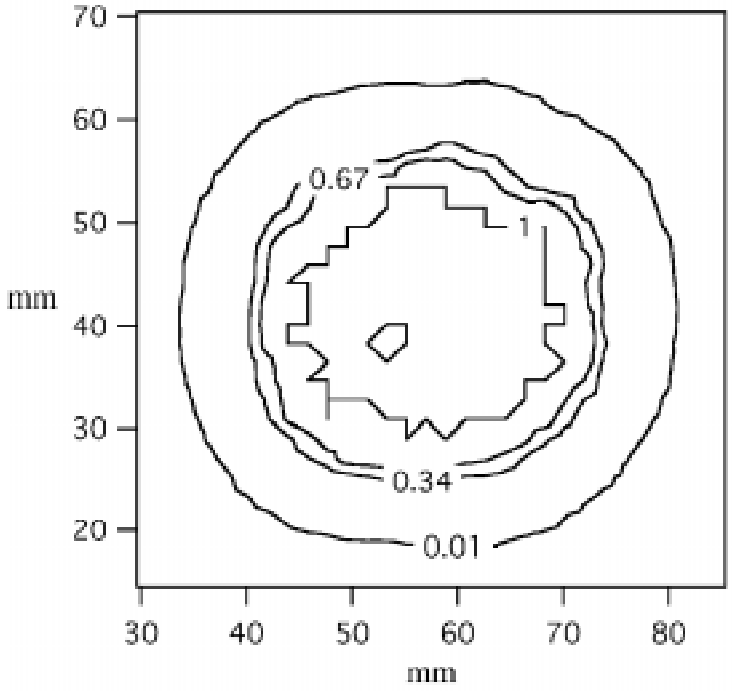

Figure 4.19 Fluorescein concentration contours at x/d = 5.0, Vs/Vp = 0.5.

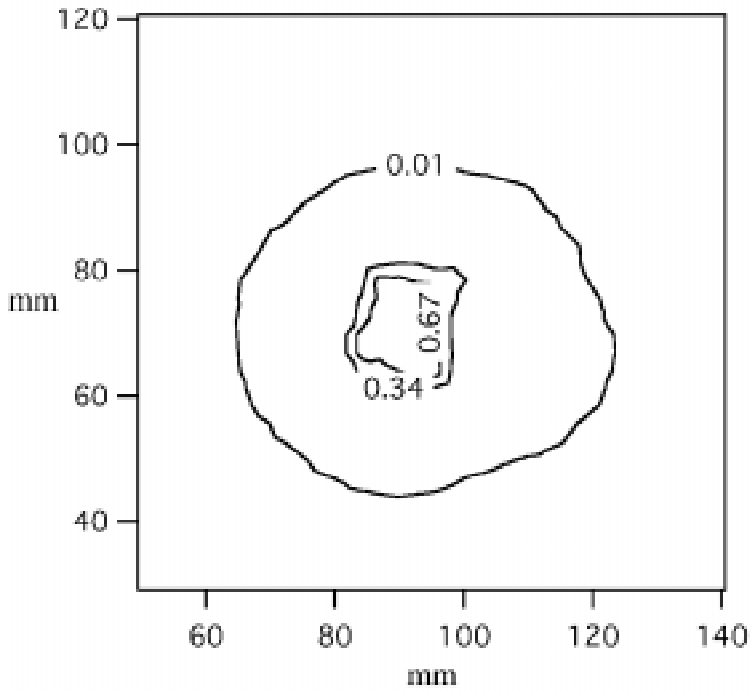

Figure 4.20 Fluorescein concentration contours at x/d = 10.0, Vs/Vp = 1.0.

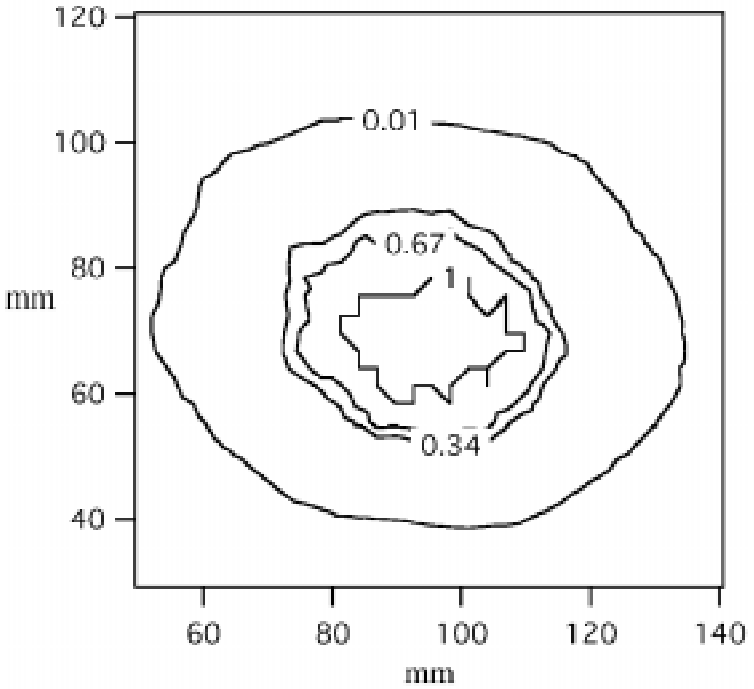

Figure 4.21 Fluorescein concentration contours at x/d = 10.0, Vs/Vp = 0.5.

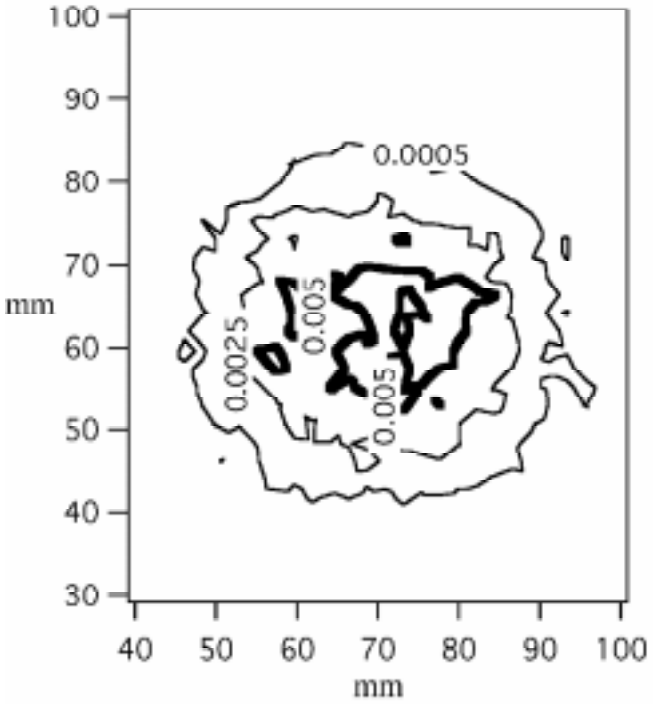

Figure 4.22 Particle concentration contours at x/d = 5.0, Vs/Vp = 1.0.

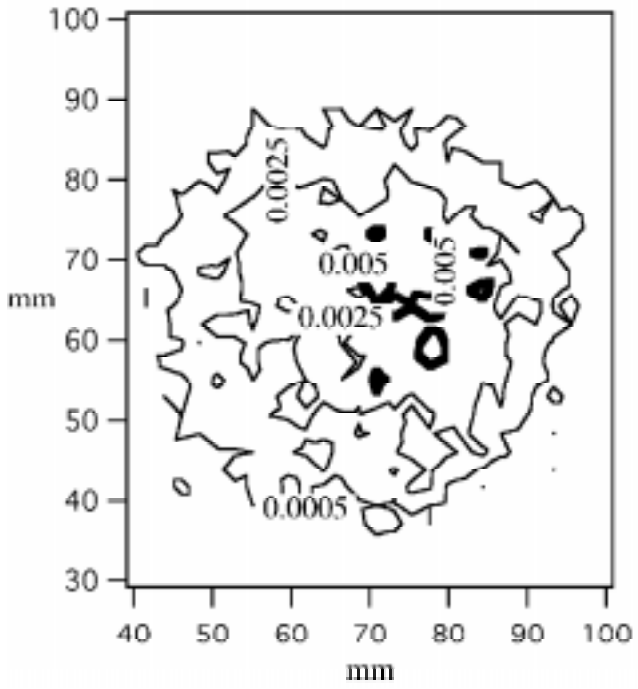

Figure 4.23 Particle concentration contours at x/d = 5.0, Vs/Vp = 0.5.

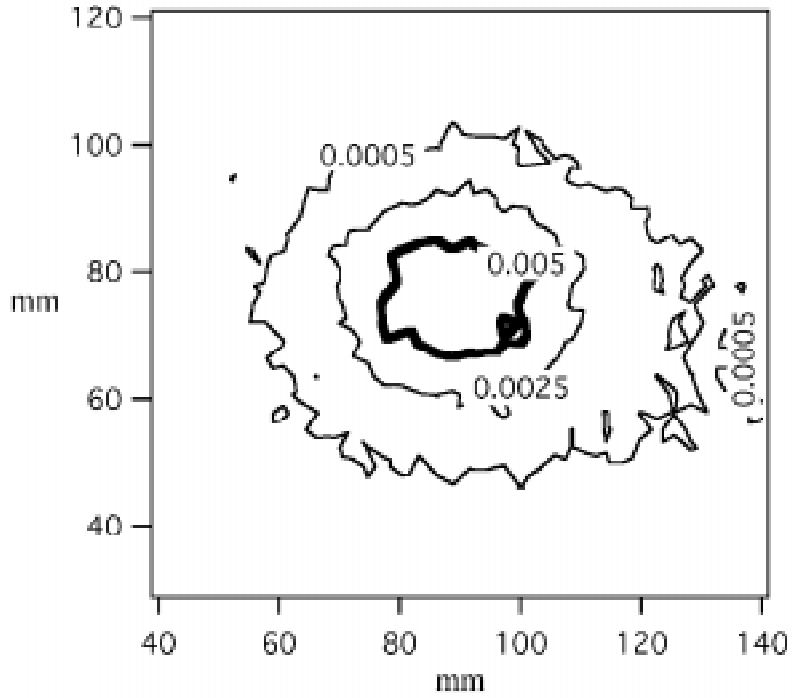

Figure 4.24 Particle concentration contours at x/d = 10.0, Vs/Vp = 1.0.

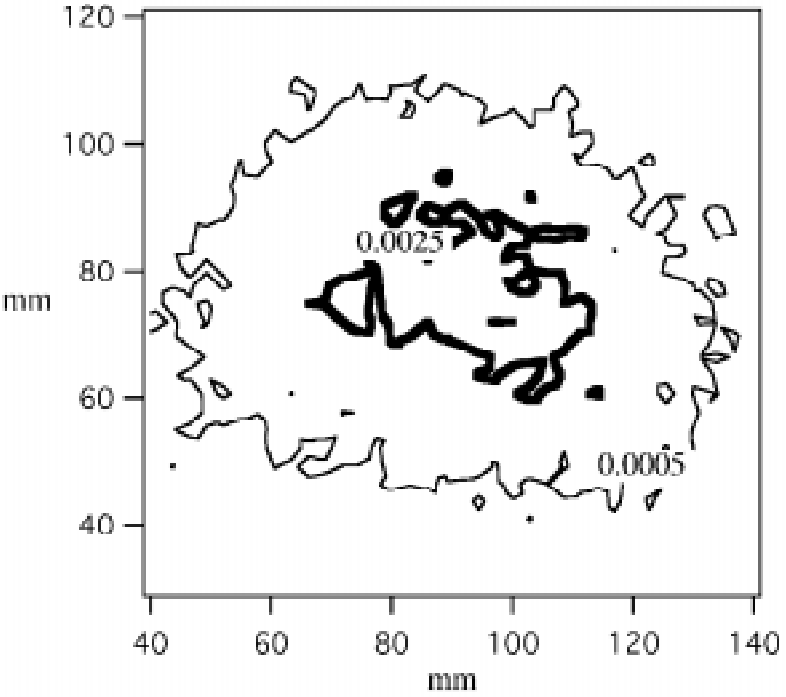

Figure 4.25 Particle concentration contours at x/d = 10.0, Vs/Vp = 0.5.

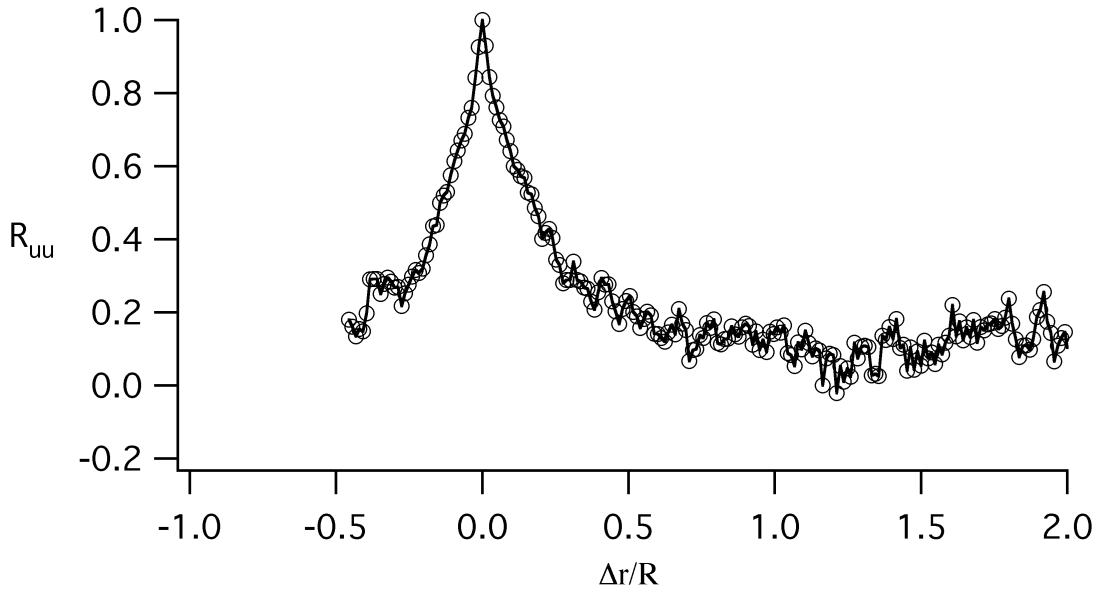

Figure 4.26 Two point spatial correlation of the axial velocity fluctuations at x/d = 7.5, Vs/Vp = 0.5, and reference point at r/R = 0.72, pure fluid case.

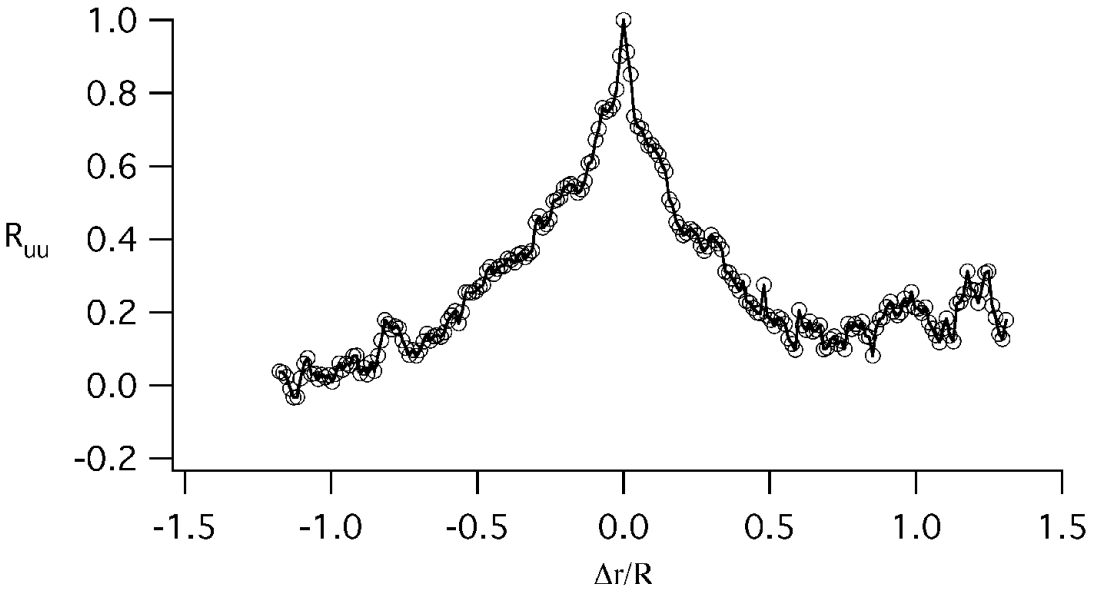

Figure 4.27 Two point spatial correlation of the axial velocity fluctuations at x/d = 7.5, Vs/Vp = 0.5, and reference point at r/R = 1.44, pure fluid case.

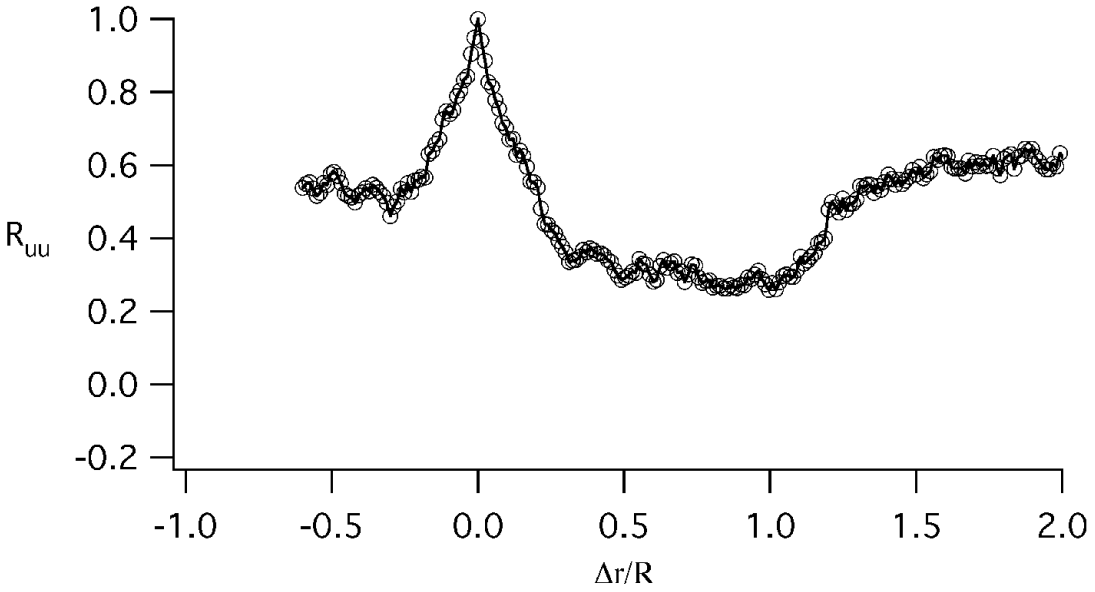

Figure 4.28. Two point spatial correlation of the axial velocity fluctuations at x/d = 7.5, Vs/Vp = 1.0, and reference point at r/R = 0.72, pure fluid case.

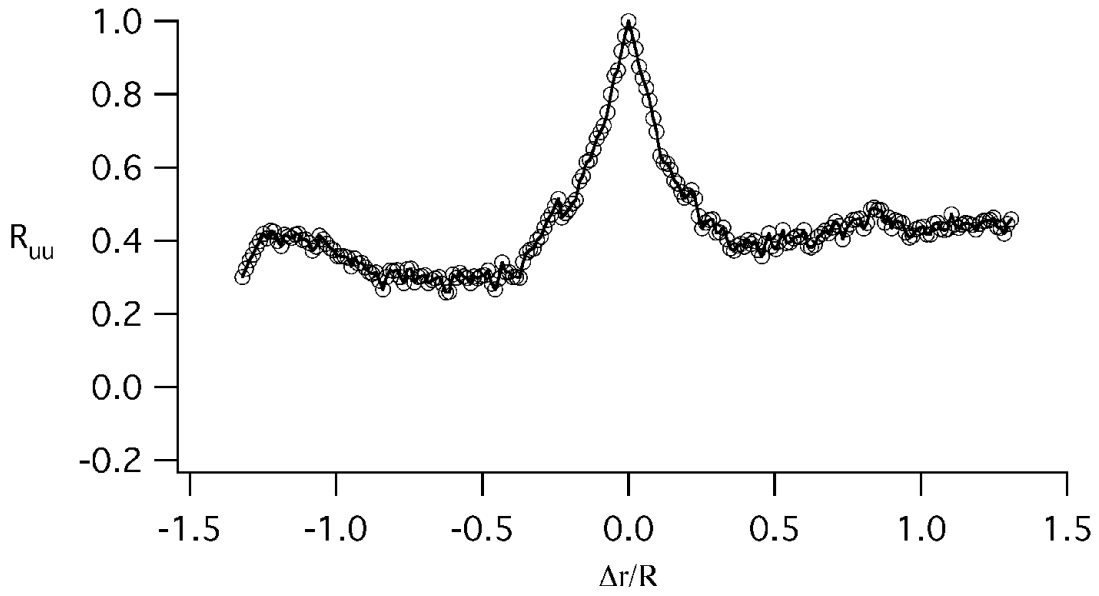

Figure 4.29. Two point spatial correlation of the axial velocity fluctuations at x/d = 7.5, Vs/Vp = 1.0, and reference point at r/R = 1.44, pure fluid case.

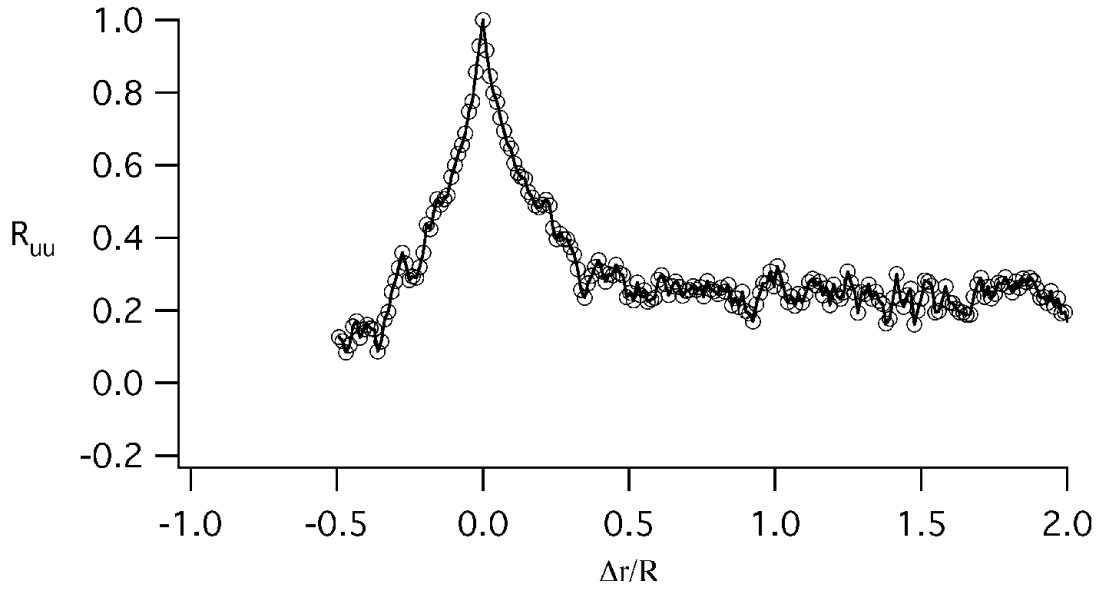

Figure 4.30. Two point spatial correlation of the axial velocity fluctuations at x/d = 7.5, Vs/Vp = 0.5, and reference point at r/R = 0.72, 5% mass particle loading.

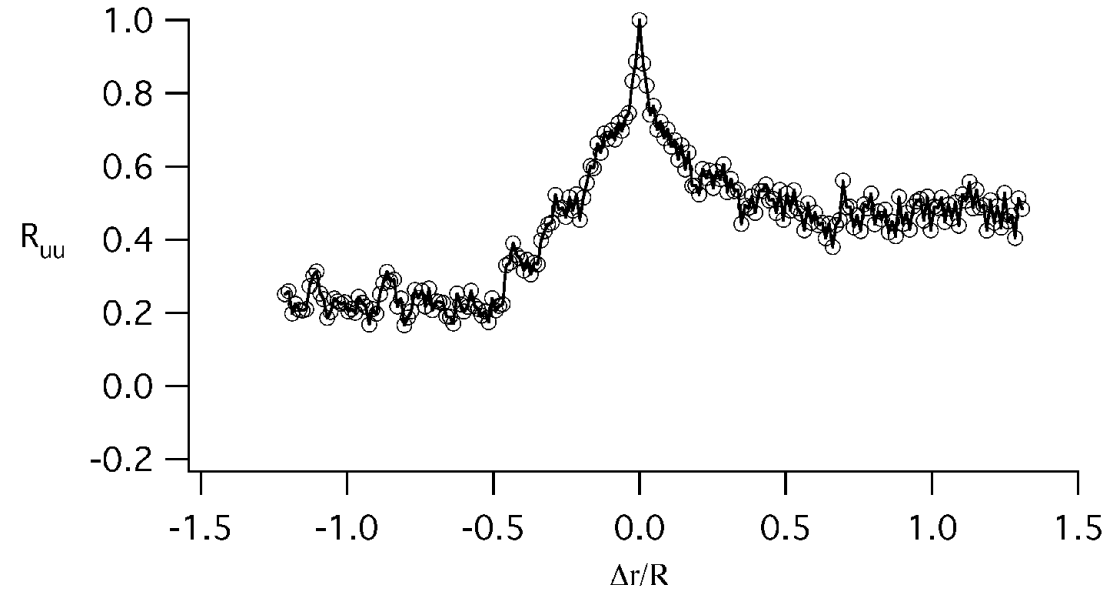

Figure 4.31. Two point spatial correlation of the axial velocity fluctuations at x/d = 7.5, Vs/Vp = 0.5, and reference point at r/R = 1.44, 5% mass particle loading.

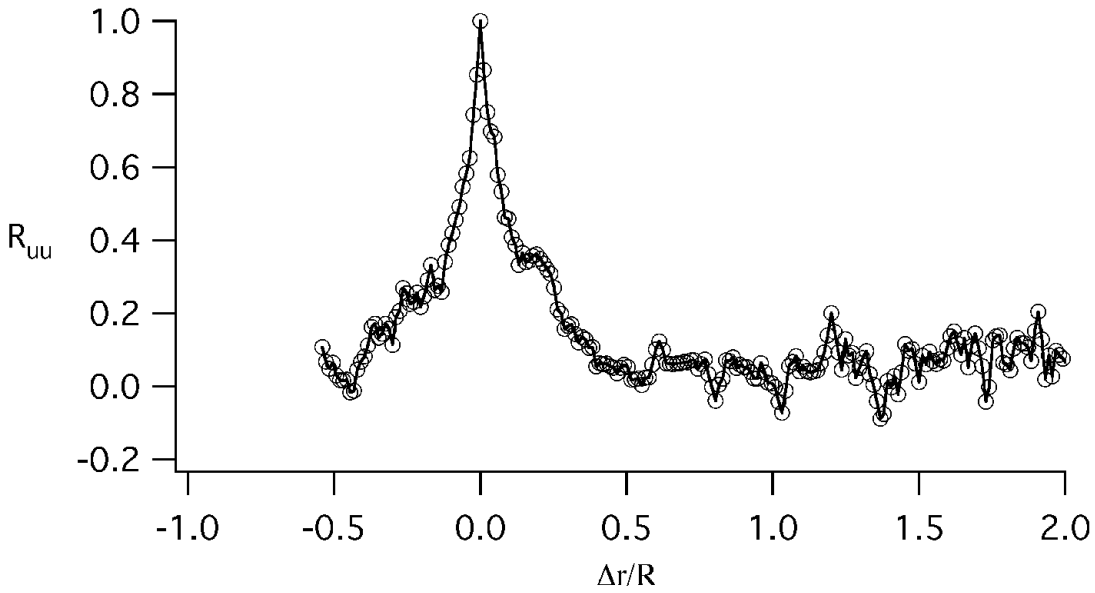

Figure 4.32. Two point spatial correlation of the axial velocity fluctuations at x/d = 7.5, Vs/Vp = 1.0, and reference point at r/R = 0.72, 5% mass particle loading.

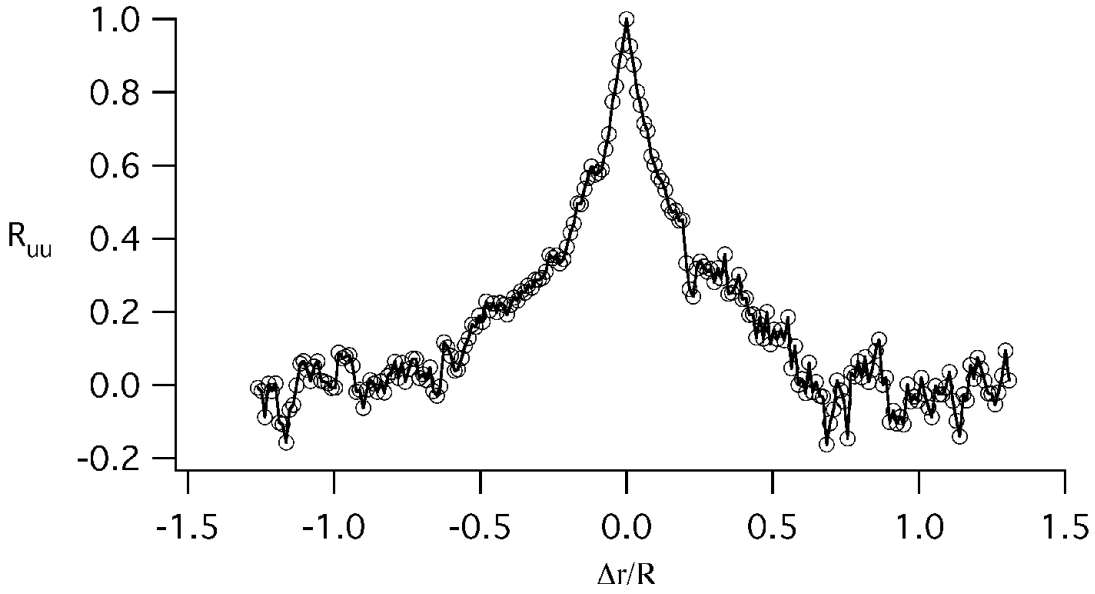

Figure 4.33. Two point spatial correlation of the axial velocity fluctuations at x/d = 7.5, Vs/Vp = 1.0, and reference point at r/R = 1.44, 5% mass particle loading.

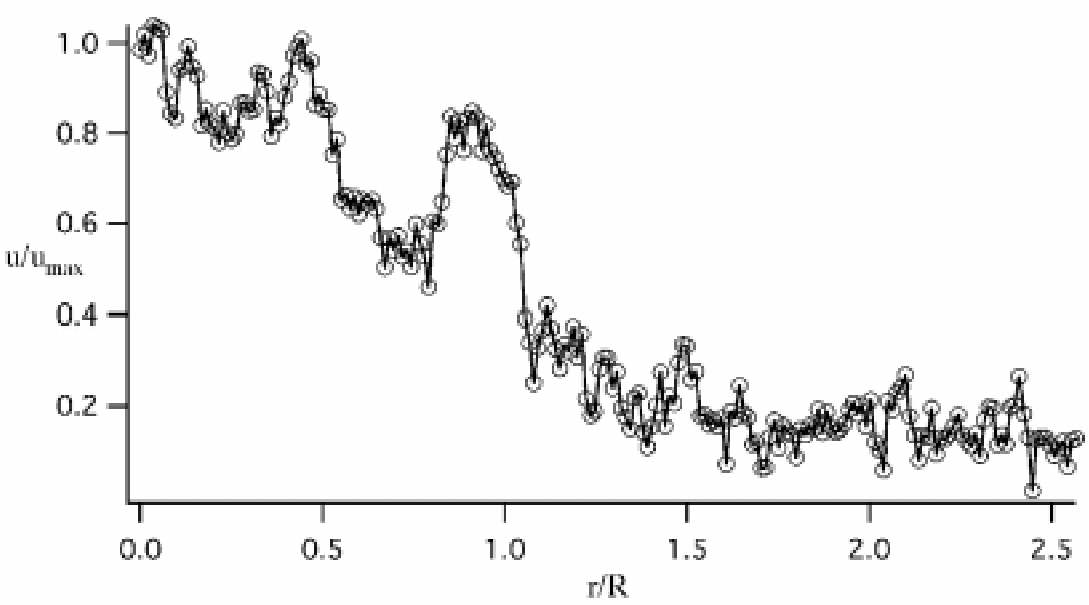

Figure 4.34. Instantaneous axial velocity profile at x/d = 7.5, Vs/Vp = 1.0, 5% mass particle loading.

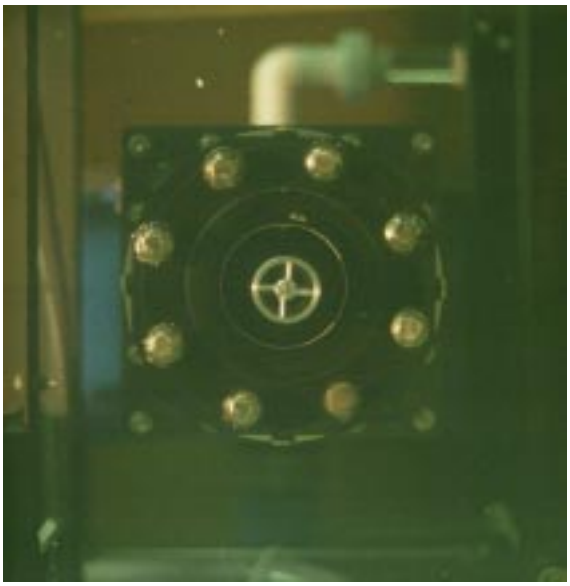

Figure 4.35. End view image of the four bladed mock coal spreader device installed in the primary jet pipe.

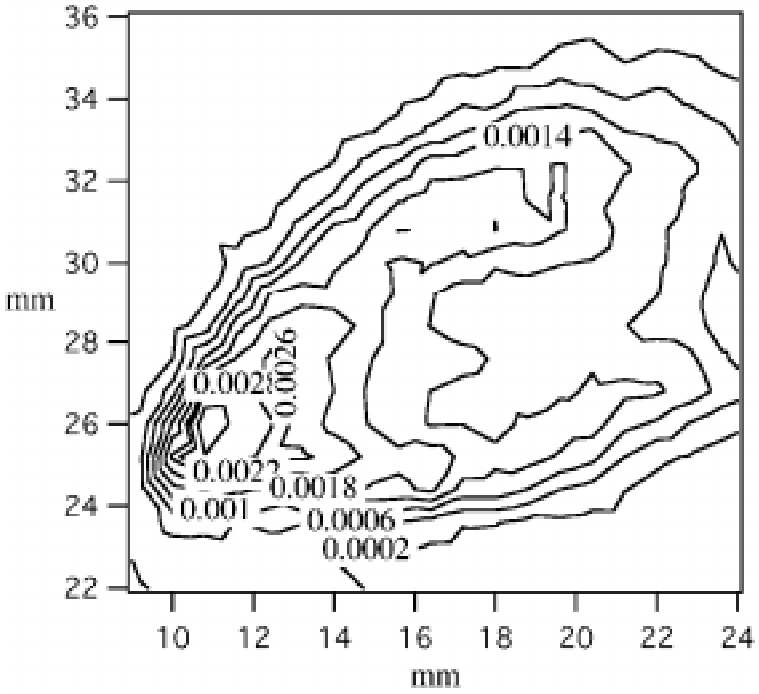

Figure 4.36. Particle concentration contours associated with the upper left flow quadrant of the coal spreader device depicted in Figure 4.35, 5% particle mass loading.

5.0 RESULTS AND DISCUSSION - COMBUSTION

5.1 TEST EQUIPMENT

5.1.1 BENCH-SCALE FURNACE

The bench-scale combustion facility referred to as the "U-furnace" used during this program is a 29 kW (100,000 Btu/hr) down-fired test facility located at the University of Utah combustion laboratory (see Figure 5.1). The combustion chamber is 7.3 m in length with an inner diameter of 16 cm. The combustor walls consist of three different refractory materials to provide adequate insulation. There are six modular sections with numerous access ports. A residence time of 2.5 seconds can be achieved in the combustion chamber. A multi-fuel 29 kW (100,000 Btu/hr) burner fires vertically downward in the furnace to an ash removal zone. Thereafter, the gases pass through a heat removal zone, an isothermal zone and then exit the furnace. The combustion and heat removal zones are designed to provide a variety of operational configurations. Fuels and other reactants can be injected together through the burner or separately at numerous locations in the facility. In addition, multiple sample ports exist throughout the facility for complete combustion and heat removal evaluation.

The furnace is divided into three sections, a primary zone, a convective zone, and an SNCR zone (for traditional selective noncatalytic reduction programs at lower temperatures under fuel-lean conditions). Each section has sufficient observation/sample ports to complete mass and energy balances and/or to permit injection of fuels or additives in several different combustion temperature regions. The exhaust gases leave the furnace and pass through a quench column and then exit the combustion laboratory through a stack. Common gas analyses include O_2, CO, CO_2, NO_x, SO_2 and hydrocarbons.

The facility has complete monitoring of all input and output streams. In addition, specialized instruments such as a mass spectrometer or FTIR can be attached to the exhaust gases for more detailed analyses. The control room logs all process variables on a personal computer for data storage and reduction.

5.1.2 PILOT-SCALE FURNACE

The University of Utah pilot-scale combustion test furnace referred to as the "L1500" is a nominal 15 MMBtu/hr pilot-scale furnace designed to simulate commercial combustion conditions. A major objective of this combustion facility is to study pollutant formation and control, carbon utilization, and ash management in a system which operates similar to commercial boilers. Therefore, the L1500 pilot-scale furnace has the following characteristics:

- Simulates the range of time/temperature histories that are found in commercial units.
- Includes both the ability to fire single or multiple gas burners and/or coal burners.
- Has the provision for evaluating different slag screen designs for improved ash management.

- Has the capability to test different reburning and burnout air injection locations and velocities for emissions control.
- Provides simulated waterwall area (if desired) for deposition studies.
- Has a nominal firing rate of 15 MMBtu/hr with gas and 7 MMBtu/hr with coal.
- Permits multiple locations for coal injection such that coal and/or gas can be used as reburning fuels independent of main firing burner.
- Has adequate sample/observation ports for measuring all inputs and outputs as well as ports to allow detailed species and temperature profiles to be obtained.
- Has a completely instrumented control room adjacent to the facility to control the operation of the furnace and to record and analyze data.

Figure 5.2 is a schematic diagram of the L1500 combustor. The horizontal-fired combustor is 1.1 m x 1.1 m square and nearly 12.5 meters long. The walls have multiple-layered insulation to reduce the temperature from about 1925 K on the fire-side to below 330 K on the shell-side. The combustor is modular in design with numerous access ports and optional cooling panels in each section. This allows the flue gas temperature profile to be adjusted to better simulate commercial equipment. The access ports are used for visual observations, fuel and/or air injection, and product sampling.

The overall combustion facility includes the air supply system, water supply and cooling system, L1500 combustor, fuel supply systems (either gas or coal or both), a flue-gas cooling chamber, scrubber, and induced-draft fan and a stack. The facility meets all environmental regulations.

5.1.3 BENCH-SCALE BURNERS

Two burner types were used in this study, a fuel jet with gas stabilization and a segregated premixed pulverized coal burner (SPPC). The SPPC burner, is shown schematically in Figure 5.3. This unique burner design allowed for premixing two separate and controllable coal/air streams prior to the combustor. The inner injector had the coal stream injected vertically upward, directly into the incoming air stream. Surrounding this air/coal stream, a second premixed coal/air stream was created by injecting the coal in the opposite tangential direction to the incoming air. A flame arrester is attached at the bottom of the burner to prevent any flame flashbacks into the burner.

The purpose for this burner was to investigate the effects of varying the amount of fuel provided in the inner versus outer premixed chambers. This would simulate an inherently stratified commercial burner.

5.1.4 PILOT-SCALE BURNERS

The pulverized coal burner used on the L1500 combustion facility is similar in design concept to pilot-scale burners developed at the International Flame Research Foundation in Ijmuiden, Holland. The REI dual concentric swirl burner is designed to provide excellent flame stability and

offer a wide range of swirl stabilized flames. Central to the burner are two sets of moveable blocks, one set in each of the inner and outer secondary air streams, which generate the angular momentum in the secondary air streams. In this burner, the secondary swirl number can be varied, on-line, from 0 (a long slender flame) to a maximum of 2 (a shorter bushy flame) in each of the secondary air streams. This allows the flame shape to be varied to better simulate different heat release patterns.

Figure 5.4 is a general schematic of the REI dual concentric swirl burner showing the inner and outer secondary air chambers. The burner has separate primary and secondary air lines. Because the flowrate of each of these lines is measured, excellent combustion conditions can be maintained. The metered secondary air enters either the inner or outer secondary air plenum and is forced through the respective moveable blocks. The inner and/or outer secondary air swirl is adjusted by rotating a set of 10 moveable blocks which rest on top of a set of stationary blocks. The angled channels between the blocks provide the degree of swirl desired. When the moveable blocks are next to the fixed blocks (as shown in the Figure), all secondary air is directed toward the center of the burner and no swirl is imparted. This condition corresponds to zero swirl or a long diffusion flame. When the moveable blocks are rotated next to the fixed blocks on the right, all secondary air is given maximum swirl and is directed toward the tangent to the secondary air duct. This produces the highest swirl number, resulting in a short bushy flame. With the moveable blocks in between the fixed blocks, part of the air is swirled and a portion is not; this gives rise to the intermediate swirl levels.

The dual secondary air channels allow for investigations of low-NO_x firing similar to commercial wall-fired burners. Each secondary air stream is metered and can be accurately controlled to investigate the effects of dual secondary air streams and swirl on combustion emissions and carbon burnout. Inserts can be placed in the secondary air stream to effectively vary secondary air velocity while maintaining constant secondary air splits and overall firing rate. In addition to the secondary air inserts, the primary air/coal nozzle is easily changed to different configurations to investigate coal injection conditions on final emissions and carbon conversion.

The coal nozzle used for the tests described herein was a triple-concentric fuel nozzle, in which gas or coal could be fed in either of two annular nozzle regions, or down the center fuel nozzle. For these tests, stabilizing natural gas was fed through the outermost annulus and two separate coal feeders were used to supply coal to either of the inner annular region or the center coal pipe.

5.1.5 BENCH-SCALE MEASUREMENT SYSTEMS

The U-furnace bench-scale combustion facility is well instrumented for flue gas analyses. Samples are withdrawn from the furnace in a water-cooled sample probe, pass through an ice bath water trap to condense moisture and then proceed to the gas analyses equipment. The combustion gas is continuously monitored for NO_x, CO_2, CO, O_2, and hydrocarbons. Table 5.1 lists the continuous on-line analyzers, the manufacturer of the analyzer and the concentration range available. Data from these analyzers are recorded using an Omega Bench data acquisition system which is controlled by a personal computer.

In addition to the continuous gas analyzers, a Nicolet Model 550 Magna Fourier Transform Infrared (FTIR) analyzer was used to measure gas composition throughout the furnace. The species measured with the FTIR included nitrogen oxide, nitrogen dioxide, nitrous oxide, carbon monoxide, methane, acetylene, ethylene, ammonia and hydrogen cyanide. By varying the location of the

sample probe throughout the furnace, axial and radial profiles of combustion species can be obtained.

5.1.6 PILOT-SCALE MEASUREMENT SYSTEMS

A separate set of analytical instruments are used in the L1500 pilot-scale combustion facility. Table 5.2 describes the instruments available for this combustor. The sampling procedures are very similar to those at the U-furnace; i.e., a water-cooled sample probe removes the flue gas sample, it then passes through a filter, water trap and then proceeds to the analyzers. All data are recorded on the computer.

5.1.7 COAL PROPERTIES

The coal used in the combustion tests in the bench- and pilot-scale furnaces was a low sulfur, Utah Subbituminous coal from the Mining Division of Pacific Corp. (formerly Utah Power and Light) Deer Creek mine in Huntington, Emery County, Utah. Table 5.3 lists the proximate and ultimate analyses of the coal. The coal was pulverized by Vortec Company in California and shipped to the combustion laboratory in one ton sealed tote bags.

5.2 BENCH-SCALE STUDIES

The bench scale studies can be divided into three groups:

- NO Reduction Process - comparison of heterogeneous and homogeneous NO reduction using coal, natural gas, carbon monoxide and combustion products.
- Integrated Control Concepts - experiments to define process conditions that allow NO reduction at the same time as promoting carbon burnout.
- Characterization of Carbon Burnout - studies carried out under controlled conditions to characterize carbon burnout under different combustion conditions.

5.2.1 NO REDUCTION PROCESSES

Figure 5.5 compares the effectiveness of three fuels: coal, natural gas and CO within a conventional reburning experiment. The reburn fuel injection temperature was 2100^{o}F at a reburn zone residence time of 0.4 seconds. These data are presented as NO versus the reburning zone stoichiometric ratio for each of the fuels. The initial NO value of the combustion products entering the reburn zone was approximately 500 ppm for all of the cases. Notice that for these conditions the best reburning reductions for NO_x (about 61% reduction) are achieved by coal reburning at a reburn stoichiometric ratio of about 0.85. Natural gas provides about 51% reduction and CO about 40% reduction for these same conditions. The NO reduction from coal reburning is better than that achieved by CO throughout the stoichiometry range investigated and better or equal to that of natural gas in this same range. It is important to note that this reburning temperature is lower than that which is optimal for CO reburning. Also, under these low temperature conditions, significant amounts of CO and unburned carbon were emitted for the coal reburning case.

A similar comparison of reburning fuel types is presented in Figure 5.6. The experimental conditions are for an initial NO_x level of 500 ppm, a reburn fuel injection temperature of 2650^oF, and a reburn zone residence time of 0.4 seconds. For these conditions, natural gas is the superior reburning fuel throughout the range of stoichiometries investigated. Coal reburning leads to NO reductions of nearly 60% at SR = 0.82 and CO reburning leads to NO reductions of nearly 40% at SR = 0.86. Recall that this reburning fuel injection temperature (2650^oF) is greater than the optimal temperature for CO reburning. Even so, at a given stoichiometric ratio, CO reburning can still account for nearly 80% of the total NO reduction observed for each of the hydrocarbon fuels (natural gas and coal) presented in Figure 5.6.

Figure 5.7 presents a similar comparison but in this case the initial NO_x concentration is 200 ppm. With low initial NO_x of 200 ppm, the performance of coal as a reburning fuel is noticeably worse than that of other hydrocarbon fuels (wood and natural gas in this case). This is due to the fuel nitrogen content which for low initial NO_x conditions leads to the formation of increased fixed nitrogen species in the reburning zone which can be subsequently oxidized in the burnout zone. The natural gas contains no fuel nitrogen species, while the wood contains 0.1% by weight compared to the coal which contains 1.42% nitrogen.

CO is not a source of hydrocarbon radicals and the NO reductions shown for CO in Figures 5.5 and 5.6 cannot be explained by our existing chemical kinetics. Detailed measurements at several axial locations were made in a coal reburning jet to provide data for model development/validation. A premixed natural gas burner was doped with NH_3 to set the initial NO_x concentration to 500 ppm at a stoichiometric ratio of 1.05. A water-cooled injection probe with a 90^o angle and 0.245 inch injector diameter was inserted into the primary section of the U-Furnace at an axial distance of 4.5 ft from the burner throat. Coal and carrier air were injected through this probe as a large downward fired jet located at the centerline of the U-Furnace. The firing rate of the coal was set to 32,500 BTU/ hr in order to obtain an overall stoichiometry in the reburn zone of SR = 0.85. Burnout air addition was accomplished downstream from the large reburning jet at an axial distance of 9 ft. from the burner throat bringing the exhaust stoichiometric ratio up to SR = 1.15. Gas samples in the reburning zone were extracted through an angled water-cooled gas sampling probe and sent to the Fourier Transform Infrared (FTIR) analyzer. At least 4 samples were obtained at each sampling location to test for repeatability. Radial profiles of species concentrations were obtained at axial locations of 9 in., 21 in. and 33 in. downstream from the coal reburning jet injection location.

Species that have been identified and quantified in the reburning zone of the large coal reburning jet include:

- nitrogen oxide, NO
- carbon monoxide, CO
- methane, CH_4
- acetylene, C_2H_2
- ethylene, C_2H_4
- ammonia, NH_3

- hydrogen cyanide, HCN

Although the FTIR was capable of detecting other nitrogenous compounds (e.g., nitrogen dioxide (NO_2), and nitrous oxide (N_2O)), these species were not present in concentrations above detection limits (~ 1 ppm).

Figure 5.8 presents the profiles of NO_x concentration obtained at the three axial locations across the diameter of the furnace. At the 9 in. axial location NO_x values peak at the centerline at concentrations of about 580 ppm with values near the wall of about 400 ppm. This indicates net NO_x formation in the coal jet with no significant reduction of NO_x outside the jet. At the 21 in. axial location the NO_x concentrations become more uniform and are lower relative to their earlier concentrations at the 9 in. axial location. NO_x levels in the center peak at around 450 ppm and drop off to about 300 ppm near the wall. This indicates overall reduction of NO_x due to reburning. At the 33 in. axial location the NO_x profile exhibits a decreased centerline NO_x concentration along with lower NO_x concentrations near the walls. Concentration profiles for other species are presented also:

- carbon monoxide concentration profiles are presented in Figure 5.9.
- methane concentration profiles are presented in Figure 5.10.
- acetylene concentration profiles are presented in Figure 5.11.
- ethylene concentration profiles t are presented in Figure 5.12.
- ammonia concentration profiles are presented in Figure 5.13.
- hydrogen cyanide concentration profiles are presented in Figure 5.14.

The presence of HCN can be attributed to the evolution of fuel nitrogen compounds from the coal and also as an intermediate in the reburning process involving hydrocarbon species. It is noteworthy that HCN concentration is lowest on the furnace axis at an axial location of 33 inches; at this time the reburning fuel is distributed across the whole width of the furnace and HCN concentrations are highest where the NO is lowest.

The final NO concentration at the exhaust was 190 ppm due to the oxidation of the remaining hydrocarbon species in the absence of oxygen. However, it is also possible that the decrease was, in part, associated with the presence of CO and char. It is also interesting to note that the reduction occurs relatively uniformly across the furnace radius once the reburning fuel has spread in search of the available oxygen.

Again there is experimental evidence that NO can be reburned by a mechanism that does not involve hydrocarbon radicals, but it is not possible to neglect the heterogeneous effects associated with the presence of char. Unfortunately it is not simple to isolate the importance of heterogeneous NO reduction reactions under realistic combustion conditions; however, two different approaches were used to evaluate this issue. Figure 5.15 shows the results of reburning experiments where the reburning fuel was a wood char containing essentially no volatiles and fuel nitrogen (less than 0.2% by weight). These experiments were conducted with and without oxygen present to evaluate the importance of O_2 on the process. The primary zone stoichiometry was operated slightly fuel rich to eliminate oxygen from the primary flow. The char was transported with nitrogen containing a

controlled amount of oxygen. The initial NO (with no char injection) was approximately 500 ppm. As the data in Figure 5.15 indicate, a 60% NO reduction was achieved when the char transport stream was normal air (21% O_2). Reductions greater than 80% were achieved when the entire system was operated oxygen deficient. It must be recognized that, particularly in the case where oxygen is present, the reburning reduction is likely due to a combination of homogeneous and heterogeneous effects:

- in the presence of oxygen heterogeneous oxidation of the char to form CO and subsequent homogeneous reaction of the CO with NO

- because NO reduction occurs at low oxygen concentrations, it appears likely that some heterogeneous reduction of NO on char is occurring.

It should also be noted that the char used in these studies has a relatively high surface area because it was prepared from a wood pyrolysis process.

It is far less complicated to evaluate the homogeneous path for non-hydrocarbon NO reduction. Figure 5.16 presents reburning curves for four different reburning fuels. The reburning curves are presented as NO_x (corrected to 3% O_2) versus the stoichiometric ratio in the reburning zone. The first two reburning fuels are natural gas and pure CO which achieve the same NO_x reduction at stoichiometric ratios less than or equal to 0.8. CO reburning is slightly less effective than natural gas at reburning stoichiometries greater than 0.8. The third and fourth reburning fuels included in Figure 5.16 are CO with added NO in the amounts indicated (210 and 490 ppm). This amount of NO corresponds to the amount required to increase the initial NO_x concentration by the amount indicated. Therefore, although the NO_x levels achieved for the CO+NO reburning fuels are higher in most cases, the overall NO_x reduction achieved by these CO+NO reburning fuels is greater than that of natural gas or pure CO as shown in Figure 5.16. The overall NO_x reduction achieved by the use of these four reburning fuels is plotted versus reburning stoichiometric ratio in Figure 5.17, for the fuels with added NO, the “initial” NO is the sum of the primary NO plus that NO added to the reburning fuel. Notice that the NO_x reduction is substantially greater for both of the CO+NO reburning fuels. Also, at a stoichiometric ratio of 0.85 the overall NO values are quite low for each of the CO+NO reburning fuels and lowest for the CO+210 ppm NO case. Sr = 0.85 appears to be an optimal stoichiometry for CO+NO reburning.

Figure 5.18 presents the dependence of the CO+NO reburning reaction on the injection location of the CO+NO mixture. In each case the amount of CO+NO mixture that was injected lead to a reburning stoichiometric ratio of 0.854, which is close to the optimal value for CO+NO reburning as indicated above. These data indicate an optimal injection location for CO+NO reburning which occurs at a distance of 7.5 feet from the burner throat which probably represents an optimum temperature for NO reduction by CO. This optimal temperature, as measured by a suction pyrometer, is between 2300 and 2500^{o}F.

Similar experiments, changing the reburning fuel injection location were conducted to compare methane with CO. In these experiments the initial stoichiometric ratio of the combustion product stream produced by the burner was SR = 1.05. Various amounts of reburning natural gas and reburning CO were injected subsequently into the combustion products with a constant flow of NO that would give an equivalent exit NO concentration of 723 ppm at various axial locations downstream from the burner. Burnout air was injected downstream from the reburning fuel injection

location to bring the overall stoichiometric ratio up to SR = 1.15 in all cases. Figure 5.19 compares CO with natural gas. The data are presented as the NO_x reduction percentage (as determined by the measured NO_x in the exhaust) versus the axial location of reburn fuel injection. The upper panel data differs from that of the lower panel only in that the burnout air is injected at a different axial location. The burnout air injection location of the top panel was 10.5 ft. from the burner while that of the bottom panel was 12.4 ft. from the burner. Notice that the CO reburning case shows optimal NO_x reduction percentages at the 7.5 ft. location regardless of the burnout air injection location. This optimal location is believed to correspond to an optimal temperature window for CO reduction of NO as indicated above. The natural gas injection data do not appear to have an optimal temperature (or injection location) as the CO data indicates. For natural gas injection the general trend is one of increasing NO_x reduction percentage with increasing fuel-rich (reburning) residence time. That is, as the injection location for the reburning natural gas injection location is moved further from the location of burnout air injection (or closer to the burner) the NO_x reduction percentage increases. Also note that the NO_x reduction achieved by CO+NO injection is substantially greater than that achieved for natural gas + NO injection for the axial injection locations corresponding to 7.5 and 9.5 ft. from the burner. This indicates that a mechanism other than hydrocarbon radical attack must participate in reburning chemistry.

In low-NO_x firing systems, NO produced in one region can mix with fuel rich combustion products formed in a different region. Experiments were carried out in the U-Furnace to determine whether fuel rich combustion products could also destroy NO.

Figure 5.20 presents data for the injection of a constant amount of NO into the fuel-rich combustion products of a premixed natural gas burner at fixed stoichiometric ratios of SR = 0.85 and SR = 0.95. These combustion products contain only equilibrium levels of hydrocarbon radicals since the burner is premixed and the residence time between the burner and the location of NO injection is large (between 0.5 and 1.3 seconds). The amount of NO injected in all of the cases is equivalent to an amount which would lead to an increase of 880 ppm in the overall NO concentration. The premixed burner produces around 100 ppm NO_x under these conditions. Burnout air was injected downstream from the NO injection location to bring the overall stoichiometric ratio up to SR = 1.15. The data in Figure 5.20 are presented as measured exhaust NO_x concentrations plotted against the NO injection location measured as the distance from the burner. The data indicate that NO can be reduced substantially by these equilibrium combustion products. NO_x reductions as large as 90% were observed for both of the stoichiometric ratios investigated at the 4.5 ft. injection location. Also, there appears to be an optimal injection location (or injection temperature) for NO_x reduction which is similar to that observed in the CO reburning data. The data of Figure 5.20 were obtained while the U-Furnace was operating at a lower temperature than the CO reburning data presented above. Measured temperatures indicate that the injection location of 4.5 ft. corresponds to the same temperature range as that required for optimal CO reburning (between 2300 and 2500^{o}F).

In order to determine whether the reduction of NO was occurring in the fuel-rich combustion products stream of the reactor or at the location of burnout air addition, measurements were made in the burnout air injection zone of the U-Furnace. Figure 5.21 presents NO_x measurements obtained just prior to the burnout air injection location and at several axial locations downstream from the burnout air injection. As indicated in Figure 5.21, the measured NO_x concentrations do not vary considerably in this burnout zone. The concentration of NO_x is approximately constant at a level of about 270 ppm. However, accounting for the dilution effect of the burnout air would lead to a substantial reduction in measured NO_x as indicated by the solid line of Figure 5.21. Thus, there is

net production of NO_x in the burnout zone which leads to concentrations in the burnout zone that are nearly constant. Also notice that NO_x concentrations vary considerably in the vicinity of burnout air injection and converge to a nearly constant steady-state level far downstream from the burnout air injection location (5 data points were taken at each axial location).

In the burnout zone, additional experiments were conducted to determine how the presence of ammonia effects final NO_x concentrations. Figure 5.22 presents exhaust NO_x concentrations versus ammonia injection location for the injection of 720 ppm worth of NH_3 at two different axial locations which straddle the burnout air injection location. Two injection methodologies were investigated, a single injector and dual opposed injectors, with similar results obtained. The data of Figure 5.22 indicate that the presence of NH_3 in the burnout air regime can lead to very low measured exhaust concentrations of NO (around 20 ppm). This is most likely due to selective non-catalytic reduction (SNCR) chemistry which can occur in the burnout zone of a reburning application. Injection of the ammonia before the burnout zone is less effective.

These studies indicate that:

- NO can be reduced by fuels other than those containing hydrocarbons.
- CO, which will be formed during staged combustion, is an effective reburning fuel.
- Although more difficult to isolate, it appears that NO can also be reduced by char particularly in the absence of oxygen.

5.2.2 INTEGRATED CONTROL CONCEPTS

As the pulverized coal must be transported with air, it must burn initially under excess air conditions and NO will form at the root of the flame. Also if large coal particles are to be burned out then it is advisable to ignite them and reduce their carbon content as much as possible before they enter the fuel rich zone. Thus it is possible to think of a complex pulverized coal flame as separate reaction products, fuel lean and fuel rich which must mix in order to complete combustion; the SPPC burner was used to investigate the effect of this process on NO. These studies were conducted at an overall firing rate of 120,000 Btu/hr and the coal split between the middle chamber was varied at constant overall excess; the range of conditions investigated covered the following:

- Overall excess air (between 5% and 30%)
- Middle chamber stoichiometry ($0.3 < SR < 3.0$)
- Annular chamber stoichiometry ($0.5 < SR < 4.0$)
- Inner/Annular chamber velocity ratio ($0.43 < V_i/V_o < 2.71$)
- Coal split between inner and annular chamber (25/75, 50/50, and 75/25)

Figure 5.23 shows the effect of the velocity ratio of the inner chamber to that of the outer chamber (V_i/V_o) for the case when 75% of the coal mass is injected through the inner chamber and 25% of the coal injected through the outer annulus. With the coal concentrated in the inner chamber most all of the velocity ratios provide the same performance except for the high velocity ratio case

(V_i/V_o = 2.71). This indicates that the stream which contains the majority of the coal should not be rapidly mixed with the remainder of the flow to obtain low NO_x. Although one might expect the low velocity ratio case to provide worse performance similar to the high velocity ratio case, the fact that the stream with the lower velocity contains the majority of the coal leads to performance that is similar to velocity ratios that are near to 1.0. This could be due to one of two factors. At this lower velocity ratio the stoichiometry of the inner chamber is lower, and the local residence time of the majority of the coal in this fuel rich regime could be longer due to the lower inner velocity. Also, one should note that Figure 5.23 indicates a monotonic increase in NO_x emissions with increasing excess air levels (i.e., increasing measured exhaust O_2 concentration) in this 5% to 30% excess air regime which is expected.

Similar data were obtained for the 25/75 coal split and the 50/50 coal split cases. Figure 5.24 presents the effect of velocity ratio on NO_x emissions versus measured O_2 concentration for the case when coal is concentrated in the annular chamber. In this case there appears to be an optimal velocity ratio which leads to lower overall NO_x emissions for the V_i/V_o = 1.75 case. In this case the annular flow which contains the majority of the coal is entering the chamber at a lower velocity than the inner chamber flow. This optimum could be due to competition between a favorable stoichiometric value for the stream containing the majority of the coal and increased mixing between the two streams which occurs at higher velocity ratios. Figure 5.25 presents the effect of velocity ratio when the coal is split evenly between the two premixed chambers. In this case the velocity ratio between the two streams is inconsequential. As Figure 5.25 indicates, a variation in the velocity ratio between 0.43 and 2.71 does not significantly affect the performance of the SPPC burner with regard to overall NO_x emissions when the coal is evenly split between the two chambers.

Figure 5.26 presents data and second order polynomial fits to the data for a variation in overall excess air ranging from 5% to 30% excess air (1.05 < SR < 1.30). The data of Figure 5.26 are presented versus the stoichiometry of the middle premixed chamber for conditions in which the coal is concentrated in the middle chamber (i.e., the coal split is 75/25). Figure 5.26 indicates that when the coal is concentrated in the middle chamber the optimal stoichiometry for operation of the middle chamber is around SR = 0.6. This is the stoichiometric ratio where chemical equilibrium calculations predict a minimum in total fixed nitrogen (TFN) for coal combustion.

Figure 5.27 presents NO_x emissions data and second order polynomial curve fits for the 50/50 coal split case and several different excess air levels versus the stoichiometric ratio of the annular premixed chamber. These data seem to indicate an optimal outer chamber stoichiometry which shifts from SR = 1.4 for the 5% excess air case to SR = 1.8 for the 30% excess air case. This same data is plotted versus the inner chamber stoichiometric ratio in Figure 5.28 for the 50/50 coal split case. Figure 5.28 indicates an optimal inner chamber stoichiometry of around SR = 0.7 for all of the excess air levels. This is likely the most significant reason for the observed optimum. It is likely that when the coal is evenly split between the two chambers it is desirable to fix the inner stoichiometric ratio at a level near the level required for minimum TFN (as predicted by chemical equilibrium this value should be around SR = 0.6).

When the coal is concentrated in the annulus (75% of the coal mass entering the annular chamber) the optimum does not appear to be fixed with respect to either of the two chamber stoichiometries as indicated in Figure 5.29 and Figure 5.30. When plotted versus the inner chamber stoichiometric ratio the data show an optimal outer chamber stoichiometric ratio that varies from

about 0.8 to 1.1 as the excess air level increases from 5% to 30% (see Figure 5.29). When plotted versus the inner chamber stoichiometric ratio, the data show minimum NO_x operation at stoichiometric ratios between 1.5 and 2.0 as indicated in Figure 5.30. Therefore, when coal is concentrated in the annular chamber, it appears that one should maintain the outer chamber stoichiometry at a level that is slightly more fuel-rich than the inner chamber for minimum NO_x emissions. Why this is so different from the case when coal is concentrated in the inner chamber may be due to mixing between the concentrated stream and the diluted stream which is more rapid in the case when coal is concentrated in the annular chamber.

Figure 5.31 through Figure 5.35 present data obtained in the SPPC burner versus the coal split utilized in each of the experiments. Figure 5.31 presents data sets for each of the overall excess air cases for operation of the two chambers at a fixed velocity ratio of 2.71. Subsequent figures present data sets for each of the overall excess air cases for operation of the two chambers at velocity ratios of 1.75 (Figure 5.32), 1.05 (Figure 5.33), 0.59 (Figure 5.34), and 0.43 (Figure 5.35). In nearly all of the data sets it is evident that concentrating the coal in either the middle chamber or the annular chamber is preferred to an even split of the coal. The 50/50 coal split cases generally lead to the production and subsequent emission of higher NO_x levels than when the coal split is 25/75 or 75/25. Also, Figure 5.31 through Figure 5.35 indicate that it is preferable to concentrate the coal in the inner chamber (most of the 75/25 coal split cases give lower NO_x emissions than the 25/75 coal split cases).

In a low-NO_x firing system it is desirable to use the low-NO_x burner as the reburning agent rather than rely on down stream fuel injection which has a serious cost penalty. In-situ reburning data was obtained for operation of the U-Furnace with the diffusion burner downward fired in the primary zone of the furnace (see Figure 5.1). This diffusion burner was operated with secondary air that was electrically pre-heated to 600^oF before entering the burner. The secondary air was injected in equal parts through a swirl chamber (containing tangential entry and swirl vanes) and a chamber containing flow straighteners for axial flow. The approximate swirl number for this secondary flow was 0.6. The primary focus of the in-situ reburning experiments was the pulverized coal injector. Several different coal injectors were constructed and tested under the current Phase I program. Figure 5.36 presents schematic sketches of the coal injector designs tested in this part of the program. The primary differences in the coal injector design include multi-annular versus single annular injectors, and variations in pipe sizes which can lead to different injection velocities for the various primary streams.

The data presented in Figure 5.37 are for two of the coal injectors presented in Figure 5.36. These injectors are single annular injectors with the only difference being the pipe wall thickness used for the inner chamber of the injector. The top panel of Figure 5.37 presents NO_x data (corrected to 3% O_2) for firing various amounts of natural gas through the central pipe of the first coal injector with an inner chamber diameter of 0.194 inches. The bottom panel of Figure 5.37 presents similar data obtained for natural gas, fired through an inner chamber of 0.152 inches (ID). In each of the two experiments data was obtained for various levels of primary air flow (10%, 15%, or 18%). Previous data obtained in the U-Furnace for pulverized coal diffusion flames indicated a strong dependence of NO_x emissions on the primary air flow rate. Detailed analysis of these data revealed that this was due primarily to the velocity of the primary stream which, when increased, leads to more rapid mixing between the primary and secondary streams leading to higher NO_x formation rates near the burner and higher overall NO_x emissions. The stoichiometry of the primary stream was found to be only a secondary factor contributing to NO_x formation and emission (Spinti et al., 1997). Because of

this understanding, investigation of in-situ reburning was parameterized by the primary air flow to span the range of burner operation with regard to overall NO_x emissions.

The data of Figure 5.37 indicate that for higher primary air flow rates (15% or 18%) the injection of natural gas from the center of the burner leads to substantial reductions in NO_x. The top panel shows a NO_x reduction from 730 ppm to 500 ppm (~ 32%) with about 17% natural gas firing in the 15% primary air case with the thinner inner wall injector. The bottom panel of Figure 5.37 shows a NO_x reduction from 715 ppm to 420 ppm (~ 41%) with about 22% natural gas firing in the 18% primary air case with the thicker inner wall injector design. These are substantial reductions considering the fact that standard reburning by secondary fuel injection can achieve maximum reductions of around 60% with comparable reburn firing rates (15-20%). However, the data obtained for lower primary air flows with either of the coal injector designs presented in Figure 5.36 indicate that no significant reduction in NO_x can be achieved by in-situ reburning with natural gas when lower primary air flow rates are used in the current pulverized coal burner injector. This is likely due to the fact that the initial conditions that are established in the near field of the burner when operating with low primary air flow rates are such that a reburning zone is established even in the absence of centrally-injected natural gas. In this case, the injection of additional amounts of fuel in the core of this flame does not enhance the reburning effectiveness in this zone. This is similar to the standard reburning scenario in which NO_x is substantially reduced by the initial injection of reburning fuel (up to reburning stoichiometries of approximately SR = 0.85) with additional amounts of reburning fuel not leading to additional NO_x reduction.

Another likely explanation of the data in Figure 5.37 is that the final NO_x produced by the U-Furnace flame with the current coal injector designs might be limited by the conversion of char nitrogen to NO_x. In this case the formation of NO_x from the char nitrogen would occur downstream from the in-situ reburning zone and would be unaffected by changes in reburning zone in the near field of the burner. To test this hypothesis, similar in-situ reburning experiments were conducted using micronized coal instead of the standard coal grind. The micronized coal was pulverized to a 90% less than 325 mesh (44 μm) specification while the standard coal grind was 70% less than 200 mesh (74 μm). The micronized coal would be expected to devolatilize more rapidly (possibly leading to increased volatile yield as well) leading to the onset of char conversion closer to the burner. This should result in an increased effectiveness of in-situ reburning if char-N conversion to NO_x is the limiting factor under conditions of low primary air flow. Figure 5.38 presents in-situ reburning data obtained for micronized coal using the same injector as that presented in the bottom panel of Figure 5.37 (the injector with the thicker inner tube wall thickness). With an initial NO_x value of around 650 ppm, in-situ reburning gives about a 40% reduction in NO_x at a natural gas firing rate of 20 scfh (corresponding to ~16% of the total firing rate). However, when the primary air flow is reduced (leading to a better burner design that delays primary secondary mixing), the addition of natural gas in-situ gives no additional reduction in NO_x.

The performance of in-situ reburning with regard to NO_x reduction with the current burner and coal injector designs for the case of micronized coal is nearly identical to the performance with a standard coal grind. Figure 5.39 presents a comparison of the micronized coal case to the standard coal grind case. Each of these experiments was conducted by varying the amount of natural gas injected through the core of the coal jet with the same burner injector (single annular with the thick walled inner tube, see Figure 5.36), parameterized by the primary air flow percentage. The data sets are very similar and indicate that substantial reductions in NO_x are only achieved when the initial NO_x values are high (between 600 and 800 ppm). The 10% primary air case with micronized coal

shows a very slight reduction in NO_x with increased in-situ reburning. This may indicate that char-N conversion plays a role in limiting the effectiveness of in-situ reburning; however, data obtained for a slightly lower primary air flow (8.75%) indicate a complete leveling off of the in-situ reburning curve (see Figure 5.38).

Similar results were obtained for in-situ reburning with natural gas for each of the injectors presented in Figure 5.36 which indicated significant NO_x reductions when initial NO_x levels were high and nearly zero NO_x reduction when initial NO_x levels were lower (~400 ppm). In order to determine whether the velocity of the injected natural gas impacted these results, a variable amount of diluent nitrogen flow was added to the in-situ natural gas injection stream. Figure 5.40 presents data obtained for variations in the diluent nitrogen flow for two of the injectors. These injectors were single annular injectors with a 3/8 inch inner tube of varying wall thickness. All of the data of Figure 5.40 was for the case of 10% primary air flow with the standard coal grind. In each case the velocity ratio of natural gas to coal does not impact the effectiveness of in-situ reburning with natural gas.

Air staging was applied to the same diffusion burner for conditions of 10% primary air flow using the 3 annulus coal injector presented in Figure 5.36. Coal was injected through the outer most annulus with no flow through the inner annulus and in-situ reburning natural gas injected through the core. The stage 1 stoichiometry for this experiment was SR = 0.85 with a staging residence time of approximately 1.1 seconds. Very low NO_x emissions (~132 ppm) can be achieved for these conditions; however, the addition of in-situ reburning natural gas leads to increases in the overall NO_x emission as indicated in Figure 5.41.

An additional experiment was conducted to determine whether or not char-N conversion to NO was limiting the effectiveness of in-situ reburning. The combustion of a simulated waste gas containing fuel nitrogen in the gas phase (as NH_3) was accomplished in the same burner as that used for the in-situ reburning experiments with pulverized coal. As indicated in Figure 5.42, in-situ reburning does not work with “waste gas”. This indicates that in-situ reburning in the coal combustion case is probably not limited by char-N conversion. Even if all N goes into gas phase immediately (as is the case for this waste gas), in-situ reburning doesn't work for low-NO_x flames. It works only if initial NO_x is high.

5.2.3 CHARACTERIZATION OF CARBON BURNOUT

To quantify the relationship between NO_x and unburned carbon under well defined conditions, a series of experiments was conducted in the 100,000 Btu/hr U-furnace under both premixed and diffusion conditions with a Utah subbituminous coal. Duplicate impactor samples were obtained for particle size and composition analysis at four distinct conditions, each with an overall stoichiometric ratio of 1.15. The measured NO values for these conditions were:

- Premixed, base case; NO_x = 912 ppm
- Diffusion burner, axial flame; NO_x = 484 ppm
- Premixed, staged, short rich zone residence time case; NO_x = 500 ppm
- Premixed, staged, long rich residence time case; NO_x = 166 ppm

These small scale results are in good agreement with full scale data; as the NO_x emissions are decreased, the unburned carbon losses increase. The following observations are significant:

1. The gas-stabilized, axial flame provides significant NO_x reduction with only a modest increase in carbon loss relative to the idealized premixed case.

2. The carbon loss seems to be dominated by the largest particles (greater than 10 microns) and, in the very low-NO_x case, it appears that the carbon problem is simply large particles which were not completely burned within the combustion zone prior to the thermal quench.

3. While a long, fuel rich residence time is highly desirable for NO_x control purposes, it will likely lead to LOI problems.

4. There is some evidence of soot formation based on the very fine particulate data collected in these experiments.

These results clearly suggest that if one wishes to simultaneously achieve good carbon burnout and low NO_x emissions, it will be necessary to provide sufficient oxygen early in the combustion process to ensure that the largest particles are completely burned. This will inevitably result in the production of significant NO_x which must subsequently be destroyed. Therefore, one major focus of this project was on the chemical mechanisms for destruction of NO_x after it has been produced. The next two subsections focus specifically on the optimization of the homogeneous and heterogeneous mechanisms for this destruction. The final portion of this section examines practical concepts designed to embody the optimized reduction processes without negative impact on carbon burnout.

5.3 NO DESTRUCTION MODELING

The experiments discussed earlier indicate that the reburning modeling included in GLACIER requires improvement and three steps were taken to improve this reburning model:

1. Independent rates for a global reburn reaction were determined based on applicable data.

2. A direct CO “reburning” step was added to describe this effect globally.

3. A new technique for estimating inlet CH_i radical concentration was developed.

The simple global reburning mechanism comprises the destruction of NO by CH_i radicals, the formation of HCN, and subsequent conversion to NO or N_2 as illustrated below:

$$NO + CH_i \rightarrow HCN \quad \begin{matrix} \xrightarrow{O_2} & NO \\ \xrightarrow{NO} & N_2 \end{matrix} \qquad 5.1$$

The first step taken in developing a working model involves developing an approach for estimating the inlet CH_i radical concentration. Inclusion of CH_i chemistry in CFD codes for

practical modeling is not possible with current computational limitations. Therefore, some ad hoc means of specifying the concentration of the fuel intermediates is required. Chen's methodology uses a CH_i concentration proportional to the inlet hydrocarbon concentration. Although this approach does not have a strong fundamental justification, chemical kinetic modeling suggests that a similar approach based on reburn stoichiometry is reasonably accurate. Since this approach is straightforward to implement it is adopted herein. Figures 5.43 and Figure 5.44 compare data and a best fit for the kinetic parameters of the global reburning expressions given above resulting in the following pre-exponential factor and activation energy:

$$A = 1.765e^{+10}\ mol/cm^3*s \text{ and } E_a = 7.5\ kcal/mol \qquad 5.2$$

While the trends are meaningful for both CO and natural gas, the effectiveness of CO as a reburning fuel is not predicted. In addition, the leveling as a function of stoichiometry at the rich extreme, which is observed during natural gas reburning, is not predicted and the slope of the data at 1400 K is much steeper than that of the prediction.

5.3.1 DETERMINATION OF A DIRECT CO "REBURNING" RATE

In order to improve the accuracy of the predictions for CO, an additional step was added to the "reburning" mechanism. Although past work has established that CO can serve as a reducing agent for NO, detailed chemical kinetic mechanisms predict very low rates of NO removal through reaction with CO. Therefore, global mechanisms for practical use in CFD codes have assumed that this reduction was insignificant in comparison to traditional hydrocarbon radical reburning. The magnitude and direction of the inaccuracy in the above predictions indicate that this assumption may not be correct. Therefore, a direct CO "reburning" step was included in the global mechanism as follows:

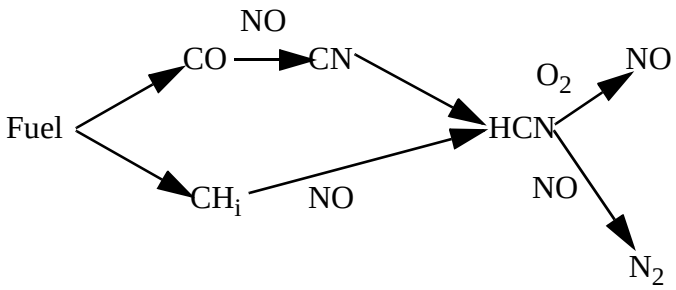

5.3

A global rate was then determined to fit the data discussed previously. In addition, this step was included in the modeling of the natural gas data. The resulting kinetic parameters are listed below and the modeling results are shown in Figures 5.45 and 5.46.

$$A_{CO}=1.0e^{+9}mol/cm^3*s,\ E_{a,CO}=15\ kcal/mol;\ A_{CHi}=1.09e^{+9}mol/cm^3*s,\ E_{a,CHi}=7.5\ kcal/mol \qquad 5.4$$

Using this approach the CO data at both 1720 and 1400 K can be fit quite well as shown in Figures 5.45 and 5.46. The fit of the natural gas however is only slightly improved (the curvature of the prediction is slightly greater).

5.3.2 DEVELOPMENT OF CH_i ESTIMATION APPROACH

As a first attempt to address the inability of the model to track the stoichiometry dependence of the reburning data, a more theoretically justifiable estimate of CH_i radical has been developed. Since hydrocarbon radical concentrations and the production rate of CO are strongly related quantities, it is possible that the amount of CO present could control the CH_i concentration. In addition, *GLACIER* has a tested kinetic scheme for determining CO concentration. In order to characterize the dependence of CH_i on CO concentration, fundamental chemical kinetic calculations were performed using Chemkin. A series of calculations were done for four simple fuels, two temperatures, and a range of stoichiometries and residence times. From these results it was determined that the integral of the CH_i radical concentration over time was nearly constant for each of the cases at a given stoichiometry and that the instantaneous CH_i radical concentration was roughly proportional to the slope of the CO concentration. Therefore, the technique used to estimate the CH_i radical concentration is to determine the magnitude of the peak CH_i concentration based on the integral mentioned previously and to determine the shape of the curve based on the proportionality with CO production rate. Figure 5.47 illustrates the results of this technique for a typical case. This approach has been included in *GLACIER*.

5.4 PILOT-SCALE FURNACE RESULTS

The pilot-scale furnace results focused on the effect of using a fine grind coal in conjunction with a standard grind coal to determine if any NO_x benefits may be achieved by separating smaller coal particles from larger ones and placing them in different regions of the coal nozzle. To this end, a standard pulverized coal grind (80% through 200 mesh) was reground to obtain a finer grind (90% through 325 mesh) and these two different coal distributions were fed through two separate coal feeders.

The test series focused on a comparison of 25% fine grind/75% standard grind coal feed with that of a 100% standard grind coal feed. To obtain a baseline NO_x curve at 100% standard grind coal, the innermost coal pipe was removed leaving the outermost annular region and single large coal pipe in the center. The outer annular remained unchanged throughout these experiments and was utilized for a flow of 5% stabilization gas. Values for NO_x as a function of excess air were taken using this configuration and the values obtained are indicated in Figure 5.48. The results, corrected to 3% oxygen, indicate an NO_x variation of over 500 ppm over the range tested. The small, inner coal pipe was then inserted and the standard coal grind was then forced to flow in an annular region around the innermost coal pipe. The flowrate of the standard grind coal was reduced to 75%. The fine grind coal was introduced through the central coal pipe at a ratio of 25% of the total feed rate. The results of this fine grind experiment are also shown in Figure 5.48. As shown, the use of 25% fine grind coal in a center core jet resulted in a NO_x reduction of order 100 ppm over most of the excess air levels tested.

As a further comparison, the standard grind coal and fine grind coal feed locations were reversed such that the 25% fine grind coal was fed through middle annulus and the 75% standard grind coal was fed through the central coal pipe. The flow area of the central coal pipe is approximately 30% of the total coal flow area, with the middle annulus comprising the other 70%. As a result of this reduction in area, in addition to the high flow rate of coal and primary carrier air for the 75% standard grind coal feed, the velocity in the central coal nozzle was considerably higher than that of the experiments summarized in Figure 5.48. Also, the velocity in the middle annular

region with the fine grind coal was lower than the corresponding velocity in the previous set of experiments. This configuration was run and NO_x values were obtained over a range of excess air as before. The results of these measurements are shown in Figure 5.49. For comparison, an additional set of measurements were taken using 100% standard grind coal through the center coal pipe and these results are also plotted in Figure 5.49. As shown, there was little difference between the two sets of NO_x curves.

A comparison of the two sets of experiments is shown in Figure 5.50. It is evident that although there was little difference when using either 75% or 100% of the standard grind down the central coal nozzle, the results obtained were similar to those obtained using the distributed fine grind in the middle annulus at lower levels of excess air. At higher levels of excess air, the standard grind flowing primarily through the center provided the lowest NO_x results.

Table 5.1 Analytical Instrumentation on U-Furnace

Measurement	Manufacturer	Concentration Range
Oxygen	Beckman	0-50%
Carbon Monoxide	Anarad	0-10%
Carbon Dioxide	Anarad	0-30%
Nitrogen Oxides	ThermoElectron	0-1%
Total Hydrocarbons	Beckman	0-1%
Heated Total Hydrocarbons	Ratfisch	0-1%
Carbon Monoxide	Thermo Environmental	0-1000 ppm

Table 5.2 Analytical Instrumentation on L1500 Furnace

Measurement	Manufacturer	Concentration Range
Oxygen	Yokogawa Model AV8C	0-25%
Carbon Monoxide/ Carbon Dioxide	California Analytical Model ZRH	0-2000 ppm (CO) 0-20% (CO_2)
Nitrogen Oxides	Thermo Environmental Model 42C	0-10,000 ppm
Hydrocarbons	VIG Industries Model 20	0-10,000 ppm

Table 5.3 Huntington Coal Analyses

Category	Value (wt%)
Proximate (as received)	
Moisture	5.48
Volatile Matter	38.51
Fixed Carbon	47.35
Ash	8.66
Ultimate (dry)	
Carbon	73.21
Hydrogen	5.44
Nitrogen	1.42
Sulfur	0.56
Oxygen	10.21
Ash	9.16

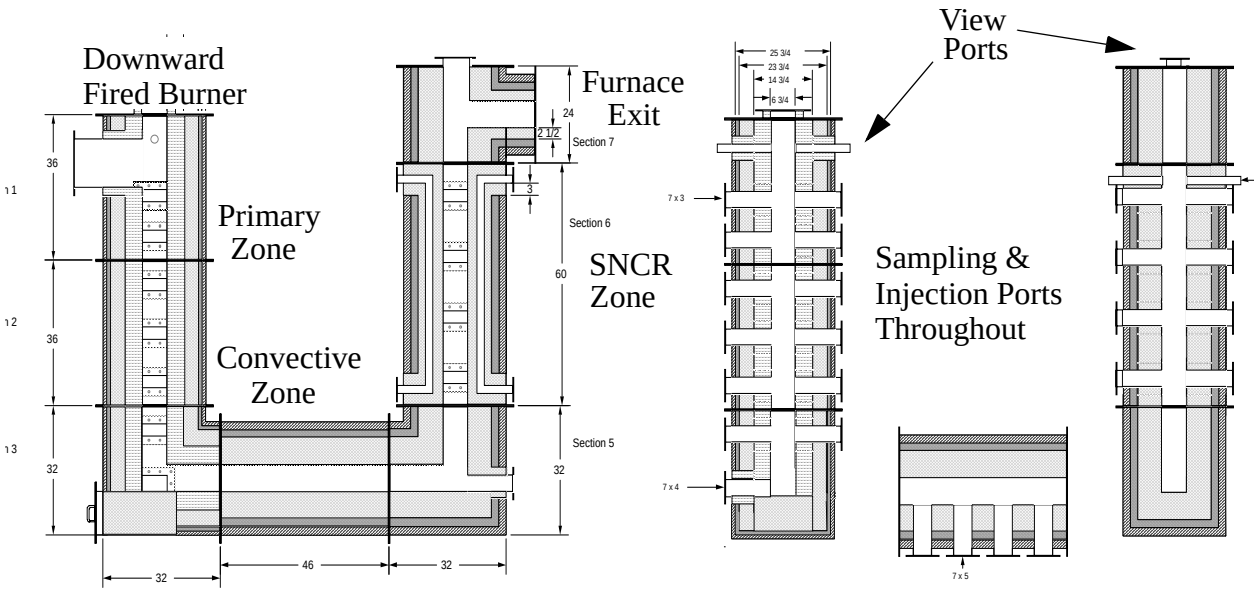

Figure 5.1 The 100,000 Btu/hr multi-fuel combustion test facility at the University of Utah referred to as the U-Furnace.

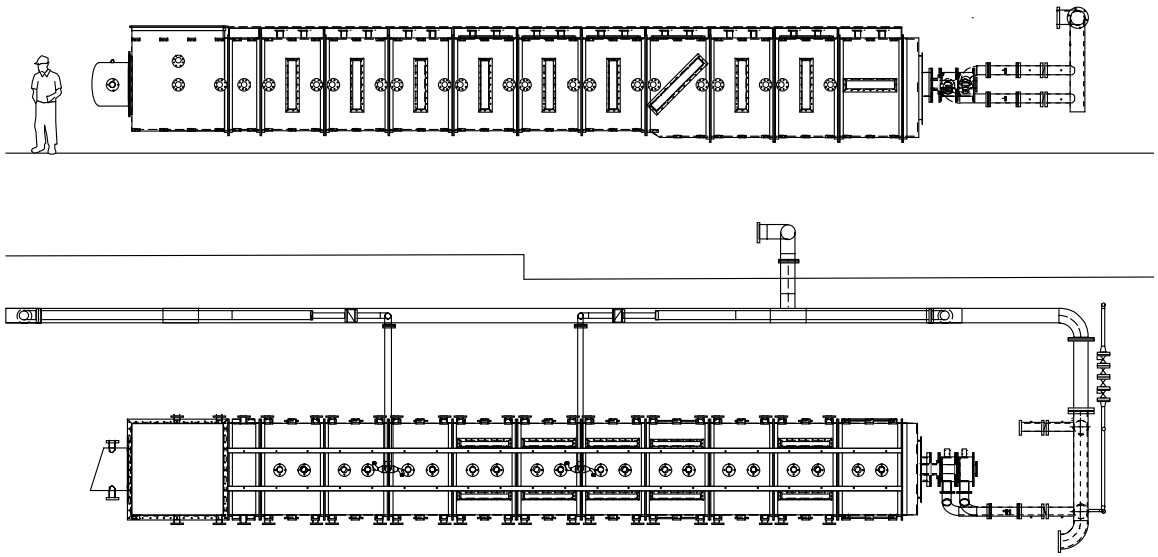

Figure 5.2 The 15 MMBtu/hr multi-fuel combustion test facility at the University of Utah referred to as the L1500 Furnace.

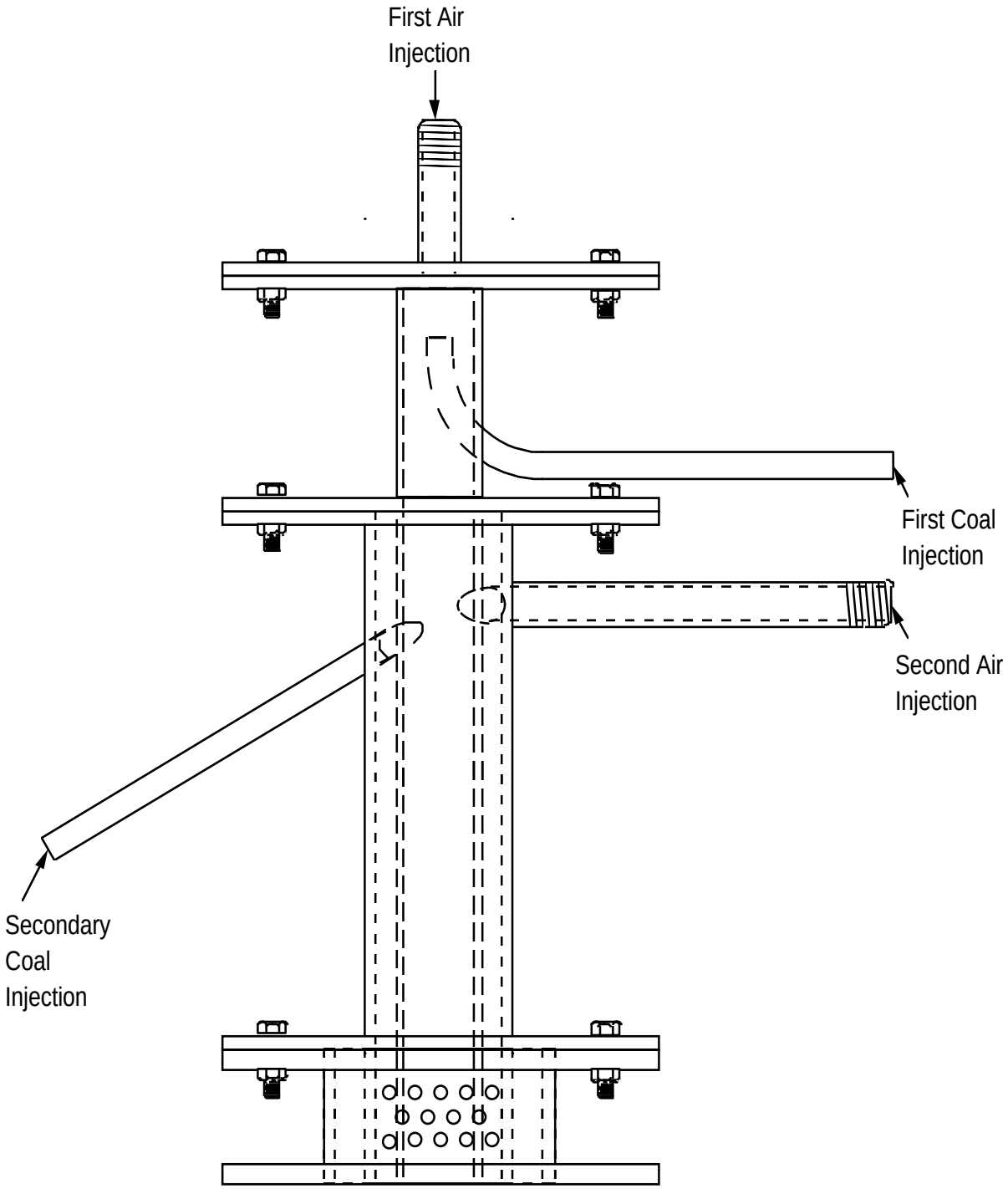

Figure 5.3 The segregated premixed pulverized coal burner (SPPC) used in the U-furnace.

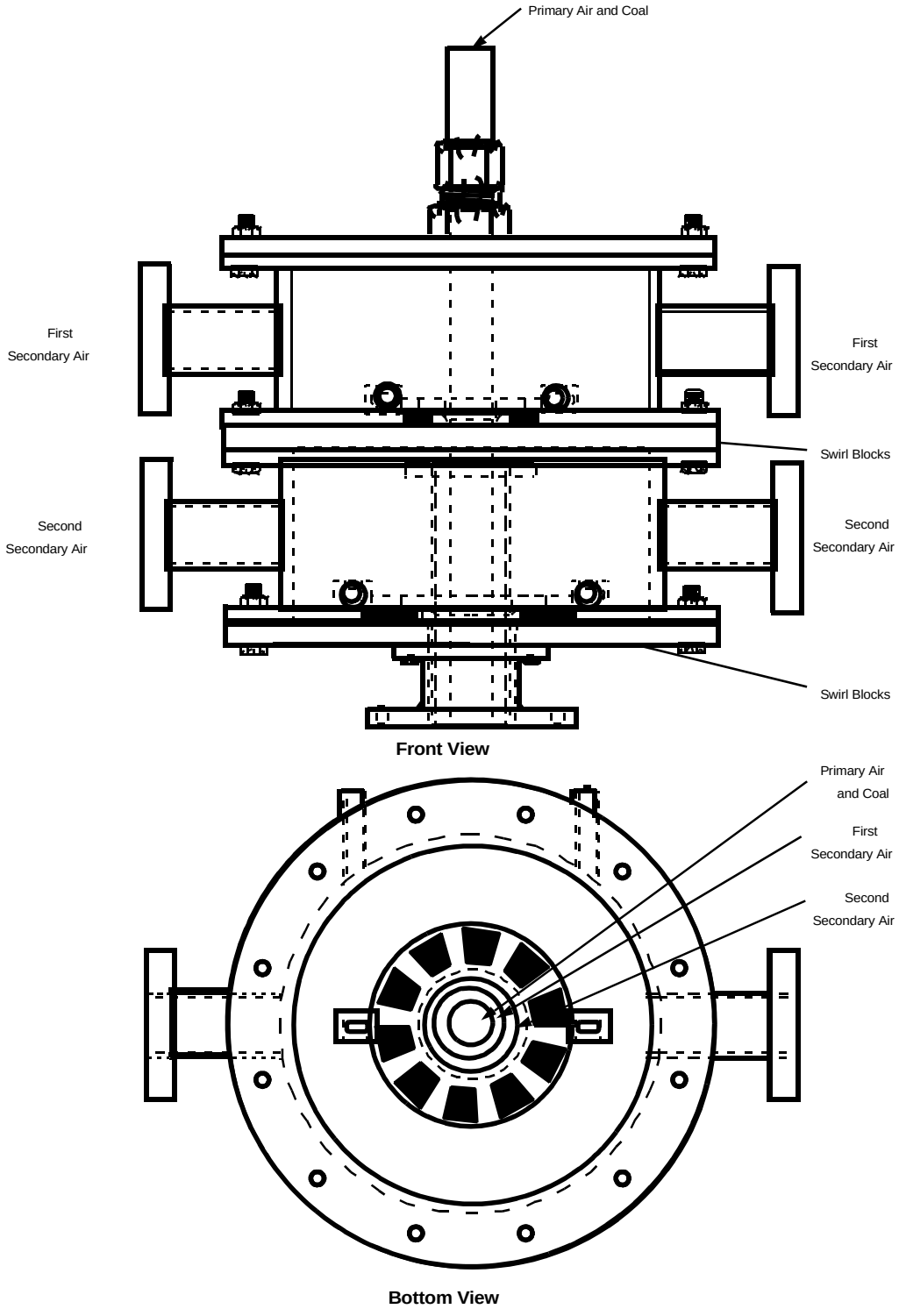

Figure 5.4 The dual concentric swirl burner (DSCB) used in the L1500 furnace.

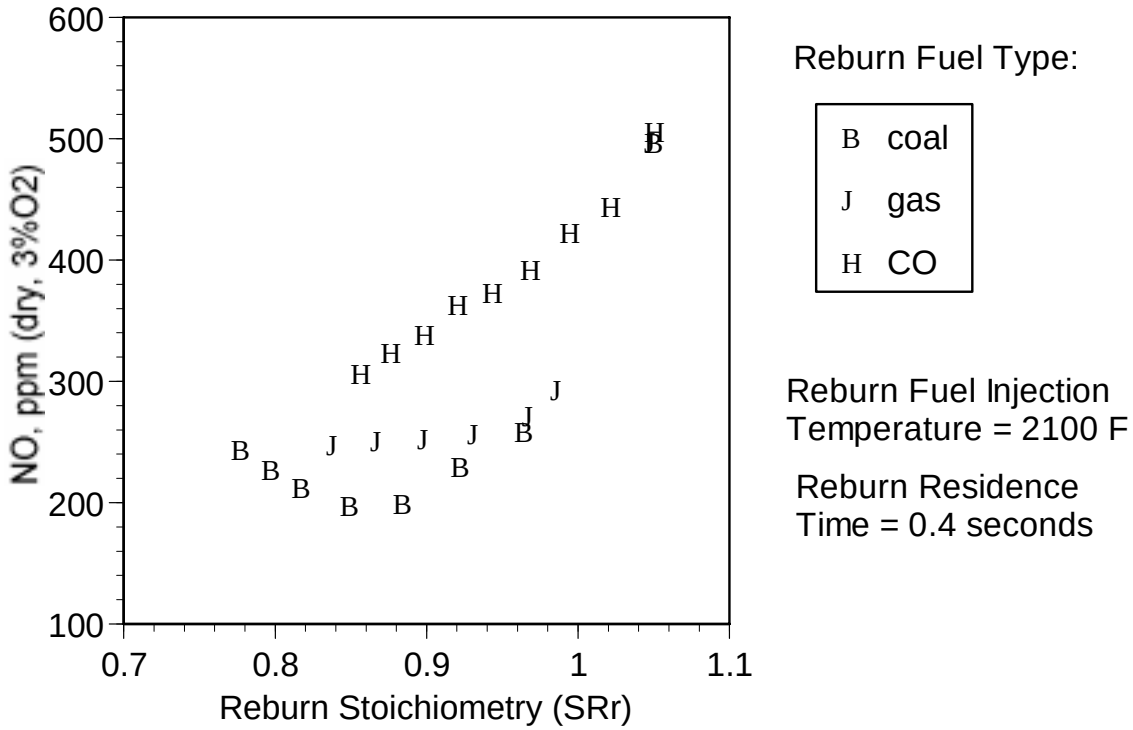

Figure 5.5 NO reduction with coal, gas and CO as reburning fuels at injection temperature of

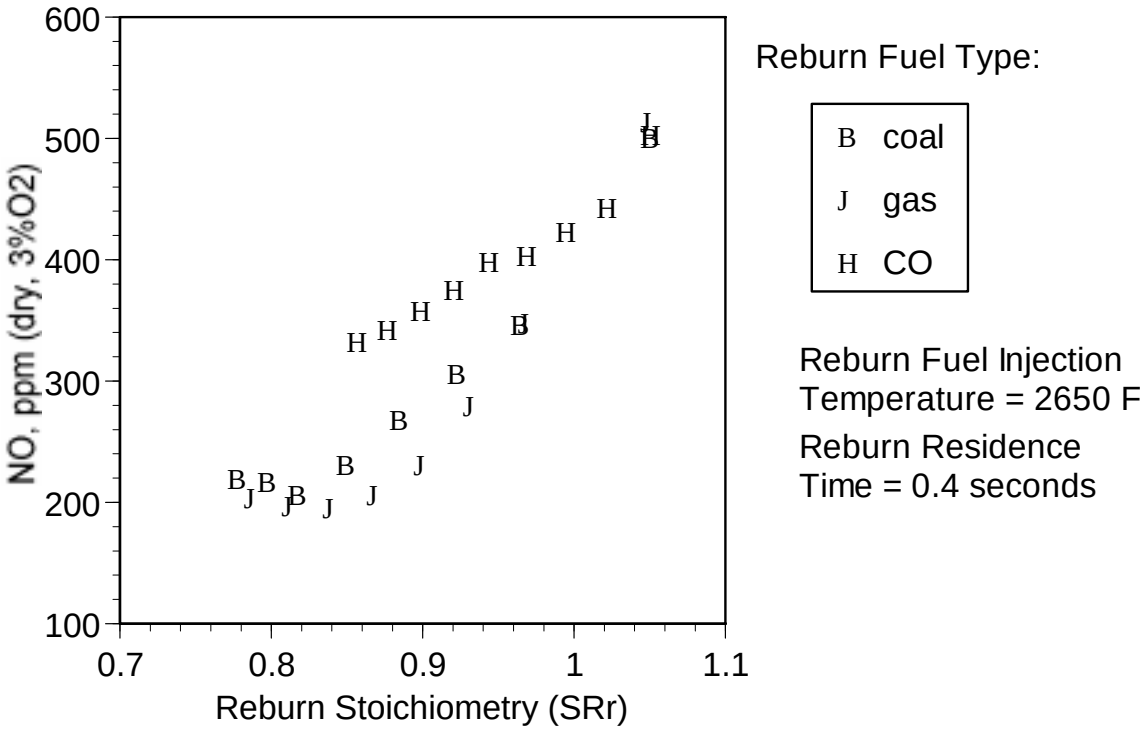

Figure 5.6 NO reduction with coal, gas and CO as reburning fuels at injection temperature of 2650^{o}F.

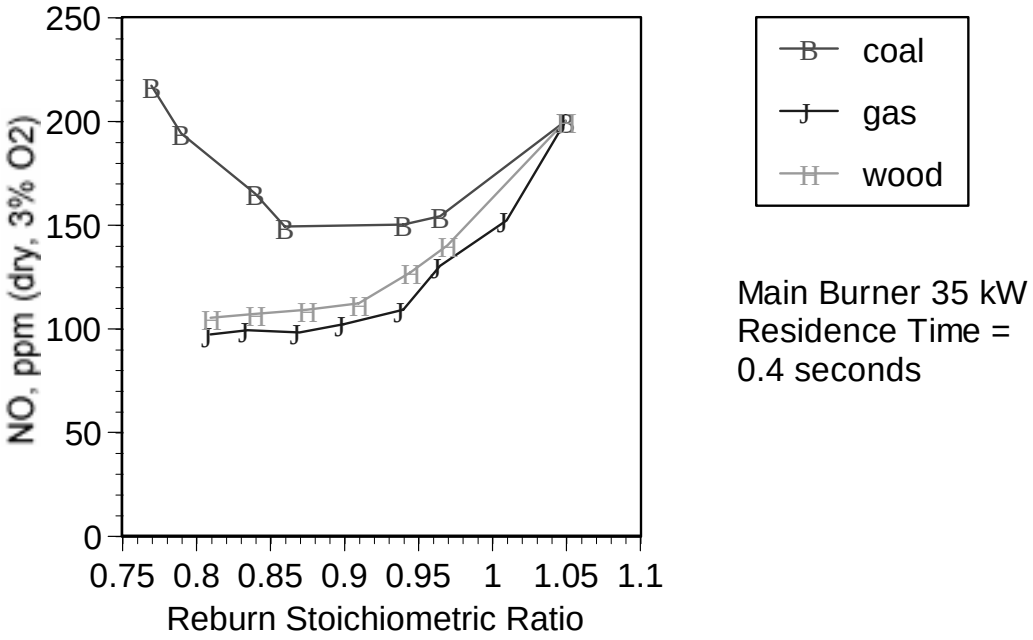

Figure 5.7 NO reduction with coal, gas, and wood as reburning fuels at initial NO concentration of 200 ppm.

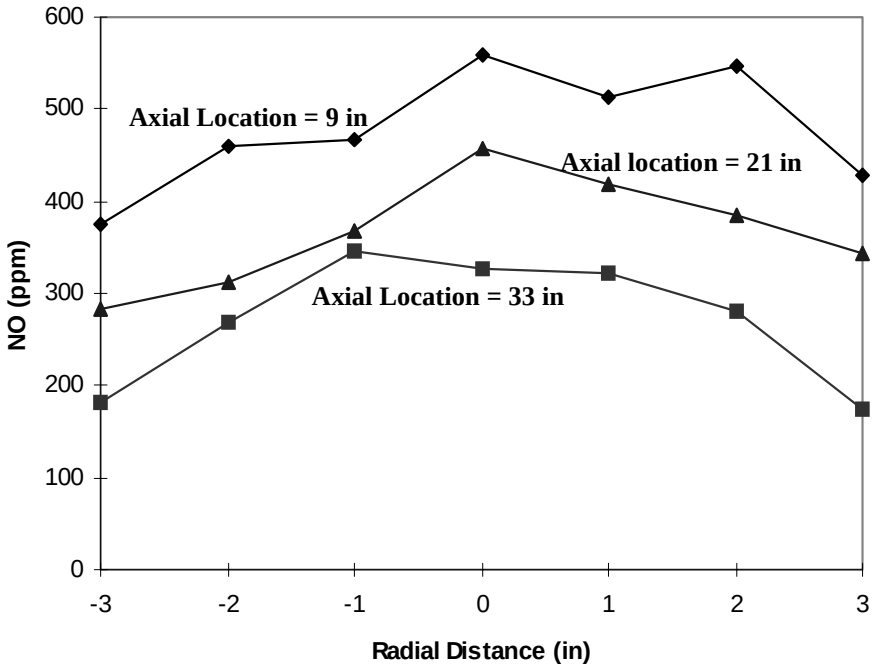

Figure 5.8 NO concentration at 3 axial locations in the large coal reburning jet as measured by the Fourier Transform Infrared (FTIR) instrument.

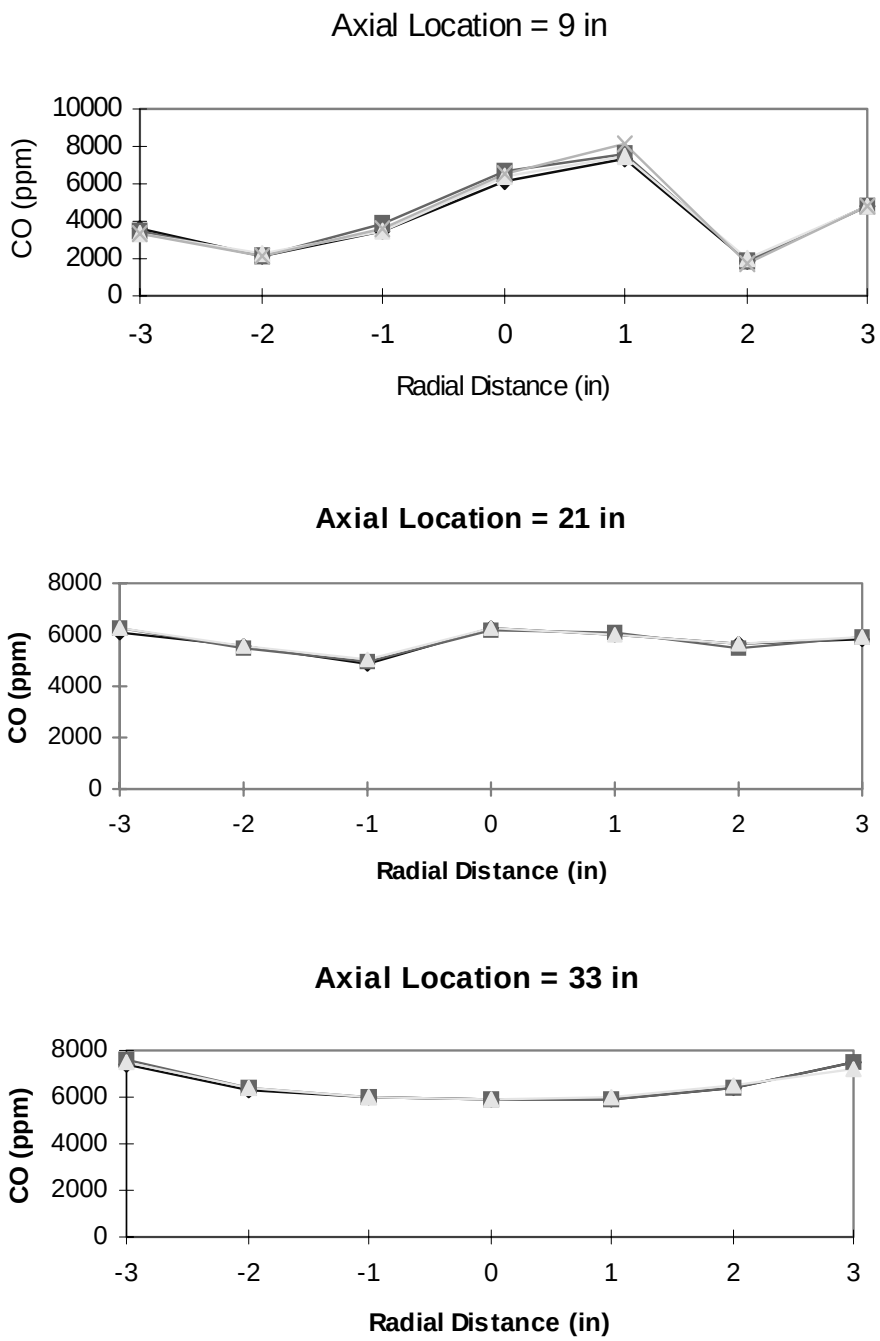

Figure 5.9 CO concentration at 3 axial locations in the large coal reburning jet as measured by the Fuorier Transform Infrared (FTIR) instrument.

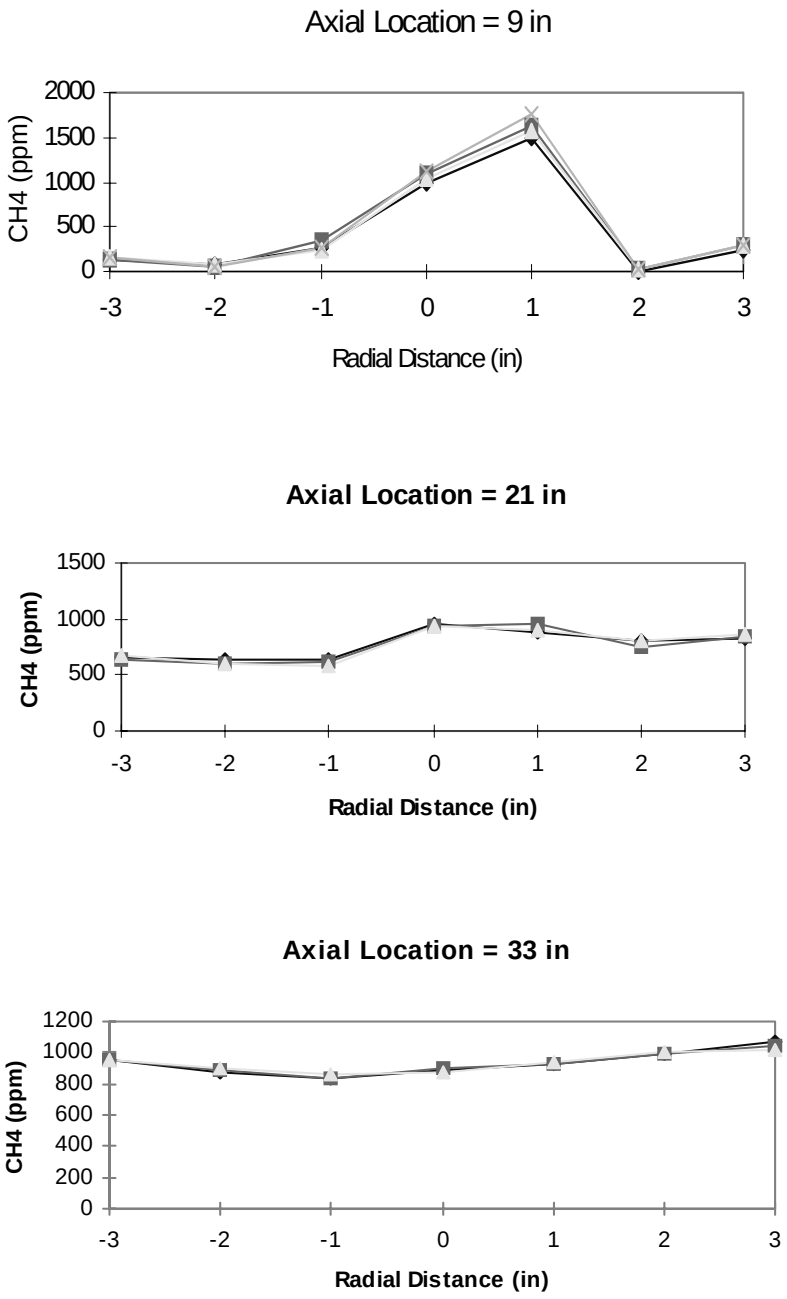

Figure 5.10 CH_4 concentration at 3 axial locations in the large coal reburning jet as measured by the Fuorier Transform Infrared (FTIR) instrument.

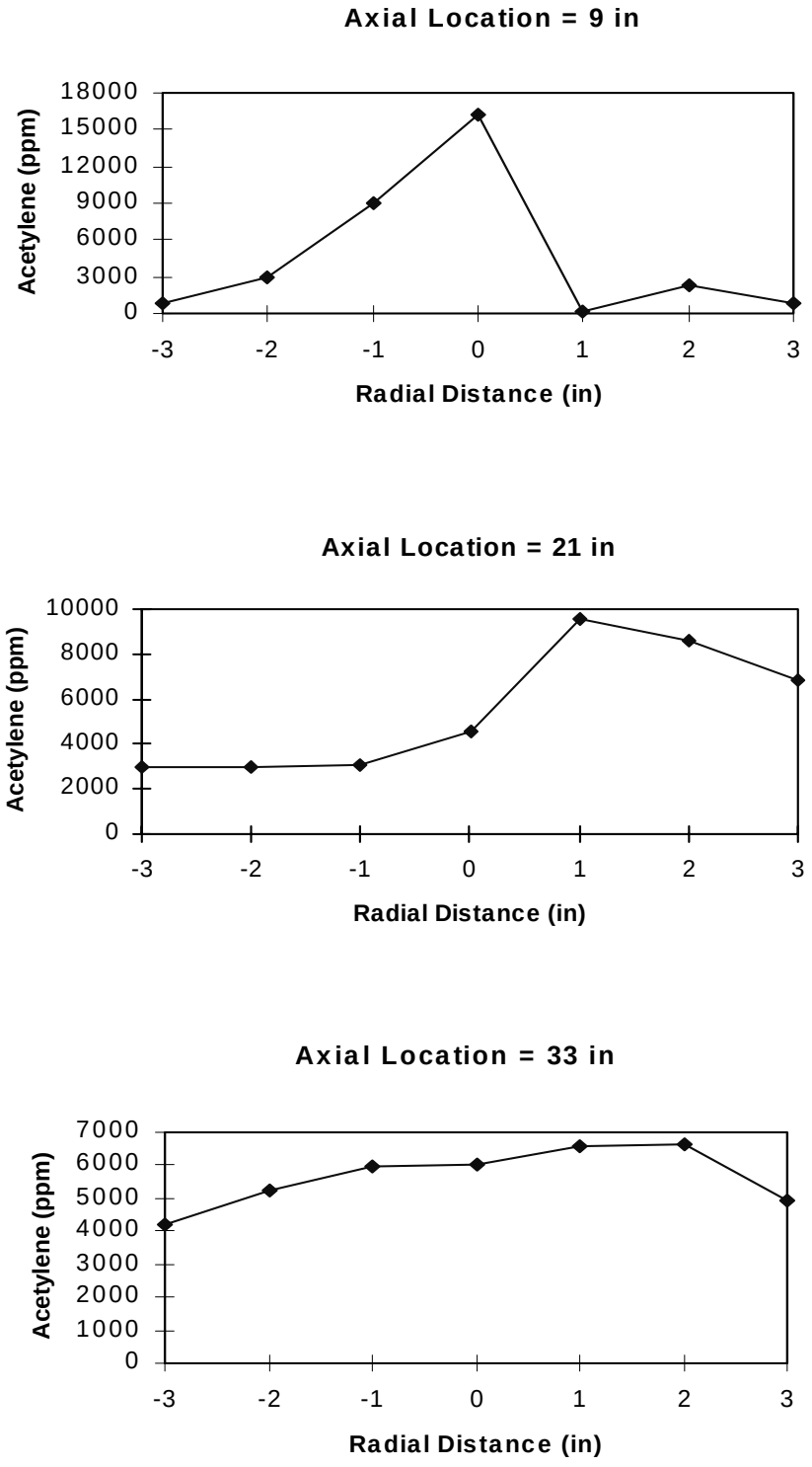

Figure 5.11 Acetylene concentration at 3 axial locations in the large coal reburning jet as measured by the Fuorier Transform Infrared (FTIR) instrument.

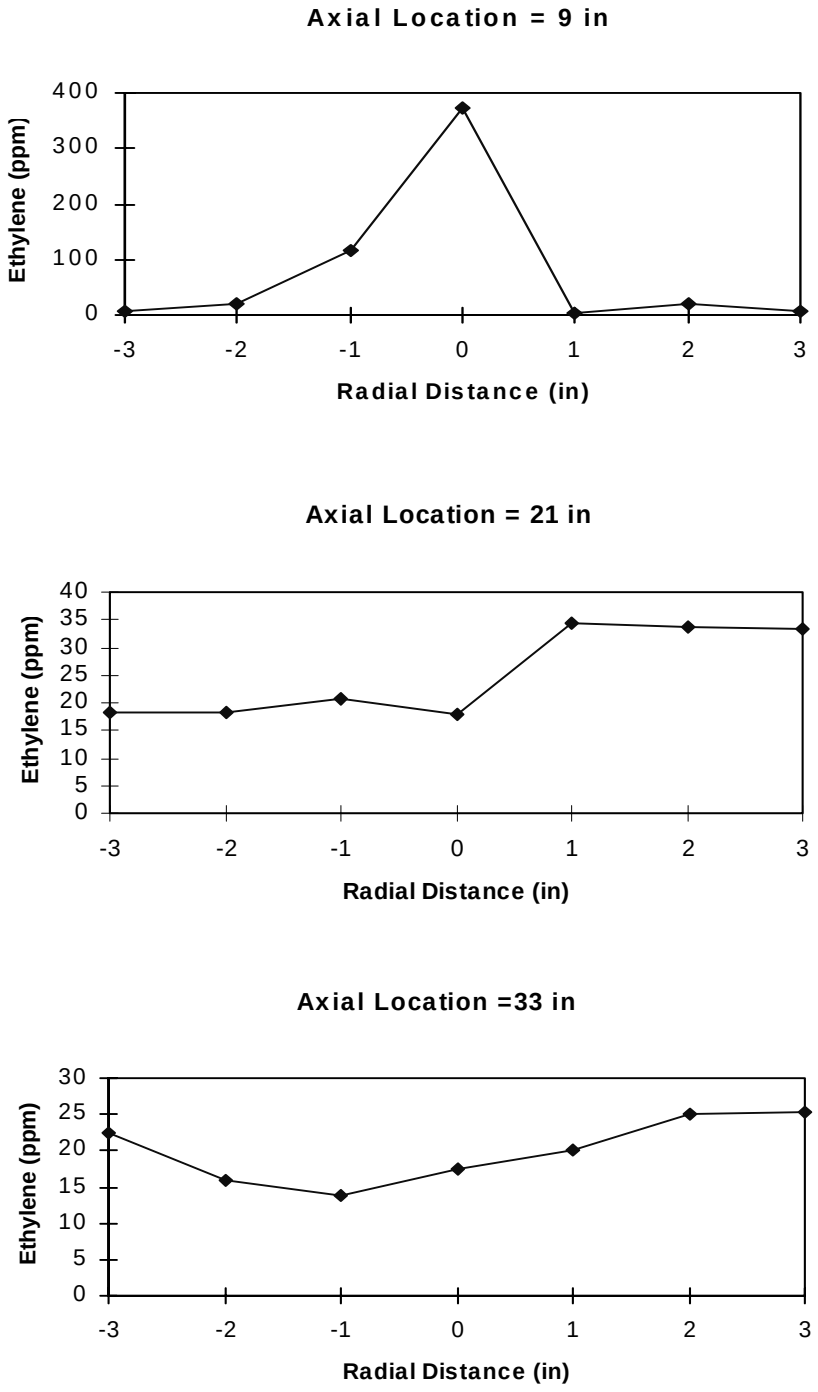

Figure 5.12 Ethylene concentration at 3 axial locations in the large coal reburning jet as measured by the Fuorier Transform Infrared (FTIR) instrument.

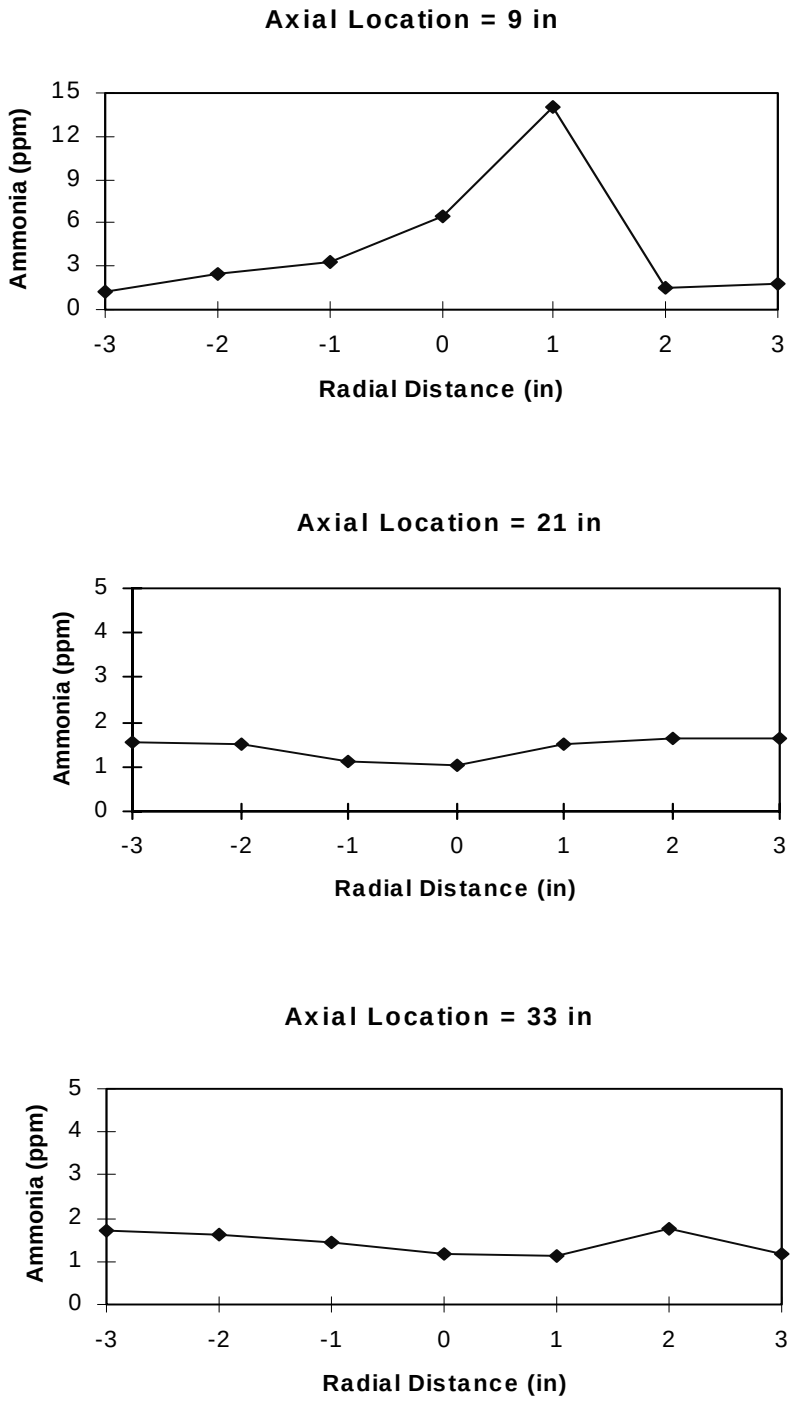

Figure 5.13 Ammonia concentration at 3 axial locations in the large coal reburning jet as measured by the Fuorier Transform Infrared (FTIR) instrument.

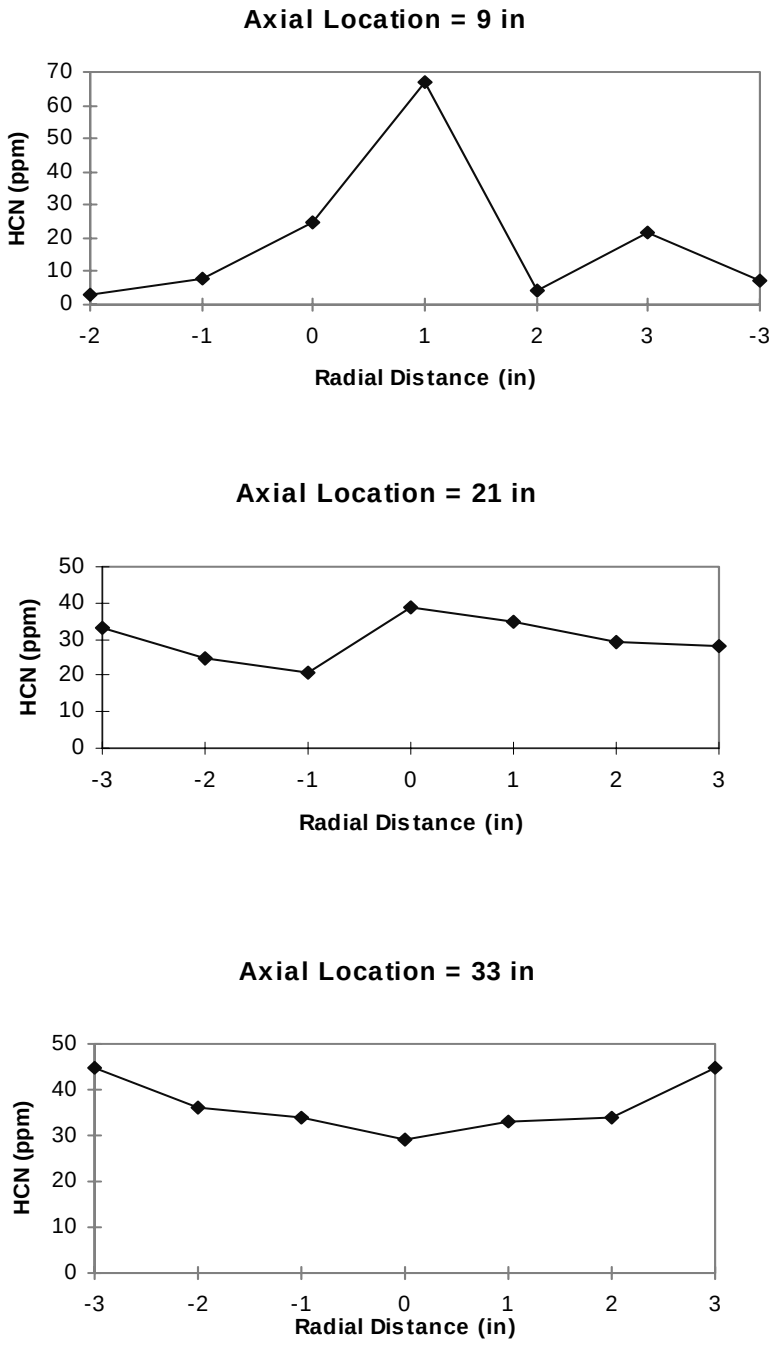

Figure 5.14 HCN concentration at 3 axial locations in the large coal reburning jet as measured by the Fuorier Transform Infrared (FTIR) instrument.

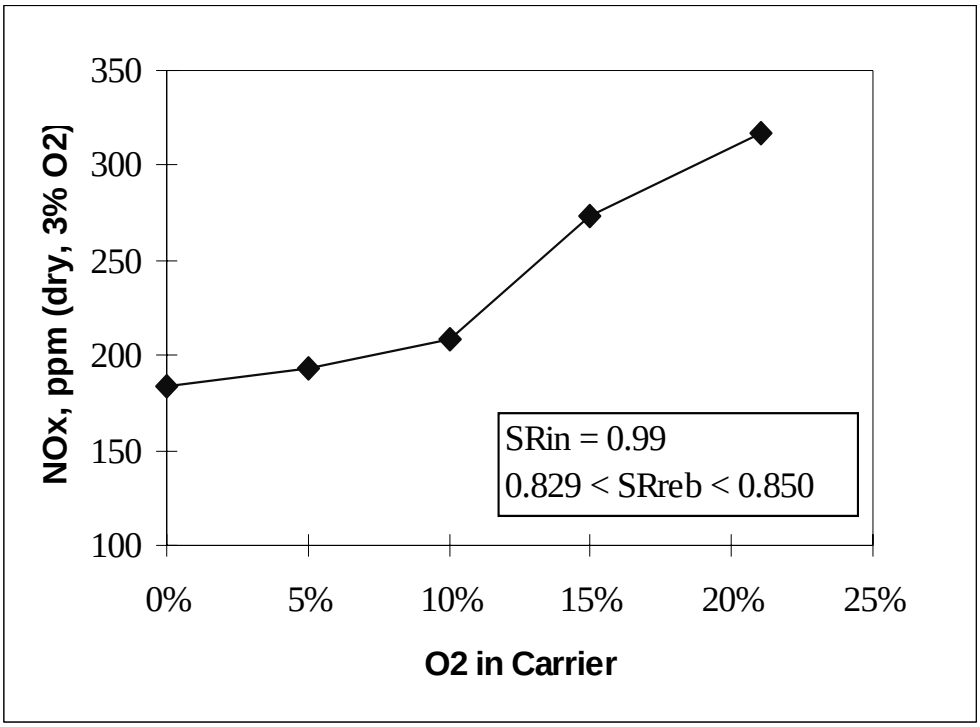

Figure 5.15 NO emissions as a function of oxygen concentration with wood as the reburning fuel.

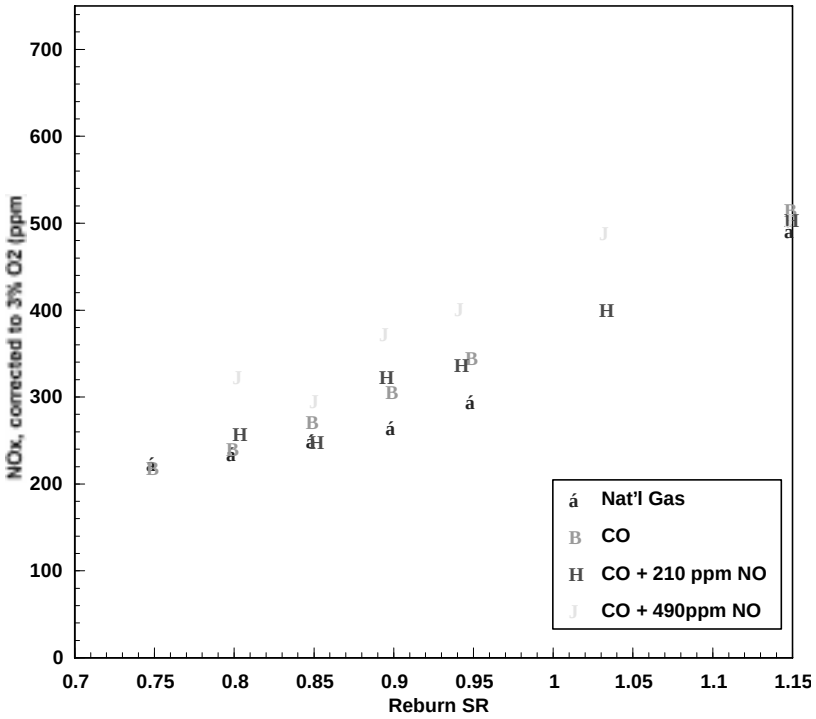

Figure 5.16 NO emissions as a function of reburning stoichiometry for four different reburn fuels.

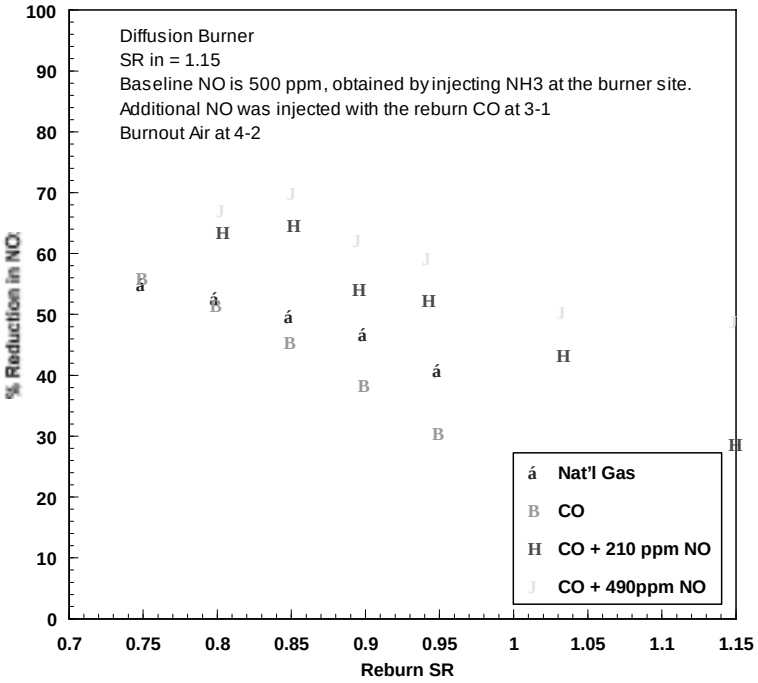

Figure 5.17 NO reduction as a function of reburning stoichiometry for four different reburn fuels.

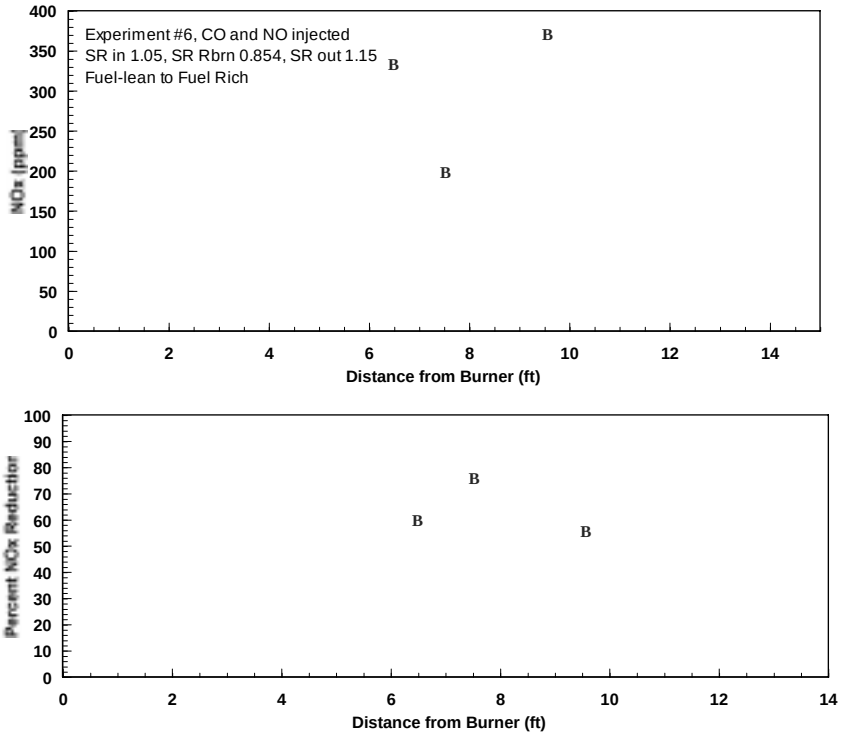

Figure 5.18 NO reduction as a function of injection location for the CO+NO mixture.

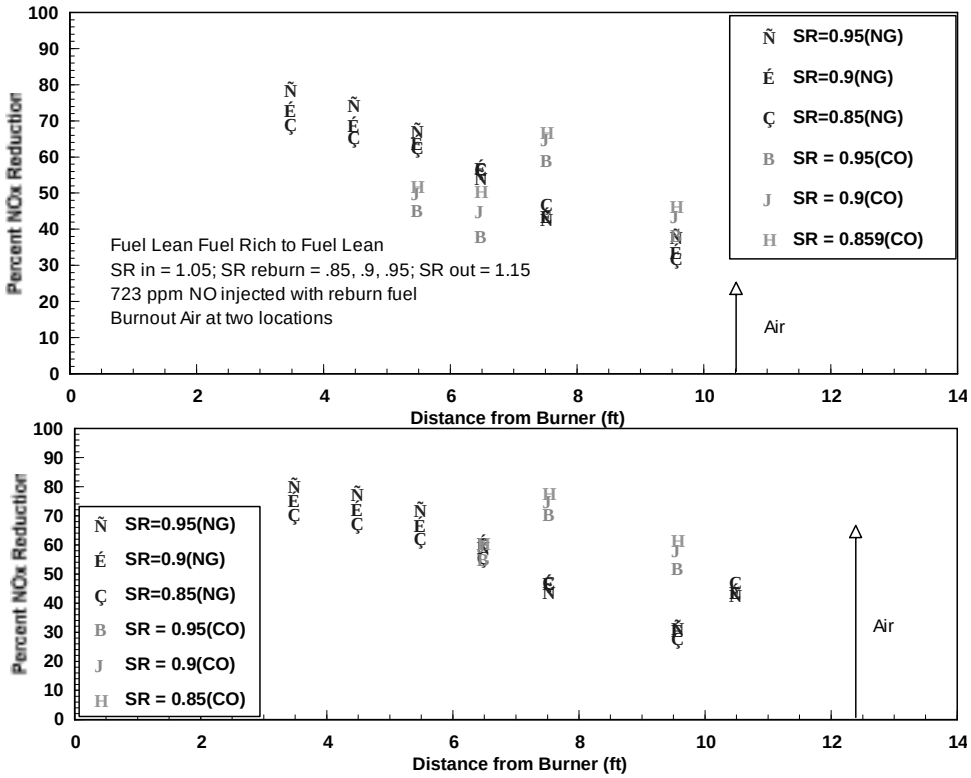

Figure 5.19 NO reduction comparing natural gas and CO as reburning fuels.

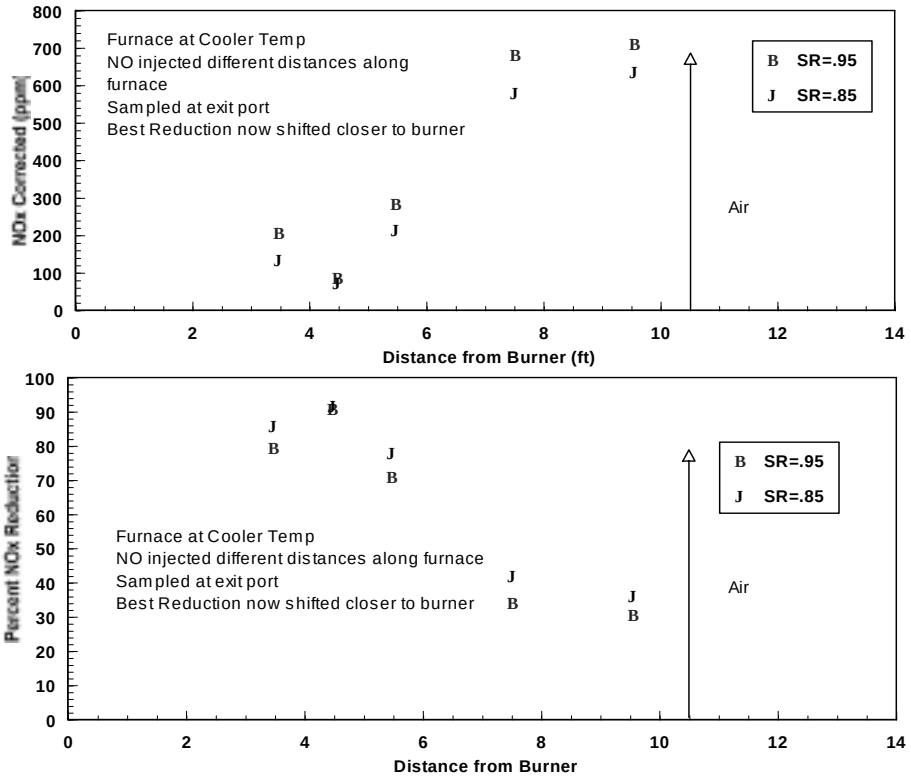

Figure 5.20 NO reduction as a function of injection location.

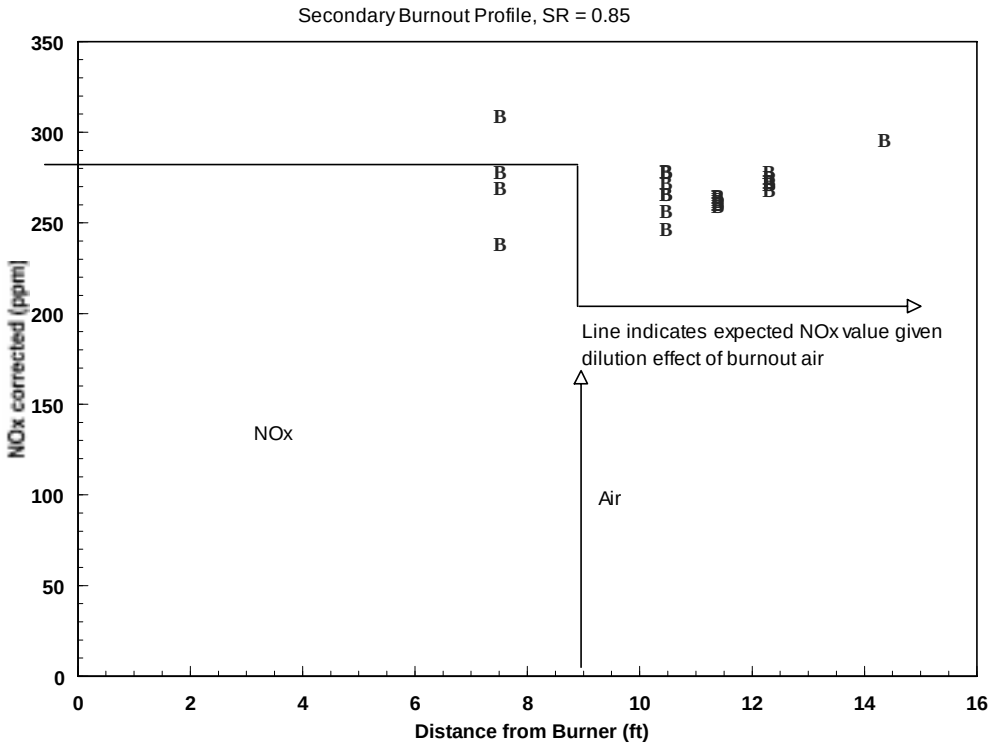

Figure 5.21 NO emissions as a function of injection location.

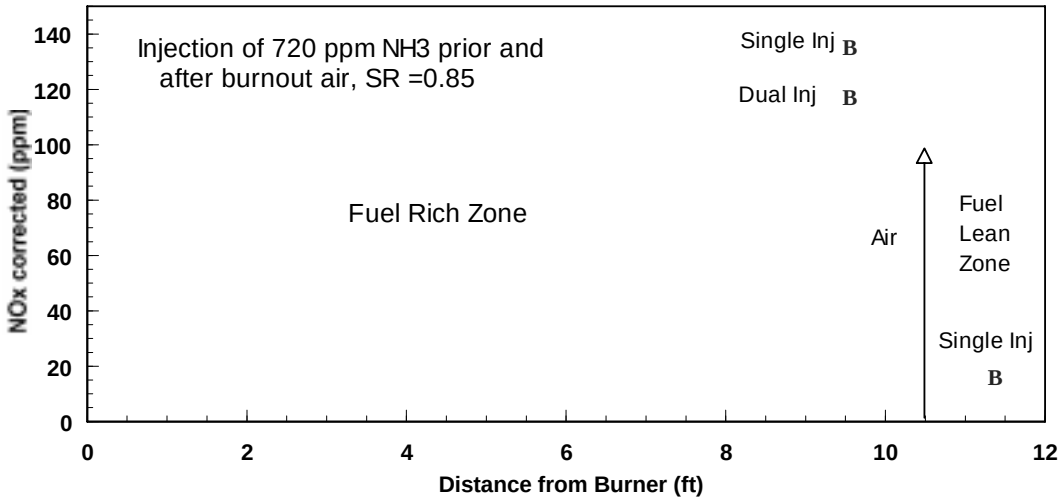

Figure 5.22 Effect of ammonia injection in the burnout region.

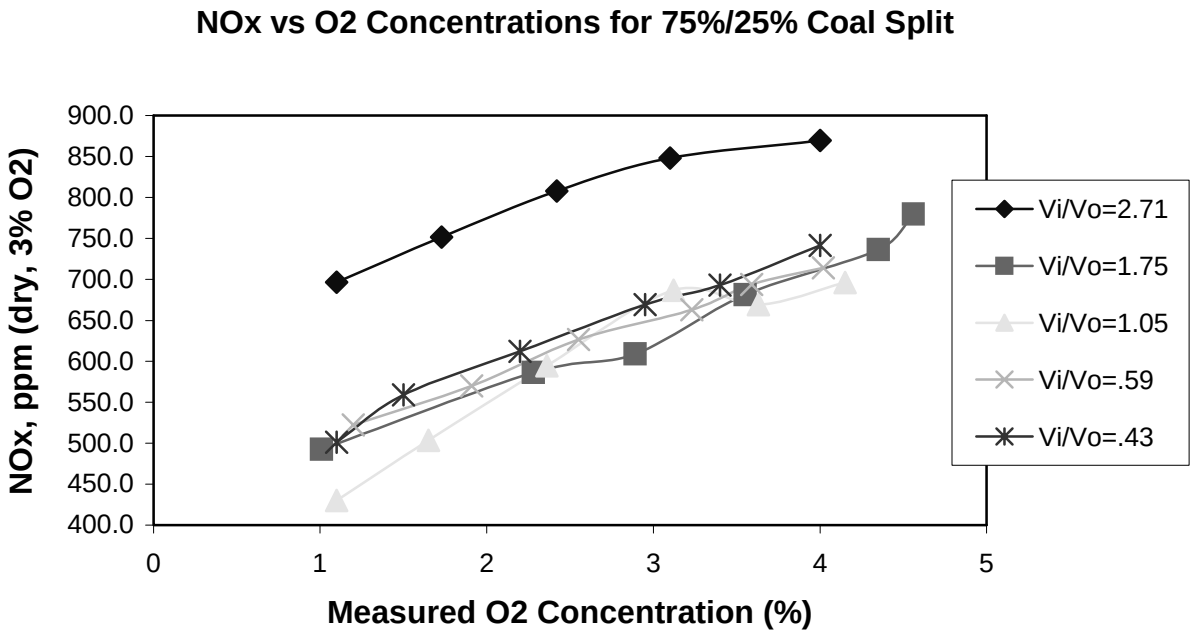

Figure 5.23 Effect of velocity ratio on NO_x emissions versus excess air levels for the 75/25 coal split (coal concentrated in middle chamber).

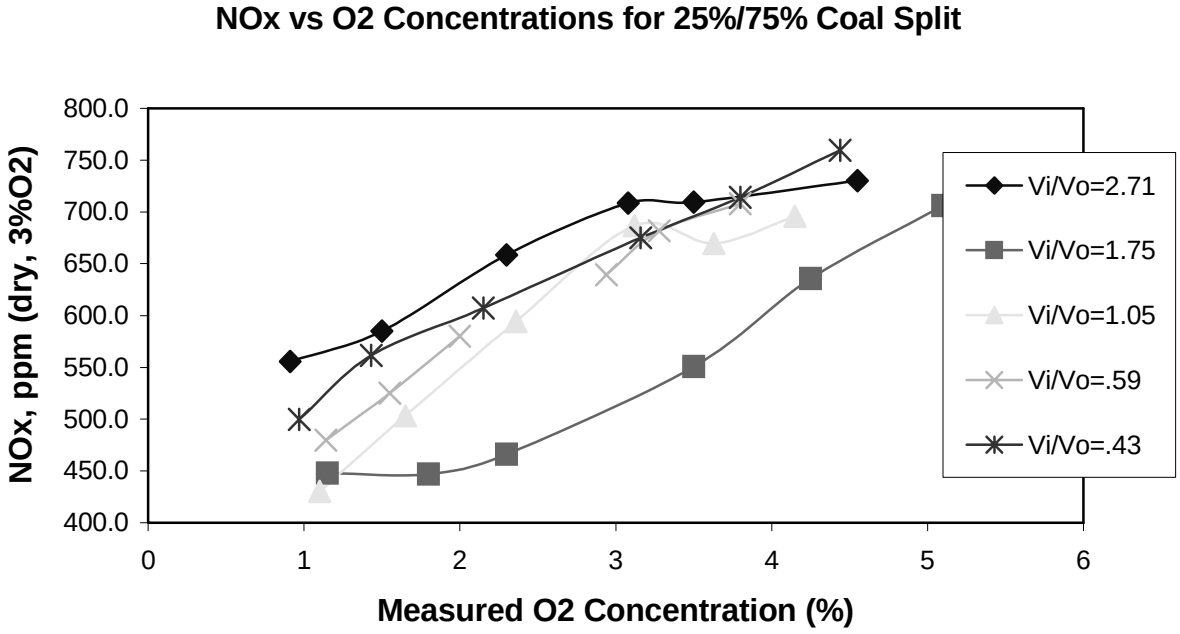

Figure 5.24 Effect of velocity ratio on NO_x emissions versus excess air levels for the 25/75 coal split (coal concentrated in annular chamber).

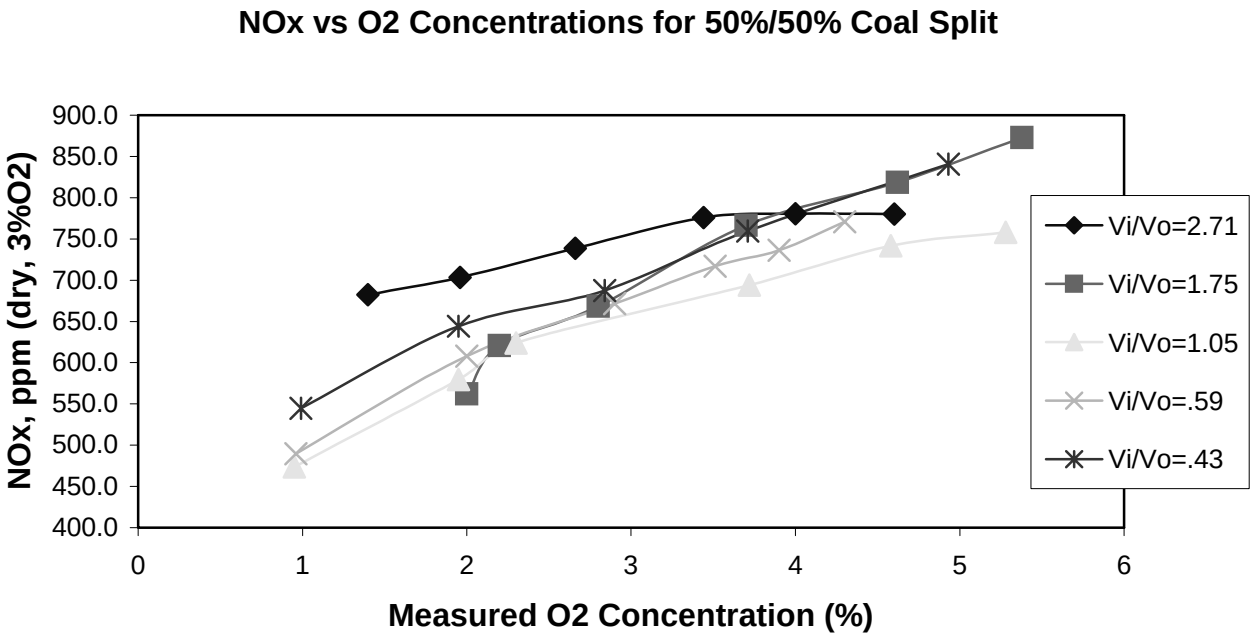

Figure 5.25 Effect of velocity ratio on NO_x emissions versus excess air levels for the 50/50 coal split (coal fed equally to both chambers).

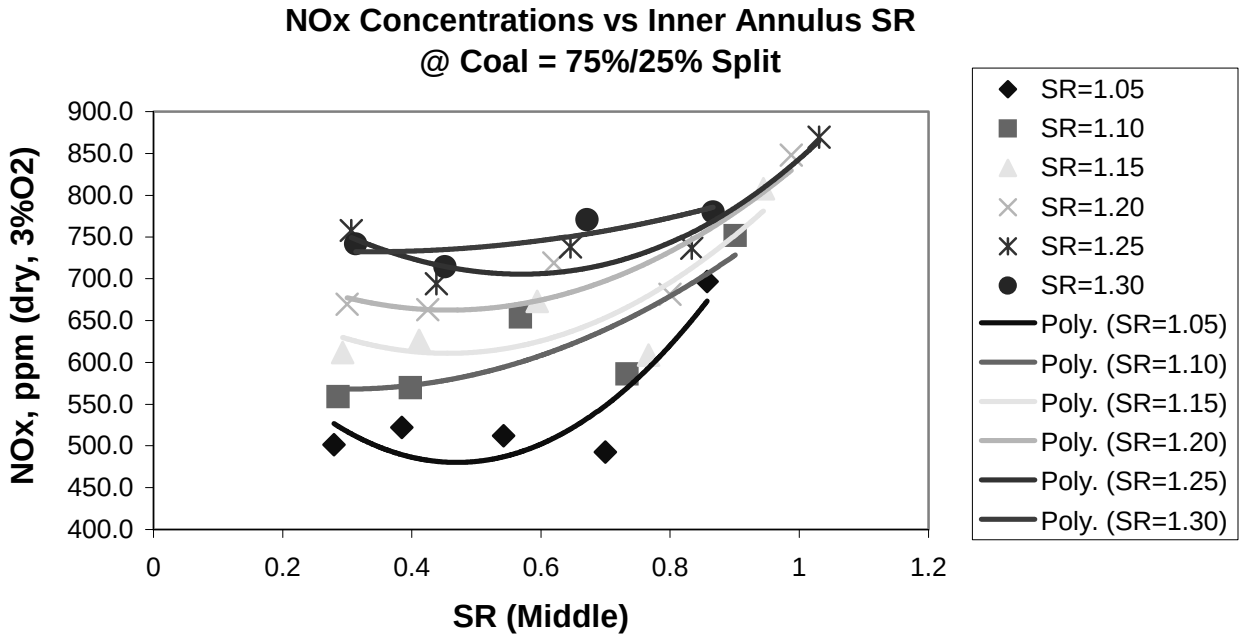

Figure 5.26 NO_x concentration as a function of inner annulus stoichiometric ratios (Coal split is 75/25).

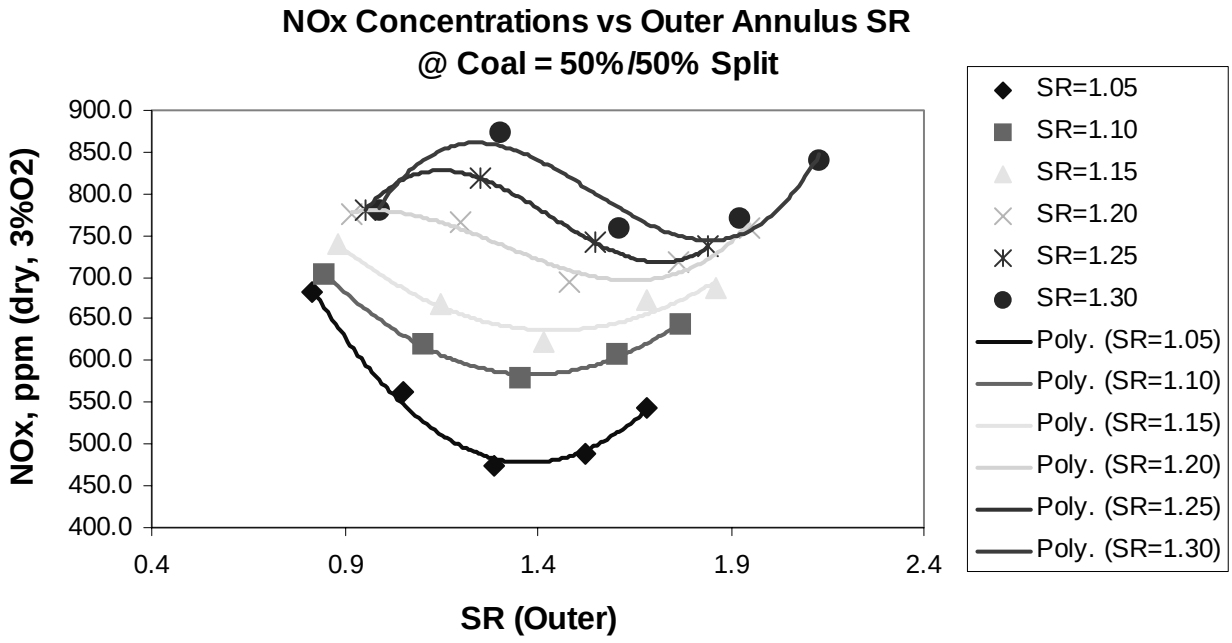

Figure 5.27 NO_x concentration as a function of outer annulus stoichiometric ratios (Coal split is 50/50).

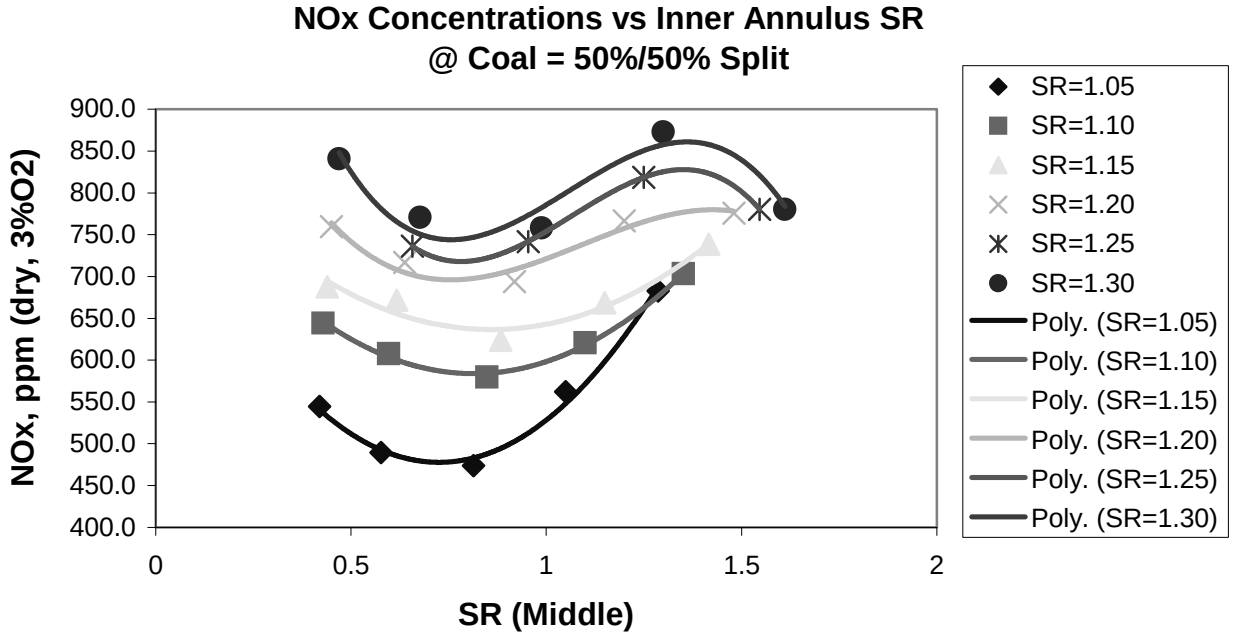

Figure 5.28 NO_x concentration as a function of inner annulus stoichiometric ratios (Coal split is 50/50).

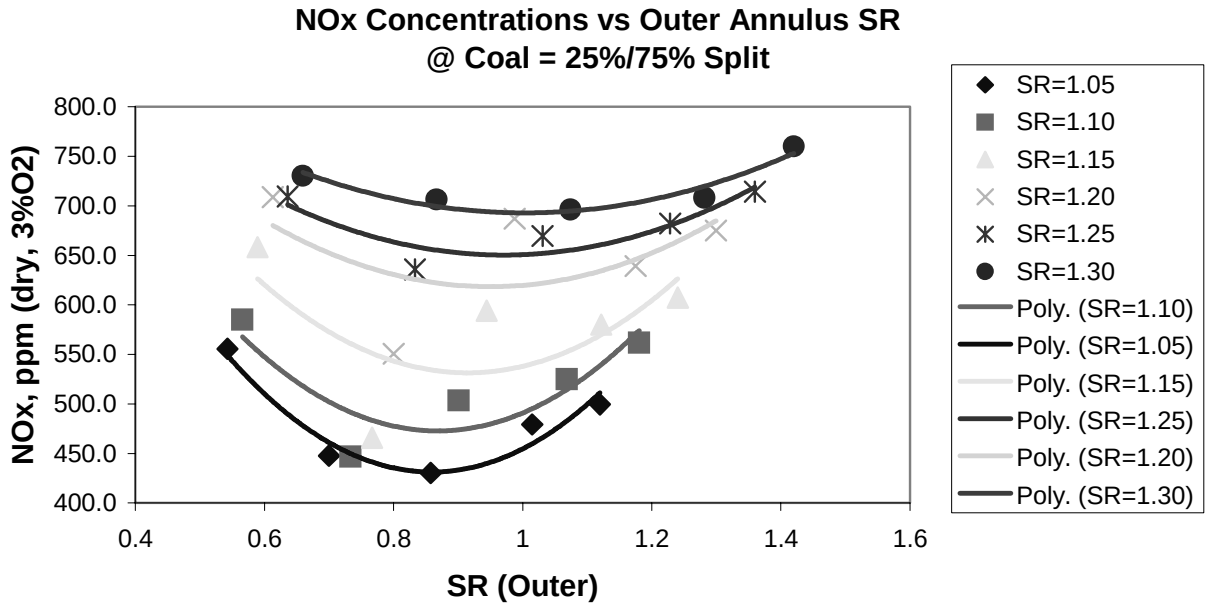

Figure 5.29 NO_x concentration as a function of outer annulus stoichiometric ratios (Coal split is 25/75).

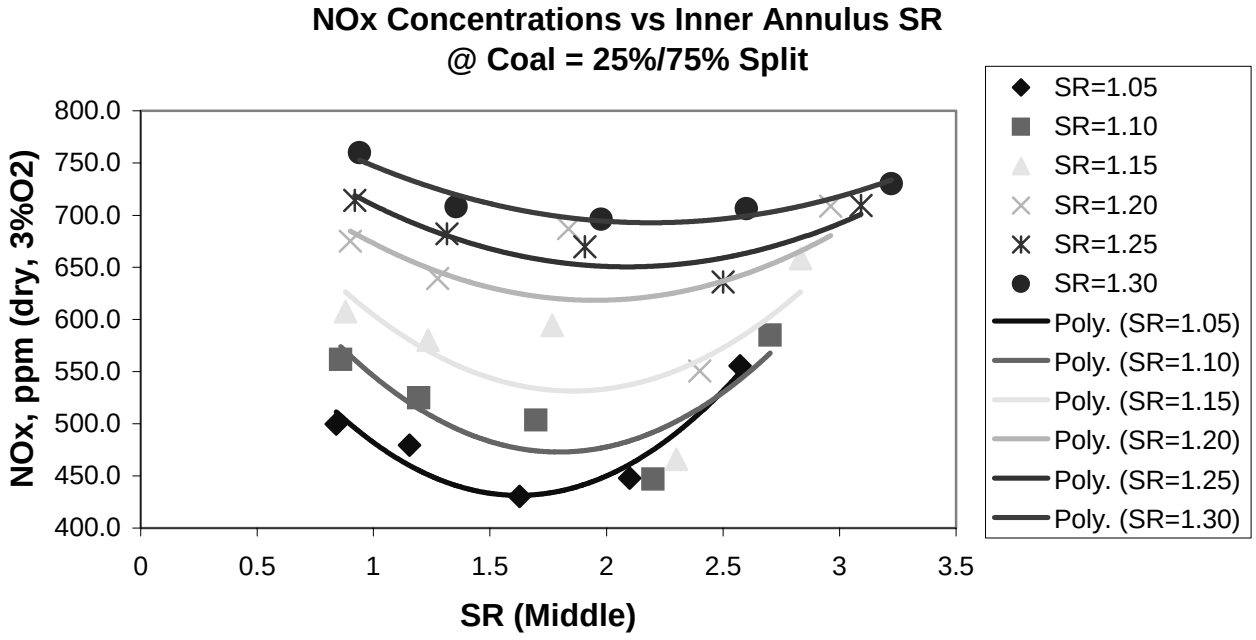

Figure 5.30 NO_x concentration as a function of inner annulus stoichiometric ratios (Coal split is 25/75).

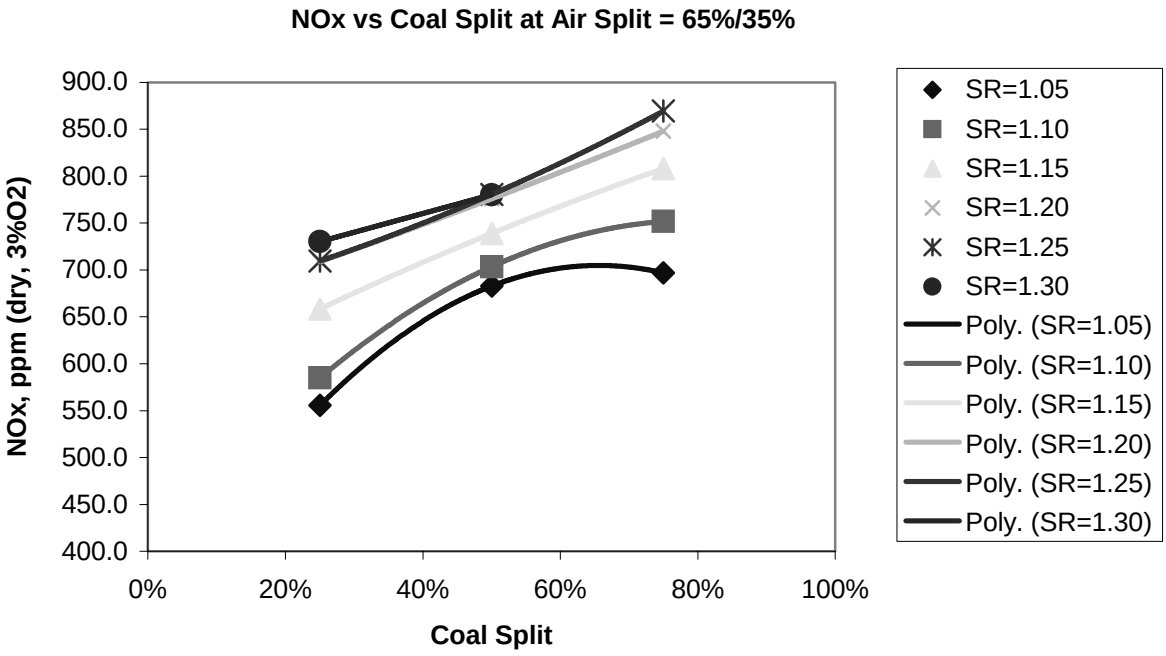

Figure 5.31 NO_x concentration as a function of coal split (Air split is 65/35).

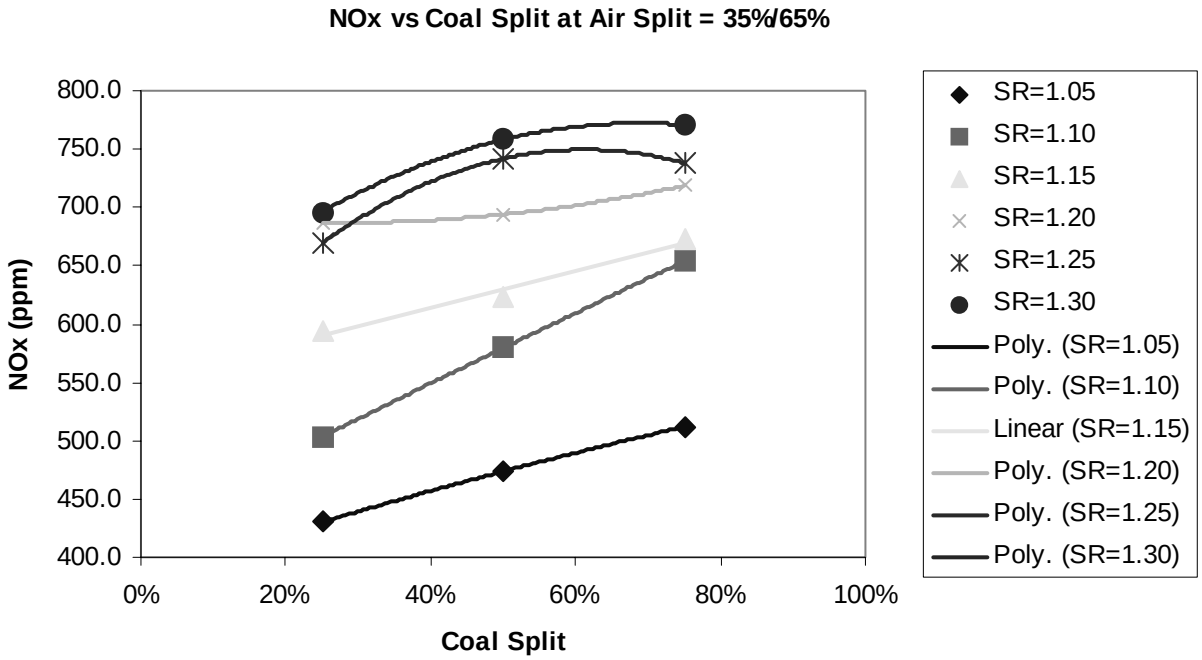

Figure 5.32 NO_x concentration as a function of coal split (Air split is 35/65).

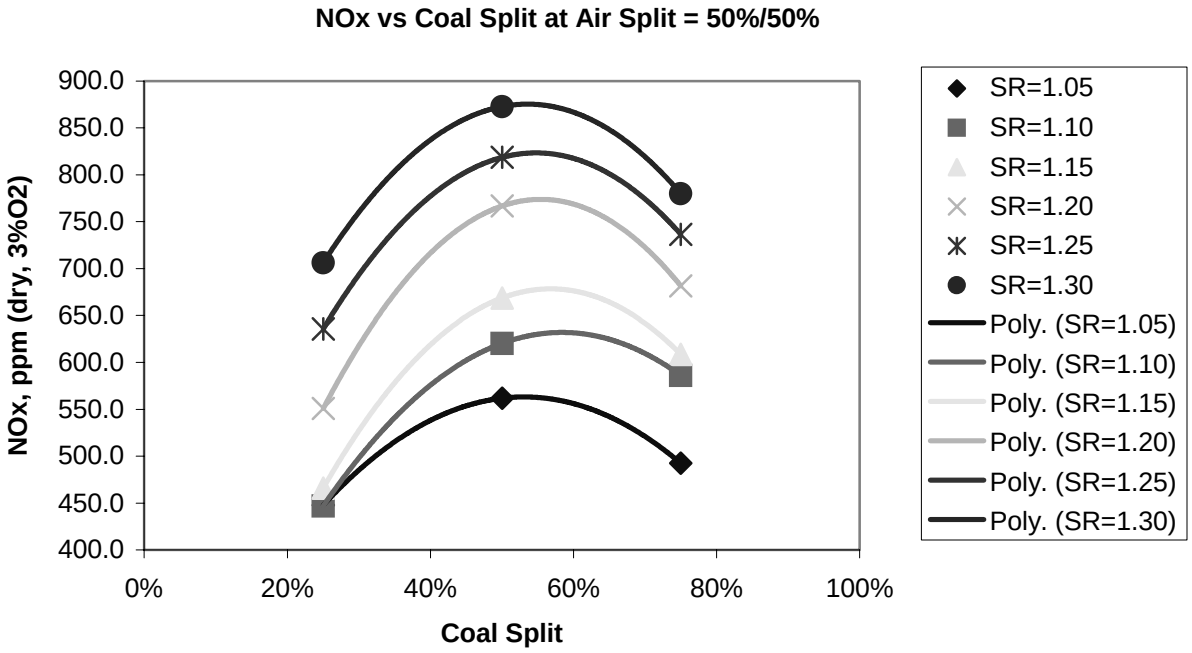

Figure 5.33 NO_x concentration as a function of coal split (Air split is 50/50).

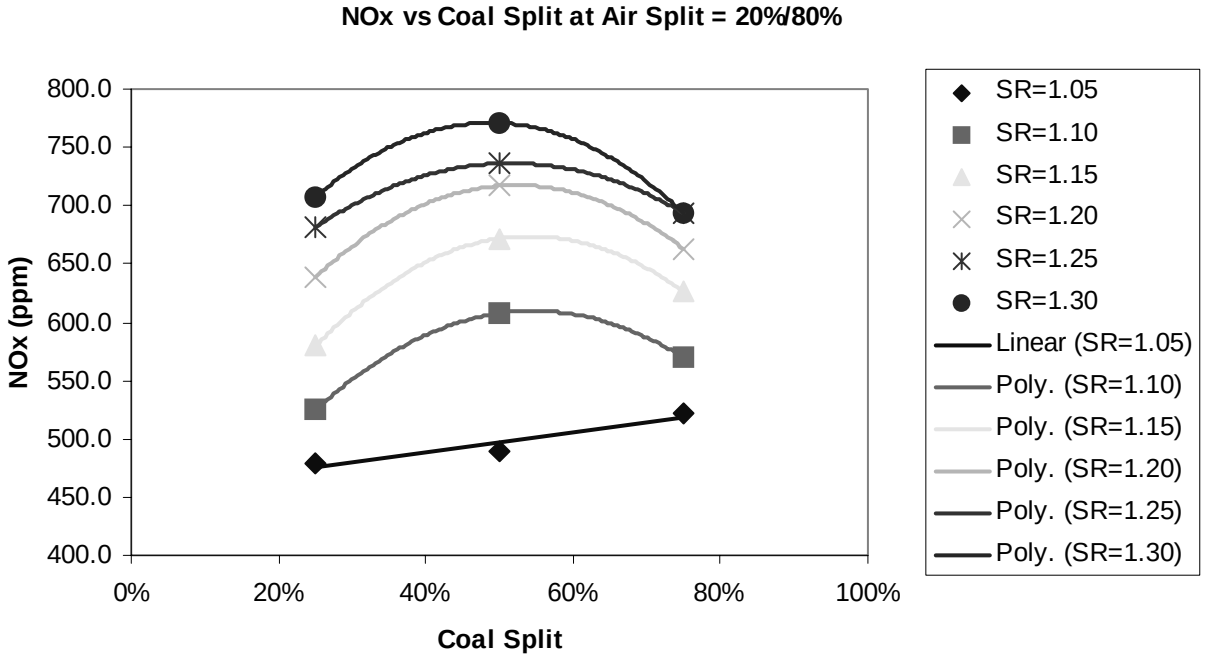

Figure 5.34 NO_x concentration as a function of coal split (Air split is 20/80).

Figure 5.36 Schematic representation of each of the coal injection nozzles tested.

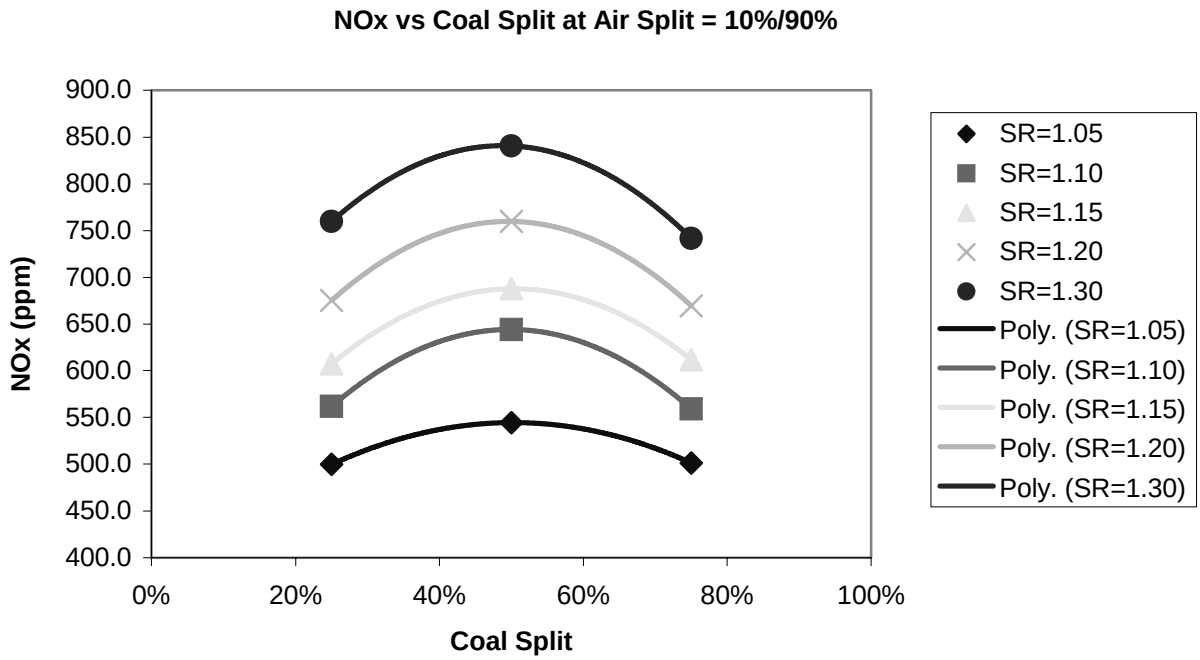

Figure 5.35 NO_x concentration as a function of coal split (Air split is 10/90).

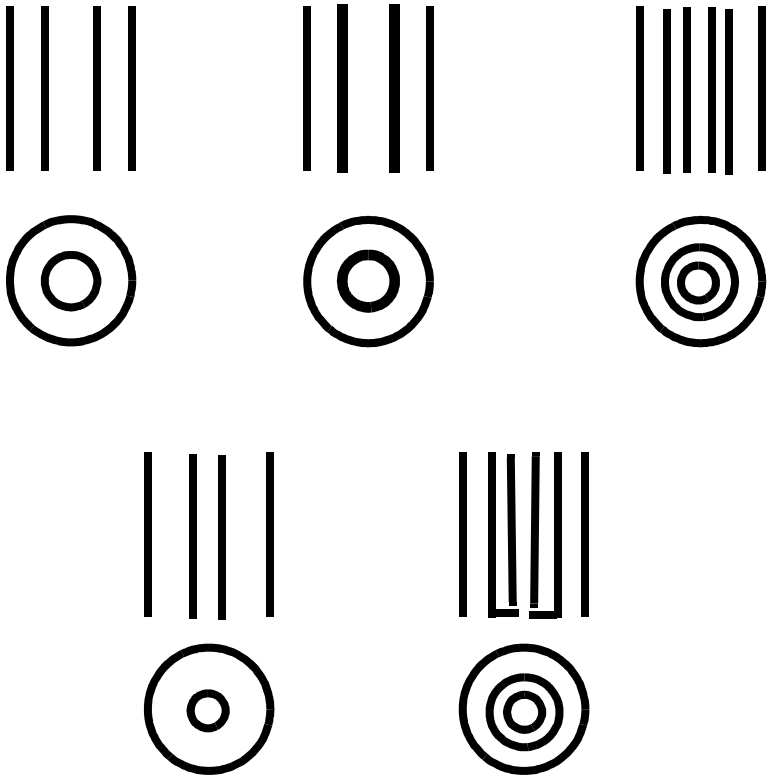

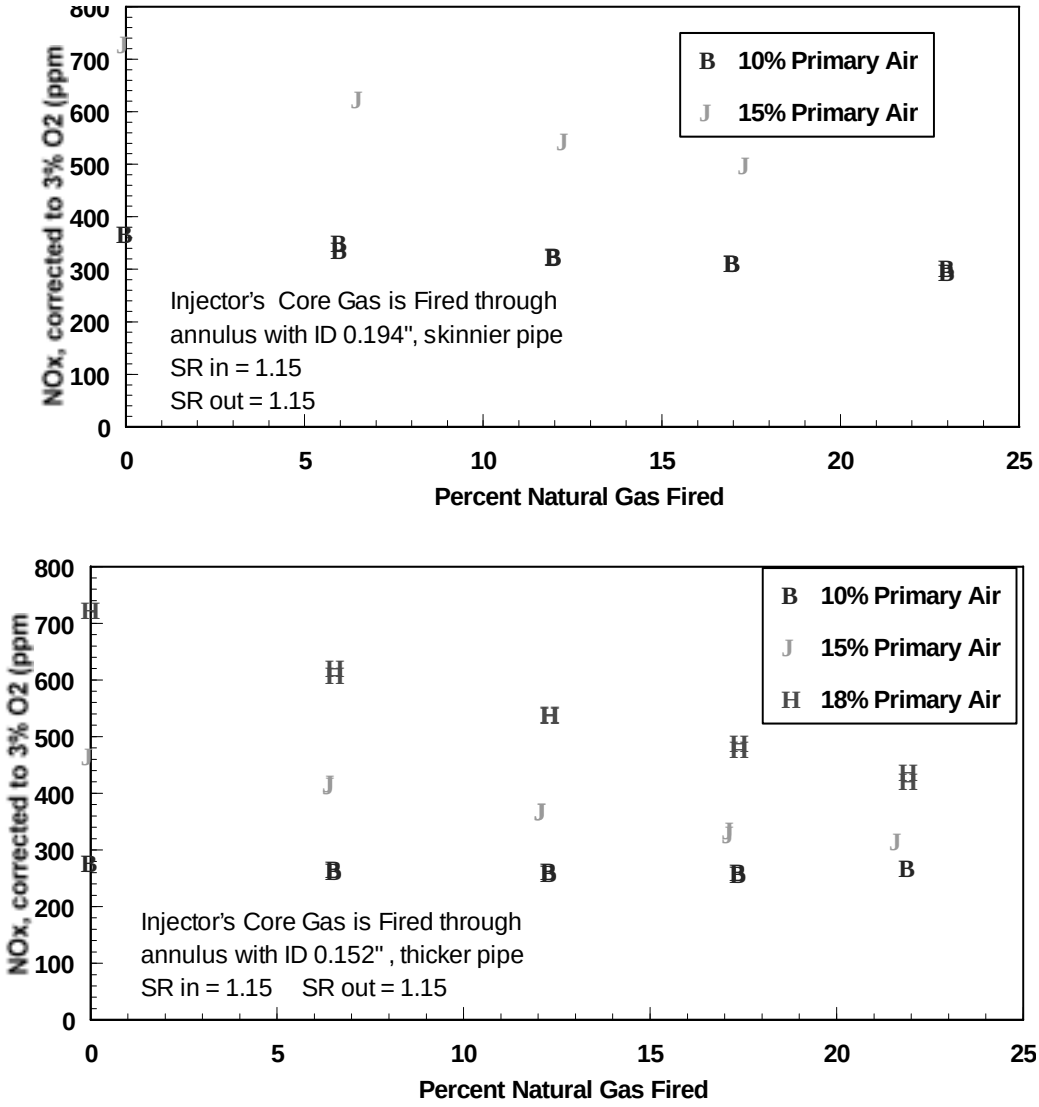

Figure 5.37 NO emissions at various primary air amounts.

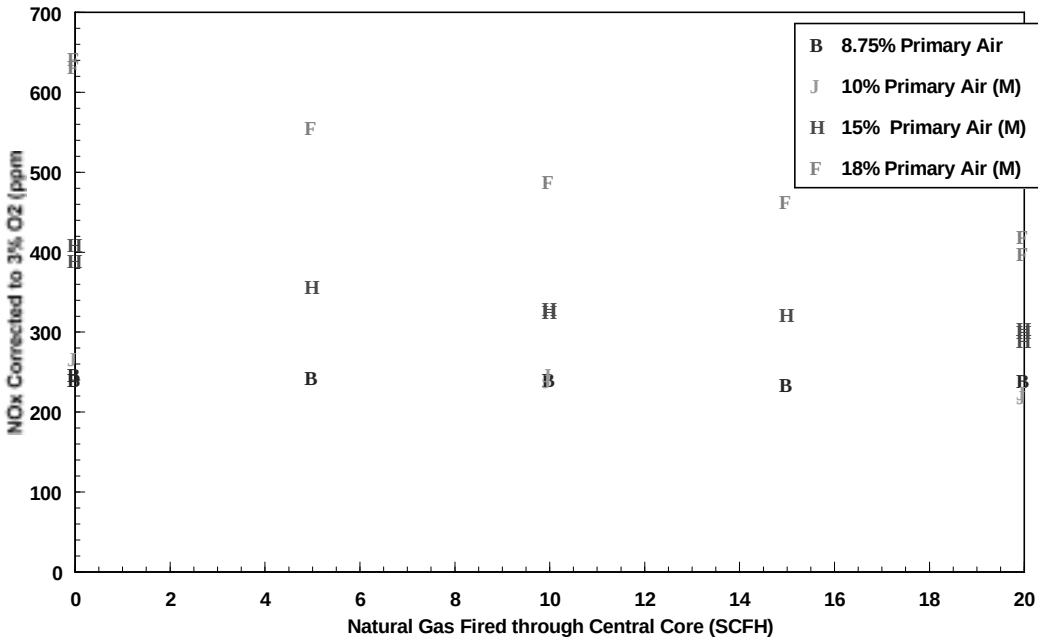

Figure 5.38 NO emissions as a function of natural gas firing.

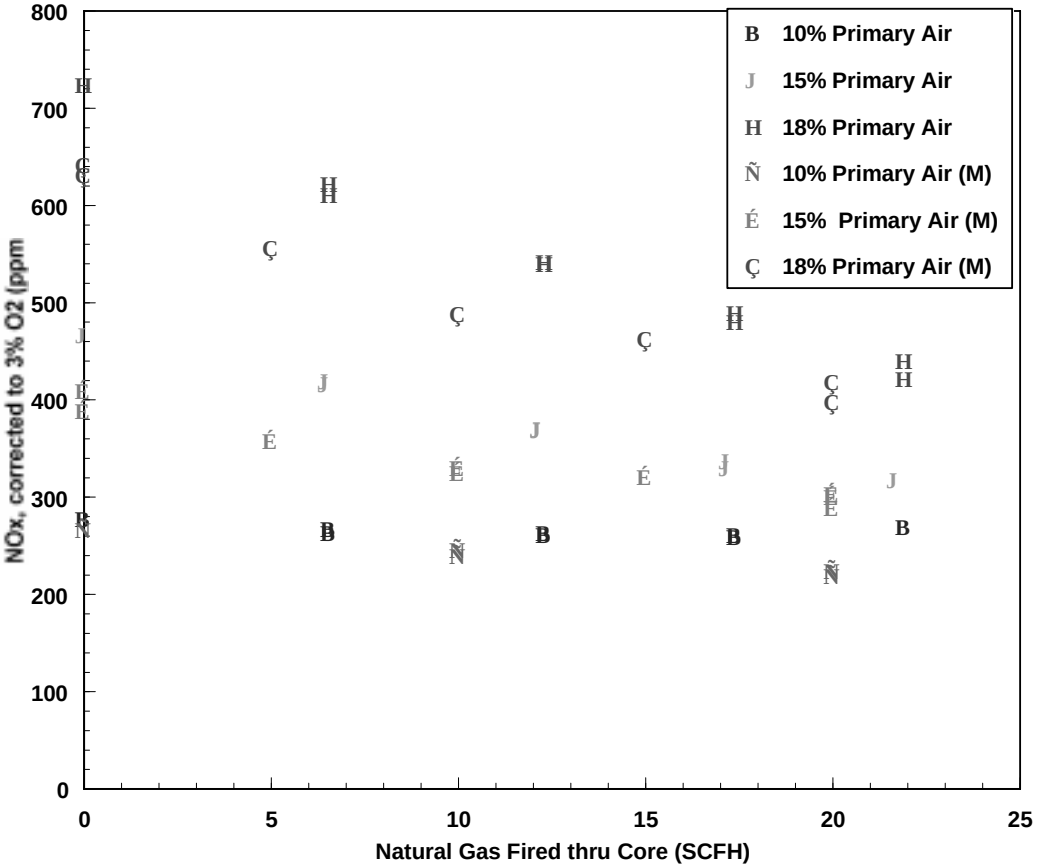

Figure 5.39 NO emissions as a function of natural gas firing through burner core.

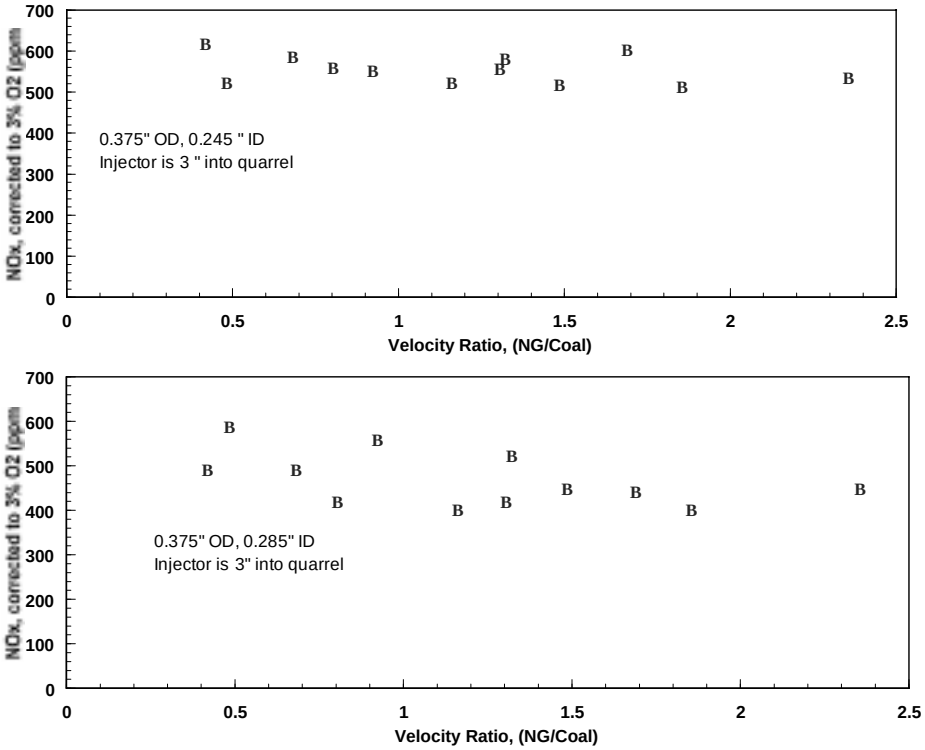

Figure 5.40 NO emissions as a function of natural gas-to-coal velocity ratio.

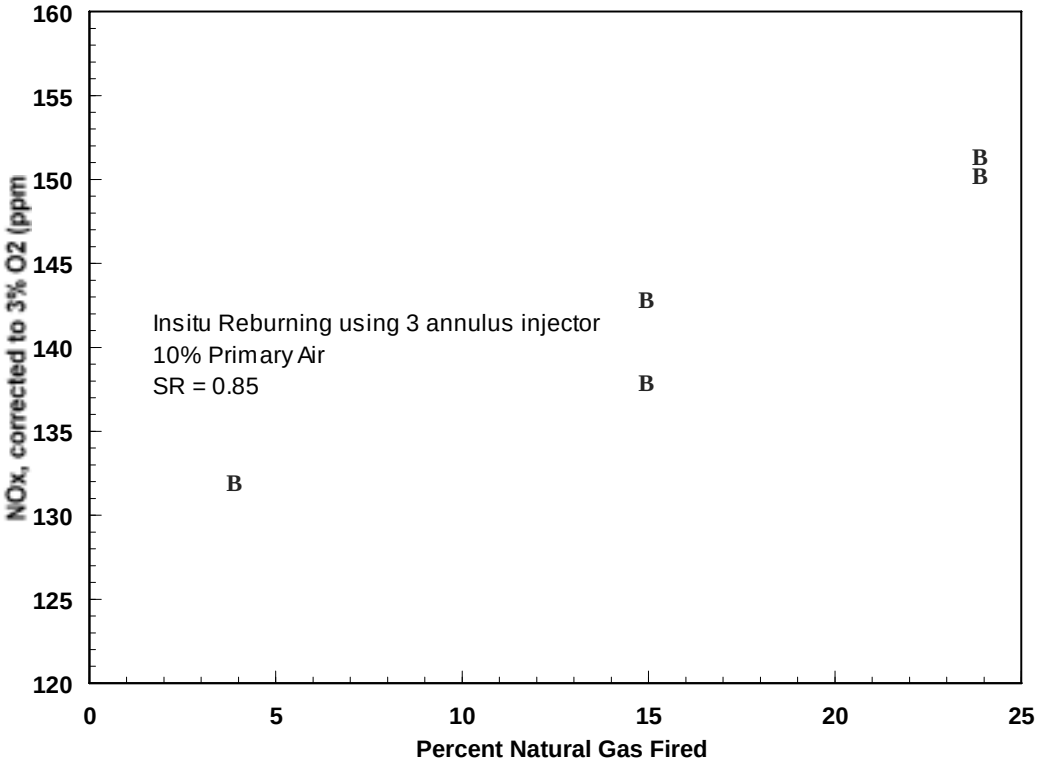

Figure 5.41 NO emissions as a function of natural gas firing.

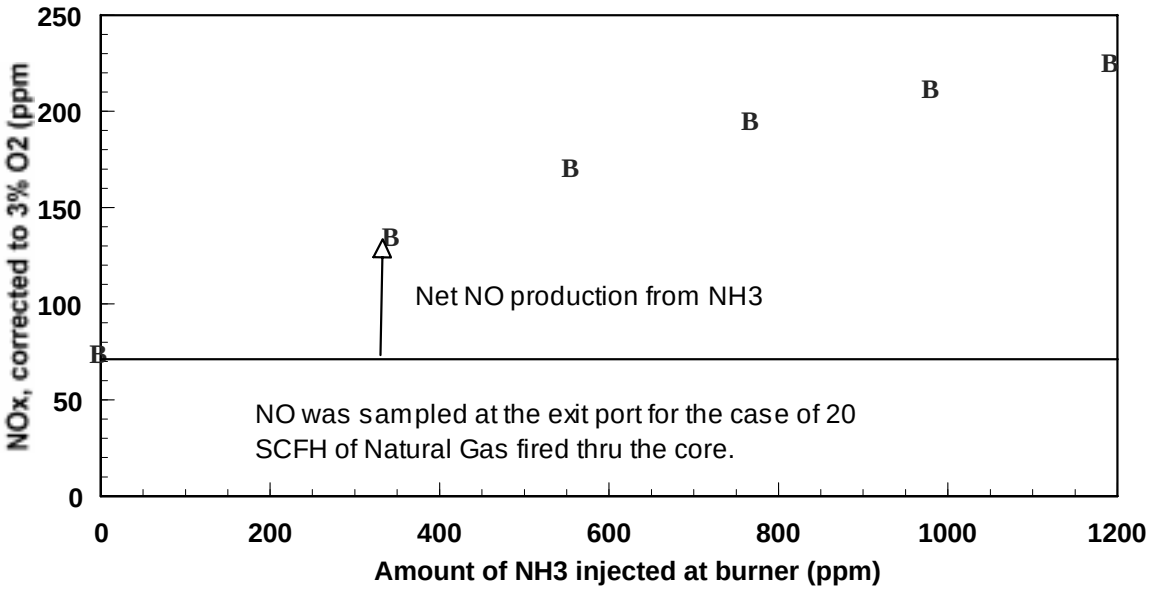

Figure 5.42 NO_x concentration as a function of ammonia injection.

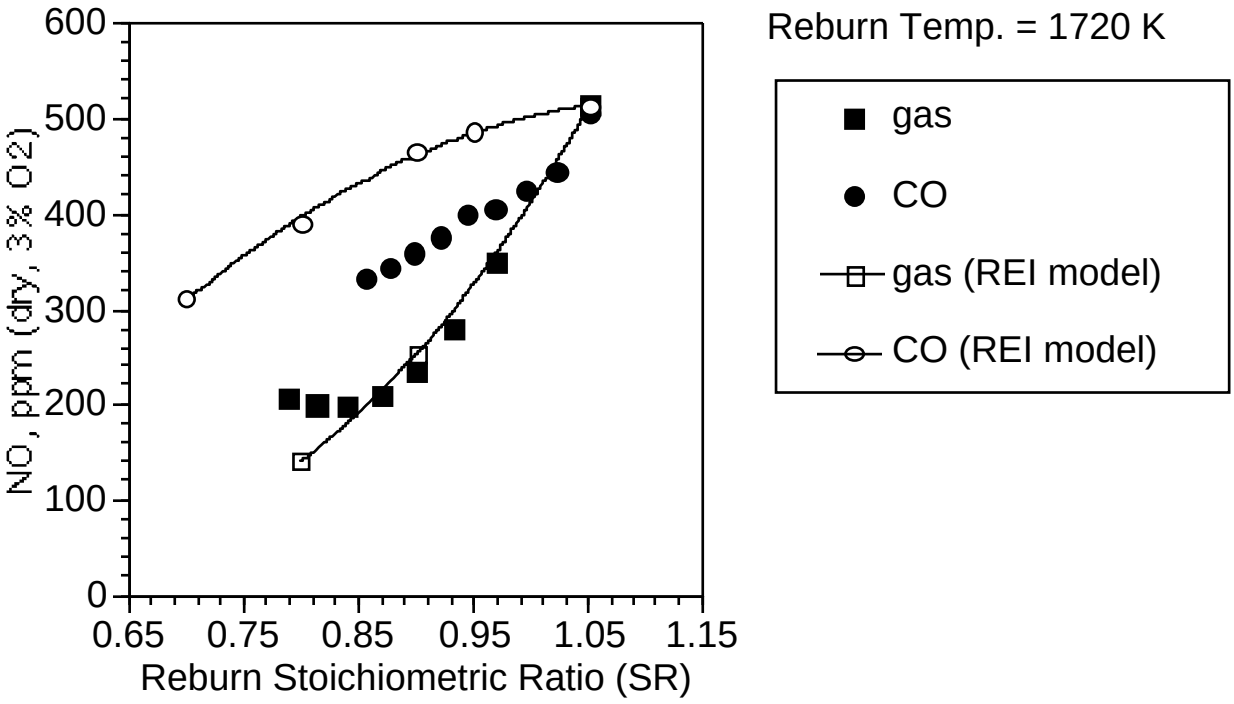

Figure 5.43 NO reduction during reburning with two fuels at 1720 K over a range of stoichiometries (corrected to 3% O_2).

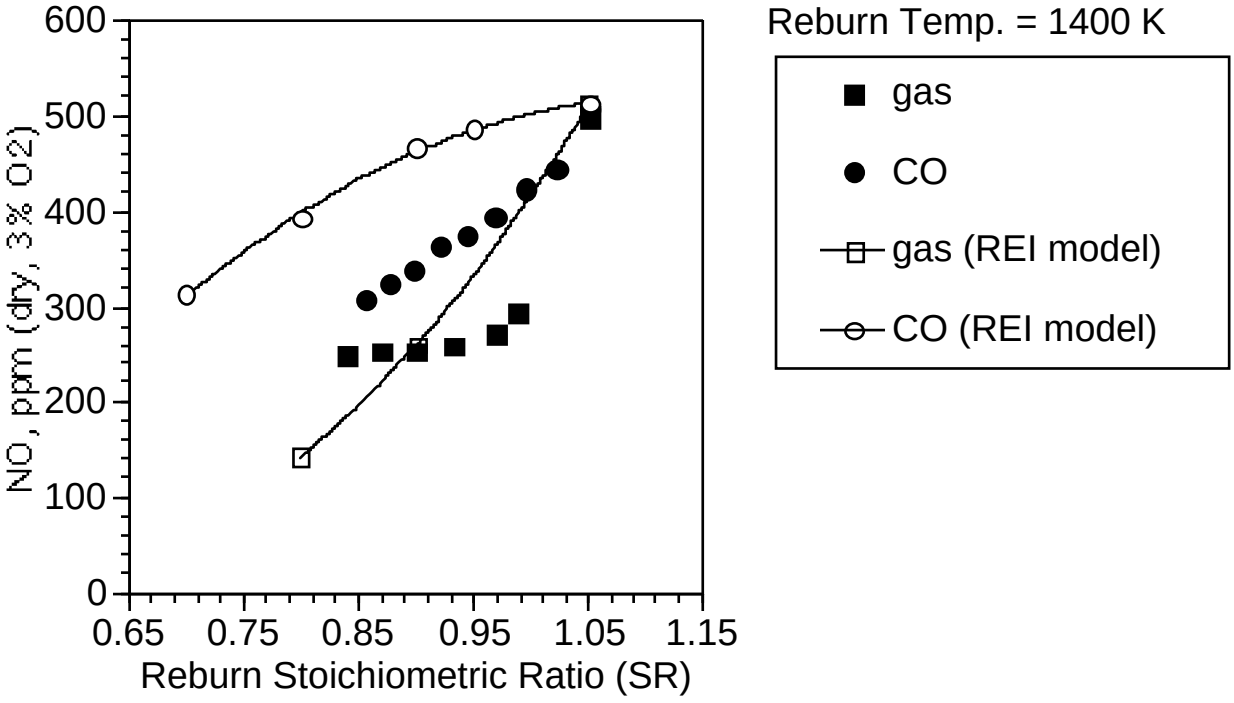

Figure 5.44 NO reduction during reburning with two fuels at 1400 K over a range of stoichiometries (corrected to 3% O_2).

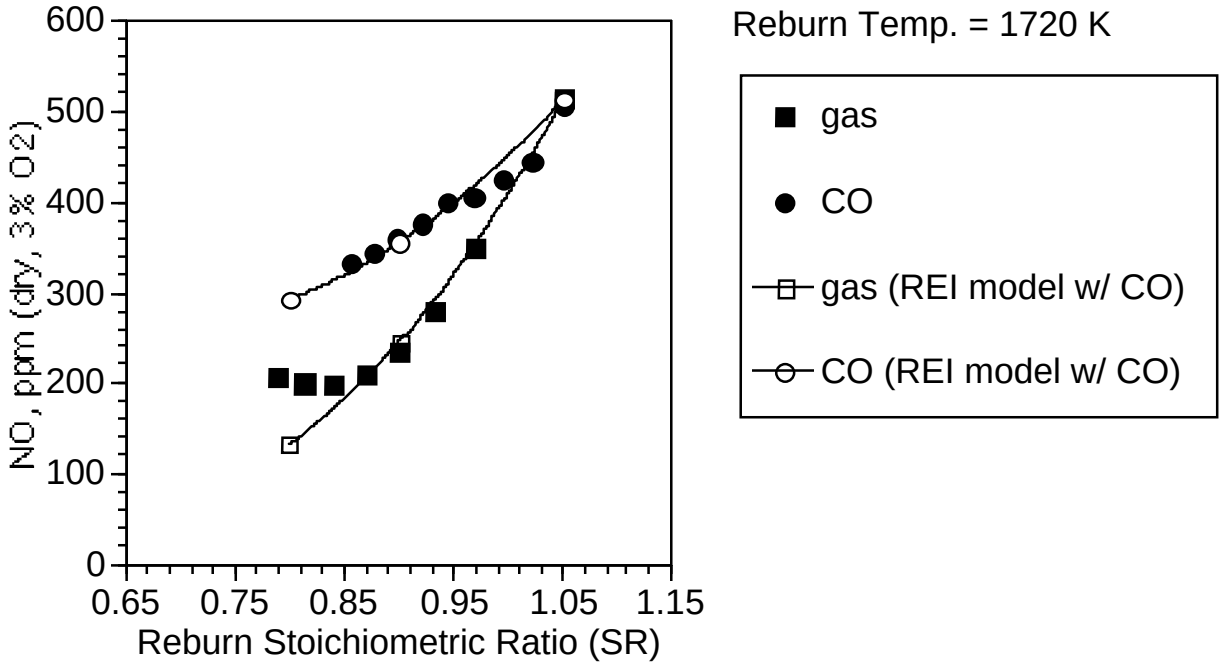

Figure 5.45 NO reduction during reburning with two fuels over a range of stoichiometries (corrected to 3% O_2).

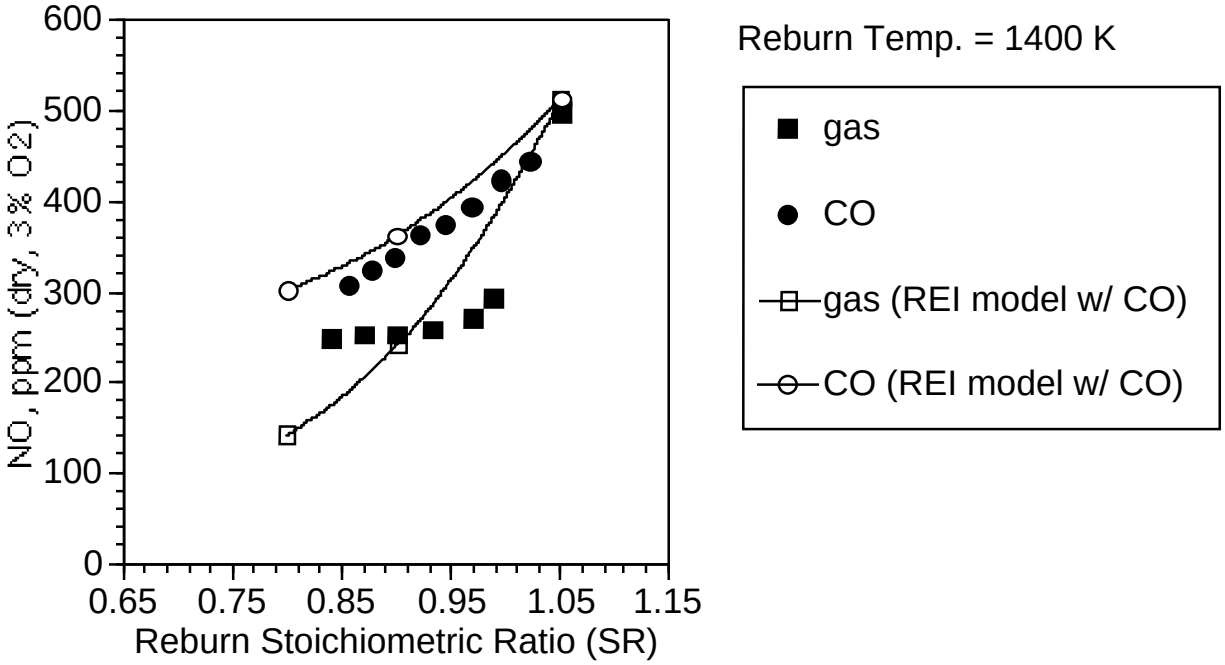

Figure 5.46 NO reduction during reburning with two fuels over a range of stoichiometries (corrected to 3% O_2).

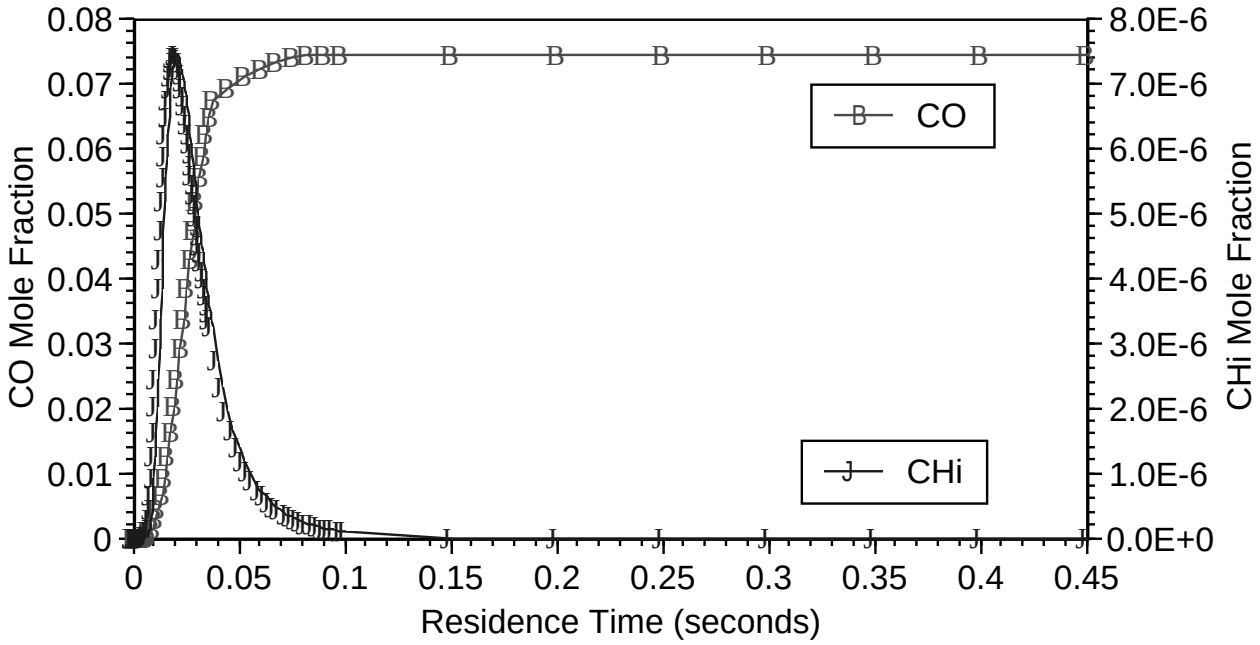

Figure 5.47 Predicted CO and CH_i concentrations as a function of residence time.

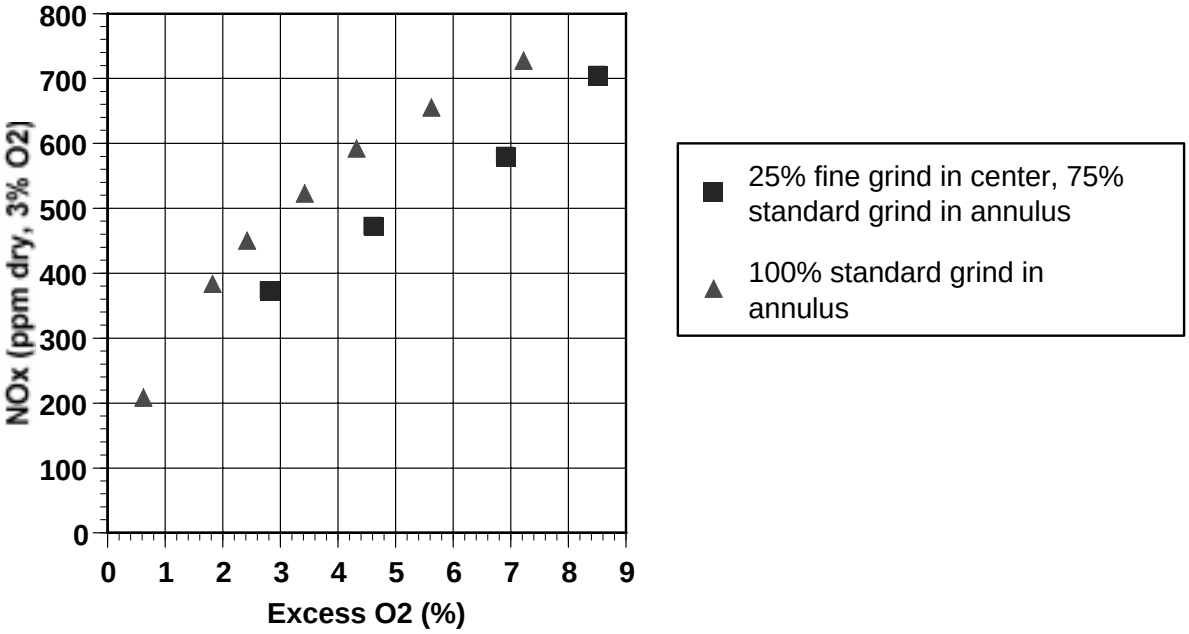

Figure 5.48 Comparison of NO_x emissions in the L1500 using a standard coal grind with a 25% fine grind feed through a separate, central coal nozzle.

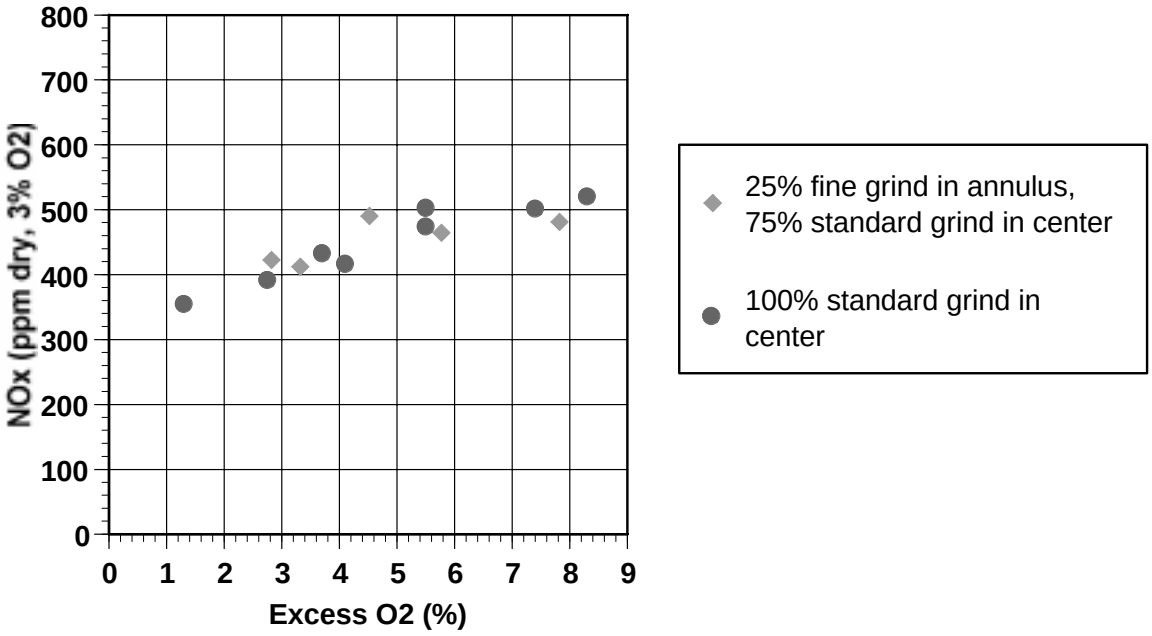

Figure 5.49 Comparison of NO_x emissions in the L1500 using a standard coal grind with a 25% fine grind feed through the middle, annular coal nozzle.

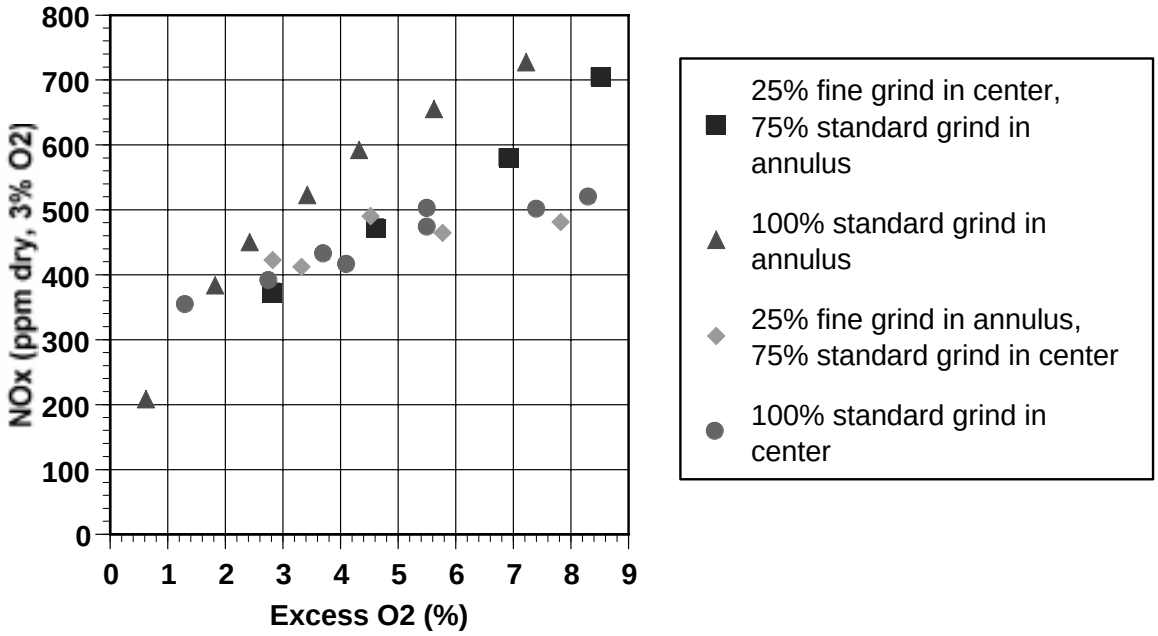

Figure 5.50 Comparison of L1500 NO_x results for both coal nozzle variations.

6.0 RESULTS AND DISCUSSION - NEAR FIELD BURNER MODELING

This section describes the use of *GLACIER*, a reacting computational fluid dynamics computer code, to simulate boilers and low-NO_x burners in order to: a) understand the processes controlling NO formation and destruction in pulverized-coal fired combustors; b) evaluate advanced carbon burnout models; and c) investigate fuel injector designs that allow reduction in nitric oxide emissions without increasing the amount of unburned carbon in the fly ash to unacceptable levels. Two EPRI sponsored programs concerned with waterwall corrosion and increased carbon in ash under low-NO_x conditions were instrumental in obtaining information on the boilers and burners modeled in this task.

6.1 ADDITION OF ADVANCED BURNOUT MODEL TO GLACIER

6.1.1 GLACIER

The computational tools used by Reaction Engineering International (REI) have been developed over the last fifteen years with the goal of addressing a wide range of problems encompassing utility boilers, pyrolysis furnaces, gas turbine combustors, rotary kilns, waste incinerators, smelting cyclones and others. The current software simulates reacting and nonreacting flow of gases and particles, including gaseous diffusion flames, pulverized-coal flames, liquid sprays, coal slurries, isothermal and reacting two-phase flows, injected sorbents, and other oxidation/reduction systems. Emphasis has been placed on simulating coal combustion and pollutant formation. REI codes, particularly *GLACIER*, include several capabilities necessary for accurate simulation of coal-fired boilers. These capabilities include turbulent particle transport with full coupling of particle and gas-phase mass and momentum; coal reaction processes such as devolatilization, char oxidation and gas-particle interchange; NO_x formation/reduction chemistry; particle convection and radiation with absorption, emission and anisotropic scattering; full coupling of gas-particle energy exchange; and ash deposition. In addition, boiler-side waterwall and radiant panel surface temperatures can be predicted as part of the computation, given a back-side (i.e., steam) temperature and surface resistance (from the deposit thickness and thermal conductivity, for example).

Char oxidation physics available in *GLACIER* prior to CBK (See Section 3.0) include a single particle model based on global reaction rates incorporating the effects of both external oxidizer diffusion and surface kinetics. The oxidation rate is a function of the kinetic rate coefficient and the oxygen concentration. The rate coefficient is of Arrhenius form, the surface reaction is 1^{st} order with respect to oxygen, and the product of the reaction is assumed to be CO. Experimentally determined rate parameters (preexponential and activation energy) are used when available. Otherwise the approximations of Baxter [1987] for ranges of coal types are used.

Through several years of industrial case studies, this simulation capability has been established as a useful tool for problem solving and design development. In addition, application of this tool to the specific issue of unburned carbon in fly ash has been successfully performed. However, the effectiveness of the model across a wide range of boiler types, operating conditions, and coal types has not been evaluated. Recent advances in the understanding of char oxidation that are unlikely to affect heat release and pollutant formation, could play an important role in predicting both quantitative information and trends relating to unburned carbon in fly ash. Therefore efforts have been made to integrate these advances into *GLACIER*.

6.1.2 Integration of CBK with GLACIER

The relationship between combustion modifications for NO_x control and detrimental effects on char burnout is complex. There are several possible reasons for this effect and they can be interrelated. A recent investigation [Walsh, 1994], which included a thorough literature review, included the following items as potential causes:

- Decrease of fuel-oxygen contact time at high temperature;
- Reduction of peak temperature regions; and
- Evolution of char reactivity during oxidation.

GLACIER includes the physics necessary for capturing the first two effects. However, char reactivity evolution, which is a strong function of a particle's temperature history was not previously included. In addition to this added feature, CBK includes a temperature dependent surface CO/CO_2 product relationship useful for low temperature regions and a rank dependent correlation for char oxidation kinetic parameters for instances when coal specific data are unavailable.

In order to prepare CBK for integration into a comprehensive CFD code, careful sensitivity analyses were carried out in an effort to reduce the computational demands of the thermal annealing submodel. Numerous test cases were examined to find the optimal limits of integration and step size, considering both accuracy and speed. REI then adapted a modified version of CBK as a post processor capable of accepting the large amounts of particle specific data available from a *GLACIER* simulation. *GLACIER* was also adapted to deliver this data in a convenient form for use by CBK and for comparisons between CBK and conventional char oxidation predictions. Coal specific properties and data describing the gas temperature, radiative environment and oxygen concentration history of each individual particle cloud (one for each starting location and particle size) are used by CBK to track char oxidation. The data used by CBK are based on an ensemble mean for a given cloud. In addition to modifications to the form of CBK inputs, CBK has been modified to assemble the results for each particle cloud and calculate furnace exit averages.

6.2 Carbon Burnout Modeling

Simulations of two utility boilers (Keystone Unit 2 and Hammond Unit 4) have been carried out. Both units have been retrofitted with low-NO_x burners/firing systems and overfire air. Some test data are available for these two boilers allowing comparisons of predictions and data and an evaluation of the relative importance of the physics included in the model and of the technologies being applied for NO_x reduction. These two facilities are examples of units that have been impacted by the increases in unburned carbon resulting from their respective retrofits. One of them, Keystone, has experienced a very significant increase in waterwall corrosion rates since retrofitting the low-NO_x firing system.

6.2.1 Boilers Simulated

Hammond

Georgia Power's Hammond Unit 4 is a 500 MW_e opposed wall-fired facility with 24 burners. Prior to low-NO_x retrofit, the unit was fitted with Foster-Wheeler's Intervane burners. During the

retrofit these burners were replaced by Foster Wheeler's Controlled-Flow/Split-Flame (CF/SF) burner. In addition, an advanced overfire air (OFA) system was installed. This consists of an independent windbox for improved penetration/control of OFA injection through 8 directly opposed ports above each column of burners, and 4 underfire air ports at the level of the bottom burner row near the walls. After retrofit, NO_x emissions from this unit were decreased substantially. However, as often happens following a low-NO_x retrofit, the LOI of the unit substantially increased as illustrated in Figure 6.1.

The coal properties and test conditions that were used to determine input values for the simulations are shown in Tables 6.1 and 6.2. Test data are available for both pre- and post-retrofit configurations through the results of DOE's Clean Coal Technology Demonstration Project performed by Southern Company Services.

The Hammond unit was modeled from bottom ash hopper to the exit of the secondary pendent superheater, with a symmetry plane along the vertical center from front to rear. This simulation was performed on a computational mesh with more than 480,000 nodes. Burner velocity and particle distribution inputs as well as near-burner mesh resolution were based on detailed coal pipe and complete individual burner simulations. Nearly 2000 statistical descriptions of particle clouds (240 starting locations and 8 particle sizes) were tracked in order to correctly simulate the complex nature of the fluid/particle injection with the CF/SF burner. Initially the furnace was only modeled to the horizontal plane at the nose but it was found that a more complete model including wing walls and extending to the beginning of the convective section was necessary to model carbon burnout. Figure 6.2 presents the interior surface and the computational mesh used in the complete furnace simulations.

Keystone

Keystone Unit 2 is a Combustion Engineering, Inc. Combined Circulation Balanced Draft Divided Furnace Steam Generator rated at 850 MW_e. It consists of two identical tangential fired furnaces sharing a common center waterwall. Each furnace has two stacks of wall mounted burners located near the corners on the front wall and two stacks on the rear wall. The burner stacks consist of eight levels of coal burners alternating with over- and under-fire air inlets.

During the winter of 1994, in order to comply with Clean Air Act NO_x emission requirements, the Keystone Unit 2 was retrofitted with an ABB C-E Services, Inc. Low-NO_x Concentric Firing System (LNCFS) Level III system. The LNCFS Level III system utilizes both Close Coupled Over Fire Air (CCOFA) and Separated Overfire Air (SOFA). Two levels of CCOFA ports are located at the top of each burner stack immediately above the top burner level and four levels of SOFA ports are located in the corners approximately 6 feet above the CCOFA ports. The low-NO_x retrofit has put Keystone Unit 2 in compliance with Federal Government NO_x emission regulations, but at the expense of increases in both waterwall tube corrosion and LOI. Corrosion rates of up to 50-70 mil/year have been observed in certain regions of the front and back waterwalls at CCOFA and SOFA inlet port elevations.

One of the twin furnaces of Keystone Unit 2 furnace (Furnace "B") was modeled from the lower end of the hopper to the nose with a 660,000 node computational grid. The post-low-NO_x retrofit version of the furnace and grid are shown in Figure 6.3 with the burner stacks and SOFA's labeled. Measured coal flow rates to each burner are used as inputs to the model with sufficient

combustion air for an excess O_2 level of 3.5% at the nose. Secondary combustion air is distributed according to inlet areas with modifications for secondary air damper positions. Coal nozzle and air inlet yaws and tilts are included. Waterwall fluid temperatures are used with a thermal resistance model to control wall heat transfer. The model has been used to examine corrosion mechanisms and particle burnout. REI's software for modeling two-phase reacting flows, *GLACIER*, predicts the deposition of both ash and unburned coal on furnace walls and thus is suited for examination of corrosion due to deposition. Coal properties and model inputs are presented in Tables 6.3 and 6.4.

6.2.2 General Results

Hammond

Evaluation of Hammond pre- and post-retrofit configuration carbon-in-ash and NO_x levels requires an accurate representation of the flow, temperature, and species (particularly O_2) fields in the furnace. Test data in the lower furnace are difficult to obtain and therefore unavailable. There are upper furnace temperature data obtained with a high velocity thermocouple probe. In addition exit NO_x levels are also available for consideration. Comparison with these data and the reasonableness of the general flow and energy fields provide credibility for NO_x and unburned carbon predictions.

Figure 6.4 includes temperature data and simulation results along paths where probes were inserted into the furnace during testing. The probes entered the furnace through the front wall at an elevation above the nose and were inserted as far as 18 feet. In general, although the magnitudes at given locations can differ by as much as 200°F, the trends and the means for the horizontal plane containing the probe paths are similar. Due to the large local gradients that exist in this plane small variations in the probe path can lead to large differences such that the error bars on the data and the simulated results are large in this region.

The overall temperature field in the furnace is illustrated in Figure 6.5. Several features of the furnace can be noted from these images. The flames in the post-retrofit case, although more closely anchored, do not result in a large high temperature region in the near-burner zone. The combustion of the fuel available from the burners is then aided by the presence of the overfire air ports, which are clearly visible due to the high velocity injection of the relatively cold air above the top row of burners. The higher degree of stratification evident in the upper furnace has been observed in testing.

The oxygen concentration field in a vertical plane at the edge of a burner is shown in Figure 6.6. Prior to devolatilization of the coal, the air issuing from the burners is roughly 21% O_2 (the black region). This plane was selected to emphasize the path of a particular particle that undergoes much less burnout in the post-retrofit case. It is clear from the images that this particle spends a large amount of time in an oxygen depleted region (the white region) and that the overfire air jets are not able to penetrate well along the particle path. Also clear from this image is the stratification of oxygen concentration in the upper furnace. Again this was also observed during the demonstration tests.

Keystone

Predicted flow patterns for the Keystone Unit 2 simulation are shown Figure 6.7. The circular fireball is evident. Because of large increases in water wall corrosion subsequent to the low-NO_x

retrofit, mechanisms influencing corrosion are of particular interest for this furnace. *GLACIER* does not predict corrosion rates; but, if a computer model is to provide insight into the cause of accelerated waterwall corrosion under low-NO_x firing conditions and allow an evaluation of potential solutions, it must provide an accurate picture of conditions close to the wall including:

- Local gas concentrations including carbon monoxide, hydrogen sulfide and sulfur dioxide;
- Heat flux to the wall, because this can affect deposit formation and slagging;
- Particle deposition rates at the wall;
- Carbon and sulfur content of the particles being deposited at the wall; and
- Deposition rates of FeS particles present in the coal stream.

Measured corrosion rates in the Keystone boiler are highest on the front and rear walls, above the close coupled over fire air, in the region of the separated over fire air, and lower on the side and center walls. Comparison of the pre- and post-retrofit simulations indicate that: 1) in the regions of highest corrosion, heat fluxes are higher in the post- than the pre-retrofit conditions; 2) the regions of highest corrosion do not correlate with highest H_2S concentrations close to the wall, but they do correlate to regions with steep gradients in oxygen concentration both along and perpendicular to the wall; and 3) on both the front and rear walls the regions of high corrosion correlate closely with the fraction of unburned carbon in the wall deposit. Figure 6.8 compares the fraction of unburned carbon in the wall deposit on the rear wall for the pre- and post-retrofit simulations. Shown also are measured wastage rates. The simulations suggest that high corrosion rates in excess of 50 mils/year occur in regions of the waterwall where there are high gradients in gas concentrations. In these simulations the gas cell closest to the wall (whose scale is on the order of 2.5 inches) may be oxidizing but one or two cells into the furnace there may be very high concentrations of H_2S. This suggests that intermittency (variation from oxidizing to reducing conditions) may be a key factor accelerating corrosion rates. The simulations also suggest that high concentrations of unburned carbon in the wall deposit accelerate corrosion rates; perhaps because of the creation of highly localized reducing conditions or perhaps they are indicative of the presence of FeS deposition.

6.2.3 Carbon Burnout Predictions

Hammond

GLACIER tracks statistical representations of particle trajectories or particle clouds that are uniquely identified by their starting location and particle size. Information is therefore available to determine the burnout of particles issuing from each burner in the Hammond unit. Table 6.5 and Table 6.6 show the carbon in ash for coal particles starting at each burner for the pre- and post-retrofit cases, respectively using *GLACIER* kinetics. Particles starting in the upper burners have the shortest residence time and therefore would be expected to have the lowest burnout; this is the case for the pre-retrofit but not for the post-retrofit condition.

Examination of the post-retrofit simulation indicates:

- The inner columns of burners produce minimal unburned carbon.

- While the bottom row again produces no unburned carbon, the middle row, not the top, results in the highest levels.

- The rear wall results in significantly higher unburned carbon levels than the front wall.

These results suggest that the particle paths and oxygen concentration/temperature fields are complicated by the presence of the low-NO_x burners and overfire air.

Simulations of the Hammond unit were performed to compare the results obtained with the more complex (CBK) char oxidation model and the mean char oxidation rate included in *GLACIER*. Because of the complexity of the CBK model these comparisons were made with the reduced furnace model; i.e., it did not extend beyond the horizontal plane of the nose A summary of the results for the pre- and post-low-NO_x retrofit configurations with the two approaches to modeling carbon burnout are presented.

As expected the burnout for the post-retrofit simulation is lower irrespective of which char oxidation model used. The results with CBK however indicate two differences between the models. First, the burnout is consistently lower with CBK. Second, the change in burnout from pre- to post-retrofit is significantly greater with CBK than with the less complex model.

Figure 6.9 presents the burnout for these four calculations as a function of particle size. The noticeable difference between the pre- and post-retrofit cases is clear for all particle sizes. However, these data also point out an interesting feature of the size dependence. In the pre-retrofit case it is clear that much of the unburned carbon results from the largest size fractions. However, in the post-retrofit case the dependence of burnout on initial size is much less non-linear, suggesting that removing the largest fraction with improved size classification may be less effective for a post-retrofit situation.

The importance of the relationship between char reactivity and particle temperature/oxygen concentration history can be see in Figure 6.10. These two plots show the temperature and oxygen concentration history of identical particles in pre- and post-retrofit simulations. The effect of the low-NO_x burners and staged air addition is clear. The oxygen is completely consumed in the near burner region and consequently the normalized reaction rate drops to zero. The particle has completely burned in the pre-retrofit case before its post-retrofit equivalent encounters the overfire air and begins to oxidize. In addition, during this time the post-retrofit particle can be thermally annealed further reducing its capability to achieve high levels of burnout.

Keystone

Carbon in fly ash for Keystone Unit 2 is shown in Table 6.7 as a function of particle diameter. As could be expected, the smaller particles burn out completely and unburned carbon in fly ash results from incomplete burning of the larger particles. *GLACIER* predicts significantly higher burnout in the pre-low-NO_x retrofit simulation; this trend has been observed in the Keystone furnace. Tables 6.8 and 6.9 show predicted carbon in fly ash as a function of burner for the pre- and post-retrofit cases. The simulations predict that most of the unburned carbon comes from the upper burner levels, since the coal coming from these levels has a shorter residence time in the furnace. More detailed information showing unburned carbon as both a function of particle size and burner is shown in Tables 6.10 through 6.13.

6.3 Fuel Injector Simulations

6.3.1 Coal Injector with Venturi and Spinner Vanes

The DB Riley low-NO_x burner includes an annular coal injector with spinner vanes (coal spreader) placed just upstream of a venturi. The impact of the spreader design on the distribution of 10, 60 and 230 micron particles was determined.

Figure 6.11 illustrates the magnitude of these differences for the standard case (low blade angle, venturi in place). These images display particle mass density at the burner exit plane in two forms - shading (black to white being 0 to 0.33 kg/m^3) and contours (each line in a 10% increase). The difference in particle dispersion as a function of particle size is obvious, particularly for the 10μm particles. However, even these small particles show notable concentration in the areas between the blades, but biased toward the leading face.The overall effect of the coal spreader and venturi appears to be to concentrate the particles into four lobes with the larger particles most prevalent at the center of the lobes. Quantitatively, 90% of the 230 μm particles are concentrated in less than 1/3 of the cross-sectional area.

In order to isolate the effects of the venturi and of the blade angle, the same simulations were performed for: (1) the current geometry without the venturi and (2) the current geometry with the blade angle doubled. Figure 6.12 illustrates the results of these design variations for the case of 60μm particles. The simulated effect of the venturi is quite noticeable. Not only does the presence of the venturi concentrate the particles in the radial direction, but it also appears to have a synergistic effect in terms of the effectiveness of the coal spreader and its concentrating effect in the tangential direction.

The increase in blade angle also serves to concentrate the particles. However, in this case the effect occurs in the tangential direction such that the bi-modal nature of the tangential distribution is substantially reduced. (The contours in Figure 6.12 go from peanut-shaped to pear-shaped.) The effect of the venturi and blade angle change on the distribution of 230μm particles is similar to that of the 60μm particles shown in Figure 6.11. The 10μm particles however are practically unaffected by the design changes and tend to be uniformly distributed regardless of the flow field.

The coal spreader and venturi affect the velocity field in addition to the particle distribution. Figure 6.13 shows the velocity magnitude at a cross section of the primary stream about two thirds of the way down the coal spreader. The wall boundary layers lead to lower velocities along the surfaces and the blades result in recirculation zones on the inner sections of the trailing faces. The coal particle concentrations in these regions are quite low because of the severe velocity gradients at the boundary of this region.

Simulations were also performed on the secondary and tertiary air streams. These simulations give useful quantitative information regarding the effectiveness of the swirl imparted at the burner exit plane and the spatial dependence of the velocity field due to the flow field boundaries, particularly the effect of the split stream resulting from the leading edge of the flow-turning flare that is placed at a slightly larger diameter than the inside of the secondary stream. Qualitatively, the flow patterns predicted are not unexpected.

Figure 6.14 displays a 60° section of the exit plane of the secondary stream. It is evident that any tangential gradients in the axial velocity induced by the presence of the vanes have been damped out and that only radial gradients exist. These radial gradients are fairly small except in the region near the flare leading edge (the blank space between the orange and blue sections). The inner portion of the flow is at a very low velocity and may serve as a flame anchor in this burner design (testing has shown that this design has excellent ignition stability). The velocity field in the tertiary stream is very similar to the outer portion of the secondary stream despite (1) the contraction that occurs approximately 6 inches from the burner exit and (2) the relative proximity of the burner exit and the swirl vanes.

6.3.2 Annular Coal Injector with Stream Splitting

Simulation of the Hammond furnace required detailed modeling of the coal injector in order to improve the accuracy of the inputs and for guidance in terms of mesh resolution. In addition, detailed modeling of the Controlled-Flow/Split-Flame burner provides insight regarding the effects of low-NO_x burner design features. This coal injector is fed through a tangential entry that imparts swirl to the flow prior to its entering a convergent annular section with anti-roping bars at the walls. In the latter section of the convergent section these bars end and the flow splits into 5 distinct streams – an inner annulus surrounded by four ellipses. These simulations were performed on geometries with and without the tangential inlet section. In order to obtain adequate resolution for the anti-roping bars, the following results from the exit of the tangential entry were mapped onto the inlet of a more detailed simulation (380,00 nodes) of the convergent section of the coal pipe:

- The tangential velocity at the inlet to the convergent section was determined from the results of the model of the tangential entry, and
- The particle loading computed based on the mass density and velocity distributions from the results of the model of the tangential entry.

A model of the nozzle including the tangential entry was performed to (1) determine the degree of “roping” of the coal particles and to (2) quantify the swirl imparted to the flow at the entrance to the convergent section. Each computational node from this coarse mesh (~700 locations) was taken as the mean location for a particle cloud starting in the refined mesh of the convergent section. Figure 6.15 illustrates the effects of the coal nozzle on various size particles. The gray surface in the center is the movable sleeve in the center of the coal pipe. The cross sectional planes are colored to illustrate variations in particle mass density and the black lines display the statistical mean of a few typical particle cloud trajectories. Three particles are shown: 20 μm (thin line), typical of the small end of the size distribution; 60 μm (medium thickness line), typical of the mass mean of the size distribution, and 200 μm (thick line), typical of the large end of the size distribution.

The larger particles from every starting location quickly reach the wall and pass axially through the coal pipe in the valleys between anti-roping bars. The smaller particles tend to follow the flow and rarely hit the anti-roping bars. The intermediate size particles, which include the majority of the total mass, impact the roping bars, but do not remain in the valleys. This tends to more evenly distribute these particles. Another effect of this design is to segregate the intermediate and large particles into the ellipses, as opposed to the annulus. Since the exit area of the annulus and the ellipses are similar, the proportion of smaller particles exiting the ellipses/annulus are also similar. Another feature of this coal pipe, despite the presence of the anti-roping bars, is the maldistribution in the angular direction.

6.3.3 Coal Injector for Tangential-Fired Boiler

In the ABB LNCFS Level III firing system currently used in Keystone Unit 2, coal is fed from the mills through a vertical pipe, past a 90^o bend and into the coal injector. Coal enters the furnace through a rectangular opening surrounded by an air shroud. In order to determine the distribution of particle sizes as coal exits the burner, the 90^o bend and coal burner have been modeled with a 135,000 node grid. A coal flow rate of 1.26 kg/s is distributed over a particle size range representative of the actual coal and is carried by primary air at the rate of 2.27 kg/s. Results of the simulation are shown in Figure 6.16. As is evident in the figure, the simulation predicts that the inertia of larger particles will tend carry them in a wider arc around the bend, while smaller particles should follow the air flow more closely and remain nearer the center of the burner. The result is that the particle size distribution at the burner exit will not be uniform; the larger particles will tend to concentrate near the upper part of the exit, as shown in Figure 6.17. At the nozzle exit plane, particle mass is concentrated in upper part of the nozzle exit while particle number density is more evenly distributed.

6.4 Low-NO_x Burner Modeling

6.4.1 The CCVII Burner

Figure 6.18 shows a schematic of the CCVII burner. The simulation of the coal injector has been discussed in an earlier section. In a separate study the burner was modeled with just air, no particles and no reaction, to understand the impact swirl and the two flares have on the air distribution within the burner divergent. Figure 6.19 shows velocity vectors and Figure 6.20 shows the distribution of axial velocity at three axial distances. The simulation indicates that the combination of swirl and flares directs both combustion air streams away from the annular coal jet. Also there is a recirculation zone on the axis caused by the bluff body effect of the coal spreader support and a region of stagnant flow within the inner flare which is required for flame stabilization.

A single CCVII burner was simulated in a test tunnel. Flow and particle inputs for these simulations were based on the results of the burner interior modeling mentioned previously. The importance of these inlet distributions in describing the primary/secondary mixing and its role on NO_x formation/destruction processes was alluded to by a previous experimental/modeling investigation. The planes and trajectories visible through the cutout in Figure 6.21 illustrate the nature of the particle distribution exiting the burner. The planes represent areas of high CO concentration and are indicative of particle devolatilization while the trajectories illustrate the mean particle paths of two (one each at the small and large end of the particle size range) of the four concentrations of particles that result from the coal spreader in the coal pipe. The size of the circles around the mean trajectory lines are proportional to the dispersion of the particle clouds as they propagate down the length of the test furnace. The color of the lines relates information regarding char formation and burnout (black - no char; white - all char). It is obvious from this image that the four lobes of concentrated particles remain intact in the near burner region. However, within 10 burner diameters these lobes are barely evident. The implications of these results in terms of NO_x formation/reduction can be better understood with respect to additional information describing the gas phase.

Figure 6.22 includes trajectory information similar to Figure 6.21 with a solid plane illustrating the four-lobed nature of the stoichiometric ratio distribution (where SR<1.0) at a location a few burner diameters downstream. The color of the grid lines in this image is related to the axial gas velocity. Black areas indicate recirculation zones. The vertical plane is the burner exit plane where the coal spreader central rod is the center circle, surrounded by the primary, inner secondary, and outer secondary annular streams. The ring of near zero velocity between the primary and inner secondary streams is a result of a flare that is near this boundary (it is positioned slightly into the inner secondary stream). Much of the internal recirculation zone shown here consists of rich gases that could be beneficial in terms of NO_x formation/destruction.

In addition to the location and stoichiometry of the internal recirculation zone of this burner, the temperature can play an important role in the near burner chemistry. Although much of the internal recirculation zone is rich, Figure 6.23 shows that the temperature in this region is relatively high. This may provide an opportunity to reduce NO in this region.

Two design variables in particular have been identified by commercial interests for initial consideration – 1) single vs. double register design, and 2) coal pipe configuration. Initial simulation efforts are studying the changes in flow, temperature, and stoichiometry from a simple single register design and the current standard dual register design with venturi and coal spreader in the coal pipe.

Prior to the concerns regarding NO_x emissions in the early 70's, burner designs focused on obtaining rapid and stable combustion in a manner that avoided equipment damage. Annular burners typically involved a single secondary stream. However, early attempts at NO_x control strategies often involved the separation of secondary streams in order to allow greater control of the fuel/air mixing process. The standard design of the burner under consideration also includes a dual register design. The necessity for this additional complication and cost however, has not been extensively evaluated.

In order to identify the benefits/effects of this additional level of mixing control, simulations were performed for a single register case with an equivalent level of swirl. Figure 6.24 presents the temperature field in the vertical plane along the burner centerline and at the quarl exit plane for first a single register and second the standard double register configuration with coal pipe modifications. These results show that the modifications result in similar aerodynamic staging of the mixing process and a stronger internal recirculation zone resulting in more rapid ignition. Their role of flow type (internal recirculation zone formation and primary jet penetration) and local concentration of fuel particles will be evaluated in further detail in subsequent efforts. This work will include calculation of NO_x distributions in the near burner region.

6.4.2 Virtual Test Facility With CF/SF Burner

6.4.2.1 Motivation

Accurate simulation of the CF/SF burners in the Hammond furnace required detailed knowledge of not only the coal pipe, but also the overall burner in order to improve the accuracy of the inputs and for guidance in terms of mesh resolution. The size of a commercial furnace is such that the application of local high resolution required to capture flow and chemistry in the near burner region must be minimized. In addition to the need to capture the size and shape of burner features, it

is important to avoid diluting areas of fuel rich concentrations and high velocity, as well as temperature gradients. The exit plane results of the simulation of the coal pipe discussed previously were used to provide improved inputs for a model of the burner as a whole in a virtual test facility (VTF). The exit plane of the burner and the mapping of the coal pipe exit plane particle distribution just off the exit plane is illustrated in Figure 6.25. The inner and outer secondary streams are at different swirl and normal velocity. The primary flow is split into the inner annulus and the four ellipses and the core flow is a small stream tapped off the windbox. The elliptical particle distributions are shown (white being the highest concentration). As the particle concentration is shown on a log scale the inner annulus particle concentration is barely noticeable.

The coal pipe simulation results were also used, in a similar manner, to determine the particle distribution at the entrance to the Hammond furnace for each of the burners. This type of mapping does not involve the computational mesh directly. Also, comparisons with the VTF results were used to refine the furnace model inputs. For example, the gradients observed in the VTF solution were used to refine the furnace mesh when required. A comparison of the grids in the burner region is shown in Figure 6.26. The VTF solution was also used to evaluate near burner phenomena such as flame location, which has important implications in terms of NO_x formation/destruction and burnout.

In addition to the usefulness of the VTF for guiding the furnace modeling effort, it also provides an ideal environment for studying a burner in isolation. Although the system as a whole may dominate many of the properties of interest (NO_x, LOI, deposition/corrosion, etc.), burners are often designed while focusing on the burner and it is difficult to separate the role of individual components without isolating them.

6.4.2.2 Results

As shown in the left column of Figure 6.27, the formation of the flame in the VTF displays a very detailed structure. Immediately upon injection, the fine coal particles in the inner annulus mix into the hot core air and begin to devolatilize leading to reaction and an increase in temperature. The four ellipses containing the bulk of the particle mass, however, do not ignite until the end of the quarl is reached. In the second image, the four lobes can be seen clearly as the outer part of each ellipse has ignited where adequate amounts of coal and air are available. The four lobes begin to merge until finally the air in the interior is largely consumed and the flame front becomes a large circle. The behavior of the annulus and the four lobes explains the counterintuitive ability of this flame to remain stably attached while also staging the air addition and providing a significant residence time, for portions of the fuel, under rich conditions.

The effectiveness of this burner in providing rich regions in which NO_x reduction can occur is also illustrated in the right column of Figure 6.27. The red regions have a high NO_x formation rate, while the blue regions have a high NO_x destruction rate. White regions mean NO_x is neither formed or destroyed. Just out of the burner, NO_x begins to form quickly and very little reduction occurs since the stoichiometry is still primarily lean. However, as the ellipses ignite, the fuel rich core of each lobe serves to form a strongly reducing environment in proximity to where the NO_x is generated. As the fuel propagates downstream, mixing tends to dilute the effectiveness of the NO_x reduction. However, even well down the furnace, slow rates of NO_x destruction (light blue) are observed.

Table 6.1 Hammond Coal Properties

Proximate Analysis

Component	Mass Fraction
Fixed Carbon	51.7 %
Volatile Matter	33.1 %
Ash	9.1 %
Moisture	6.1 %

Ultimate Analysis

Species	Mass Fraction
C	71.4 %
H	4.7 %
O	5.8 %
N	1.4 %
S	1.7 %

Coal Size Distribution Used in Simulations

Particle Diameter	Pre-Retrofit	Post-Retrofit
17 μm	0.05	0.02
27 μm	0.10	0.06
40 μm	0.22	0.28
60 μm	0.22	0.28
87 μm	0.21	0.23
122 μm	0.10	0.07
169 μm	0.07	0.04
279 μm	0.03	0.01

Table 6.2 Hammond Furnace Simulation Inputs

Component	Pre-Retrofit	Post-Retrofit
Coal	42.5 kg/s	44.8 kg/s
Primary Air	113.4 kg/s	105.4 kg/s
Total Secondary Air	393.3 kg/s	408.5 kg/s
Secondary Burner Air	-	269.3 kg/s
Secondary OFA	-	106.8 kg/s
Secondary UFA	-	32.4 kg/s

Table 6.3 Keystone Coal Properties

Proximate Analysis

Component	Mass Fraction
Fixed Carbon	46.6 %
Volatile Matter	35.0 %
Ash	12.2 %
Moisture	6.2 %

Ultimate Analysis

Species	Mass Fraction
C	69.3 %
H	4.6 %
O	4.6 %
N	1.3 %
S	1.8 %

Coal Size Distribution Used in Simulations

Particle Diameter	Mass Fraction
6 μm	0.17
18 μm	0.15
31 μm	0.11
43 μm	0.10
60 μm	0.15
85 μm	0.10
120 μm	0.12
175 μm	0.05
250 μm	0.05

Table 6.4 Keystone Furnace Simulation Inputs

Component	Flow Rate
Coal	33.3 kg/s
Primary Air	68.4 kg/s
Total Secondary Air	329.5 kg/s
Secondary CCOFA Air	15.7 kg/s
Secondary SOFA Air	100.4 kg/s

Table 6.5 Hamond Pre-Retrofit Carbon in Fly Ash by burner

Row		**Back Wall Burners**		
top	6.1 %	4.4 %	4.4 %	6.1 %
middle	1.0 %	1.3 %	1.3 %	1.0 %
bottom	0.0 %	0.0 %	0.0 %	0.0 %
Row		**Front Wall Burners**		
top	4.9 %	1.7 %	1.7 %	4.9 %
middle	3.9 %	1.2 %	1.2 %	3.9 %
bottom	0.0 %	0.0 %	0.0 %	0.0 %

Table 6.6 Hamond Post-Retrofit Carbon in Fly Ash by Burner

Row		**Back Wall Burners**		
top	16.8 %	2.0 %	2.0 %	16.8 %
middle	8.8 %	0.1 %	0.1 %	8.8 %
bottom	0.0 %	0.0 %	0.0 %	0.0 %
Row		**Front Wall Burners**		
top	12.3 %	1.8 %	1.8 %	12.3 %
middle	23.0 %	0.6 %	0.6 %	23.0 %
bottom	0.0 %	0.0 %	0.0 %	0.0 %

Table 6.7 Keystone Carbon in Fly Ash by Particle Diameter

Diameter	Pre-Retrofit % Carbon in Fly Ash	Post-Retrofit % Carbon in Fly Ash
6 μm	0.0 %	0.0 %
18 μm	0.0 %	0.0 %
31 μm	0.0 %	4.9 %
43 μm	0.0 %	5.9 %
60 μm	0.0 %	9.9 %
85 μm	0.1 %	22.1 %
120 μm	7.8 %	32.8 %
175 μm	37.8 %	47.8 %
250 μm	60.2 %	58.0 %
overall	**5.0 %**	**16.2 %**

Table 6.8 Keystone Pre-Retrofit Carbon in Fly Ash by Burner

	Carbon in Fly Ash by Burner			
Burner Level	**Front Side**	**Front Center**	**Rear Center**	**Right Side**
1	0.0 %	0.0 %	0.0 %	0.0 %
2	0.0 %	0.0 %	0.0 %	0.0 %
3	0.0 %	0.0 %	0.0 %	0.0 %
4	1.7 %	0.0 %	3.1 %	0.0 %
5	0.0 %	0.0 %	0.0 %	9.3 %
6	0.3 %	1.8 %	3.4 %	5.8 %
7	7.3 %	8.3 %	4.8 %	17.3 %
8	5.6 %	26.6 %	9.3 %	19.8 %

Table 6.9 Keystone Post-Retrofit Carbon in Fly Ash by Burner

	Carbon in Fly Ash by Burner			
Burner Level	**Front Side**	**Front Center**	**Rear Center**	**Right Side**
1	1.1 %	0.0 %	0.3 %	3.7 %
2	1.4 %	0.0 %	0.0 %	0.0 %
3	0.0 %	0.0 %	0.0 %	0.0 %
4	1.5 %	0.6 %	0.0 %	9.9 %
5	13.8 %	26.1 %	3.4 %	10.0 %
6	0.7 %	55.1 %	21.6 %	7.6 %
7	38.0 %	36.1 %	7.3 %	23.7 %
8	32.6 %	19.0 %	12.0 %	23.9 %

Table 6.10 Keystone Post-Retrofit Carbon in Fly Ash by Particle Diameter and Burner

Post Retrofit Carbon in Fly Ash for Front Side Burner

Particle Diameter

Burner Level	6 μm	18 μm	31μm	43 μm	60 μm	85 μm	120 μm	175 μm	250 μm
1	0.0 %	0.0 %	0.0 %	0.0 %	0.0 %	0.0 %	0.0 %	21.2 %	0.0 %
2	0.0 %	0.0 %	0.0 %	0.0 %	0.0 %	0.0 %	5.0 %	0.0 %	21.9 %
3	0.0 %	0.0 %	0.0 %	0.0 %	0.0 %	0.0 %	0.0 %	0.0 %	0.0 %
4	0.0 %	0.0 %	0.0 %	0.0 %	0.0 %	0.0 %	0.0 %	35.8 %	0.0 %
5	0.0 %	0.0 %	0.0 %	0.0 %	0.0 %	0.0 %	25.8 %	52.3 %	56.4 %
6	0.0 %	0.0 %	0.0 %	0.0 %	0.0 %	0.0 %	0.0 %	0.0 %	12.9 %
7	0.0 %	0.0 %	0.0 %	11.4 %	39.2 %	52.0 %	62.5 %	68.3 %	65.0 %
8	0.0 %	0.0 %	0.0 %	0.0 %	0.0 %	40.1 %	57.0 %	69.0 %	74.8 %

Table 6.11 Keystone Post-Retrofit Carbon in Fly Ash by Particle Diameter and Burner

Post Retrofit Carbon in Fly Ash for Front Center Burner

Burner Level	Particle Diameter 6 μm	18 μm	31μm	43 μm	60 μm	85 μm	120 μm	175 μm	250 μm
1	0.0 %	0.0 %	0.0 %	0.0 %	0.0 %	0.0 %	0.0 %	0.0 %	0.0 %
2	0.0 %	0.0 %	0.0 %	0.0 %	0.0 %	0.0 %	0.0 %	0.0 %	0.0 %
3	0.0 %	0.0 %	0.0 %	0.0 %	0.0 %	0.0 %	0.0 %	0.0 %	0.0 %
4	0.0 %	0.0 %	0.0 %	0.0 %	0.0 %	0.0 %	0.0 %	11.7 %	0.0 %
5	0.0 %	0.0 %	42.4 %	16.4 %	0.0 %	45.7 %	47.1 %	14.6 %	52.2 %
6	0.0 %	0.0 %	47.6 %	57.4 %	65.8 %	69.7 %	70.4 %	70.1 %	64.1 %
7	0.0 %	0.0 %	0.0 %	0.0 %	15.0 %	56.3 %	61.6 %	69.5 %	67.7 %
8	0.0 %	0.0 %	0.0 %	0.0 %	0.0 %	8.2 %	28.2 %	59.0 %	68.2 %

Table 6.12 Keystone Post-Retrofit Carbon in Fly Ash by Particle Diameter and Burner

Post Retrofit Carbon in Fly Ash for Rear Center Burner

Particle Diameter

Burner Level	6 μm	18 μm	31μm	43 μm	60 μm	85 μm	120 μm	175 μm	250 μm
1	0.0 %	0.0 %	0.0 %	0.0 %	0.0 %	0.0 %	0.0 %	6.9 %	0.0 %
2	0.0 %	0.0 %	0.0 %	0.0 %	0.0 %	0.0 %	0.0 %	0.0 %	0.0 %
3	0.0 %	0.0 %	0.0 %	0.0 %	0.0 %	0.0 %	0.0 %	0.0 %	0.0 %
4	0.0 %	0.0 %	0.0 %	0.0 %	0.0 %	0.0 %	0.0 %	0.0 %	0.0 %
5	0.0 %	0.0 %	0.0 %	0.0 %	0.0 %	0.0 %	0.0 %	0.0 %	42.7 %
6	0.0 %	0.0 %	0.0 %	0.0 %	0.0 %	38.2 %	54.0 %	55.9 %	16.3 %
7	0.0 %	0.0 %	0.0 %	0.0 %	0.0 %	0.0 %	27.9 %	17.0 %	36.9 %
8	0.0 %	0.0 %	0.0 %	0.0 %	0.0 %	0.0 %	9.7 %	43.5 %	62.9 %

Table 6.13 Keystone Post-Retrofit Carbon in Fly Ash by Particle Diameter and Burner

Post Retrofit Carbon in Fly Ash for Rear Side Burner

Burner Level	Particle Diameter 6 μm	18 μm	31μm	43 μm	60 μm	85 μm	120 μm	175 μm	250 μm
1	0.0 %	0.0 %	0.0 %	0.0 %	0.0 %	51.7 %	0.0 %	0.0 %	0.0 %
2	0.0 %	0.0 %	0.0 %	0.0 %	0.0 %	0.0 %	0.0 %	0.0 %	0.0 %
3	0.0 %	0.0 %	0.0 %	0.0 %	0.0 %	0.0 %	0.0 %	0.0 %	0.0 %
4	0.0 %	0.0 %	0.0 %	0.0 %	0.0 %	0.0 %	0.0 %	0.0 %	0.0 %
5	0.0 %	0.0 %	0.0 %	0.0 %	0.0 %	14.9 %	14.2 %	38.9 %	61.2 %
6	0.0 %	0.0 %	0.0 %	0.0 %	0.0 %	0.0 %	0.0 %	19.2 %	64.8 %
7	0.0 %	0.0 %	0.0 %	0.0 %	0.0 %	0.0 %	46.4 %	66.3 %	68.2 %
8	0.0 %	0.0 %	0.0 %	0.0 %	0.0 %	0.0 %	47.6 %	64.0 %	70.0 %

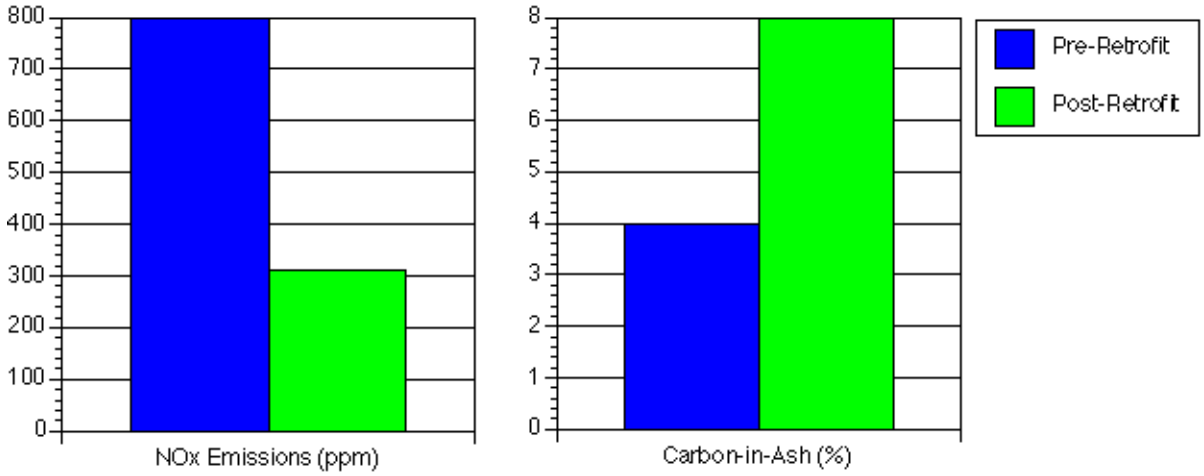

Figure 6.1 NO_x emissions and carbon-in ash before and after retrofit with low-NO_x burners and advanced overfire air system.

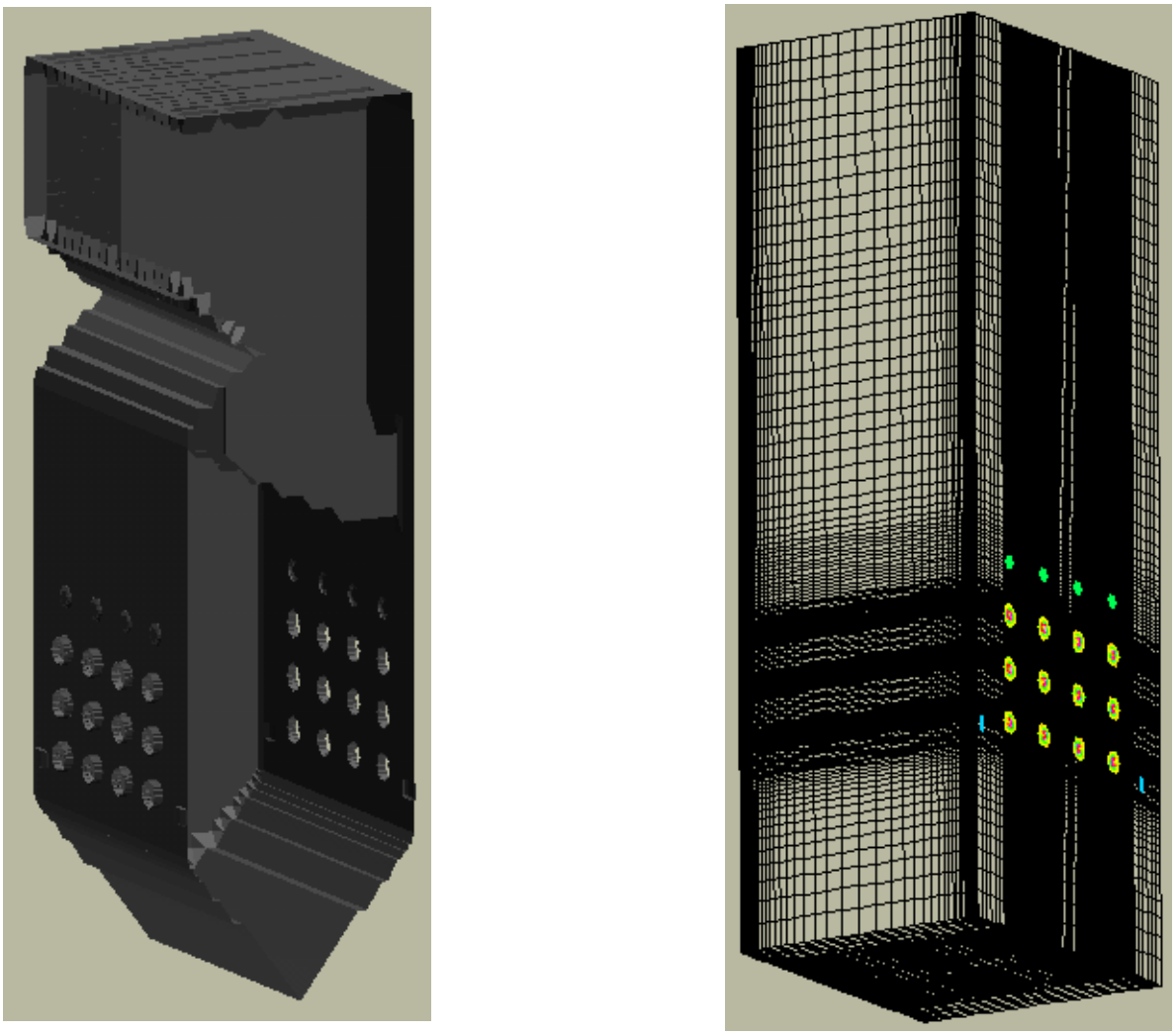

a) Interior Surface b) 480,000 Node Grid

Figure 6.2 Interior surface and computational mesh used for simulations.

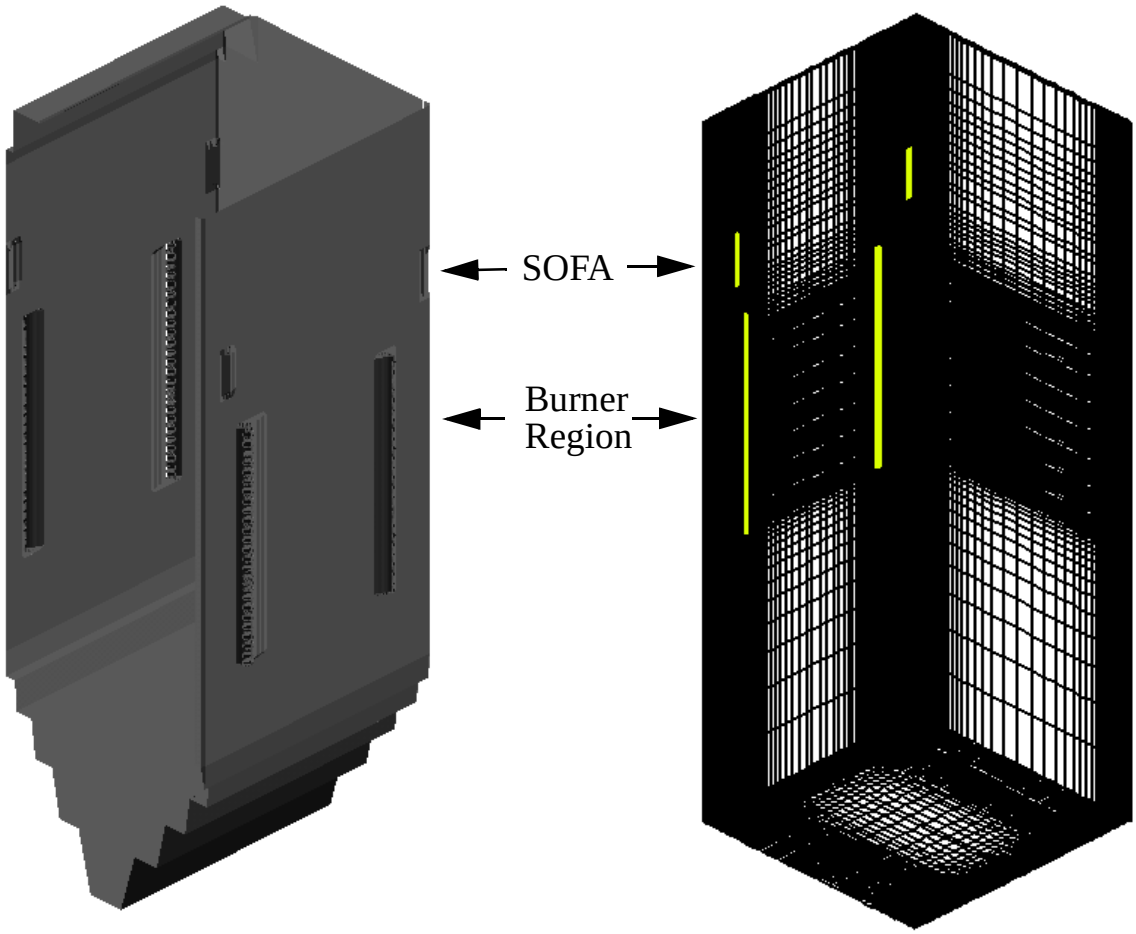

a) Furnace with center wall cut away

b) 660,000 node grid

Figure 6.3 Keystone furnace and computational grid.

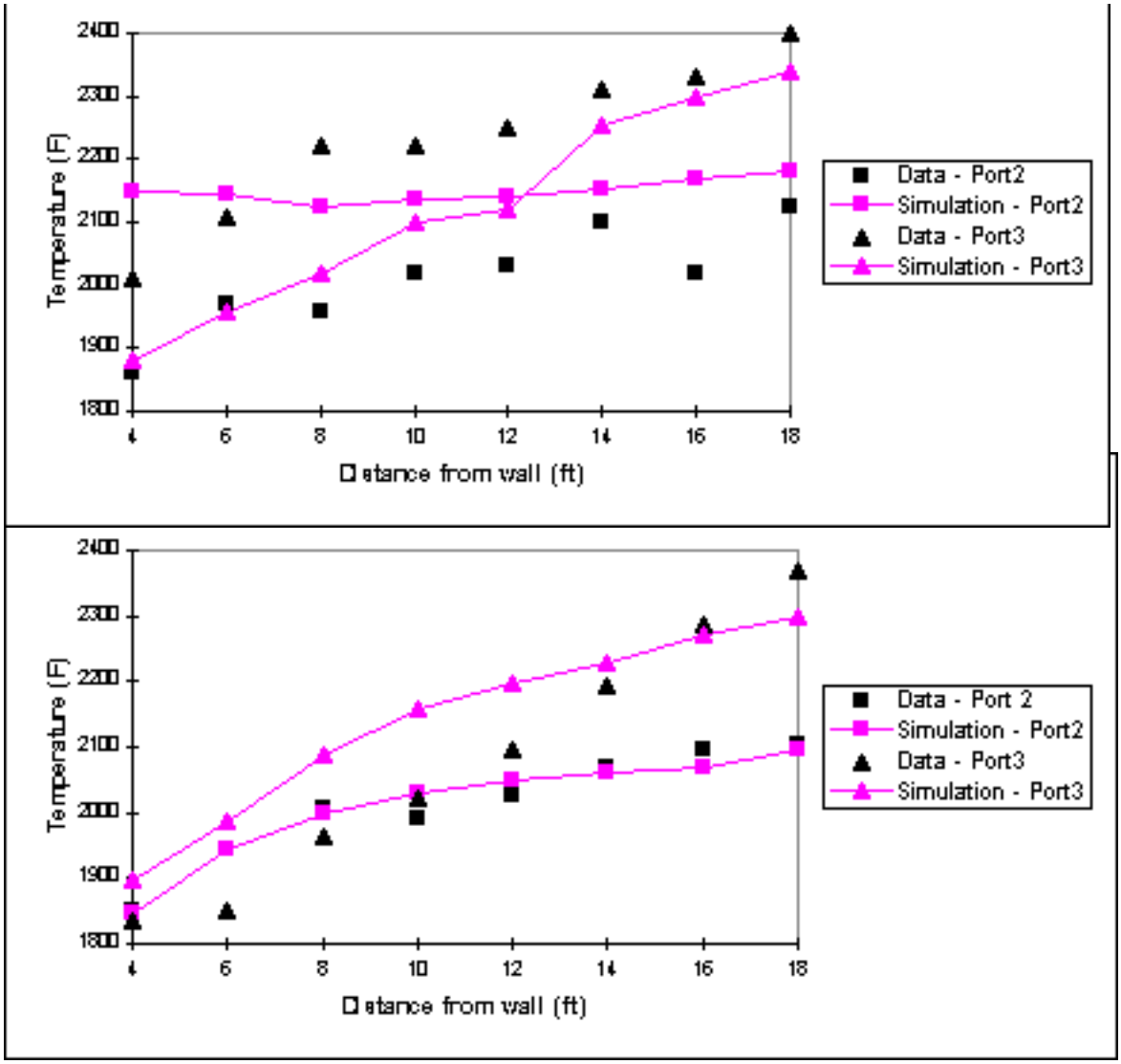

Figure 6.4 Temperature data and simulation results for probe paths.

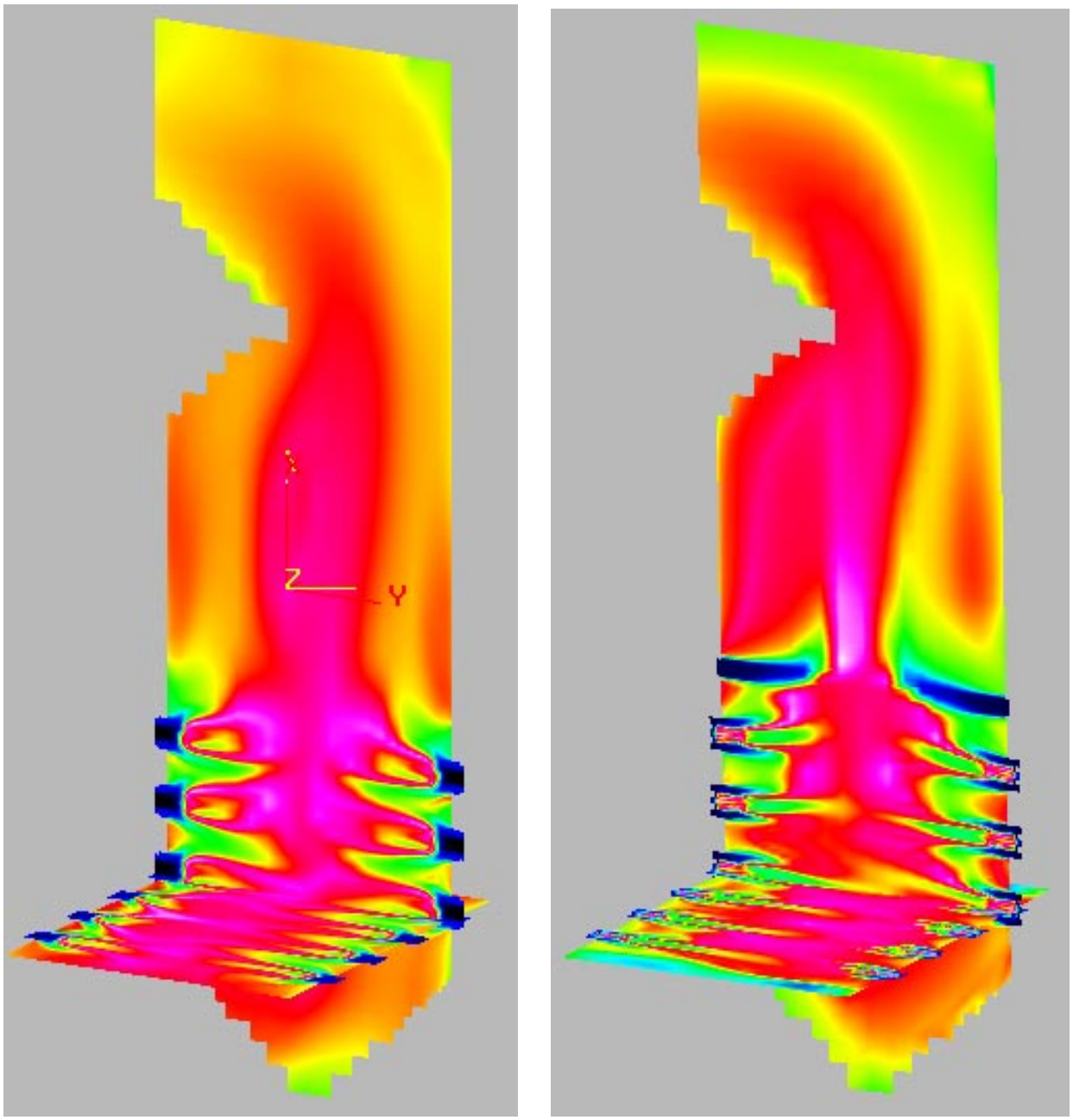

Prior to low-NO_x Retrofit

After low-NO_x Retrofit

Figure 6.5 Temperature field inside an opposed wall-fired furnace. Planes selected cut through the lowest burner row and the furthest burner column. White represents the highest temperatures, black the lowest.

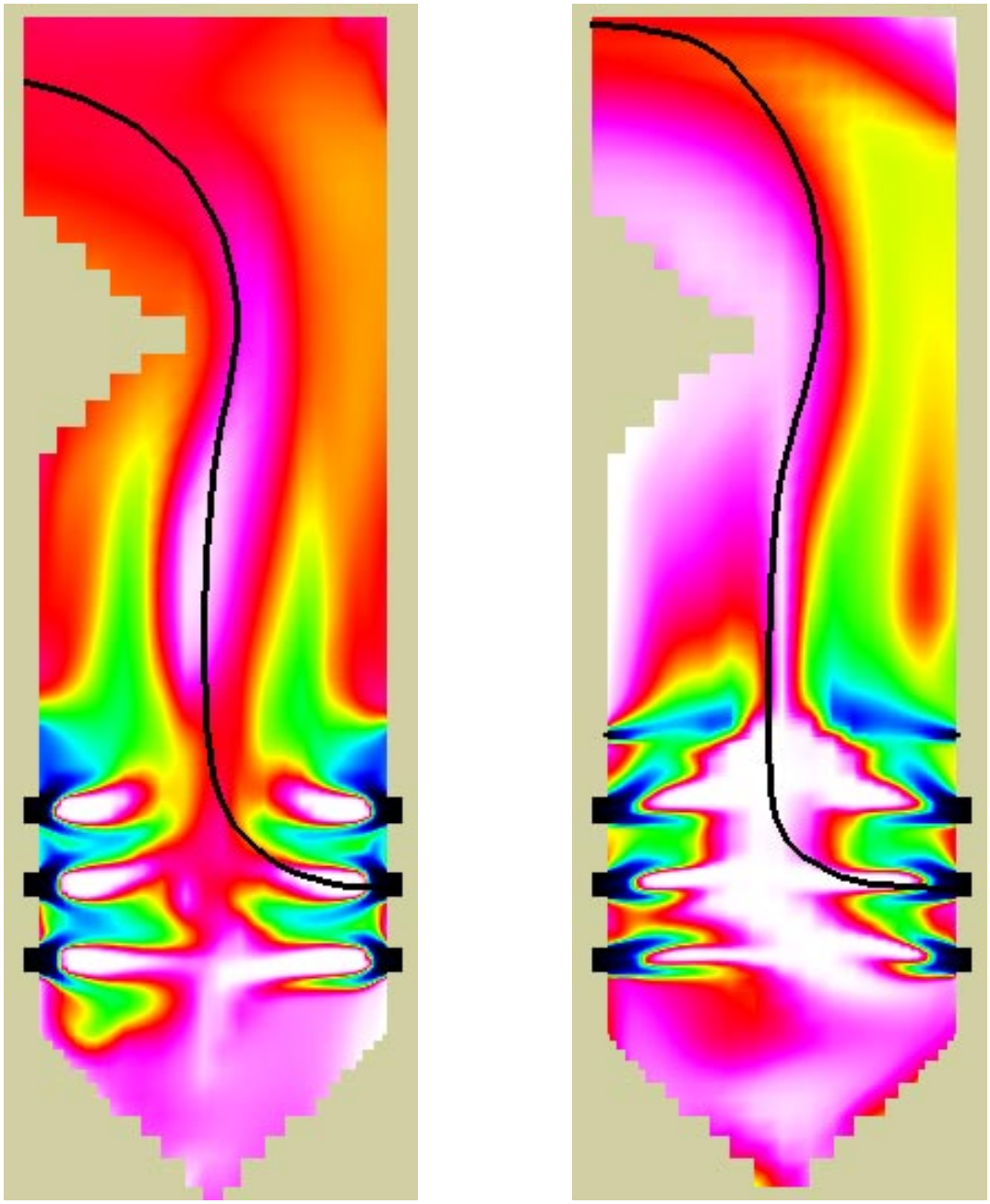

Prior to low-NO_x Retrofit

After low-NO_x Retrofit

Figure 6.6 O_2 concentration field inside an opposed wall-fired furnace. White represents the lowest O_2 concentration, black the highest.

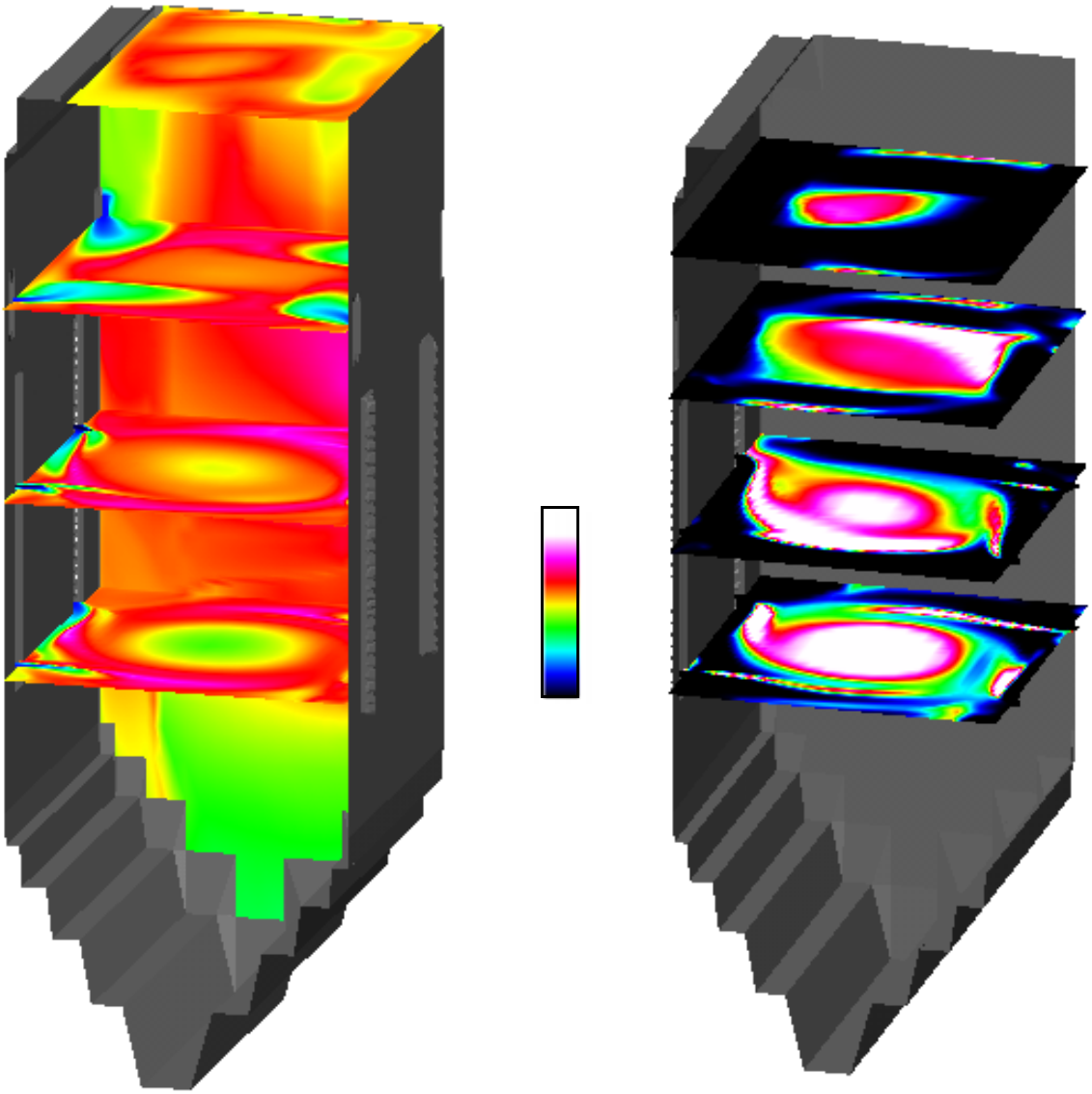

Keystone post-retrofit gas temperatures

Keystone post-retrofit H_2S concentrations.

Figure 6.7 Keystone simulation predictions.

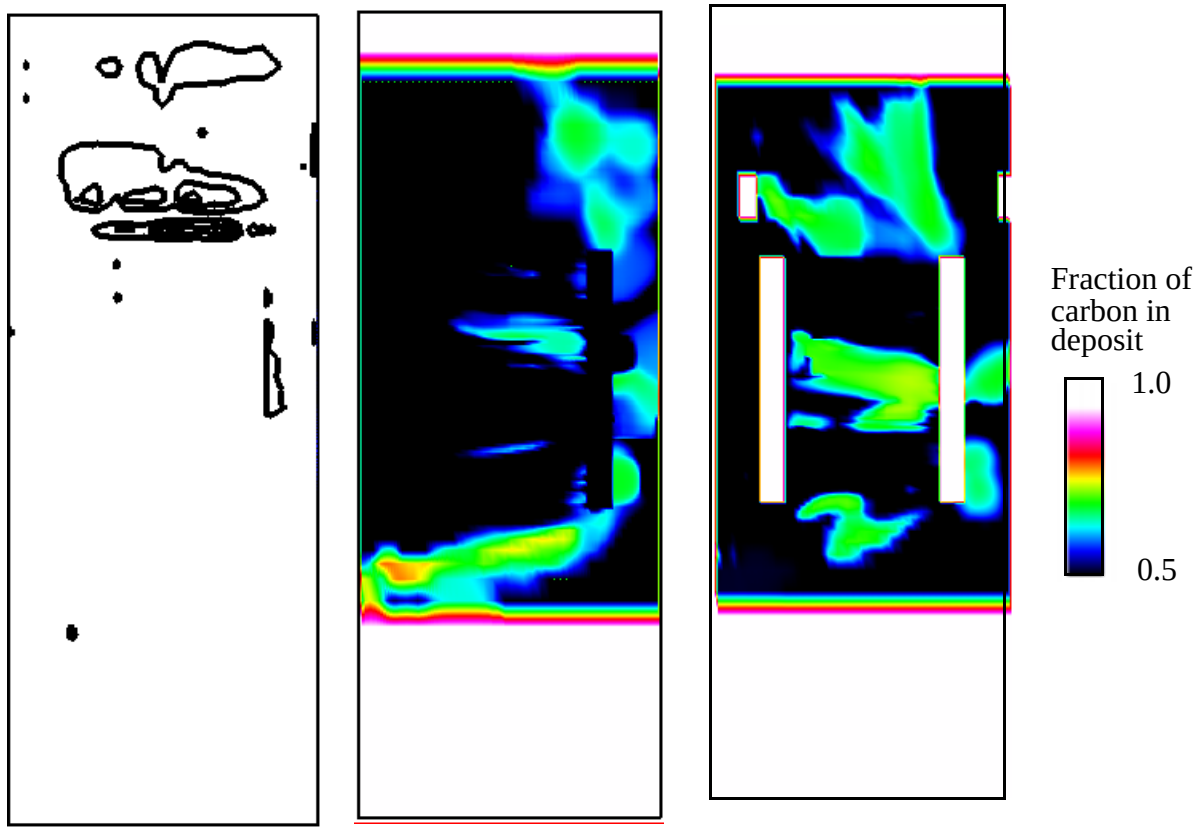

Figure 6.8 Measured corrosion on Keystone rear wall and fraction of carbon in deposit.

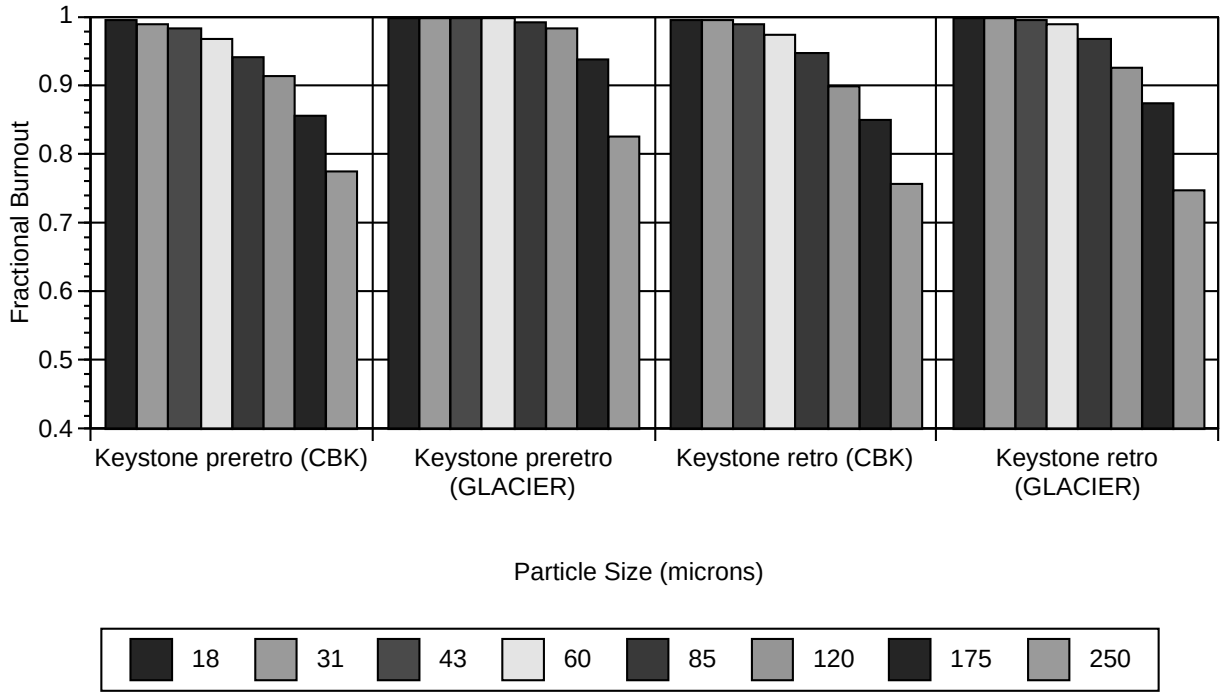

Figure 6.9 Simulated burnout as a function of particle size for pre- and post-retrofit boilers using conventional and CBK char oxidation model.

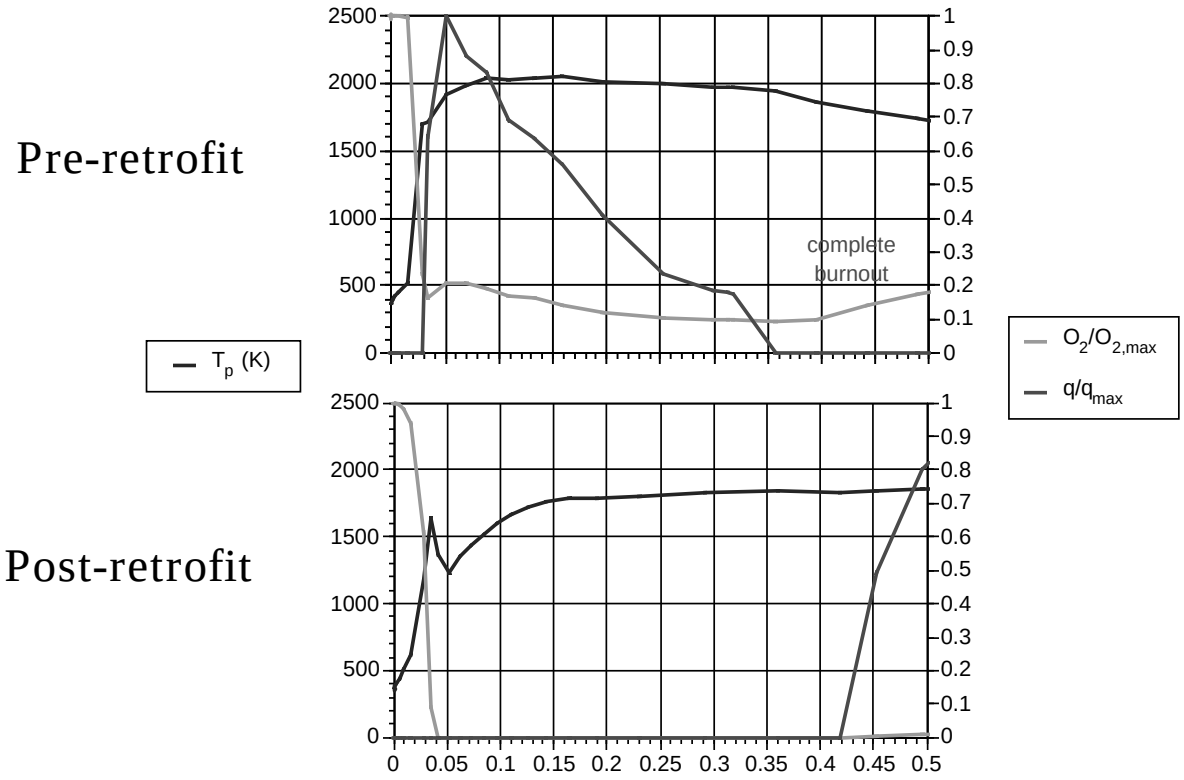

Figure 6.10 Particle temperature/oxygen concentration histories for identical particles during pre- and post-retrofit furnace simulations.

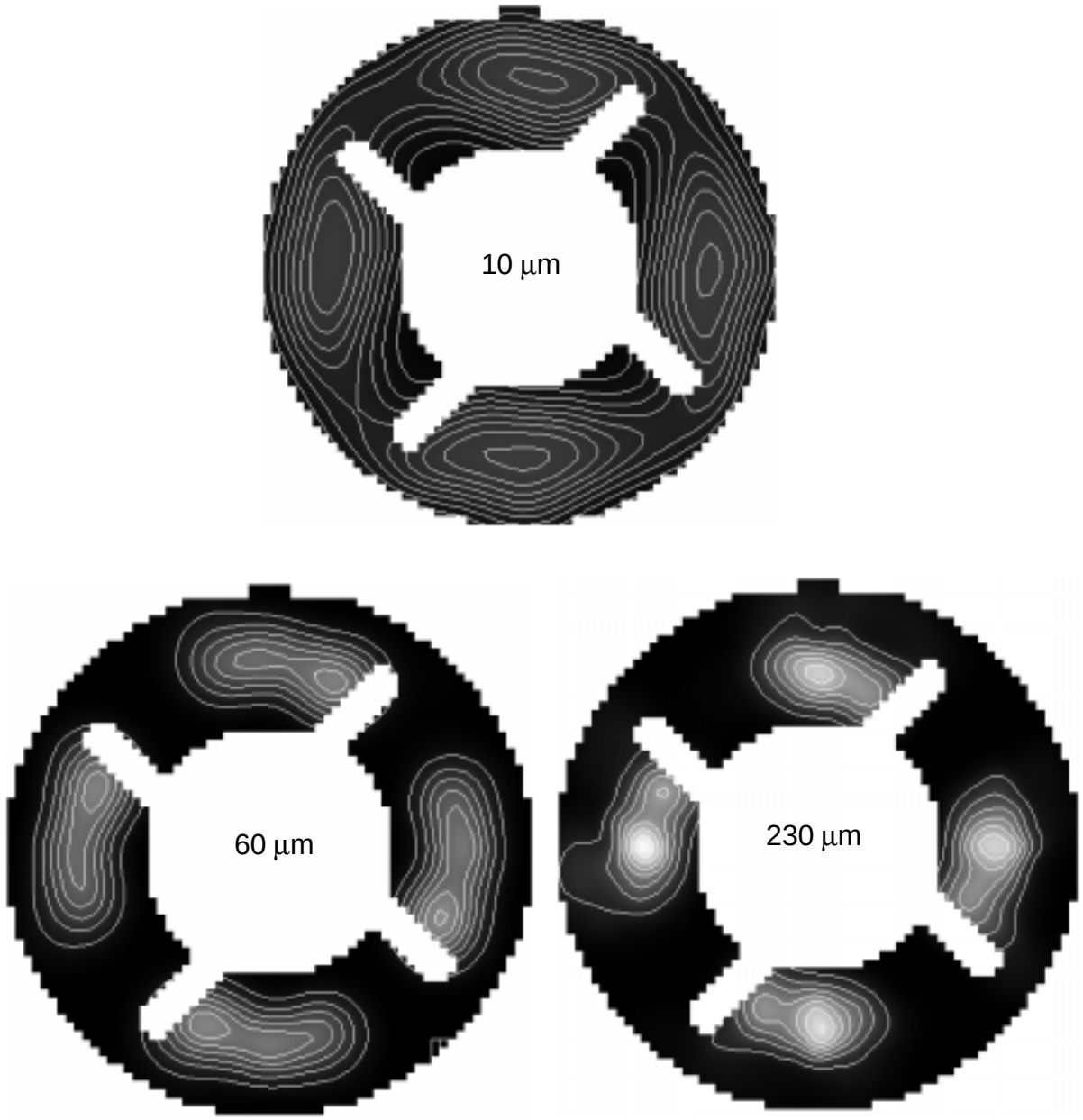

Figure 6.11 Particle mass density in the primary stream at the burner exit for three particle sizes.

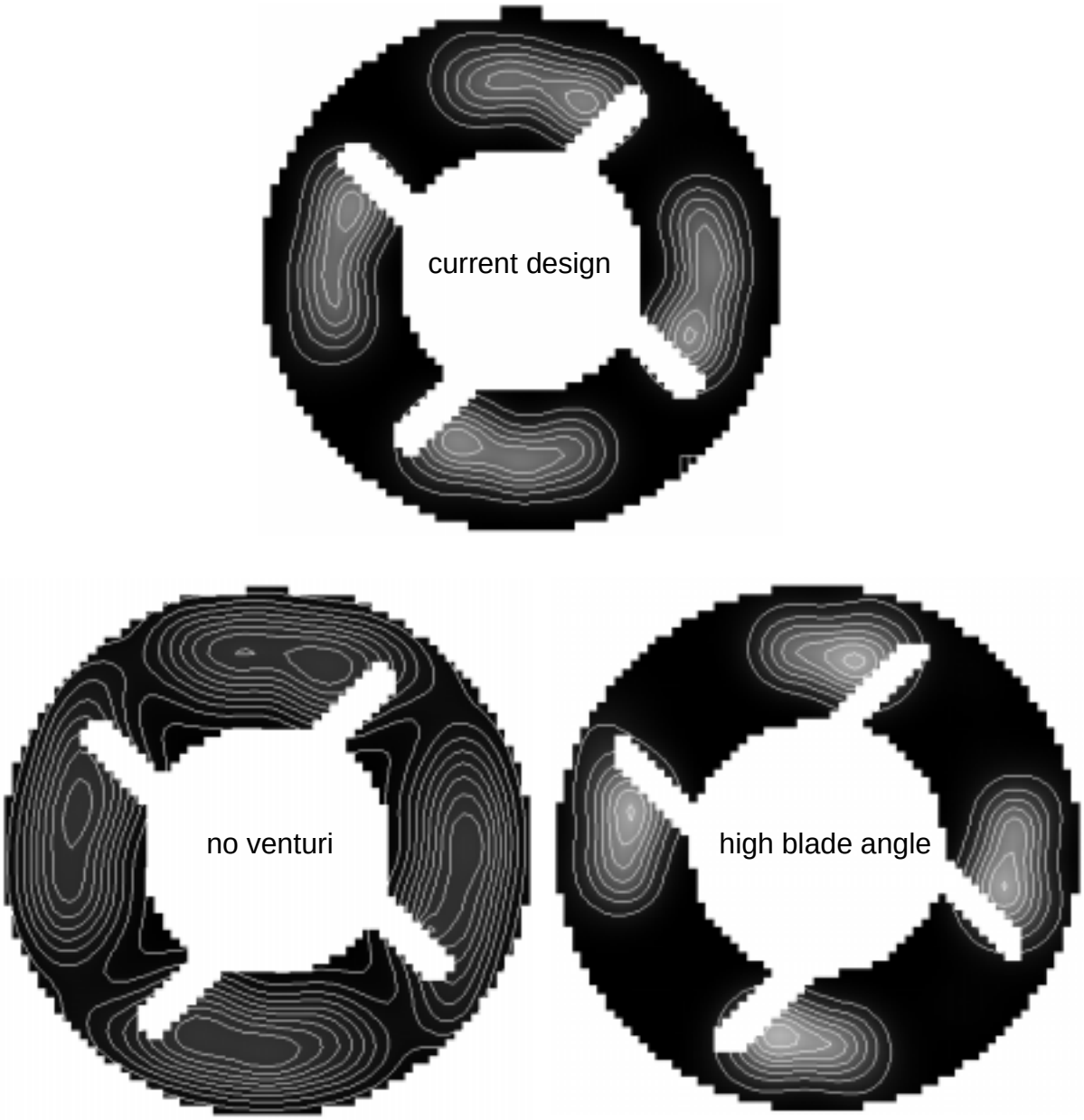

Figure 6.12 Particle mass density in the primary stream at the burner exit for three configurations for 60 μm particles.

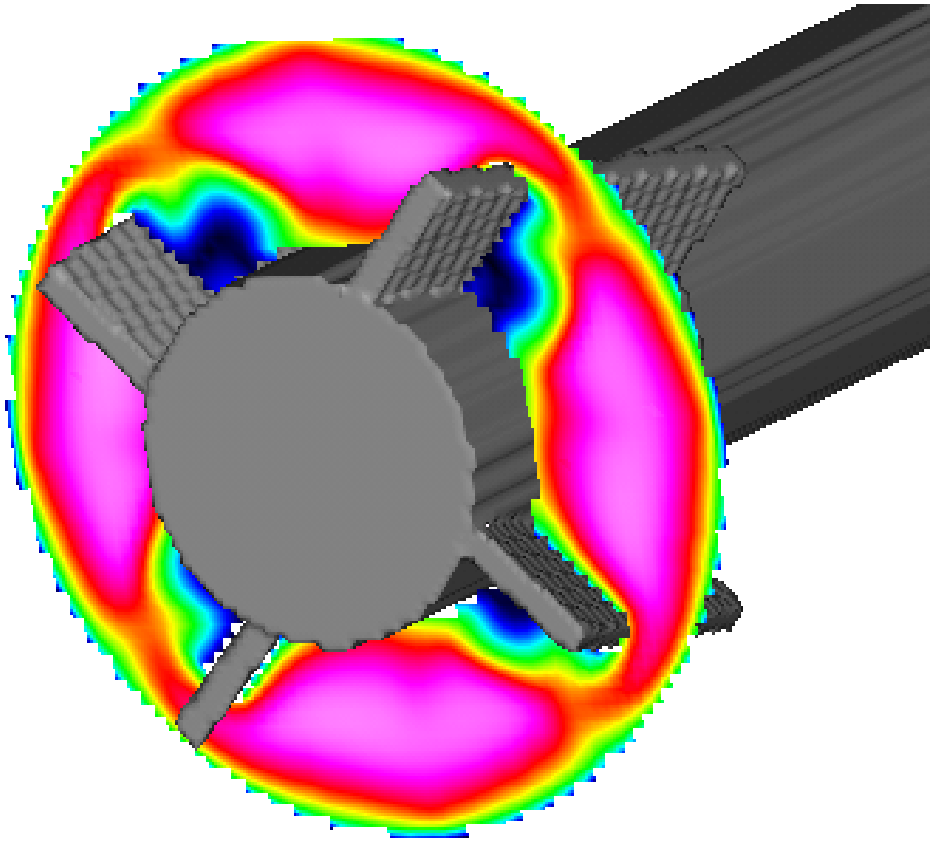

Figure 6.13 Velocity magnitude at a cross-sectional plane in the coal spreader section of the primary stream.

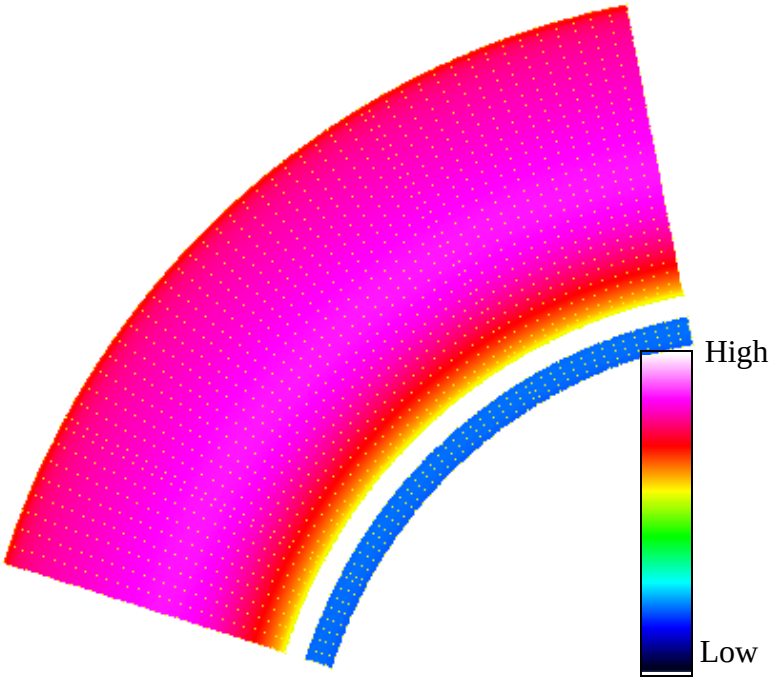

Figure 6.14 Velocity pattern over 1/6 of the exit plane in the secondary annulus. (Scale in m/sec.)

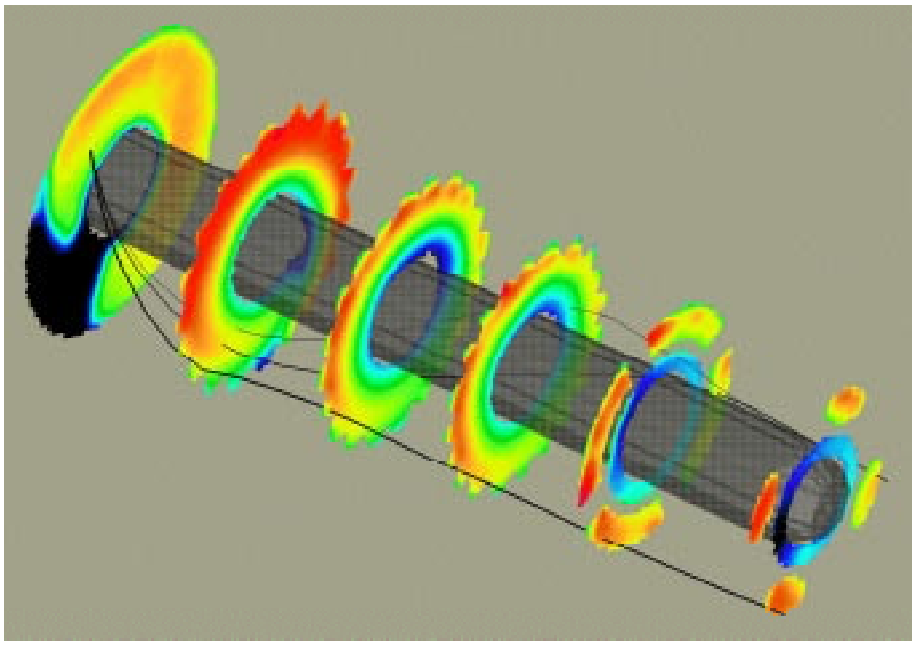

Figure 6.15 Effects of the coal nozzle on various particle sizes.

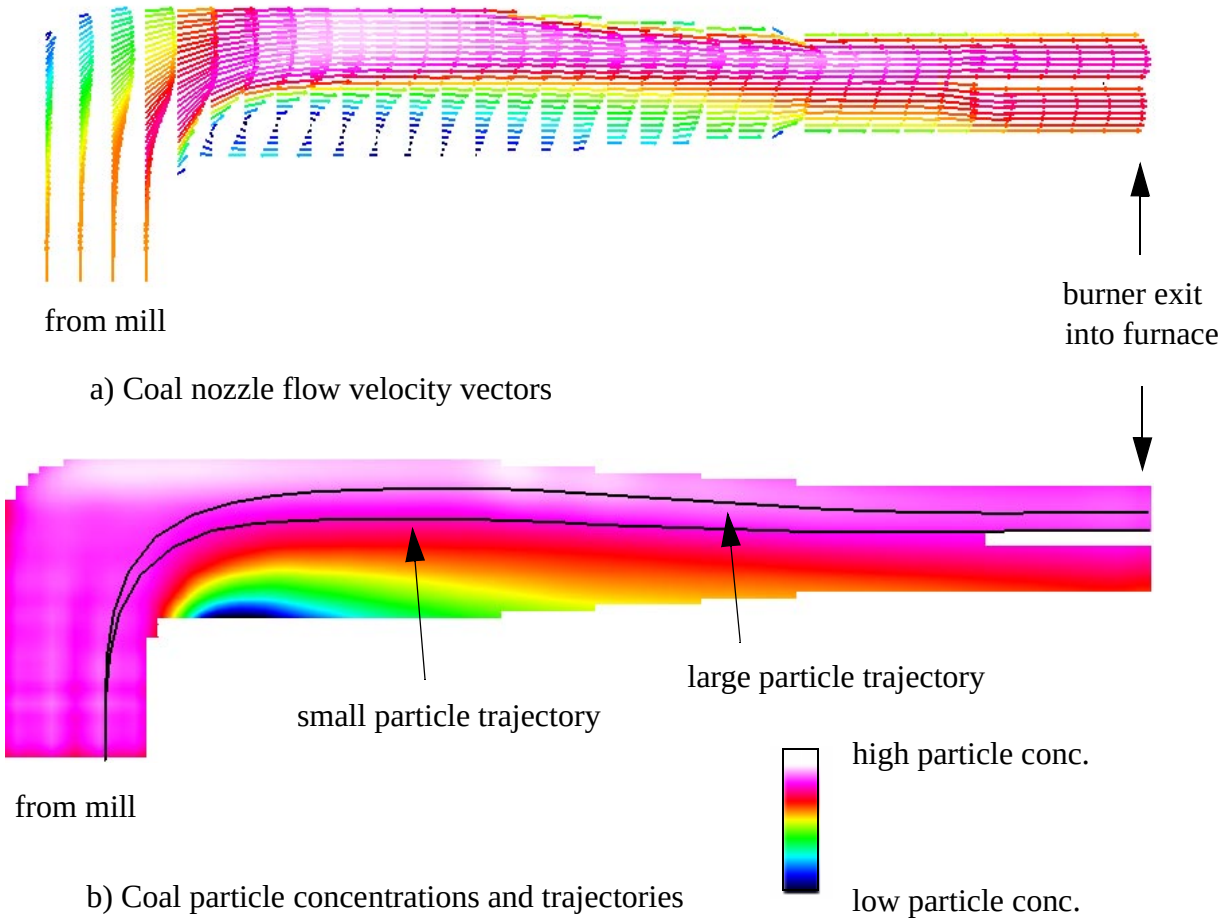

Figure 6.16 Keystone coal nozzle simulation.

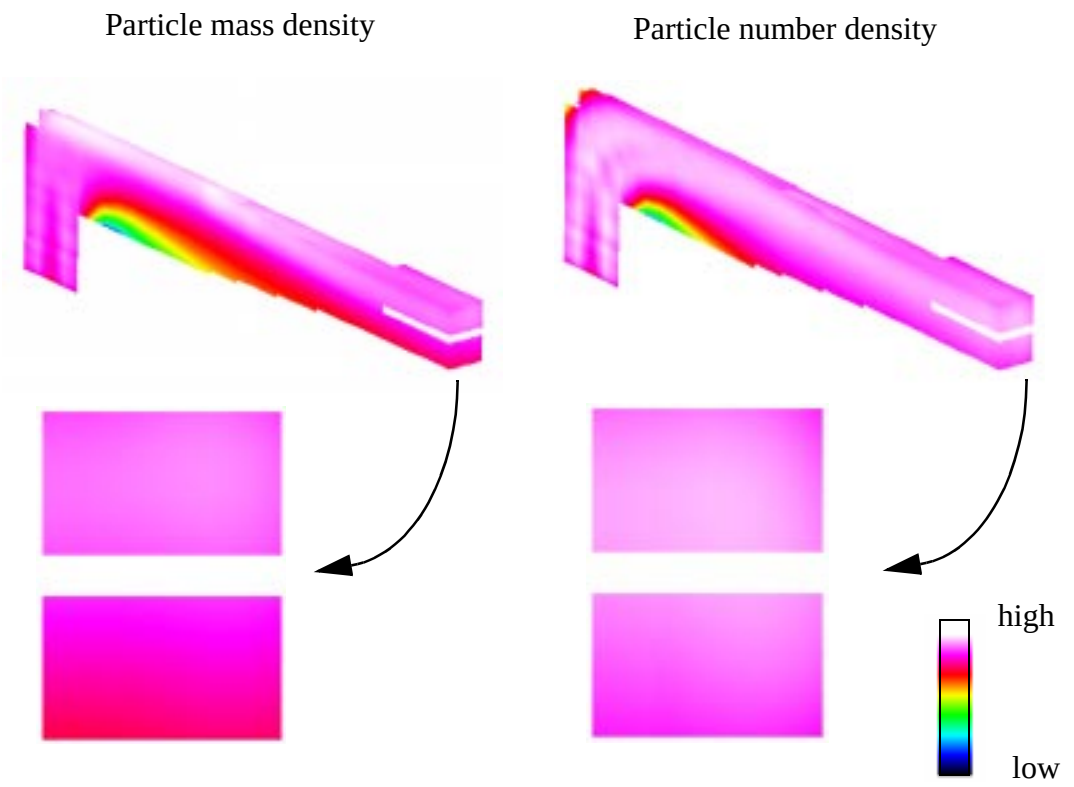

Figure 6.17 Particle mass and number concentrations at the exit plane of the Keystone coal nozzle.

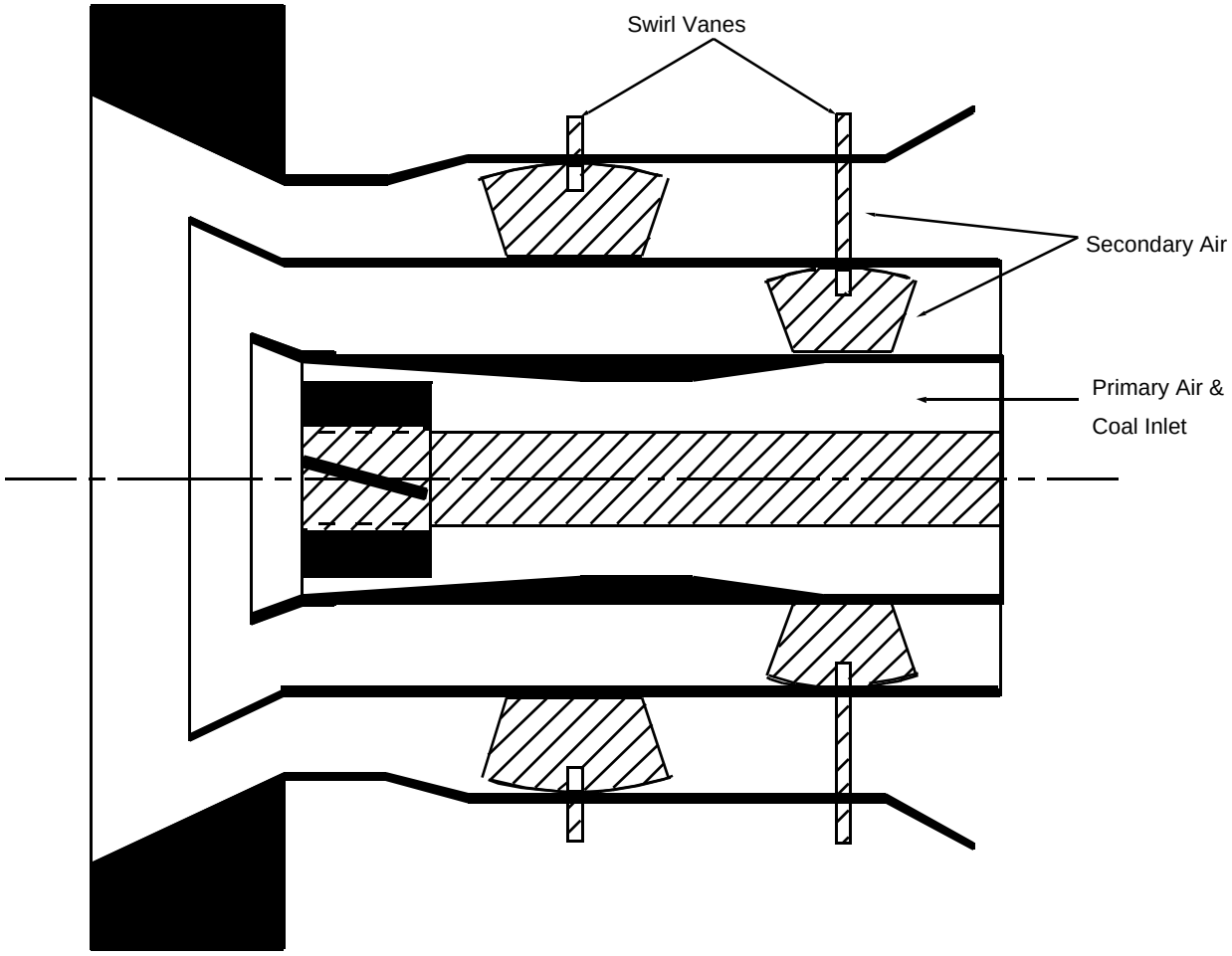

Figure 6.18 Schematic of the CCVII burner.

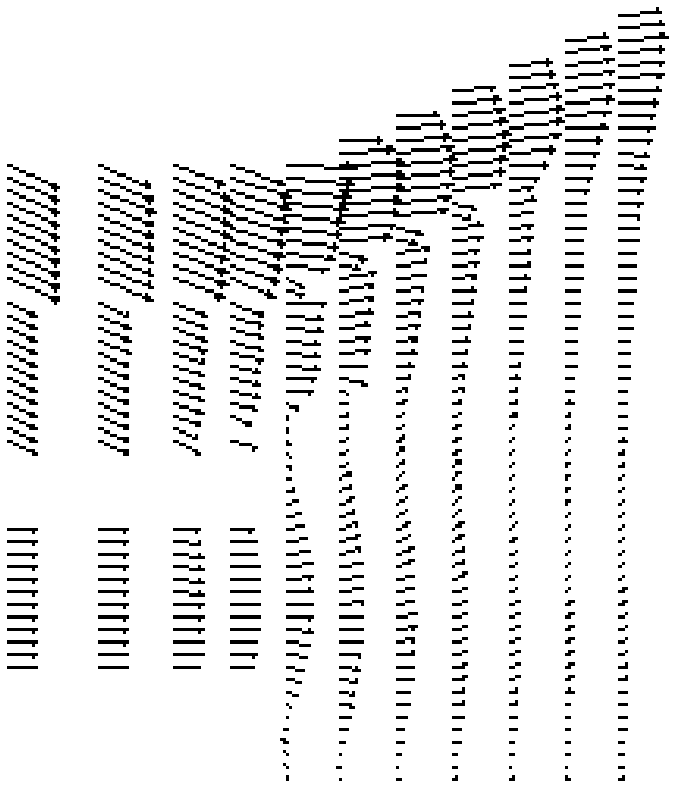

Figure 6.19 Velocity vectors in the CCVII nozzle (not all vectors shown).

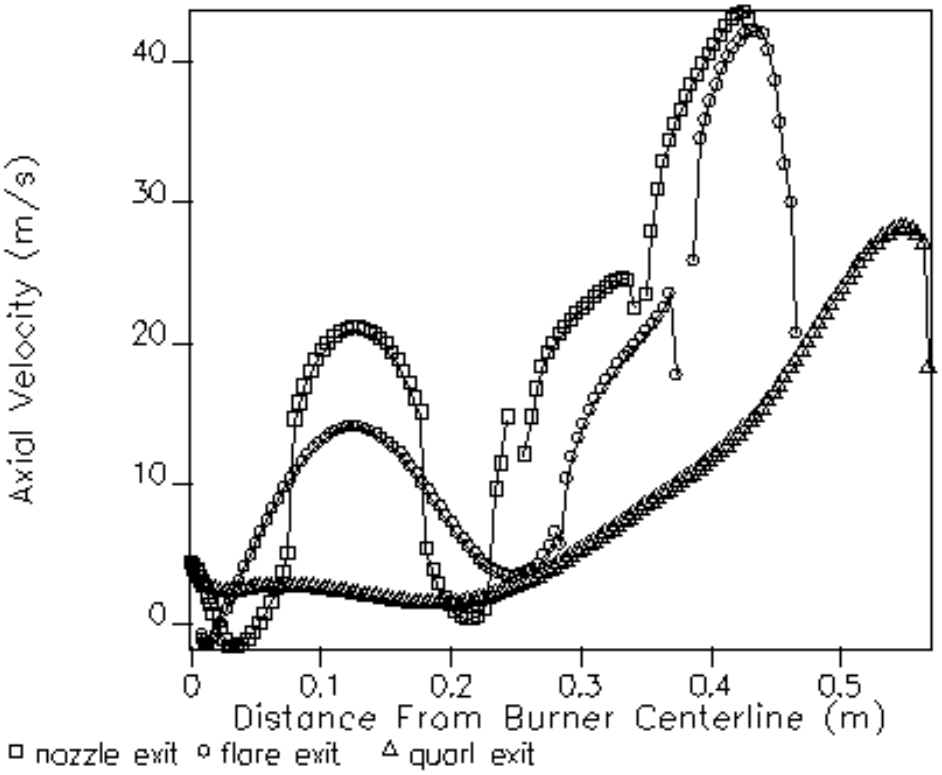

Figure 6.20 Axial velocity along selected radial locations.

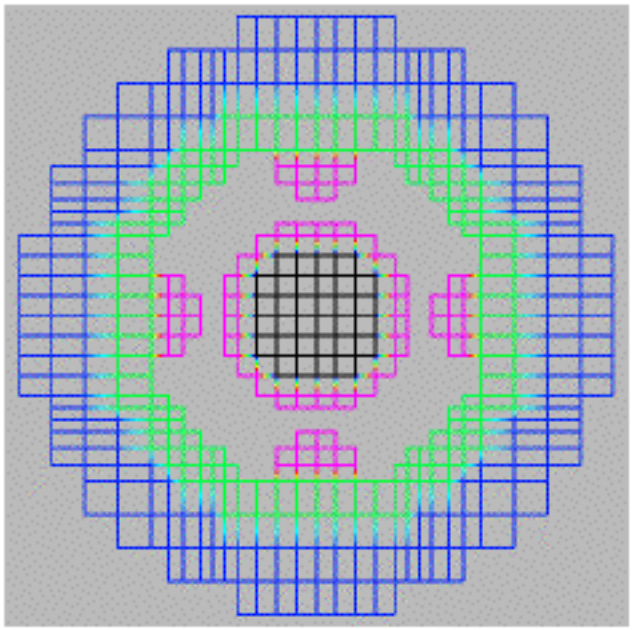

Outer Secondary
Inner Secondary
Primary Core

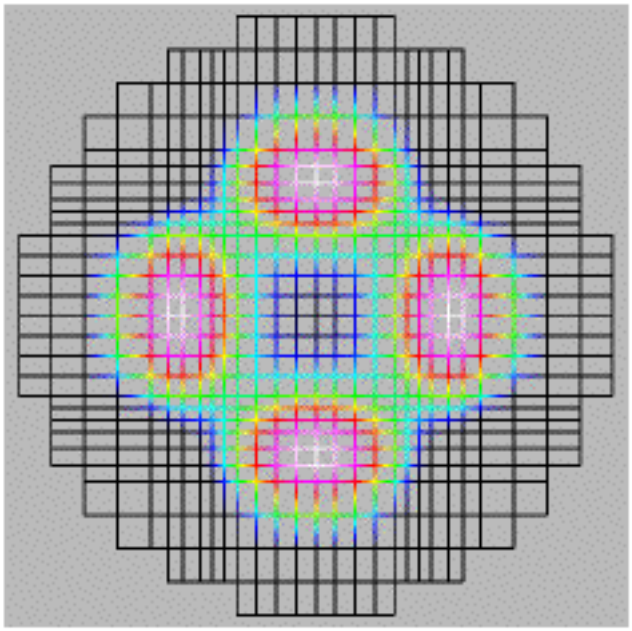

Particle Mass Density

Figure 6.25 Particle concentration mapping at burner exit as determined by coal pipe modeling.

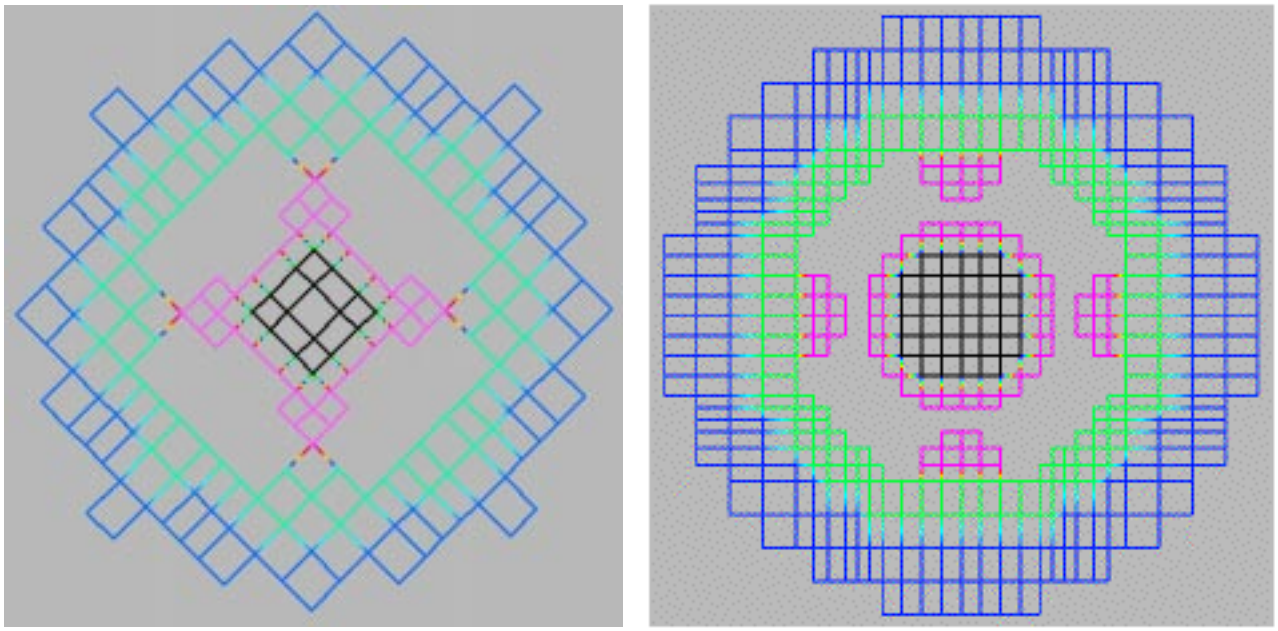

Figure 6.26 Mesh structure for the furnace and virtual test facility simulations.

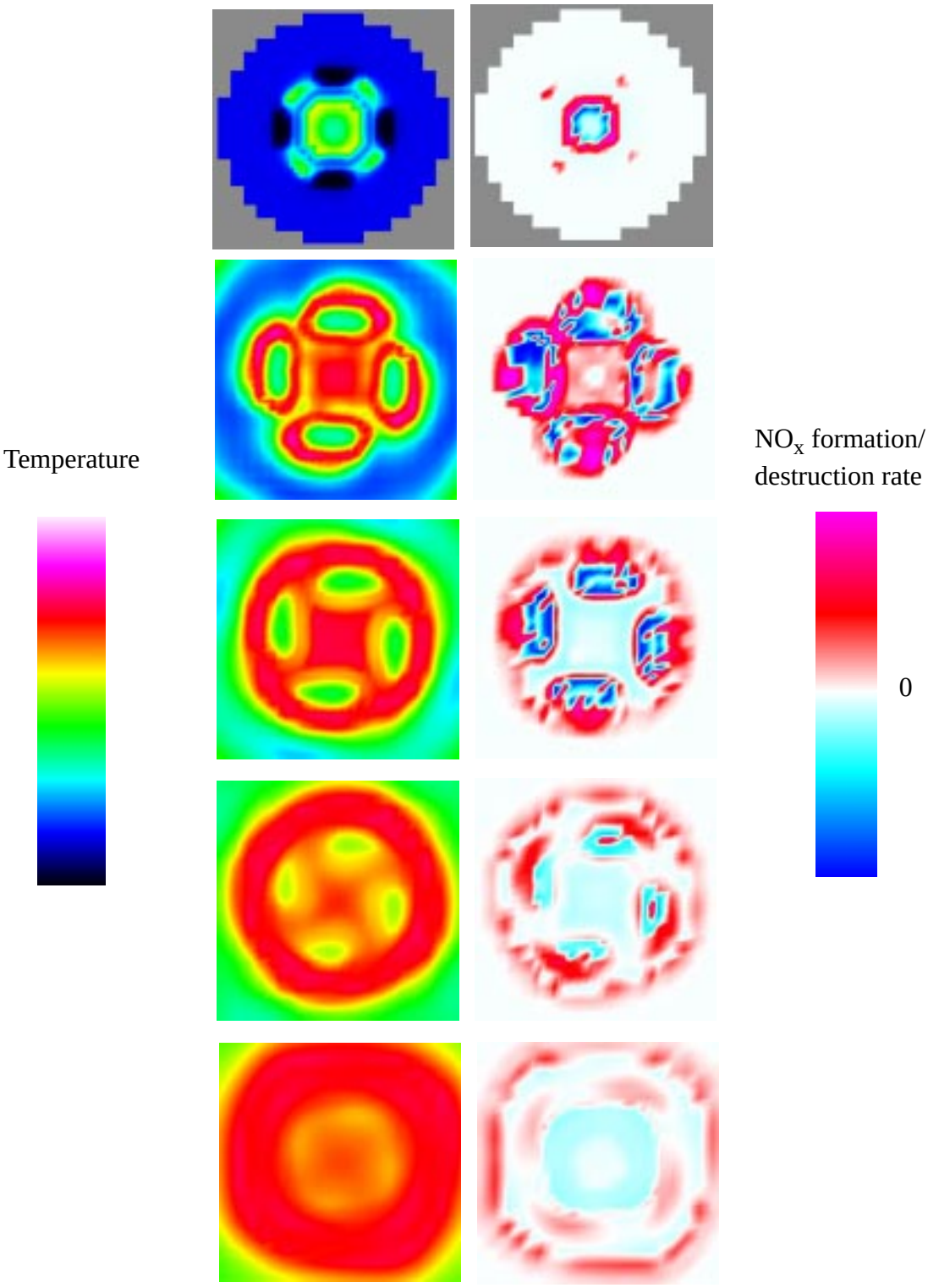

Figure 6.27 Temperature and NO_x formation rate distributions at several axial locations in the VTF.

7.0 CONCLUSIONS AND PHASE II PROJECT PLAN

7.1 CONCLUSIONS FROM PHASE I

Coal-fired boilers retrofitted with low-NO_x firing systems are experiencing problems due to an increase in unburned carbon and, in some instances, unacceptable increases in waterwall wastage rates. The goals of this program:

1. *To improve the performance of "in-furnace" NO_x control processes.* Performance is not restricted to final NO concentration but also takes into account all operational impacts such as unburned carbon, waterwall wastage, cost of improved pulverizers and potential for other pollutant emissions such as air toxics. In fact performance should relate total cost to emission reduction potential and must take account of site specific factors such as furnace design and coal.

2. *To devise new, or improve existing, approaches for maximum "in-furnace" NO_x control and minimum unburned carbon.* In addition to improved fuel injection systems this also includes overfire air port design, possible use of curtain air to protect waterwalls, and selective burner/pulverizer adjustment to reduce operational impacts without increasing NO_x emissions appreciably.

The objectives of the two phase program are to:

1 Conduct research to better understand the interaction of heterogeneous chemistry and two phase mixing on NO reduction processes in pulverized coal combustion.

2 Improve our ability to predict combusting coal jets by verifying two phase mixing models under conditions that simulate the near field of low-NO_x burners.

3 Determine the limits on NO control by in-furnace NO_x control technologies as a function of furnace design and coal type.

5 Develop and demonstrate improved coal injector designs for commercial low-NO_x burners and coal reburning systems.

6 Modify the char burnout model in REI's coal combustion code to take account of recently obtained fundamental data on char reactivity during the late stages of burnout. This will improve our ability to predict carbon burnout with low-NO_x firing systems.

The technical approach involves:

- Fundamental experiments to define NO reduction mechanisms in flames and reburning jets.
- Laboratory experiments and computer modeling to improve our ability to describe mixing of coal and air in the near field of pulverized coal flames.
- Evaluation of commercial low-NO_x firing systems using computer simulations.

- Development and demonstration of coal injectors for reburning and low-NO_x burners at commercial scale.

Central to this approach is the use of computer simulation to interpret data, help guide development and to evaluate the performance of full-scale systems.

7.1.1 Evaluation of Low-NO_x Firing Systems

Two pulverized coal fired boilers have been modeled using *GLACIER*, REI reacting CFD model, Keystone Unit 2 and Hammond Unit 4. Both units have been retrofitted with low-NO_x burners/firing systems and overfire air. Both units that have been impacted by the increases in unburned carbon resulting from their respective retrofits. One of them, Keystone has experienced a very significant increase in waterwall corrosion rates since retrofitting the low-NO_x firing system.

Keystone is a twin furnace, tangentially-fired unit with eight burner levels firing from four stacks on the front and rear walls. Figure 7.1 shows the predicted carbon burnout as a function of burner level and burner location for pre- and post-retrofit designs. Similar predictions, burnout as a function of burner, are available for Hammond and allow the same general conclusions to be drawn which are:

1 The predicted burnout shows that all burners do not contribute equally to the final burnout level.

2 Particle burnout varies with burner height and location.

3 As expected unburned carbon is highest for the post-retrofit cases.

These predictions of unburned carbon point to one major conclusion:

- Any evaluation of an in-furnace NO_x control technology must consider the total system and may be very boiler specific.

Consider possible methods for improving burnout without creating any undue impact on NO_x emissions. Increasing the fineness of the coal delivered to each burner is not necessary. It may not be necessary to modify every burner, it might be possible to operate the bottom rows more fuel rich and add air to the upper burners. Initial analysis of the overfire air (OFA) systems suggest that burnout could be improved by an improved design. But all the options require an accurate fireside simulator for a proper evaluation.

Although not part of the original scope, *GLACIER* has been used to determine the conditions that might lead to waterwall corrosion at Keystone. *GLACIER* does not predict corrosion rates but does provide an accurate picture of conditions close to the wall that might contribute to corrosion including:

- Local gas concentrations including carbon monoxide, hydrogen sulfide and sulfur dioxide.

- Heat flux to the wall; because this can affect deposit formation and slagging.

- Particle deposition rates at the wall.
- Carbon and sulfur content of the particles being deposited at the wall.
- Deposition rates of iron sulfide particles present in the coal stream.

The measured corrosion rates in the Keystone boiler are highest on the front and rear walls, above the close coupled over fire air, in the region of the separated over fire air, and lower on the side and center walls. The simulations suggest that high corrosion rates in excess of 50 mils/year occur in regions of the waterwall where there are high gradients in gas concentrations.

Figure 7.2 compares the burnout history for one particle cloud starting from the same location in the fuel injector for both the pre- and post-retrofit cases. Figures 7.2a and 7.2b show two particle sizes entering from the burners on the front wall at level six near the center wall. The smaller particle does not burnout in the post-retrofit case. Figure 7.2c presents the same information but for a particle cloud entering from the front side nozzle at the same level. This particle cloud burns out very rapidly in both the pre- and post-retrofit cases. This emphasizes the point made earlier that in order to solve the problems attributed to low-NO_x firing, it is necessary to consider the total system if the most cost effective solution is to be identified.

7.1.2 Improved Burnout Models

The fundamental studies carried out at brown University reached the following conclusions concerning carbon burnout kinetics and carbon burnout in low-NO_x systems:

1. Simple char oxidation models cannot predict a number of key features of recent char combustion data, including the low reactivity of residual carbon samples from commercial combustion systems and the low reactivities of laboratory samples at high conversion. Such simple models are not suitable for the specific application of carbon burnout prediction in pulverized coal combustion systems; special kinetics are required that incorporate submodels of char deactivation as a function of conversion and boiler environment.

2. The key features of recent char combustion data can be predicted by an integrated model that combines the single-film model of char oxidation with descriptions of thermal annealing, statistical kinetics, statistical densities, and ash inhibition in the late stages of combustion. The resulting Carbon Burnout Kinetic Model (CBK) is a coal general formulation that is specifically designed to predict the total extent of carbon burnout and ultimate fly ash carbon content for prescribed temperature/oxygen histories typical of pulverized coal combustion systems. The CBK model has been implemented in a computationally efficient FORTRAN code suitable for stand alone use or for incorporation into CRF-based simulators, as a subroutine or post-processor.

3. Simple simulations of idealized, but realistic furnace environments using the new CBK model reveal that carbon burnout and the corresponding loss-on-ignition (LOI) values for pulverized fuel fly ash are sensitive to a wide variety of fuel-related effects. These include: particle size distribution, ash content, char reactivity, char yield (volatile yield), thermal annealing, coal heterogeneity, swelling, ash/carbon interactions. No single

property of the fuel determines its carbon burnout propensity, and techniques based on a single property measurement will not likely be widely successful. The prediction of carbon burnout, or even the relative carbon burnout propensity of different fuels, requires a modeling tool that accounts quantitatively for multiple fuel-related effects.

4. Simulations of idealized furnace environments indicate that staging increases LOI by two mechanisms: (1) A decrease in available residence time in oxygen-rich post-flame regions, and (2) char annealing in the fuel-rich zone prior to the onset of oxidation. The calculations give an estimate of the relative importance of these two effects, which is dependent on flame temperature. Below 1800 K the residence time effect is more significant than annealing, and above 2000 K annealing makes a larger contribution. A third mechanism, especially important for overfire air systems is persistent unmixedness, extending beyond the near burner zone, an effect whose contribution cannot be estimated by the simple techniques employed with this model but they can be evaluated with *GLACIER*.

5. Further simulations of idealized furnace environments indicate the presence of an optimal flame temperature for simultaneous minimization of NO_X and LOI. By coupling CBK with the fuel nitrogen release kinetics of Pohl and Sarofim, and conducting one-dimensional two-zone simulations at constant LOI, the fraction of fuel nitrogen released in lean (oxygen-containing) zones was observed to pass through a minimum at a flame temperature of 1850 K. This optimum arises due to annealing, and to the knowledge of the project team this is the first prediction of the existence of such optimal flame conditions.

GLACIER includes a char oxidation model with a mean oxidation rate. The CBK model has been added as an option. Table 7.1 compares burnout calculated by the two mechanisms with the actual field measurements. The data and the predictions are very similar and show the expected

Table 7.1: Predicted and Measured Unburned Carbon (%)

	Measured	Glacier	CBK
Keystone Pre-retrofit	4 to 5	5	6.7
Keystone Post-retrofit	8 to 12	16.2	14
Hammond Pre-retrofit	4	3	4
Hammond Post-retrofit	8	7	

increase in unburned carbon as the NO decreases. Table 7.2.compares measured and predicted NO emissions. In both cases the predicted trend follows the measured data. There are some differences in the actual levels but it should be remembered that generic coal data are being used since coal specific kinetic information is not available.

Table 7.2: Predicted and Measured NO_x Emissions

	Measured ppm	Glacier ppm
Keystone Pre-retrofit	505	6.7
Keystone Post-retrofit	275	14
Hammond Pre-retrofit	727	800
Hammond Post-retrofit	305	310

7.1.3 NO Reduction Mechanisms

It is now well established that reburning or secondary fuel injection can be used to reduce previously formed NO and one of the hypotheses upon which this program plan was based concerned the mechanism of the reduction process:

- NO destruction processes are key in both low-NO_x burners and coal reburning and that there are indications that heterogeneous chemistry may play a role.

Detailed measurements have been made in a reburning jet suggesting that indeed heterogeneous effects may play a role but also that CO can destroy NO.

Conventional reburning chemistry is based on reactions between NO and hydrocarbon radicals. Figure 7.3 shows the results from simple reburning experiments in which CO or natural gas was added downstream of the primary flame. In each case the initial (primary zone) NO was 500 ppm. At stoichiometries near 1.0 (lower amounts of reburning fuel), CO is not as effective as natural gas at incinerating the primary zone NO. However, by a reburning stoichiometry of 0.8, the results are indistinguishable. These results clearly demonstrate that CH radical attack is not the only mechanism for reducing NO.

To confirm the importance of CO reactions, a series of experiments was conducted where NO was injected into combustion products at different distances along the furnace. Figure 7.4 summarizes these results for initial stoichiometries of both 0.85 and 0.95. Notice that at the optimum NO injection location, which is an indication of an optimum temperature, NO reductions on the order of 90% were achieved.

Unfortunately it is not easy to isolate the importance of heterogeneous NO reduction reactions under realistic combustion conditions; however, two different approaches were used to evaluate this issue. Bench-scale studies carried out at the University of Utah indicate that, in the absence of oxygen, char can reduce NO. Fundamental studies conducted at Brown University also indicate the possibility of heterogeneous reactions. Data were obtained for lignite chars, Illinois #6 chars, and petroleum cokes. These data were collected in a laboratory flame reactor where the different solid materials were injected downstream of a primary flame producing 1,000 ppm NO with 1% oxygen. The temperature at the point of fuel injection was approximately 2450°F and the downstream residence time was nominally 100 msec. The data are reported as NO reduction reactivity expressed as an apparent heterogeneous rate constant. The char and coke samples did produce reactivities on the same order as the highest reactivity kinetics measured by Aarna and Suuberg.

7.1.4 Two Phase Mixing Studies

An experimental system was developed and tested at the University of Utah to study two phase mixing for model development and provide information on the performance of different coal injection devices. The conclusions from these studies may be divided in to two categories:

1) The development and demonstration of significant new capabilities regarding the detailed study of particle dispersion, and

2) The application of these capabilities supporting the overall goals of developing improved low-NO_x burners.

Regarding item 1), the following are concluded:

- A coaxial annular jet facility has been designed and constructed that allows detailed and controlled study of a variety of factors affecting two phase dispersion phenomena in a geometry, and over a range of parameters, having broad relevance to coal-fired furnace injectors.

- A variation of Molecular Tagging Velocimetry (MTV) has been developed and demonstrated in the present two phase flow applications. This technique allows instantaneous velocity profile information to be measured to within about 8% uncertainty for mass particle loadings up to about 10%. A powerful outcome of this development is that the spatial structure of particle laden flow may be studied without having to resort to “surrogate measures” such as the single point temporal autocorrelation.

- A simple yet effective method of determining particle concentration information that employs an image processing based particle counting technique has been developed and applied.

Regarding item 2), we summarize what are felt to be the major results from the jet studies discussed above.

- Changes in the primary-to-secondary jet velocity ratio can have dramatic (and what at first seemed to be contradictory) effects on the net momentum, passive scalar, and particle transport produced by the coaxial annular jet.

- For the mass particle loading of 5% examined, the effects of particles on the annular jet (at any given axial location) and on its downstream development produced only very subtle feature variations in the mean and root mean square (RMS) axial velocity statistics.

- Comparison of two point axial velocity correlation data for radial separations revealed that important underlying structural changes occurred in the turbulence between both the V_s/V_p = 0.5 and 1.0 cases and, perhaps more significantly, between the pure fluid and particle laden cases. In particular, by an axial position of x/d = 7.5 the correlations indicated that both the pure fluid and particle laden V_s/V_p = 0.5 jet contains a single dominant turbulence structure having a radial scale that nearly spans the entire jet half

width. In contrast, the pure fluid results at $V_s/V_p = 1.0$ suggested the existence of two smaller scale but highly interacting structures. The addition of particles tended to slightly increase turbulence length scales, but more significantly, for the $V_s/V_p = 1.0$ case dramatically diminished communication (and presumably transport) between the inner and outer structures. The correlation results provided clear indications as to why the comparisons between the passive scalar and particle dispersion measurements produced apparently contradictory results.

- An initial study of the effects of a primary jet coal spreader geometry qualitatively validated *GLACIER* code simulations of a similar geometry.

7.1.5 Integrated Control Concepts

Figure 7.5 summarizes the results of a series of experiments designed to investigate the impact of combustion conditions on NO formation and carbon burnout. These results clearly indicate that if one wishes to simultaneously achieve good carbon burnout and low NO_x emissions, it will be necessary to provide sufficient oxygen early in the combustion process to ensure that the largest particles are completely burned. This will inevitably result in the production of significant NO_x which must subsequently be destroyed.

Data obtained at bench- and pilot-scale indicate that an improved coal injector might overcome the problem of increased unburned carbon when NO emissions are reduced. It is based on the following concepts:

- Radially stratified stoichiometries;
- Segregated particle size - larger particles are injected on the periphery of the coal jet to maximize their time under fuel lean condition;
- Smaller particles are injected on the center of the jet because they will spend the maximum time under fuel rich conditions. However, because they are smaller they will have the maximum opportunity to burnout; and
- A central fuel jet provides for in situ reburning thus reducing the need for deep furnace staging and reducing the demands on the OFA system.

Radial stratification is indicated by the bench-scale studies carried out with the SPCC burner. Table 7.3 shows the measured NO as a function of coal split between the inner and outer burners at a constant overall excess air. Under uniform conditions at an overall stoichiometric ratio of 1.05 the

Table 7.3: Dual Premixed Burner (overall SR = 1.05)

Inner/Outer Split (%)	SR_i	SR_o	ppm NO
75/25	0.5	2.6	480
50/50	0.8	1.3	460
25/75	1.6	0.9	425

NO emission was 650 ppm showing that radial stratification reduces NO. Overall these results suggest that if the largest coal particles were concentrated in an outer stream which was operated under excess air conditions, it should be possible to achieve high burnout and low emissions.

In a previous DOE funded program we discovered that if a small amount of natural gas was added around the periphery of an axial coal jet (to ensure firm flame anchoring on the fuel injector) significant emission reductions could be achieved. In the current program we discovered this process could be even further enhanced by adding the natural gas on the axis of the pulverized fuel jet which we refer to as in-situ reburning. Figure 7.7 summarizes these results which are of particular interest because, when properly designed, this scheme would allow the pulverized coal to be burned under near stoichiometric conditions which favor the carbon oxidation. NO emissions of only 132 ppm were achieved with 4% natural gas and a coal jet stoichiometry of 0.9. Similarly low emissions were also achieved for even higher coal jet stoichiometries, but more gas was required. Emission levels below 150 ppm and low unburned carbon without the use of any selective reduction chemicals would be very economically attractive.

Figure 7.7 illustrates how the concept would be applied to a real burner. The larger particles would be stripped from the coal stream at the tangential entry to the coal pipe. This stream of large particles would be injected through the outer annulus. The remainder of the coal stream would be injected through the inner annulus. Thus the large particles would "see" mainly fuel lean conditions; although they will generate NO, this will be reduced as the fuel lean stream mixes with the fuel rich stream formed by the bulk of the coal injected through the inner annulus. The fuel injected on the axis could be gas, oil or coal (preferably gas or oil) and this is the reburning fuel.

7.2 PHASE II PROJECT PLAN

We envisage two products proceeding to maturity level III as a result of this program: 1) improved fuel injection systems for four types of low-NO_x firing systems, circular burners for wall-fired units, circular burners for vertically-fired units, tangentially-fired units and reburning systems, and b) a fireside simulator based on *GLACIER* that will run on a personal computer.

Because of the problems being experienced by those utilities that have retrofitted low-NO_x firing systems and the need of other utilities who must apply NO_x control technology to meet Phase II CAA rules, there is considerable pressure to find solutions to the problems of increased unburned carbon and waterwall wastage. EPRI has indicated that if the pilot-scale testing shows promising results then a field demonstration at full-scale could be initiated without single burner, full-scale testing. Because of the urgency and the potential for early commercialization, we have changed the emphasis of the program and reduced the amount of full-scale testing.

The simulations for the Hammond and Keystone units clearly indicate that it is not possible to evaluate low-NO_x firing systems and their potential problems without some methodology which takes account of burner-to-burner variations. In the original proposal it was thought that one of the products from this effort would be "to upgrade REI's coal combustion simulation codes." Because of the improved performance of pc computers, it is not necessary to rely on expensive workstations to run fireside computer simulations. Also, many utilities have several units of almost identical design. Thus, as part of Phase II we propose to develop a customized fireside simulator for a specific class of units with a "windows" type interface that will allow the non-CFD practitioner the capability to simulate a pulverized coal fired boiler and to explore a finite range of operational

variations. In addition we intend to add an air toxics module. Since different particles experience widely different temperature histories, then, just as carbon burnout will change so will metals release. This module will add to the value of the fireside simulator.

The four technical tasks **(Task 1** being the development of the Work Plan) described in the original program form the basis for the Phase II Project Plan which will be executed by the same organizations that carried out Phase I.

7.2.1 Task 2: Injector Development

The injector development studies will be carried out at the University of Utah in the test facilities described in this report.

Task 2.1 Two Phase Mixing Studies

Having established the experimental facility and techniques described in Section 4.0, the recommended course for future work is to utilize these capabilities to:

1) Continue to map out the flow features and the basic underlying mechanisms of particle dispersion in the annular jet (as a function of velocity ratio, swirl, and particle loading), and, more importantly

2) Add and explore modifications to the annular jet that contain features having specific and direct relevance to low-NO_x burners.

As we have shown because of the unusual capabilities of the MTV technique, we are able to measure instantaneous velocity profiles. This allowed, for example, two point correlations to be computed. The usefulness of these correlations was apparent in that they provided a clear explanation as to why the particle and scalar concentration data exhibited apparently contradictory results. Thus, an essential component of the continuing research relevant to the second item above should be to use the strengths of the MTV technique to better understand how and why some coal injector designs lead to mixing behaviors that produce low NO_x emissions. Similarly, these data, as well as the continuing work on the basic mechanisms in the annular jet, should further enhance code development and validation.

Regarding the data analysis capabilities provided by the MTV technique, it also needs to be stated that many other important measures of the turbulence can be computed, and should be explored. In particular, differentiation of the instantaneous profiles yields the radial velocity gradient profiles. These gradients provide the largest contributions to the dominant component of vorticity in the flow. As mentioned in Section 4.0, it has been readily established that large scale coherent vortical motions have a disproportionate effect on the turbulent transport of particles. Thus, by quantifying, for example, the effect that a particular flow management device (e.g., coal spreader) has on the velocity gradient field (and on the spatial structure of the velocity gradient field via two point correlations), a description of the flow management device in terms of the mechanisms they employ/enable, rather than the net symptoms they create, may be derived. From a design standpoint, this, of course, has obvious advantages. Furthermore, owing to the fact that velocity gradients have the units of s^{-1}, they represent perhaps the most accurate measure of the turbulent time scale(s). Thus both instantaneous and statistically based measurements of the Stokes number, as a function of

radial and axial position, may also be used to characterize the effect of, for example, a particular swirl generator.

Finally, part of the continuing work should be devoted to establishing the capability to measure instantaneous spatial distributions of the fluid velocity and particle concentration (and/or particle velocity) simultaneously. A primary attribute for such a capability is that it will allow joint fluid-particle statistics (as a function of spatial separation) to be computed. The need for these statistics are twofold. First is that, for purposes of flow management device characterization, these statistics provide direct information relating to how the instantaneous turbulent motions created by a particular device affect particle dispersion. Second is that a number of joint statistics appear in the equations describing two-phase transport. These equations are, of course, the basis for the models employed in the large scale computer codes that are use to simulate industrial furnace applications. Thus, the benefits of such statistics to further code development would be highly significant.

Task 2.2 Bench-Scale Studies

Experiments in the U-Furnace are extremely cost effective and help direct device development at the more expensive pilot-scale.

Series A - objective to quantify the impact of particle size and stoichiometry distribution on carbon burnout in a realistic combustion environment. The premixed burner will be used with three different size-classified coals. NO, carbon burnout and fly ash particle size will be measured as a function of:

- initial coal particle size,
- final excess oxygen, and
- burner stoichiometry.

Series B- objective to demonstrate that low NO emissions and high carbon burnout can be achieved by segmenting the coal particle size classes and the stoichiometry. The SPCC will be used with the same three coals but dual coal feeders will be used to deliver different sizes of coal to the core jet and the outer annulus. Thus, coal flow rate and particle size can be controlled independently. NO, carbon burnout and fly ash particle size will be measured as a function of:

- initial coal particle size,
- final excess oxygen, and
- burner stoichiometry.

Series C- objective to determine whether under ideal conditions there is an optimum flame temperature for minimum NO and maximum burnout as suggested by the modeling with CBK at Brown University. The premixed burner will be used at different furnace heat loads and NO_x and burnout will be measured for the three coal types.

Series D - objective to evaluate to what extent unburned carbon in ash correlates with the conversion of iron sulfide to iron oxide. A high pyrite coal will be burned in the premixed burner and the fly ash will be collected and analyzed for carbon and iron sulfide for the following variables:

- initial particle size,
- burner stoichiometry, and
- excess air.

Task 2.3 Pilot-Scale Studies

These studies will continue the initial pilot-scale work that is currently being carried out. Three classes of burner systems will be evaluated:

- circular burners (wall fired);
- stacked axial flame burners (corner fired); and
- vertically fired systems (down or U-fired).

Series A: U-Fired Operating the L1500 without cooling allows the simulation of a wet-bottom unit. The in situ reburning concept will be tested for application to the LEBS program. The double concentric swirl burner will be configured to duplicate the DB Riley CCVII burner but with an in situ reburning injector. Tests will be carried to compare the performance of this burner with the Riley design for different reburning fuels under staged and unstaged conditions.

Series B: Wall Fired The double concentric swirl burner will be used to evaluate the radially stratified axial swirl concept described in the previous section. The furnace will be set up with water cooling to simulate the thermal conditions of a dry bottom unit. Two coal feeders will be used to control the feed rate to different annuli and the following variables will be investigated:

- coal distribution;
- reburning fuel type coal, oil or gas;
- firing rate;
- excess air;
- burner stoichiometry;
- swirl distribution; and
- coal type.

Measurements will be made of NO and carbon in ash.

Series C: Stacked Burner Studies A new vertically stacked burner array will be constructed with one fuel nozzle two air nozzles placed above and below. The fuel and air nozzles will be capable of

yaw but not tilt. Two separate coal feeders will be used to vary the coal particle size across the rectangular coal nozzle. The following variables will be investigated:

- coal distribution;
- reburning fuel type coal, oil or gas;
- firing rate;
- excess air;
- burner stoichiometry;
- swirl distribution; and
- coal type.

7.2.2 Task 3: Char Reactivity

The major objectives of Phase I work in this task were achieved, comprising (a) the completion, transfer, and initial application of the CBK model of the carbon burnout process, and (b) the measurement of the NO reduction activity of very young chars representative of those found in flames and reburning zones. Both major Task 2 activities produced promising leads that will be exploited in phase II to obtain a better understanding and predictive / design abilities for simultaneous NO_x/LOI minimization. This section of the Phase II work plan outlined below is essentially unaltered from the original proposal, but contains an additional subtask on the connection between combustion conditions and the properties (rather than amount) of unburned carbon. This subtask was prompted by interesting new leads arising out of parallel DOE/EPRI-sponsored work at Brown University and can be accomplished without significant additional resources, as it will be carried out in connection with the experiments already planned on the entrained flow reactor facility.

Task 3.1 Computational Studies of Carbon Burnout

Work in Phase I has provided computational tools for exploring the effects of furnace design, grinding practices, fuel properties, etc. on unburned carbon. Initial applications of CBK in idealized furnace environments and as a post-processor on REI's simulation packages have demonstrated the sensitivity of carbon burnout to most of the major model features, including thermal annealing, statistical kinetics, and ash inhibition. In Phase II, emphasis will be placed on the application of the tools to address key issues in carbon burnout, including

- the effect of particle size segregation (intentional or unintentional) in low-NO_x burners or flames on LOI characteristics. Recent work has shown the existence of an optimum size and temperature for the fuel-rich zone in an idealized staged combustion system for simultaneous minimization of LOI and NO_x. Further, the optimum values are dependent on particle size. This raises the possibility of reducing NO_x/LOI through partial size classification in the burner or flame and the creation of tailored environments for the different particle size fractions. Preliminary simulations with separately optimized parallel streams of course and fine particles indicate some real potential for reductions in LOI (at constant NO) below the optimum already found for

non-segregated flows. More calculations are needed to establish the potential of this approach.

- the potential for reducing LOI by elimination of the highest temperature regions in flames (through the annealing mechanism). One-dimensional calculations show the presence of an overall optimum temperature, but the effect of peak-temperatures in distinct zones within a real flame requires multidimensional calculations, and has not yet been investigated.

- the potential for reducing NO_x/LOI through improved pulverizers/classifiers. Next generation pulverizers and classifiers offer better performance, but the extent of the benefits to boiler operators is not clear. To what extent can LOI be reduced by finer or narrower particle size distributions? Is there a law of diminishing returns in LOI as progressively finer particles are rejected by the classifier and returned to the mill? Simulations are needed under realistic conditions to assess the potential for LOI reduction through improved grinding practices.

These questions will be addressed both through calculations in idealized environments and/or by perturbation analysis applied by post-processing to results obtained by multidimensional simulation. The latter technique will be carried out in collaboration with REI or with other groups offering complete sets of particle trajectories from converged simulations.

Task 3.2 Kinetics of Heterogeneous NO Reduction

Phase I work demonstrated high NO reduction reactivities for very young chars representative of those found in flames and reburning zones. This result suggests that heterogeneous processes have a significant effect in reburning, at least for some coal types. As envisioned in the original proposal, Phase II work will focus on the acquisition of quantitative kinetics needed for the design and optimization of reburning and other low-NO_x systems. Specific issues of special interest are:

- the role of residual volatile matter in very young chars. The high activity observed for bituminous chars in Phase I work may be attributable to a homogenous effect related to residual volatile matter. Experiments will be carried out with synthetic volatile matter to assess this contribution and separate it from the heterogeneous process.

- the effect of oxygen. Oxygen is present in the early stages of reburning environments and in the post-flame region of low-NO_x burner systems, but there is significant controversy over the effect of O_2 on NO reduction rates. The groups of Suuberg and Tomita have both observed enhancement of NO reduction by O_2, while Chen observes an inhibition.

- the effect of parent coal rank. Work by Chen et al. indicates large differences between the NO reduction activity of bituminous and lignite chars. The effect is larger than that seen in other oxidizing gases and requires confirmation and more data.

- the effect of char-bound nitrogen. Recent work by Spinti and Pershing show the apparent yield of char nitrogen to NO_x decreases with increasing NO level in the starting gas stream implying that the yield is a net value incorporating some NO/carbon reduction. Also, the Phase I results of this work include any NO produced from char

nitrogen in the reburning zone. To unravel the two competing effects, selected experiments will be performed in Phase II with nitrogen-free chars prepared from phenol-formaldehyde resins. These mineral and nitrogen-free chars have reactivities similar to coal chars and have been used extensively at Brown in gasification/ combustion studies.

To obtain the residence times and gas environments required for quantitative kinetics, Phase II experiments will be conducted in an electrically heated reactor (as foreseen in the original proposal). This reactor system is identical in most respects to the Phase I reactor, but uses electrical heating rather than vitiated air to maintain temperatures for longer residence times.

Task 3.3 Effect of Combustion Conditions on Carbon Adsorptive Properties

The largest driving force for reducing unburned carbon emissions is the set of regulations governing maximum permissible carbon content in fly ash for its use in concrete. Unburned carbon adsorbs the specialty surfactants used in concrete mixes, and can reduce the amount of entrained air below that required for adequate freeze/thaw resistance.

Recent work at Brown on a large set of fly ash samples from the field has shown that the deleterious effect of carbon is related not only to the amount of carbon present, but also to its specific adsorptive properties. The recent work clearly shows that the properties of unburned carbon are not constant, but vary depending on unit, parent coal, and firing configuration, etc.

One aspect of this problem that is not currently being addressed is the effect of combustion conditions on carbon adsorptivity. (The current projects focus on analysis of ash samples and techniques for mitigation). It is important that combustion studies that focus on carbon burnout, such as the ones proposed for Phase II, consider not only LOI, but also the specific adsorptive properties of the carbon formed and how they can be altered by temperature/oxygen histories during combustion or by parent coal choice. It is interesting that carbon limits in concrete are typically much lower in the western U.S. than in the eastern U.S. and it is not known to what extent this is necessary or reflects the rank-dependence of unburned carbon adsorptive properties.

Within the Brown University task we propose to carry out a limited set of experiments exploring this new issue. The experiments will be carried out in the same flame reactor facility as in Task 3.2, and under controlled conditions in which the temperature/oxygen history of the char particles is known. The activity of the samples toward concrete surfactants will be measured as a function of combustion residence time for two parent coals of differing rank. Additional experiments may be carried out at low oxygen concentration to mimic fuel-rich regions in the furnace that may produce highly nonpolar carbon surfaces that have been “cleaned” of surface oxides by the high-temperature reducing environment.

7.2.3 Task 4: Scale-Up Testing

The radially segmented in situ reburning nozzle developed at pilot-scale for U-fired systems will be tested in the DB Riley U-fired test facility as described in the original proposal.

7.2.4 Task 5: System Modeling

GLACIER will be used to aid the nozzle development, determine system impacts and form the basis of a fireside simulator.

Task 5.1 Burner System Modeling

GLACIER will be used to model the burner systems that will be tested in the L1500. The objective is to guide design and interpret the data. Once the optimum injection system has been defined for the three burner types, the appropriate furnace model will be modified to simulate the new injection system to assess how the firing system will perform at full-scale.

Task 5.2 Air Toxics Model Development

State of the art models describing the vaporization and condensation processes that control the formation of air toxics during coal combustion will be incorporated into *GLACIER* in this task. Drawing on the early studies at MIT, the refinements of the models by the DOE-sponsored research headed up by PSI on the "Toxic Substances from Coal Combustion-A Comprehensive Assessment", and the results coming out of the EERC Center on Air Toxic metals will be review and appropriately applied to the comprehensive codes. The model will be used to calculate the distribution of the toxic elements released by coal during combustion between the residual fly ash, the submicron condensation aerosol, and for selected elements (primarily mercury and thallium) the vapor phase. The model consists of components describing the vaporization and the formation of a submicron condensation aerosol at combustion temperatures and the post-combustion surface reaction and condensation of trace elements.

The mass of the submicron aerosol is composed primarily of the refractory oxides of iron, silicon, magnesium, and calcium and can be calculated using the model of Quann and Sarofim (1983) which takes into account the augmentation of vaporization of the refractory oxides to the suboxide (SiO) or the element (Fe, Mg, Ca). The rate of vaporization of the refractory oxides is a function primarily of the particle temperature and element concentration but is also a function of the char particle size and the mineral inclusion size. The strong temperature dependence of the extent of vaporization as shown in Figure 7.8 for the vaporization of the elements in a Montana lignite (Mims et al., 1980); this underlines the importance of having the correct particle temperature distribution in any air toxic model, one of the strengths of using the *GLACIER* code for the simulation. The extent of vaporization is small enough that it will not influence the particle temperature and therefore it can be calculated in a post processing routine in *GLACIER* from the temperature and burnout histories of individual coal/char particles.

The mixtures of SiO, Fe, Ca, and Mg produced by the char particles, once they diffuse out of the locally reducing atmosphere within the char particles, will reoxidize in the particle boundary layers and form a submicron aerosol the size of which can be calculated from amount vaporized and the residence time from the equations governing aerosol dynamics (e.g., Neville and et al., 1981). In *GLACIER* this is achieved by calculating the vapor accumulation of a particle ensemble along a trajectory and obtaining the size and mass of the submicron aerosol.

The fractional vaporization of individual trace elements is often higher than that of the refractory oxides as is seen in Figure 7.9 and 7.10 for zinc and arsenic; but the mass of trace elements in the aerosol will be small relative to those of the refractory oxides (sodium is a special

case of a volatile species which is not in trace amounts and which may, for some high sodium coals, represent a major fraction of the submicron aerosol). The vaporization of the trace element is a function primarily of particle temperature and coal type. The coal type dependence is primarily one of concentration as was shown by Quann et al. (1990) in a study of the combustion of twenty coals at a fixed furnace temperature and oxygen concentration. For example, the amount of arsenic in the submicron aerosol was found to be approximately proportional to the concentration of the arsenic in the coal (Figure 7.10). Under the DOE funded research at PSI (Senior et al., 1997), it was found that the arsenic vaporization can be calculated by modifying the Quann vaporization model to allow for the fact that the arsenic is present primarily in trace amounts in pyrites and that its vapor pressure is accordingly reduced, due to its reduced activity and the diffusion resistance in the pyrite inclusions. Other trace elements associated with the pyrites or the aluminosilicates can be treated by the same modified Quann model in which the activity of the trace elements in the mineral inclusions is used to correct the vapor pressure used in the vaporization equation. Elements that are bound in the organic matrix need to be modeled differently, assuming that the organically bound material is released with a high efficiency, deduced from the existing experimental database, with the volatiles.

Finally the air toxic model needs to allow for the post-flame reaction and condensation of the trace elements on the fly ash. A number of the vaporized elements are known to react with the silicates in the ash in the post-flame zone. Indirect evidence for this is provided by the reduction in the amount of sodium that is found in the submicron ash by increases in silica in the ash and the reduction of arsenic and zinc with increases in the concentrations of the calcium. The results of the zinc vaporization for the twenty coal study shows the reduction in the vaporization rates for the zinc for the lower rank coals (open symbols) which have a high calcium content. Kinetics to calculate the post flame capture by the silicates for sodium and other trace elements are being developed Wendt (1997 and co-workers). These kinetics as they are developed will be incorporated into *GLACIER* to calculate the post-flame capture of the trace elements by the ash from the concentrations, temperatures, and ash surface areas along particle trajectories.

Condensation on the ash as the combustion products are cooled will be calculated using the Fuchs-Sutugin relation to allow for the transition from free molecular to continuum diffusion in going from free molecular to residual ash. Mercury needs to be treated differently as it does not condense but is absorbed by carbon in the ash. The absorption of mercury can be estimated from: 1) the carbon content of the ash, values for which are currently calculated by *GLACIER*; 2) the speciation of mercury, which can be obtained by calculating, along gas flow paths, the fractional transformation of elemental mercury to mercuric chloride using recently developed kinetics for the chlorine-mercury reaction; and 3) adsorption kinetics for the different mercury species on char, best measured for the char in question or estimated from the limited data on comparable chars in the literature.

Task 5.3 Simulator Development

After consulting our utility partners who will help us define the requirements for a fireside simulator that can be operated on a personal computer by a non-CFD expert, we will prepare a beta version for delivery to the Utility for testing.

The simulator which could be for a wall- or corner-fired unit will have the capability to assess the impact of low-NO_x firing conditions on unburned carbon and air toxic emissions. The variables that can be evaluated will include, but not necessarily be limited to:

- coal type,
- coal size by burner,
- air distribution through burners and OFA to vary vertical staging,
- OFA location, and
- coal distribution at the injector.

7.3 REFERENCES

Mims, C. A., Neville, M., Quann, R. J., House, K., and Sarofim, A. F., (1980), J. Amer. Inst. Chem. Eng. Symp. Ser.,76, 201, 186-194.

Neville, M., Quann, R. J., Haynes, B. S., and Sarofim, (1981),A. F., Eighteenth Symposium (International) on Combustion, pp. 1267-1274, The Combustion Institute, Pittsburgh, PA,.

Quann, R. J., and Sarofim, A. F., (1983), Nineteenth Symposium (International) on Combustion, pp. 1429-1440, The Combustion Institute, Pittsburgh, PA,.

Quann, R. J., Neville, M., and Sarofim, A. F., (1990),Comb. Sci. and Tech., 74, 245-265.

Senior, et al., (1997), 'Toxic Substances from Coal Combustion – A Comprehensive Assessment", Advanced Coal-Based Power and Environmental Systems '97 Conference, FETC, Pittsburgh, PA.

Wendt, J. O. L., (1997), "Mechanisms Governing the Partitioning of Semi-Volatile Alkali and Toxic Metals During Waste and Waste Fuel Combustion", Keynote Paper, First International Symposium on Incineration and Flue Gas Treatment Technologies, I. Chem. E., Rugby, U.K.

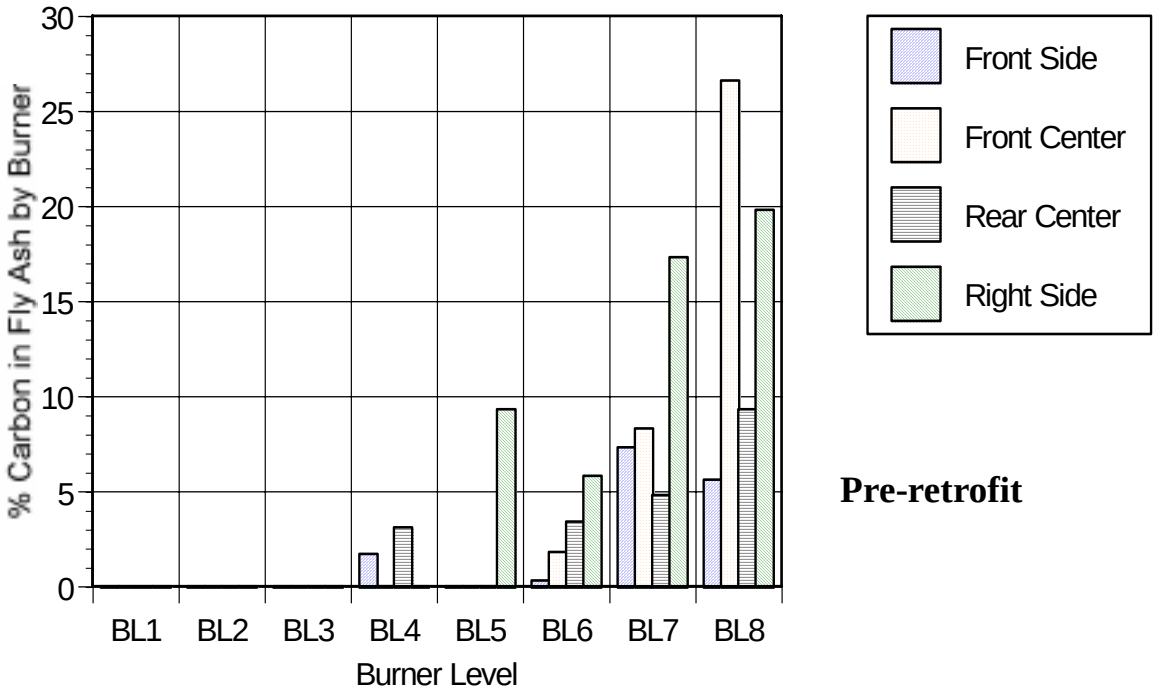

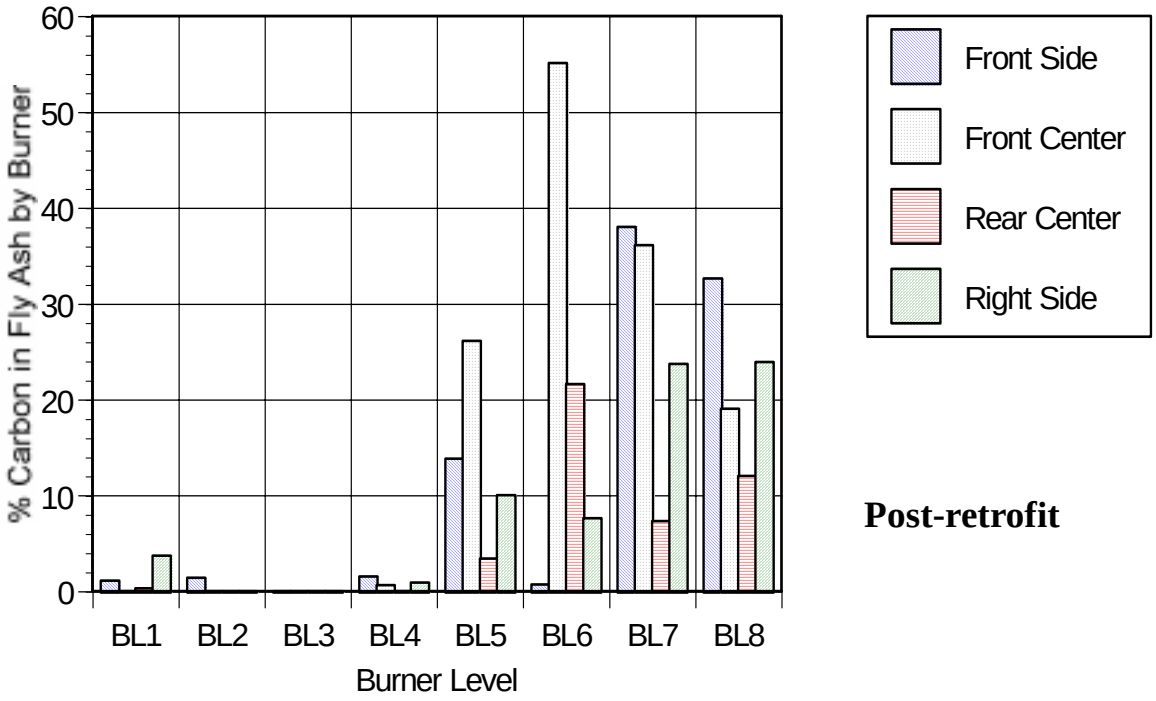

Figure 7.1 Pre-retrofit and post-retrofit carbon in fly ash by burner.

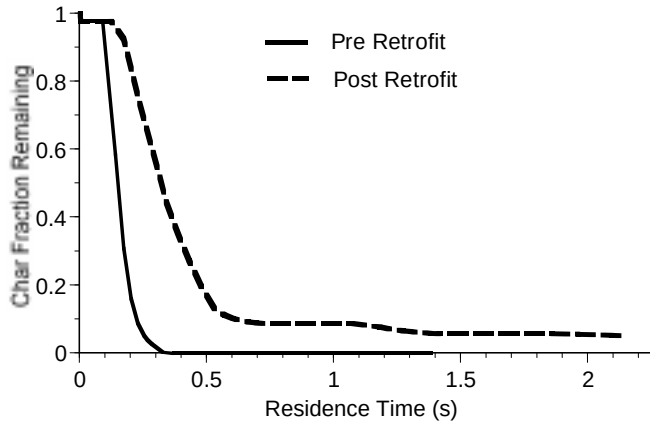

a) 43 micron coal particle entering from the front center level 6 in nozzle

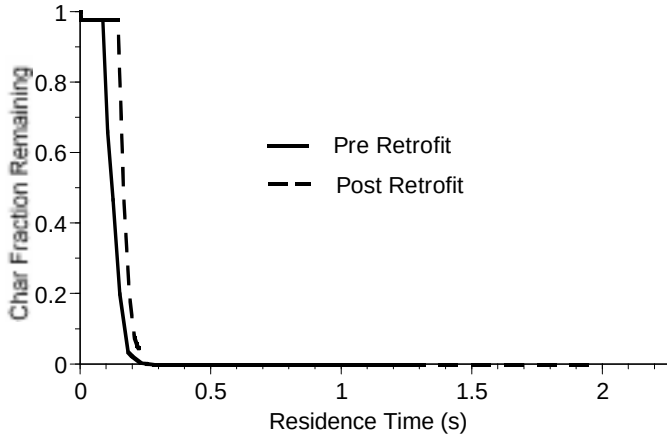

b) 85micron coal particle entering from the front center level 6 in nozzle

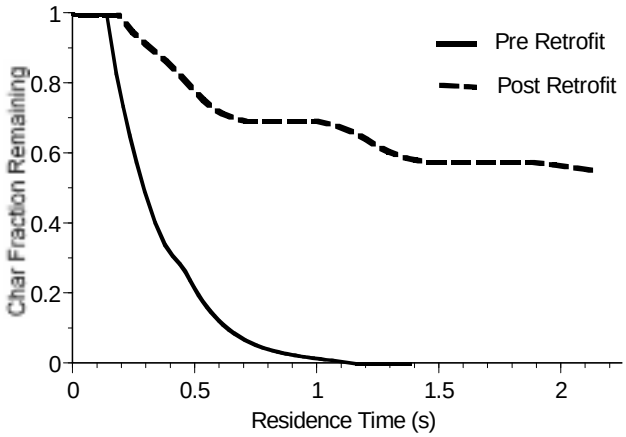

ca) 43 micron coal particle entering from the front side level 6 in nozzle

Figure 7.2 Fractional char remaining as a function of residence time.

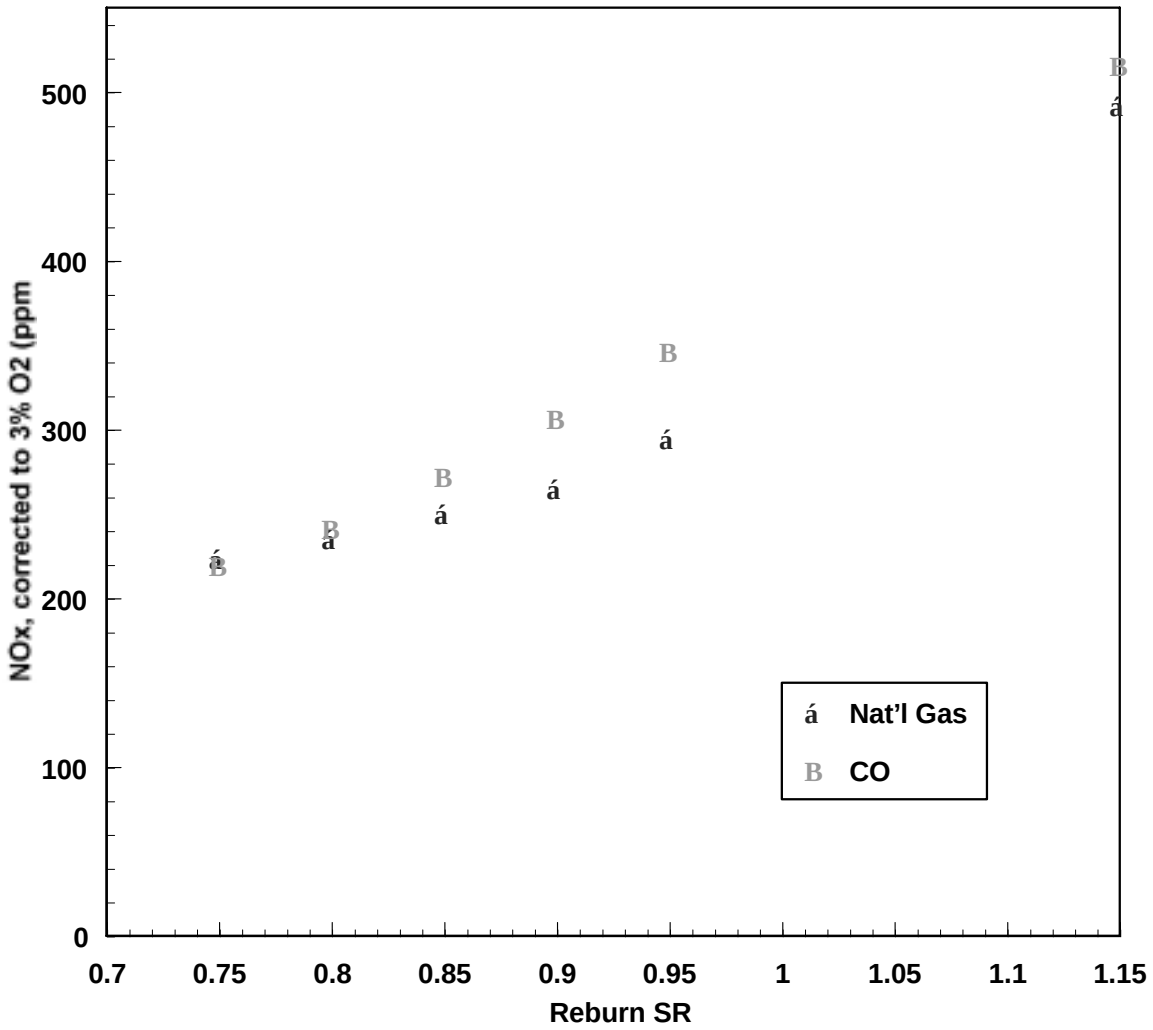

Figure 7.3 NO_x as function of reburn stoichiometric ratio for natural gas and CO injection.

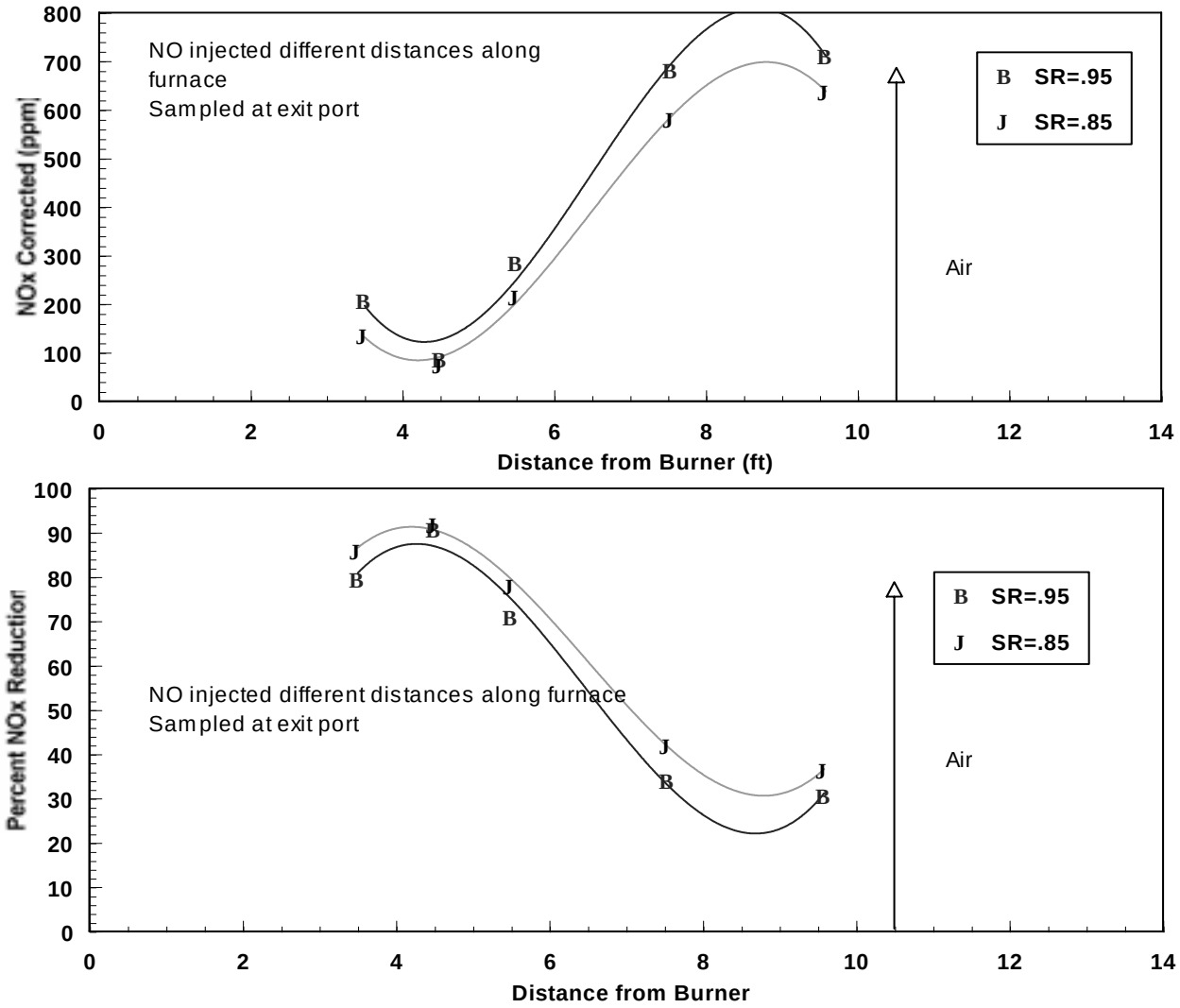

Figure 7.4 NO Rreduction for SR = 0.85 and SR = 0.95.

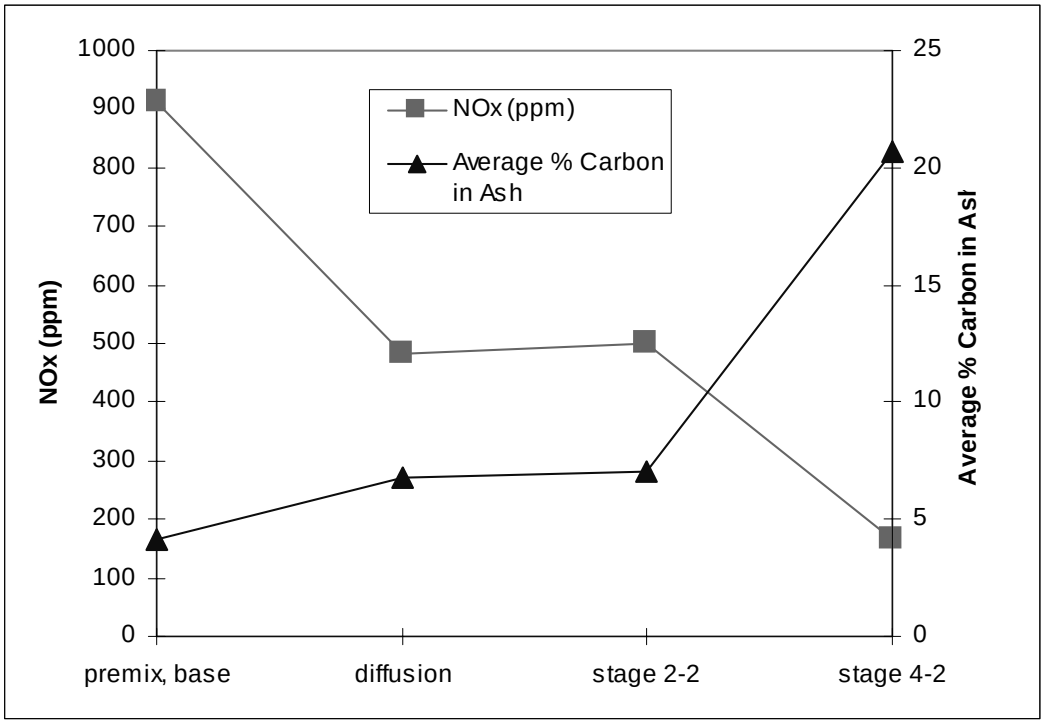

Figure 7.5 Impact of combustion conditions on NO formation and LOI.

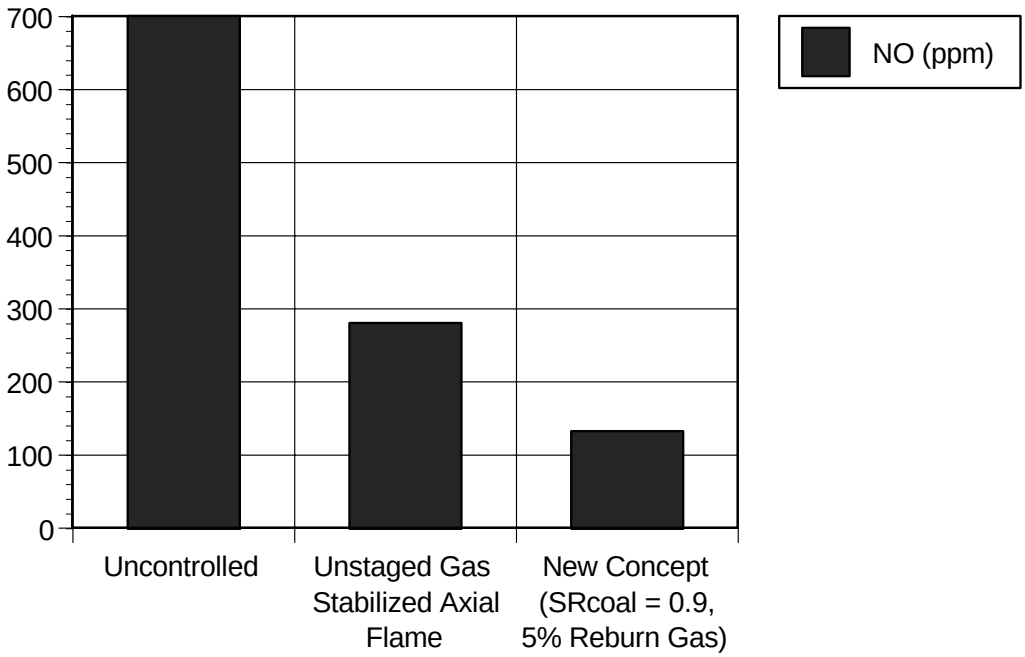

Figure 7.6 Effectiveness of in situ reburning.

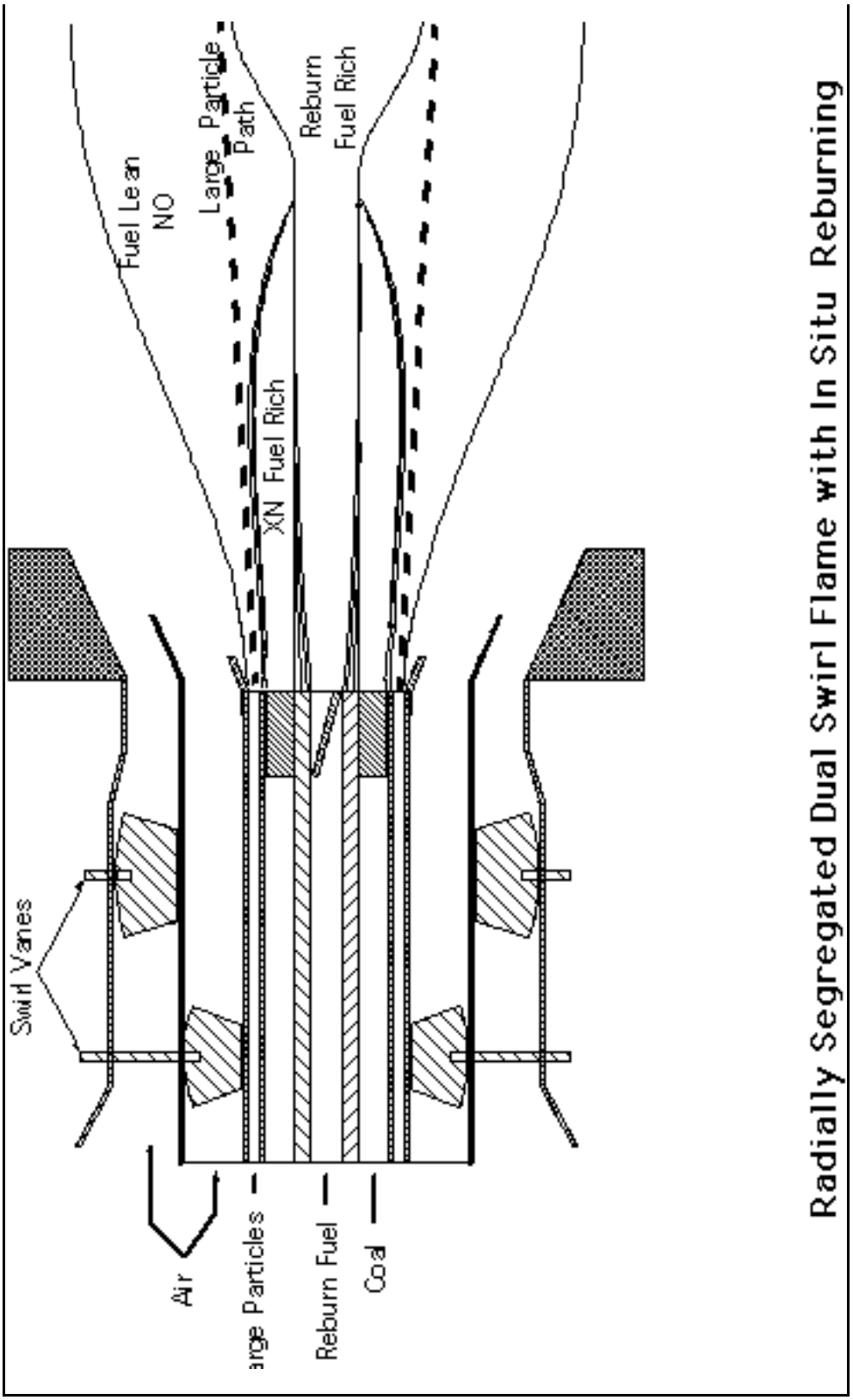

Figure 7.7 SPPC burner.

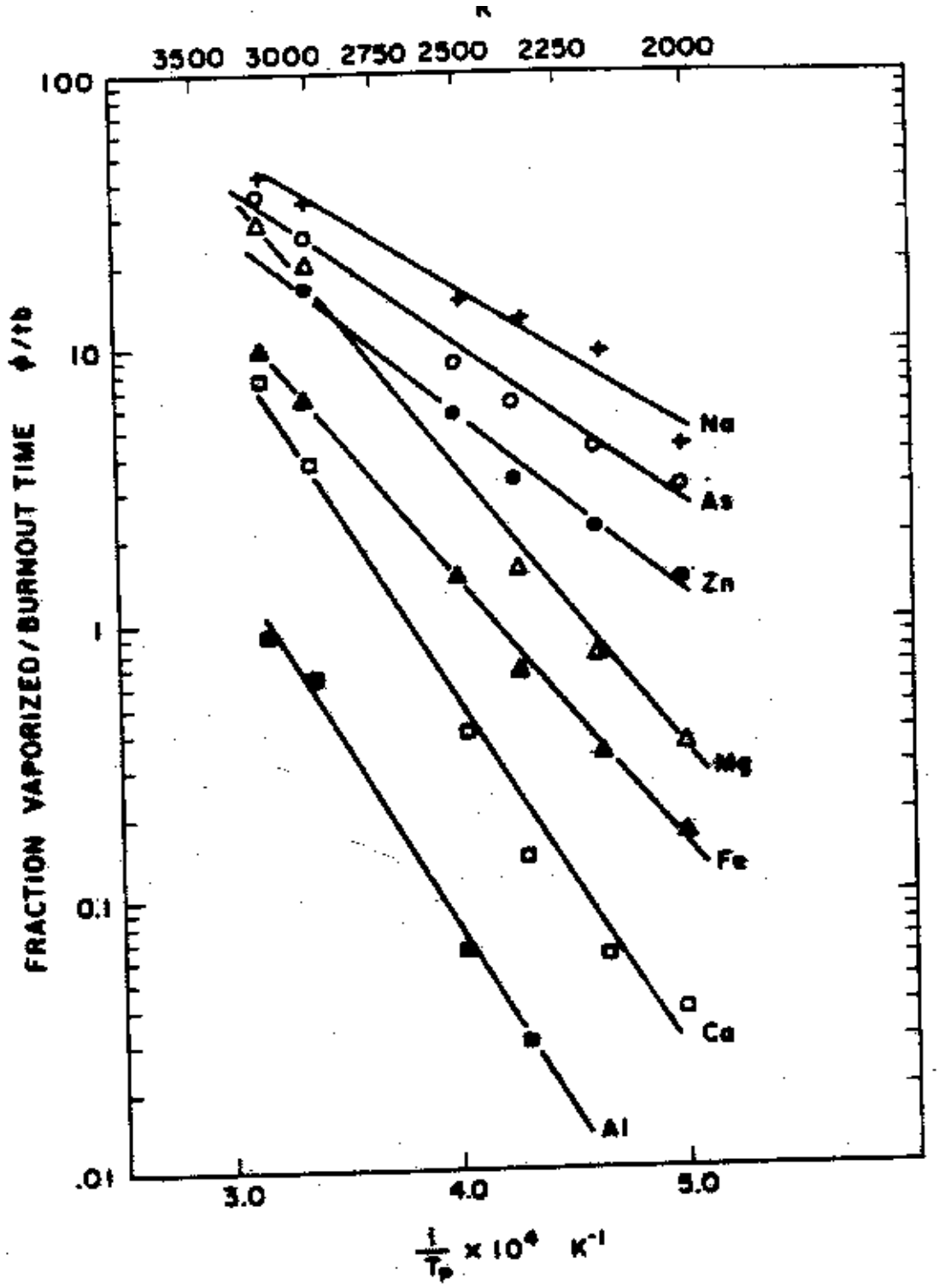

Figure 7.8 Elemental vaporization as a function of temperature.

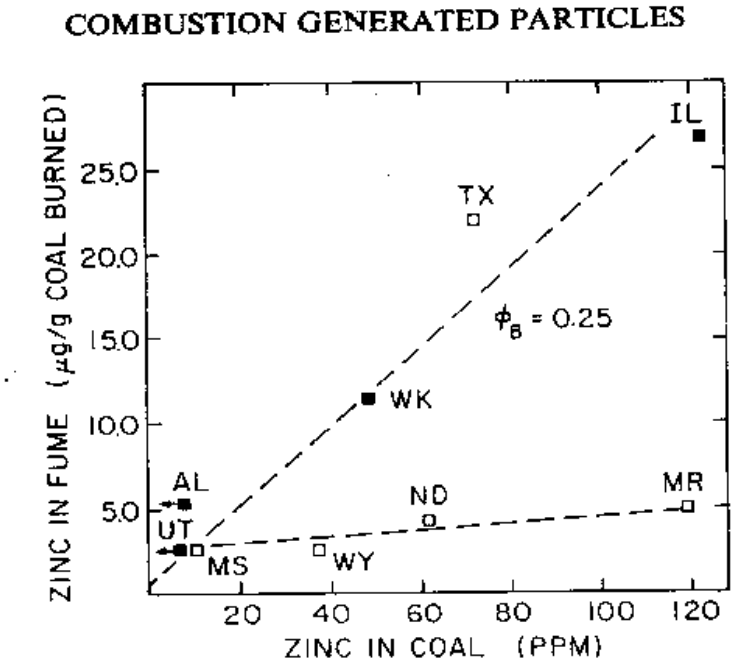

Figure 7.9 Effect of zinc in coal on zinc in fume.

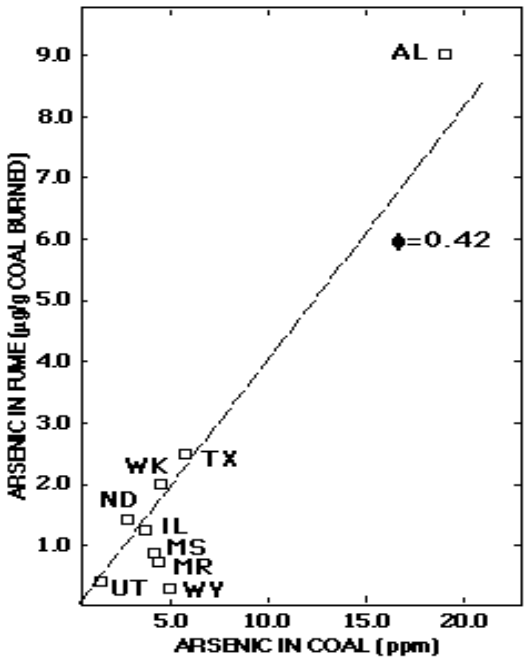

Figure 7.10 Effect of arsenic in coal on arsenic in fume.